Theoretical Investigation of Cold Alkali Atom Collisions

by

James Patrick Burke, Jr.

B.S., Georgia Institute of Technology, 1989

M.S., Georgia Institute of Technology, 1991

A thesis submitted to the

Faculty of the Graduate School of the

University of Colorado in partial fulfillment

of the requirements for the degree of

Doctor of Philosophy

Department of Physics

1999

This thesis entitled:
Theoretical Investigation of Cold Alkali Atom Collisions
written by James Patrick Burke, Jr.
has been approved for the Department of Physics

Chris H. Greene

John Cooper

Date

The final copy of this thesis has been examined by the signatories, and we find that both the content and the form meet acceptable presentation standards of scholarly work in the above mentioned discipline.

Burke, Jr., James Patrick (Ph.D., Physics)

Theoretical Investigation of Cold Alkali Atom Collisions

Thesis directed by Prof. Chris H. Greene

Theoretical techniques are developed to solve the coupled Schrödinger equations that describe cold magnetically trapped alkali atom dynamics. In particular, a multichannel quantum defect formulation is presented to separate cleanly the atom-dependent from the atom-independent contributions to the final scattering matrices. The resulting approach provides a more comprehensive understanding of cold alkali collisions and improves substantially on the efficiency of calculations. Improved Rb two-body interaction potentials are extracted from measured ^{87}Rb inelastic collision rates and from the measured position and width of a ^{85}Rb Feshbach resonance. Using these state-of-the-art potentials, specific atomic hyperfine states have been identified whose collisional properties suggest intriguing possibilities for interesting and novel degenerate gas studies. In addition, a detailed analysis of ^{39}K photoassociation lineshapes has permitted the determination of accurate two-body interaction potentials for this atom as well. Finally, three-body recombination of doubly polarized trapped atoms is investigated. Two qualitatively different mechanisms which control the recombination rate are identified for positive and negative two-body scattering lengths a. Surprisingly, the recombination rate is found to scale approximately as a^4 in both cases.

To Angela

Acknowledgements

This work would not have been possible without support from many people. First and foremost, I would like to thank my advisor Chris Greene. Chris has shown uncommon patience and determination in his attempt to teach me the finer points of atomic collision theory. I feel very fortunate to have had this opportunity to study under a person of his stature.

I am also grateful that Chris guided me in the direction of cold atomic collisions. In the course of this study I have crossed paths with a number of outstanding scientists. Notable among this group is John Bohn, who arrived at JILA at about the time this project started. John has proved to be an extremely patient "sounding-board" during my ongoing struggles with this subject and in the process, he has managed to teach me a great deal of physics. John has been involved to some degree in almost all of the work presented here, and he has provided many constructive comments on this dissertation.

The Greene group has had a number of postdocs and graduate students from whom I have benefited. Of this group, I would like to single out Brett Esry who has helped me appreciate the fine art of numerical computing and taught me a great deal about many-body physics. Chapter 8 is the outgrowth of a project Brett and Chris originally started. In addition, I would like to thank Hugo van der Hart, Dörte Blume, William Clark, Kurt Meyer, and Brian Granger for many useful discussions.

An advantage of working at JILA is the active experimental program that is being pursued. In particular, I would like to thank the Cornell-Wieman-Jin experimental group studying BEC and degenerate Fermi gases for providing us with the opportunity to model some really marvelous experiments. I would like to thank Chris Myatt, Eric Burt, Jake Roberts, Neil Claussen, and Rich Ghrist for providing a glimpse into the experimental world. In addition, I want to recognize the members of my thesis committee, John Cooper, Eric Cornell, Carl Wieman, and David Nesbitt for constructive comments on this manuscript.

The photoassociation work presented in Chapters 6 and 7 resulted from a collaboration with the experimental group of Bill Stwalley, Phil Gould, and He Wang. I would like to thank them for allowing us to analyze their data and for being so cooperative with what probably seemed like an endless barrage of questions.

Also, I would like to thank Paul Julienne, Carl Williams, and Eite Tiesinga for many useful discussions regarding both photoassociation theory and cold collision theory.

On a personal note, I am indebted to my parents for their support and encouragement over all these years. My wife has probably worked harder for my degree than I have. Without her sacrifice, I would have had to end my involvement with this project long ago. Angela, thank you for hanging in there. And last but certainly not least, I want to recognize my children, Julia and Joel, just for putting a smile on my face each day.

This work would not have been possible without financial support from the National Science Foundation.

Contents

Chapter

Figures

Figure

Tables

Table

Chapter 1

Introduction

The study of particle collisions has a long and storied history in the annals of scientific exploration. Much of our understanding of the fundamental nature of particles and their underlying microscopic interactions has been derived from scattering experiments. A famous example is the work of Ernest Rutherford, who in 1911 scattered alpha particles off thin gold foil. He quickly realized that the only explanation for the observed distribution of backscattered particles was the presence of a charged massive core concentrated within a tiny spatial region. He thus discovered the nucleus and proposed a celestial model for the atom, with electrons orbiting a massive central nucleus. Soon thereafter, Neils Bohr combined his quantum theory of light with Rutherford's model to build a theory of the hydrogen atom and with it modern atomic physics was born.

The existence of atoms (or at least something called atoms) had been accepted in some scientific circles hundreds of years earlier. One of the first gas dynamics experiment was performed by Robert Boyle who discovered in 1662 the inverse relationship between the volume and pressure of a gas. This relationship was independently verified by Mariotte[1] five years later. However, it was probably Bernoulli (1739) who first recognized that the pressure of a gas is a result of collisions between the particles and the container. The development of the kinetic theory of gases by Maxwell, Boltzmann, Krönig, and Clausius, among others, was begun in the mid-1800's to combat the hopeless task of evaluating each individual particle's contribution to the bulk properties of the gas. Kinetic theory replaces the individual particle motion with average quantities based on the statistics of the sample. From these considerations, Maxwell developed his theory of velocity distributions (1860). A key concept in kinetic theory is that any disturbance in one part of the gas is transmitted throughout by particle collisions. In this manner, energy (thermal conductivity), momentum (viscosity), and mass (diffusion) can be moved around within the gas. Boltzmann (1872) (improving on an earlier result of Maxwell's) derived a nonlinear integrodifferential equation that describes the evolution of an initially non-uniform gas and, from which, these transport properties can be calculated. Treating the gas particles as tiny classical "billiard balls" bouncing off one another, Maxwell found that the viscosity of a gas is independent of its density. His

subsequent experiments validated this surprising result, which proved to be one of the first successes for the classical kinetic theory of gases and thus for the underlying mechanism of particle collisions. (Later measurements showed that this result is not exact for real gases but it is a good approximation at moderate densities).

With the development of quantum mechanics and a better understanding of the structure of atoms, it became clear that atomic collisions are a much more complicated process than envisioned by Maxwell and his fellow 19th century scientists. However, classical kinetic theory continues to provide a reliable method for determining the macroscopic properties of a gas, provided quantum mechanical collision cross sections are used in place of the corresponding classical scattering cross sections. In the particular case of dilute monatomic gases, Chapman (1916) and Enskog (1917) were able to show that classically, the bulk transport properties are related to integrals over the interatomic potential energy surfaces. This provided the first direct link between macroscopic properties of the gas and the underlying microscopic forces that atoms exert on one another. With it came the obvious question: can a study of the bulk properties of a gas be used to understand the underlying atomic interactions? Given the complexity of the relationship, the answer was far from obvious, but over the last half-century great strides have been made (see for example Ref.[2]). (Transport measurements are not the only avenue to obtain this information but they are the most relevant for this particular work). In particular, the temperature dependence of the viscosity of a gas has yielded useful information about the interatomic potential. This is due in large part to the fact that viscosity can be measured much more accurately than other transport properties. Measurements over the temperature ranges from tens of degrees Kelvin to several thousand degrees Kelvin have been made for both pure and binary mixtures of dilute gases, primarily by the groups of Smith[3], Guevara[4], and Kestin[5].

Further departures from the classical physics of Maxwell's day arose with the development of laser cooling and trapping of neutral atoms (1985, see Ref.[6, 7]). The translational motion of the atoms can now be slowed to the point where the effects of quantum statistics begin to affect the overall behavior of the gas. Probably the biggest single achievement in this regard has been the realization of a Bose-Einstein condensate (BEC), first seen here at JILA (1995) in a dilute gas of ^{87}Rb[8] atoms and quickly followed by observations in gases of ^{7}Li[9] and ^{23}Na[10] atoms. It has since been observed by nearly twenty groups (see http://amo.phy.gasou.edu/bec.html for the latest BEC developments). Bose-Einstein condensation is a macroscopic quantum mechanical phase transition in which a large fraction of bosons spontaneously occupies the quantum mechanical ground state as its temperature approaches absolute zero. A condensate thus exhibits purely quantum mechanical properties on a macroscopic scale, which makes it unique.

Collisions play an important role both in the road to condensation and in the behavior of the condensate itself. Cooling atoms with laser light has thus far proven insufficient to produce BEC. Instead, it has proven necessary to use evapo-

rative cooling techniques to maintain the phase space density required for condensation. With evaporative cooling, the atoms are loaded into a magnetic trap that is approximately harmonic. A radio-frequency field is then applied, lowering the trapping potential so that only the "hottest" (i.e., most energetic) atoms are removed from the trap. The remaining atoms are left to re-thermalize to a colder temperature via elastic collisions. These elastic collisions are loosely termed "good" collisions, since they are an essential part of the cooling process. On the other hand, magnetic traps are extremely weak, with depths on the order of few milliKelvin. If a pair of atoms should collide and "flip" a spin, they may end up in untrapped spin states or the collision may release enough energy to eject the pair from the trap. Either outcome constitutes a "bad" inelastic collision. A general rule of thumb devised by experimentalists is that about 100 good elastic collisions are needed for every bad inelastic collision if the cloud is to re-thermalize sufficiently quickly to condense the gas before too many atoms are lost.

Once a condensate is produced, its properties are almost wholly determined by the s-wave two body scattering length a (which is related to the elastic scattering cross section in the $T \to 0$ limit). In fact, the sign (positive or negative) of the scattering length determines whether condensates comprised of large numbers of atoms can even be produced[11]. A variety of mean-field and Hartree-Fock approaches have been introduced for evaluating condensate properties, all of which adequately approximate the strength of atom-atom interactions using a mean-field interaction term that is proportional to a. (A good review of current BEC theories is provided in Ref[12].) In addition, modern kinetic theories that describe condensate formation[13] require atomic scattering input.

Another intriguing aspect of collisions in this cold regime is the prospect of using external fields to influence the outcome. One method proposed by Stwalley[14] is to induce a Feshbach resonance using a magnetic bias field. The resonance would in principle allow control over the s-wave scattering length. This was recently realized in ^{23}Na condensates[15] and in thermal Rb[16, 17] and Cs[18] clouds. In terms of condensates, the appeal of this idea is two-fold: 1) it provides a mechanism for enhancing the elastic collision rate, which could allow condensation of isotopes that are hard to cool otherwise (this is somewhat of a fine line since generally the inelastic collision rate is also increased near the resonance), and more importantly 2) it provides for "tunable" condensate properties. (Tunability was not achieved in the Na experiment because of a large increase in the three-body recombination rate. Whether this an inherent problem or instead is isolated to this particular Na experiment is still unresolved.) Magnetic-field tuning of the scattering length is possible only because the average collision energy of the atoms is much less than the atomic hyperfine splitting.

Extremely low collision energies also imply that the atoms interact with one another for a long time during a collision event. This makes the study of cold collisions an ideal method for understanding the weak long-range forces that atoms

exert on one anther. Photoassociation spectroscopy is a tool that has been successfully applied in this regard. The idea was first proposed by Thorsheim, **et al.**[19]. In photoassociation, an excited molecular bound state is resonantly formed through photoexcitation during the collision of two atoms, (e.g. with a CW laser). The low collision energies lead to well-resolved rotational (and in some cases hyperfine) spectra with linewidths approaching the natural linewidth. In particular, this technique has been extremely useful for measuring nodes and antinodes of the ground state colliding wave function (via the Franck-Condon overlap). In this way, accurate values for the s-wave scattering lengths have been derived for most of the alkalis. In addition, retardation effects[20] have been observed in excited Na_2 bound states[21], and accurate values of atomic lifetimes for ^{23}Na[21] and ^{39}K[22] have been derived from these bound state measurements.

This dissertation has developed and extended the theoretical tools necessary to calculate and understand two-body and three-body collisions of trapped alkali atoms. In brief, ground state two-body collisions comprise Chapters 2-5, while photoassociation spectroscopy is the subject of Chapters 6-7, and three-body collisions of ground state atoms are treated in Chapter 8.

The chapters are broken down as follows: the coupled Schrödinger equations for two-body ground state alkali collisions are derived in Chapter 2. Here, definitions for cross sections, scattering event rates, and scattering lengths are provided in terms of the scattering matrix. The interactions and the corresponding Hamiltonian for the colliding atom pair are also discussed in this chapter. Numerical techniques for obtaining the scattering matrix by solving the coupled Schrödinger equations are presented in Chapter 3. Chapter 4 develops a powerful alternative approach for evaluating the scattering matrix. Here, the ideas of multichannel spectroscopy[23] are applied to the two-body collision problem. The outcome is a short-range reaction matrix that incorporates the bulk of the scattering physics, yet remains essentially energy-independent over nearly a degree Kelvin. Simple algebraic manipulations allow the scattering matrix to be evaluated in terms of this reaction matrix and a set of long-range parameters. Moreover, these long-range parameters are "standardized" in a form that makes them nearly atom-independent. In addition it is shown that the reaction matrix can be approximated, with reasonable accuracy sufficient for survey calculation in most systems, entirely in terms of single channel parameters and a recoupling matrix.

The theory developed in the previous chapters is then applied to a set of collision experiments conducted here at JILA. These results are discussed in Chapter 5. The new experimental information permitted us to refine the Rb interatomic interaction potentials. Based on these state-of-the art potentials, predictions of scattering observables are then provided for other Rb isotopes. The theory of photoassociation lineshapes is presented in Chapter 6. This theory is then applied in Chapter 7 to analyze measured rovibrational spectra of the ^{39}K 0_g^- state. This analysis extracted the first accurate values of the ^{39}K scattering lengths. Finally, Chapter 8 presents a

theory of three-body recombination, a process in which two atoms recombine into a molecule along with the conversion of the excess binding energy into kinetic energy. Three-body recombination is an extremely difficult problem and Chapter 8 will only scratch its surface. However, from our investigation of doubly-spin-polarized atoms using model potentials, we have been able to uncover universal systematics of the recombination process.

Chapter 2

Coupled Schrödinger equations for two-body collisions

This chapter presents the two-body scattering theory of cold ground state alkali atoms. Section 2.1 begins with the coupled Schrödinger equations that describe the two-body collision dynamics. In addition, the appropriate scattering boundary conditions applied to these coupled differential equations are discussed. Physical observables of primary interest include scattering cross sections, event rates, and scattering lengths which are derived in subsections 2.1.1 and 2.1.2. In particular, the identical particle aspects of scattering by spin-dependent potentials are handled in detail. Section 2.2 discusses the physical interactions included in the coupled Schrödinger equations. These are the Born-Oppenheimer potentials (subsection 2.2.1), the atomic hyperfine Hamiltonian (subsection 2.2.2), the magnetic dipole-dipole interaction (subsection 2.2.3), and the effects of an external magnetic field (subsection 2.2.4). The coupled Schrödinger equations can be solved in any of several different angular momentum representations. Those of greatest importance are discussed in section 2.3. Subsection 2.3.1 develops the symmetrization of each representation while subsection 2.3.2 presents the unitary transformations between representations.

2.1 Scattering theory

Quantum two-body scattering theory is a well established subject presented in numerous textbooks (see for example, Ref.[24, 25]). However, scattering of identical particles with spin is still a tricky subject which can often lead to factor of two errors if one is not careful. I begin by briefly deriving a very general form of the coupled Schrödinger equations. The most general form of boundary conditions applied here is given in terms of a scattering amplitude $f(\theta, \phi)$. Subsection 2.1.1 relates the symmetrized scattering amplitude $f(\theta, \phi) + f(\pi - \theta, \pi + \phi)$ to the scattering cross section and and to the event rate. While these relationships are derived within the Born approximation, they should have applicability to nonperturbative processes. At the end of this subsection, the physical observables are still given in terms of the Born integrals over the potential. These integrals are related to

symmetrized scattering $\underline{S}$ and transition $\underline{T}$ matrices in subsection 2.1.2. In particular, the four spin permutations of identical particle scattering for both isotropic and anisotropic potentials are examined carefully, tracking all factors of two. The final relationships among the cross sections, event rates, and scattering lengths in terms of the symmetrized $\underline{S}$- and $\underline{T}$-matrix elements are given in this subsection.

The forces on an atom in a trap depend, to a good approximation, only on the atom's position in the trap and not explicitly on time. The time independent Schrödinger equation

$$H\Psi = E\Psi \tag{2.1}$$

is therefore a proper starting point to describe the collision physics. A standard approach for solving two-body collision problems is to separate the center-of-mass motion from the relative motion of the atoms. This step is valid provided the forces on the two colliding atoms (labeled a and b) depend only on their relative orientation $\vec{R} = \vec{r}_a - \vec{r}_b$ and not their absolute position. Separating coordinates sounds a little counterintuitive since the goal of this theory is to describe **trapped** atoms. The "degree" of coordinate separability can be established by considering the relevant length scales in our problem. First, the range of a cold scattering event is roughly $R \leq 10^3$ Bohr. Typical magnetic trapping fields can be described accurately by an anisotropic harmonic potential which in the center-of-mass coordinate system is given by $V = \frac{1}{2}\mu(\omega_x x^2 + \omega_y y^2 + \omega_z z^2)$. Here $R^2 = x^2 + y^2 + z^2$, μ is the reduced mass of the pair, and ω the angular frequency of the trapping field. A pure quadratic field is still separable as is evident from the coordinate dependence in V. It is only the presence of anharmonic terms (e.g., $V \propto R^3$) which would couple the center-of-mass and relative motions. However, these anharmonicities are several orders of magnitude smaller than the quadratic potential. Considering the isotropic case and plugging in typical values for ^{87}Rb collisions ($\omega \sim 100$ Hz), the harmonic trapping potential adds an additional 1μK of energy only when the internuclear separation is larger than $R \sim 3(10^6)$ a.u., well beyond the distance one needs to consider for collisions. The trapping fields can therefore be safely neglected, which permits the center-of-mass motion to be removed from the scattering problem.

A multicomponent wave function representing the relative motion of the particles can be written in spherical coordinates as

$$\Psi = R^{-1} \sum_{lmk} F_{lmk}(R) Y_{lm}(\theta,\, \phi) \chi_k \ . \tag{2.2}$$

Here, the angular degrees of freedom are represented by an expansion in spherical harmonics Y_{lm}. (This is the partial wave expansion treated in textbooks). The spin degrees of freedom are labeled χ_k and $F_{lmk}(R)$ represents a set of radial functions to be determined. Insertion of this form for Ψ into Eq. 2.1 and projection onto $Y_{l'm'}\, \chi_{k'}$

leads to an infinite set of coupled differential equations of the form ($\Phi_i \equiv Y_{lm}\chi_k$)

$$\sum_f \left[\delta_{fi}\left(-\frac{1}{2\mu}\frac{\partial^2}{\partial R^2} + \frac{l_f(l_f+1)}{2\mu R^2} - E\right) + V_{fi}(\vec{R})\right] F_{fi} = 0 \ . \tag{2.3}$$

The interaction potentials $V_{fi}(\vec{R})$ will be discussed in section 2.2. If the interaction potentials are isotropic, a finite set of coupled Schrödinger equations are obtained for each partial wave l, of which, only l=0-4 typically need to be considered for collision energies below a few mK. The coupled Schrödinger equations (Eq. 2.3) are solved subject to the following boundary conditions:

$$\begin{aligned} F_{fi}(0) &= 0 \\ F_{fi}(R) &\overset{R\to\infty}{\longrightarrow} \sqrt{\frac{2\mu}{\pi\hbar^2 k_i}}\left[\frac{e^{-i(k_i R - l_i\pi/2)}\delta_{fi} - e^{i(k_i R - l_i\pi/2)}S_{fi}}{2i}\right] \end{aligned} \tag{2.4}$$

where $k_i = \sqrt{2\mu E_i/\hbar^2}$. The amplitude of the wave scattered from channel i into channel f is given by the scattering matrix element S_{fi}. All experimentally observable collision quantities can be expressed in terms of the scattering matrix. In practice, it is more convenient to work with a real-valued reaction matrix $\underline{K}$ instead of the complex-valued $\underline{S}$ matrix. This will be discussed in Section 3.2. The asymptotic boundary condition on F_{fi} implies that the total wave function behaves in the large R limit as:

$$\Psi_i^+ \overset{R\to\infty}{\longrightarrow} \sum_f \Phi_f \left(e^{i\vec{k_f}\cdot\vec{R}}\delta_{fi} + \frac{e^{ik_f R}}{R} f_{fi}(\theta,\phi)\right) \tag{2.5}$$

Here, the scattering amplitude $f_{fi}(\theta,\phi)$ takes on the role of the scattering matrix and the exact relationship between the two quantities is derived in Section 2.1.2. In the case of identical particle scattering, the total wave function must be an eigenfunction of the nuclear permutation operator P_{12}, i.e. the wave function must be symmetrized. The boundary condition on the symmetrized wave function Ψ^+ is then given by

$$\begin{aligned} \Psi_i^+ \overset{R\to\infty}{\longrightarrow} \sum_f \Phi_f \Bigg(&\frac{e^{i\vec{k_f}\cdot\vec{R}} + e^{-i\vec{k_f}\cdot\vec{R}}}{\sqrt{2}}\delta_{fi} \\ &+ \left[\frac{(f_{fi}(\theta,\phi) + f_{fi}(\pi-\theta,\pi+\phi)}{\sqrt{2}}\right]\frac{e^{ik_f R}}{R}\Bigg) \end{aligned} \tag{2.6}$$

and the physical observables are determined by the symmetrized scattering amplitude $f_{fi}(\theta,\phi) + f_{fi}(\pi-\theta,\pi+\phi)$. The scattering amplitudes will be related to the physical quantities of interest in cold collisions (i.e., cross sections, event rates, and scattering lengths) in the next subsection.

2.1.1 Derivation of the cross section and event rate formulas

The Born approximation can be used to derive cross section and event rate formulas, in a way that brings out the structure of the scattering amplitudes and therefore makes the identical particle aspects of the scattering theory more transparent. First, consider the scattering of two non-identical spinless particles. The initial wave function in the center-of-mass coordinate system can be described by a plane wave e^{ik_iZ} Here, particles a and b approach from $\theta = 0$ and $\theta = \pi$, respectively. The time-independent wave function that obeys outgoing-wave boundary conditions obeys the integral equation[25]

$$\Psi^+ = e^{ikZ} + \int d^3R'\, G^+(R,R')\, V(R')\, \Psi^+(R') \tag{2.7}$$

where $\vec{k}_i = k\hat{Z}$ and the free particle Green function is

$$G^+(\vec{R},\vec{R}') = -\frac{2\mu}{4\pi\hbar^2}\frac{e^{ik|\vec{R}-\vec{R}'|}}{|\vec{R}-\vec{R}'|}\ . \tag{2.8}$$

In the limit of large R, $|\vec{R}-\vec{R}'| \simeq R - R'\hat{R}\cdot\hat{R}'$ and the Green function becomes

$$G^+(\vec{R},\vec{R}') \cong -\frac{2\mu}{4\pi\hbar^2}\frac{e^{ik_fR}}{R}\, e^{-i\vec{k}_f\cdot\vec{R}'} \tag{2.9}$$

where $\vec{k}_f \overset{R\to\infty}{\longrightarrow} k\hat{R}$. Using the first Born approximation for Ψ^+, I obtain a final expression for the scattered wave function

$$\Psi^+ \overset{R\to\infty}{\longrightarrow} e^{ikZ} - \frac{e^{ikR}}{R}\,\frac{\mu}{2\pi\hbar^2}\int d^3R'\, e^{-i\vec{k}_f\cdot\vec{R}'}V(R')e^{ikZ'}\ . \tag{2.10}$$

The non-identical particle scattering amplitude $f(\theta,\phi)$ can then be extracted by comparing equation 2.5 with 2.10. The integrals in equation 2.10 will be expressed in terms of T-matrix elements in subsection 2.1.2

I turn next to the adaptation of this derivation to the case of identical particle scattering. The permutation operator P_{12} commutes with the Hamiltonian of our system and can be used to obtain new eigenfunctions with the proper symmetry. For the moment, the spin degrees of freedom will be suppressed. These will be taken into account when actually evaluating the scattering amplitude integrals (subsection 2.1.2). For the sake of clarity, I will only treat collisions between identical bosons. The new wave functions are

$$\left(\frac{1+P_{12}}{\sqrt{2}}\right)\Psi_i = \frac{e^{ik_iZ}+e^{-ik_iZ}}{\sqrt{2}} \tag{2.11}$$

and

$$\left(\frac{1+P_{12}}{\sqrt{2}}\right)\Psi_f \quad \stackrel{R\to\infty}{\longrightarrow} \quad \frac{e^{ik_fR}}{R}\,\frac{\mu}{2\pi\hbar^2}\times \int d^3R'\,\frac{e^{i\vec{k}_f\cdot\vec{R}'}+e^{-i\vec{k}_f\cdot\vec{R}'}}{\sqrt{2}}\,V(R')\,e^{ik_iZ'}\ . \tag{2.12}$$

Here, P_{12} acts only on the unprimed coordinates (recall $\vec{k}_f = k\hat{R}$).

Equation 2.12 still needs a little work. First, note that the integral in Eq. 2.12 is symmetric in the Z' coordinate. Adding an integral over $e^{-ik_iZ'}$ and then dividing by two, gives the following properly symmetrized expression

$$\Psi_f \quad \stackrel{R\to\infty}{\longrightarrow} \quad \frac{e^{ik_fR}}{\sqrt{2}R}\,\frac{\mu}{2\pi\hbar^2}\times \int d^3R'\left(\frac{e^{i\vec{k}_f\cdot\vec{R}'}+e^{-i\vec{k}_f\cdot\vec{R}'}}{\sqrt{2}}\right)\,V(R')\,\left(\frac{e^{ik_iZ'}+e^{-ik_iZ'}}{\sqrt{2}}\right)\ . \tag{2.13}$$

Comparing Eq. 2.13 with Eq. 2.6, we find the following relationship for the symmetrized scattering amplitude

$$f(\theta,\phi)+f(\pi-\theta,\pi+\phi) \;=\; -\frac{\mu}{2\pi\hbar^2}\bar{M}_{fi} \tag{2.14}$$

where

$$\bar{M}_{fi} \;=\; \int d^3R'\left(\frac{e^{i\vec{k}_f\cdot\vec{R}'}+e^{-i\vec{k}_f\cdot\vec{R}'}}{\sqrt{2}}\right)\,V(R')\,\left(\frac{e^{ik_iZ'}+e^{-ik_iZ'}}{\sqrt{2}}\right)\ . \tag{2.15}$$

Mott and Massey[24] define the identical particle differential cross section as the ratio of the scattered radial flux to the incident flux in a **single** beam. The result is

$$\frac{d\sigma}{d\Omega_f} = \frac{k_f}{k_i}\left|f(\theta,\phi)+f(\pi-\theta,\pi+\phi)\right|^2\ . \tag{2.16}$$

This expression for the differential cross section will be rewritten in terms of symmetrized T-matrix elements in subsection 2.1.2. The numerical solution of equation 2.3 to obtain these symmetrized T-matrix elements is the subject of chapter 3.

We are interested not only in the scattering cross section but also in the event rate for collisions. To that end, consider the scattering of two particles from a different perspective. Place the particles into a large box of dimension L on each side. The Born approximation treats scattering of particles in a box as a transition between discretized eigenstates of the box (see, for example Ref[26]). The total transition rate Γ_{fi} from eigenstate $i \to f$ is an integral of the state-to-state transition

rate W_{fi} over all distinguishable final states. The "Fermi golden rule" can be used to determine W_{fi}, resulting in

$$\begin{aligned}\Gamma_{fi} &= \int k_f^2 d\Omega_f dk_f \left(\frac{L}{2\pi}\right)^3 W_{fi} \\ &= \frac{2\pi}{\hbar}\int d\Omega_f\, k_f^2 dk_f |M_{fi}|^2 \delta(E_f - E_i)\left(\frac{L}{2\pi}\right)^3 \end{aligned} \tag{2.17}$$

where $\left(\frac{L}{2\pi}\right)^3$ represents a density-of-states factor and the matrix element M_{fi} is given by

$$M_{fi} = \langle \Psi_f | V | \Psi_i \rangle = \int d^3R \left(\frac{e^{i\vec{k}_f\cdot\vec{R}} + e^{-i\vec{k}_f\cdot\vec{R}}}{\sqrt{2L^3}}\right) V(R) \left(\frac{e^{i\vec{k}_i\cdot\vec{R}} + e^{-i\vec{k}_i\cdot\vec{R}}}{\sqrt{2L^3}}\right) . \tag{2.18}$$

The integral over dk_f in Eq. 2.17 is rewritten as an energy integral using $dE_f = \hbar^2 k_f dk_f/\mu$, which gives

$$\Gamma_{fi} = \frac{\mu}{4\pi^2\hbar^4 L^3}\int d\Omega_f k_f |\bar{M}_{fi}|^2 \tag{2.19}$$

where $\bar{M}_{fi} = L^3 M_{fi}$. Equation 2.19 represents the probability per second for the two particles to make a transition from state i to all final states f. The event rate constant K is defined as the transition probability per pair of particles to make the transition from state i to state f per volume per second. It is obtained by dividing Eq. 2.19 by the number of pairs per unit volume in our box $1/L^3$ and is given in terms of the scattering amplitude by

$$K_2 = \int d\Omega_f \frac{k_f}{\mu} |f(\theta,\phi) + f(\pi-\theta)|^2 = \frac{k_i}{\mu}\sigma . \tag{2.20}$$

2.1.2 Relating the scattering amplitude to the scattering matrix

The symmetrized scattering amplitude $f(\theta,\phi) + f(\pi-\theta,\pi+\theta)$ can now be expressed in terms of a corresponding symmetrized T-matrix. In general, it is necessary to include the spin degrees of freedom. I will consider the four different possibilities of scattering identical particles in distinguishable or indistinguishable initial and final spin states. The terminology "distinguishable" and "indistinguishable" is reserved for the spin degrees of freedom. Although the scattering of identical particles is considered here, an experiment can still identify these particles according to their spin state. Identical atoms in the same spin state are therefore truly indistinguishable. To simplify the presentation, consider collisions between

two spin-1 particles. The symmetrized initial plane waves are

$$\begin{aligned}\Psi_i^I &= \left(\frac{e^{ik_iZ}+e^{-ik_iZ}}{\sqrt{2}}\right)|10,10\rangle \\ \Psi_i^D &= \frac{e^{ik_iZ}|11,1-1\rangle+e^{-ik_iZ}|1-1,11\rangle}{\sqrt{2}}\end{aligned} \tag{2.21}$$

and final state wave functions are

$$\begin{aligned}\Psi_f^I &= \left(\frac{e^{i\vec{k}_f\cdot\vec{R}}+e^{-i\vec{k}_f\cdot\vec{R}}}{\sqrt{2}}\right)|10,10\rangle \\ \Psi_f^D &= \frac{e^{i\vec{k}_f\cdot\vec{R}}|11,1-1\rangle+e^{-i\vec{k}_f\cdot\vec{R}}|1-1,11\rangle}{\sqrt{2}}\end{aligned} \tag{2.22}$$

where the I or D superscripts indicate indistinguishable or distinguishable spin states. The spin ket notation is $|f_am_a,f_bm_b\rangle$. The plane waves can be expanded using the following identities[27]

$$\begin{aligned}e^{ikZ} &= \sum_{l=0}^{\infty} i^l(2l+1)P_l(\cos\,\theta)j_l(kR) \\ e^{i\vec{k}\cdot\vec{R}} &= \sum_{l=0}^{\infty}\sum_{m=-l}^{+l} 4\pi i^l Y_{lm}^*(\theta_f,\phi_f)Y_{lm}(\theta,\phi)j_l(kR)\ .\end{aligned} \tag{2.23}$$

Analogous expansions of the complex conjugates of the above plane waves introduce additional $(-1)^l$ factors. Inserting the plane wave expansions, the initial and final state unperturbed wave functions become

$$\begin{aligned}\Psi_i^I &= \sqrt{2}\sum_{l_i=\text{even}} i^{l_i}(2l_i+1)P_{l_i}(\cos\,\theta)j_{l_i}(k_iR)\chi^I \\ \Psi_i^D &= \sum_{l_i} i^{l_i}(2l_i+1)P_{l_i}(\cos\,\theta)j_{l_i}(k_iR)\chi^D\end{aligned} \tag{2.24}$$

and

$$\begin{aligned}\Psi_f^I &= \sqrt{2}\sum_{l_f=\text{even}}\sum_{m_f} 4\pi i^{l_f}Y_{l_fm_f}^*(\theta_f,\phi_f)Y_{l_fm_f}(\theta,\phi)j_{l_f}(k_fR)\chi^I \\ \Psi_f^D &= \sum_{l_f}\sum_{m_f} 4\pi i^{l_f}Y_{l_fm_f}^*(\theta_f,\phi_f)Y_{l_fm_f}(\theta,\phi)j_{l_f}(k_fR)\chi^D\end{aligned} \tag{2.25}$$

where $\chi^I=|10,10\rangle$ and $\chi^D=\frac{1}{\sqrt{2}}\left[|11,1-1\rangle+(-1)^l|1-1,11\rangle\right]$ represent symmetrized spin basis functions. Note that the expansions for the indistinguishable

spin states are summed over **even** values of the partial wave. In the case of identical fermions scattering in indistinguishable spin states the sums would include only **odd** l's.

The first example will be outlined in detail. The steps are the same in all cases, so I will only quote final results for the last three. For concreteness consider a spin-dependent isotropic potential $V^S(R)$;

i) **indistinguishable spin state $\rightarrow$ indistinguishable spin state**

$$\begin{aligned}\bar{M}_{fi} &= \langle \Psi_f^I | V^S | \Psi_i^I \rangle = 8\pi \sum_{l_i, l_f, m_f} i^{l_f + l_i} (2l_i' + 1) Y_{l_f m_f}(\theta_f, \phi_f) \\ &\int d\Omega P_{l_i}(\cos\,\theta) Y^*_{l_f m_f}(\theta,\,\phi) \int R^2 dR j_{l_f}(k_f R) \langle \chi^I | V^S | \chi^I \rangle j_{l_i}(k_i R)\ . \end{aligned} \tag{2.26}$$

Using $P_l(\cos\,\theta) = \sqrt{\frac{4\pi}{2l+1}} Y_{l,0}$ and the orthogonality properties of the spherical harmonics, the angular integral ($\int d\Omega = 4\pi$) can be evaluated giving

$$\begin{aligned}\bar{M}_{fi} &= 8\pi \sum_{l_i = \text{even}} (2l+1) P_{l_i}(\cos\,\theta_f) \\ &\delta_{l_i, l_f} \int R^2 dR j_{l_f}(k_f R) \langle \chi^I | V^S | \chi^I \rangle j_{l_i}(k_i R)\ . \end{aligned} \tag{2.27}$$

Introducing energy normalized radial wave functions[27] $\sqrt{\frac{2\mu}{\pi k}} k R j_l(kR)$, the radial integral can be related to a scattering $\underline{S}$- or transition $\underline{T}$-matrix element[27]

$$\begin{aligned}\{T\}_{fi} &= \frac{\{S\}_{fi} - \delta_{fi}}{2i} \\ &= -\pi \int dR \sqrt{\frac{2\mu}{\pi k_f}} k_f R j_l(k_f R) \langle \chi^I | V^S | \chi^I \rangle \sqrt{\frac{2\mu}{\pi k_i}} k_i R j_l(k_i R)\ . \end{aligned} \tag{2.28}$$

The brackets on $\{T\}_{fi}$ indicate that the matrix element is calculated in a symmetrized spin basis. The final result for the matrix element is then given by

$$\bar{M}_{fi} = -\frac{4\pi}{\mu} \frac{1}{\sqrt{k_i k_f}} \sum_{l_i = \text{even}} (2l_i + 1) P_{l_i}(\cos\,\theta_f) \{T\}_{fi} \tag{2.29}$$

ii) **indistinguishable $\rightarrow$ distinguishable**

$$\bar{M}_{fi} = -\frac{2\sqrt{2}\pi}{\mu}\frac{1}{\sqrt{k_i k_f}}\sum_{l_i=\text{even}}(2l_i+1)P_{l_i}(\cos\,\theta_f)\{T\}_{fi} \tag{2.30}$$

iii) **distinguishable** $\rightarrow$ **indistinguishable**

$$\bar{M}_{fi} = -\frac{2\sqrt{2}\pi}{\mu}\frac{1}{\sqrt{k_i k_f}}\sum_{l_i=\text{even}}(2l_i+1)P_{l_i}(\cos\,\theta_f)\{T\}_{fi} \tag{2.31}$$

iv) **distinguishable** $\rightarrow$ **distinguishable**

$$\bar{M}_{fi} = \frac{2\pi}{\mu}\frac{1}{\sqrt{k_i k_f}}\sum_{l_i=0}^{\infty}(i)^{2l_i}(2l_i+1)P_{l_i}(\cos\,\theta_f)\{T\}_{fi} \tag{2.32}$$

The last step required to obtain a total cross section or event rate constant is evaluation of the integral over final states $\int d\Omega_f$ in equations 2.16 and 2.20. In the case of distinguishable final spin states this integral is taken over **all space**. However, for indistinguishable final spin states we must restrict the integral over **half space** ($\int d\Omega_f = 2\pi$) to avoid double counting. The results for the four cases are quoted below. To derive these, one must keep in mind the caveat on the angular integration limits.

i) **indistinguishable** $\rightarrow$ **indistinguishable**

Plugging $\bar{M}_{fi}$ from equation 2.29 into equations 2.16 and 2.20 and using the orthogonality properties of the Legendre polynomials gives

$$\begin{aligned}\sigma &= 8\pi\sum_{l_i=\text{even}}(2l_i+1)\frac{|\{T\}_{fi}|^2}{k_i^2}\\ K_2 &= 8\pi\sum_{l_i=\text{even}}(2l_i+1)\frac{|\{T\}_{fi}|^2}{\mu k_i}\end{aligned} \tag{2.33}$$

This cross section expression can be checked in the s-wave limit. The scattering length is defined as $\lim_{k_i\rightarrow 0} a = (-\tan\delta/k)$ [24], where δ is the elastic phase shift. In the zero energy limit, $\{T\}_{fi} \rightarrow \delta$ and we find $\sigma = 8\pi a^2$ as expected. In practice, I calculate the scattering lengths from the $\underline{S}$-matrix. The diagonal $\underline{S}$-matrix elements are related to the phase shift[24] by $\{S\}_{ii} = e^{2i\delta_i}$. The scattering length in channel i is then given by

$$\lim_{k_i\rightarrow 0} a_i = -\frac{\ln\{S\}_{ii}}{2ik_i}\ . \tag{2.34}$$

ii) **indistinguishable → distinguishable**

$$\begin{aligned} \sigma &= 8\pi \sum_{l_i=\text{even}} (2l_i+1)\frac{|\{T\}_{fi}|^2}{k_i^2} \\ K_2 &= 8\pi \sum_{l_i=\text{even}} (2l_i+1)\frac{|\{T\}_{fi}|^2}{\mu k_i} \end{aligned} \tag{2.35}$$

iii) **distinguishable → indistinguishable**

$$\begin{aligned} \sigma &= 4\pi \sum_{l_i=\text{even}} (2l_i+1)\frac{|\{T\}_{fi}|^2}{k_i^2} \\ K_2 &= 4\pi \sum_{l_i=\text{even}} (2l_i+1)\frac{|\{T\}_{fi}|^2}{\mu k_i} \end{aligned} \tag{2.36}$$

iv) **distinguishable → distinguishable**

$$\begin{aligned} \sigma &= 4\pi \sum_{l_i=0}^{\infty} (2l_i+1)\frac{|\{T\}_{fi}|^2}{k_i^2} \\ K_2 &= 4\pi \sum_{l_i=0}^{\infty} (2l_i+1)\frac{|\{T\}_{fi}|^2}{\mu k_i} \end{aligned} \tag{2.37}$$

In the case of non-identical particle collisions, the cross section and event rate formulas are given by case iv) and the $\underline{T}$-matrix element is calculated in an unsymmetrized spin basis.

There is one more identical particle detail that must be considered. The event rate K_2 describes the rate at which **pairs** of atoms collide, whereby K_2 inelastic events will generally lead to $2K_2$ atoms lost in unit trap volume per unit time. Generally, the most useful parameter is the **atom-loss** rate constant, the coefficient of the density squared in the rate equation. This quantity is $L_2 = K_2/(1+\delta)$. The denominator (1 + δ) is needed because the number of pairs depends on the initial spin state. If the initial spin states are the same $\delta = 1$, otherwise $\delta = 0$. For example, a gas of N identical atoms initially in indistinguishable spin states will have $N(N-1)/2$ pairs as opposed to the distinguishable case which will have $N_a N_b$ pairs. However, these additional factors of two are easily accommodated since K_2 in equations 2.33 and 2.35 is a factor of two larger than in equations 2.36 and 2.37.

The definition for the atom loss rate constant will therefore be taken as

$$(L_2)_{fi} \equiv 4\pi\,(2l_i+1)\frac{|\{T\}_{fi}|^2}{\mu k_i}\ . \tag{2.38}$$

The rate equation controlling the number of α spin state atoms would thus read:

$$\frac{dn_\alpha}{dt} = \sum_\beta \sum_{\{\gamma\delta\}} (1+\delta_{\alpha,\beta})[L_2(\gamma\delta \to \alpha\beta) n_\gamma n_\delta - L_2(\alpha\beta \to \gamma\delta) n_\alpha n_\beta] \tag{2.39}$$

where n_α is the density of atoms in the α spin state. There is some confusion in the literature regarding this terminology. Generally, the published results that were termed "event rate constants", e.g. in Ref.[28], are understood to be the coefficient of the density squared in the rate equations, (i.e., what we call the atom-loss rate). However, our definition of L_2 used in the above rate equation agrees with the "standard" definition of K_2.

The last situation that needs to be examined is the case of an anisotropic spin-dependent potential $V^S(R,\Omega)$. Returning to the first indistinguishable spin isotropic example (case i), equation 2.26 can be generalized as follows

$$\begin{aligned} \bar{M}_{fi} &= 8\pi \sum_{l_i,l_f,m_f} i^{l_i+l_f}(2l_i+1) Y_{l_f m_f}(\theta_f,\phi_f) \\ &\quad \sqrt{\frac{4\pi}{2l_i+1}} \int R^2 dR j_{l_f}(k_f R) \langle \chi^I Y_{l_f m_f}(\Omega) | V^S | Y_{l_i 0}(\Omega) \chi^I \rangle j_{l_i}(k_i R)\ . \end{aligned} \tag{2.40}$$

The new expressions for the perturbative $\underline{S}$- and $\underline{T}$-matrix elements are

$$\begin{aligned} \{T\}_{fi}^{l_f m_f l_i} &= \frac{\{S\}_{fi}^{l_f m_f l_i} - \delta_{fi}}{2i} \\ &= -\pi \int dR \sqrt{\frac{2\mu}{\pi k_f}}\ k_f R\ j_{l_f}(k_f R) \\ &\quad \langle \chi^I\, Y_{l_f m_f}(\Omega) | V^S | Y_{l_i 0}(\Omega)\, \chi^I \rangle \sqrt{\frac{2\mu}{\pi k_i}}\ k_i R\ j_{l_i}(k_i R) \end{aligned} \tag{2.41}$$

which can be substituted back into the equation above to give

$$\bar{M}_{fi} = -\frac{4\pi}{\mu}\frac{4\pi}{\sqrt{k_i k_f}} \left| \sum_{l_f=\text{even}} \sum_{m_f} \sum_{l_i=\text{even}} \sqrt{2l_i+1}\, Y_{l_f m_f}(\Omega_f) \{T\}_{fi}^{l_f m_f l_i} \right|\ . \tag{2.42}$$

The matrix element $\bar{M}_{fi}$ for cases ii) and iii) will again be a $\sqrt{2}$ smaller than the one given in Eq. 2.42 and case iv) a factor of two smaller. The cross sections and

event rates are obtained in the same fashion, although one should keep in mind the caveats on the $d\Omega_f$ integration limits. The final results for the anisotropic potential can be summarized as follows

$$\sigma = 4\pi \left| \sum_{l_f m_f l_i} \sqrt{2l_i + 1}\, \frac{\{T\}^{l_f m_f l_i}}{k_i} \right|^2 (1 + \delta) \tag{2.43}$$

and

$$L_2 = \frac{4\pi}{\mu k_i}\, n \left| \sum_{l_f m_f l_i} \sqrt{2l_i + 1}\, \{T\}^{l_f m_f l_i} \right|^2 . \tag{2.44}$$

An anisotropic potential couples the different partial waves and therefore these must be added coherently (with the appropriate limits on the sum over the initial and final partial waves). Finally, the δ function in Eq. 2.43 is one if the two atoms are initially in the same spin state and zero if the two atoms are initially in distinguishable spin states.

2.2 Interaction potentials

The complete description of two interacting multi-component atoms is extremely complex. Levy and co-workers[29, 30] have identified a fourteen term Hamiltonian valid for diatomic molecules in the Born-Oppenheimer limit[31]. However, most of these interactions are vanishingly small for two ground state alkali atoms. In fact, most of the interesting cold collision physics comes about simply because the collision energies are much smaller than the atomic hyperfine splittings. Consequently the collision partners can in some cases resonate (i.e. at a Feshbach resonance in asymptotically closed channels). Moreover, if the partners change hyperfine states, enough energy can be liberated to eject the atoms from the trap. Or if the trap is magnetic, the collision can produce untrapped hyperfine states and again the atoms are lost. These hyperfine changing collisions are generally termed spin-exchange collisions, although one should keep in mind that other interactions besides electronic spin-exchange can also change the hyperfine states. True spin-exchange collisions can be viewed as resulting from a transformation between angular momentum coupling schemes. At small internuclear separations R, the two electronic spins tend to lock and precess around the total angular momentum vector. At large R the electrostatic exchange splitting decays exponentially and the electron spin on each atom now prefers to couple to the corresponding nuclear spin, precessing around the total atomic angular momentum vector of each atom. However as the atoms recede, the small R evolution of the total electronic spin states will not in general allow the spins to recouple in exactly the same hyperfine states

that initially approached. Spin-exchange coupling is generally strong, leads to large trap loss rates, and is something to be avoided. This can be arranged either through the choice of symmetry (e.g., by trapping doubly polarized spin states, also known as "stretched states") or else through energetic considerations. A second and much weaker loss process frequently occurs via the magnetic dipole-dipole interaction between the two valence electrons. It can usually be neglected unless one needs the loss rate from a spin-exchange forbidden collision.

Complete descriptions of these interactions are provided in this section. Subsection 2.2.1 describes the construction of the Born-Oppenheimer potentials. The hyperfine Hamiltonian is presented in subsection 2.2.2 and the magnetic dipole-dipole Hamiltonian in subsection 2.2.3. Finally, magnetic field induced Feshbach resonances will be discussed in subsection 2.2.4.

2.2.1 Constructing the Born-Oppenheimer potentials

The motion of the constituent charged particles of the diatom is controlled by two very different time scales. The electrons are much lighter than the nuclei and therefore move at greater velocities. The Hamiltonian describing the complete system, $H = H_N + H_e$, can be approximately separated into a nuclear and electronic component. This is known as the Born-Oppenheimer limit[31]. The Born-Oppenheimer potential curves are constructed by freezing the interatomic separation at a given value R, and then evaluating the energies of the resulting electronic eigenstates of H_e. These energies vary with R and constitute a set of potential energy curves. The physics underlying these potentials is qualitatively different in regions of small and large internuclear separations. The division between these two regions is determined by the overlap of the atomic electronic clouds, which begins to become exponentially small beyond $R \sim 20$ a.u. in the alkalis. Information regarding these two regions is generally collected from different sources and must then be smoothly connected through the transition region near $R \sim 20$ a.u.

The small R region is characterized by large overlaps of the electronic clouds; here one must use molecular concepts to correctly describe the interaction of the collision pair. In the case of alkali atom ground state collisions, the potential energy depends solely on the internuclear separation R and the orientation of the two atom's valence electronic spins (s_i=1/2) which couple into singlet (S=0), where ($\vec{S} = \vec{s}_a + \vec{s}_b$) or triplet ($S$=1) configurations. The Hund's case (a) designations for these states are $X^1\Sigma_g^+$ and $a^3\Sigma_u^+$ for the singlet and triplet respectively. The spin dependence of the potential energy is a consequence of the Pauli exclusion principle which requires the wave function to have an odd permutation symmetry under exchange of electrons[32]. As one can imagine, **ab initio** calculations to determine the interactions of multi-electron alkali atoms require sophisticated numerical techniques[33]. Fortunately, molecular spectroscopicists have devoted a great deal of attention to measuring ro-vibrational spectra. In turn, these spectra can be

inverted to determine a corresponding potential using standard techniques such as RKR[34] or inverted perturbation analysis (IPA)[35]. References for the small R Born-Oppenheimer potentials used in this work are given in Table 2.1.

The physics simplifies as the overlap of the electron clouds decreases. The residual overlap leads to a long range exchange term of the form $V^{\rm ex} = \pm AR^{\alpha}\exp^{-\beta R}$ where $+$ is used for the triplet state and $-$ for the singlet. Analytical values for α and β are derived in Ref.[36]. These expressions are given in terms of the valence electron binding energy E_b, which for identical atoms becomes $\alpha = \frac{7}{2\sqrt{2E_b}} - 1$ and $\beta = 2\alpha$. The value of the overall scaling coefficient A is determined from the difference $V_{S=1} - V_{S=0}$ near the transition $R \sim 20$ a.u., (see for example Ref[37]). The remaining large R electrostatic interactions are a result of "instantaneous" multipole moments. The motion of the electrons leads to small fluctuations in the charge density surrounding each atom. In turn, one atom can polarize the other setting up an momentary dipole moment which then attracts the first. This is the van der Waals or dispersion force. In the case of two alkali atoms colliding in their atomic ground states, the dispersion potential is given by $V^d = -\mathrm{C}_6/R^6 - \mathrm{C}_8/R^8 - \mathrm{C}_{10}/R^{10}$. **Ab initio** calculations[38, 39, 40] for the dispersion coefficients C_n have proven reliable to within a few %. Ref.[38] is used for the C_8 and C_{10} coefficients. C_6 coefficients are taken from a variety of sources which are listed in Table 2.1. The dispersion potentials will also be modified by retardation effects. However, current experiments have not been able to separate ground state retardation effects from uncertainties associated with other interactions. Retardation effects are therefore neglected. (Retardation effects have been observed in pseudo-bound excited state measurements, see for example Ref.[21]). The Rb Born-Oppenheimer potentials used in this work are shown in Fig. 2.1.

Table 2.1: Sources of information for constructing the Born-Oppenheimer potentials. The singlet and triplet columns list the method used in the corresponding reference to obtain the small R part of the potential. The C_6 coefficients are the nominal values used in this work and are cited along with the corresponding reference.

Atom	Singlet	Triplet	C_6
Li	RKR[41]	RKR[41]	1393.4[42]
Na	RKR[43]	RKR[43]	1538.9[44]
K	IPA[45]	RKR[46]	3897.0[39]
Rb	IPA[47]	**ab initio**[33]	4700.0[17]
Cs	IPA[48]	**ab initio**[33]	6851.0[39]

The potentials as given are still not accurate enough for ultracold collision calculations. Typically, the highest bound state measured with conventional molecular spectroscopy is more than 2 cm^{-1} below the dissociation threshold. Ex-

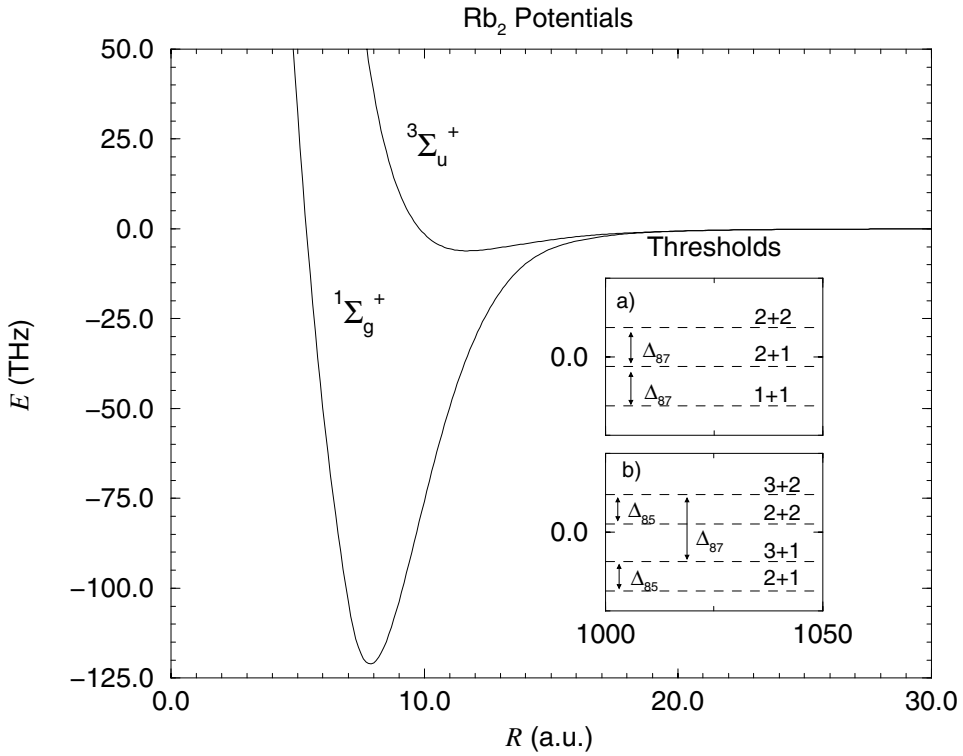

Figure 2.1: Singlet and triplet Rb_2 Born-Oppenheimer potentials. Hyperfine split thresholds are indicated in the inset for a)two ^{87}Rb atoms and b) ^{87}Rb + ^{85}Rb collision. The atomic hyperfine quantum numbers $f_a + f_b$ are indicated at each threshold. The values of the energy splittings are Δ_{87} = 6.835 GHz and Δ_{85} = 3.036GHz

trapolating the Born-Oppenheimer potentials beyond this point has proven unreliable. In order to obtain collision parameters which agree with experiment we add a correction to the inner wall of the singlet and triplet potentials of the form[49]

$$\Delta V(R) = \begin{cases} C_S \tan^{-1}\left[\left(\frac{R-R_e}{\Delta R}\right)^2\right], & R < R_e \\ 0, & R > R_e \end{cases} \tag{2.45}$$

where R_e denotes the minimum of the well and ΔR is a width parameter generally taken to be 2 Bohr. The energy dependence of the phase shifts has been tested using other functional forms for the correction, such as quadratic, cubic, and quartic polynomials in R, all of which give nearly identical results.

2.2.2 Atomic hyperfine Hamiltonian

The atomic hyperfine Hamiltonian represents the coupling of an electron with the electromagnetic field created by the charged nucleus. In general, for nuclei with spin $i > 1/2$ the Hamiltonian is quite complicated. For example, electric and magnetic multipole terms of order k $\leq 2i$ are allowed[50]. However, expectation values of these multipole terms average to zero for spherically symmetric atoms (L=0) which will be the case for alkali atoms in their ground state. The lone remaining term, commonly referred to as Fermi's "contact term", is a result of the non-zero spatial extent of the nucleus and can be expressed as[51]

$$H^{\mathrm{ahf}} = \frac{-8\pi}{3} \left|\Psi_e(0)\right|^2 \langle \vec{\mu}_e \cdot \vec{\mu}_n \rangle \tag{2.46}$$

where $\vec{\mu}_e$ and $\vec{\mu}_n$ are the magnetic moments of the electron and nucleus, respectively. Evaluation of H in this representation is complicated by the existence of the electronic wave function term $|\Psi_e(0)|^2$. We can avoid this problem by introducing measured hyperfine splitting energies. (The review paper by Arimondo, **et al.**[52] is an excellent resource for this information.) H can be rewritten in the following form

$$H^{\mathrm{ahf}} = C(\vec{f}_a^{\,2} - \vec{s}_a^{\,2} - \vec{i}_a^{\,2}) \tag{2.47}$$

where $\vec{f}_a = \vec{s}_a + \vec{i}_a$ and C is a constant which can be related to the hyperfine splitting Δ. H^{ahf} is diagonal in the basis $|f_a(s_a i_a) m_{f_a}\rangle$. Requiring the barycenter of the alkali hyperfine Hamiltonian to be E=0, C is given by

$$C = \Lambda \frac{\Delta}{2i+1}. \tag{2.48}$$

Here, $\Lambda = +1$ if the nuclear magnetic moment $\vec{\mu}_n$ is positive or $\Lambda = -1$ if it is negative. The sign determines whether the hyperfine structure is "standard" (i.e.,

$E(f = i + s) > E(f = i - s)$) or "inverted" ($E(f = i + s) < E(f = i - s)$). The total hyperfine Hamiltonian $H^{\rm hf}$ for the collision complex taken to be simply the sum of the two atomic hyperfine Hamiltonians $H^{\rm ahf}$

$$H^{\rm hf} = \Lambda_a \frac{\Delta_a}{2i_a + 1}(\vec{f}_a^{\,2} - \vec{s}_a^{\,2} - \vec{i}_a^{\,2}) + \Lambda_b \frac{\Delta_b}{2i_b + 1}(\vec{f}_b^{\,2} - \vec{s}_b^{\,2} - \vec{i}_b^{\,2}). \tag{2.49}$$

The hyperfine split thresholds for both homonuclear and heteronuclear Rb collisions are shown in the inset of Fig. 2.1. The intra-atomic hyperfine Hamiltonian as well as any R-dependence in $H^{\rm hf}$ are neglected.

2.2.3 Magnetic dipole interaction

The magnetic dipole Hamiltonian can be constructed by treating the interaction of a magnetic dipole (i.e., valence electron a) with the field created by a second dipole (valence electron b). Starting with the classical expression for this interaction[51] and substituting quantum mechanical expressions for the electronic moments leads to the following relationship (in a.u.)

$$H^{\rm ss} = -\vec{\mu} \cdot B(\vec{r}) = -\alpha^2 \left(\frac{3(\hat{n} \cdot \vec{s}_a)(\hat{n} \cdot \vec{s}_b) - \vec{s}_a \cdot \vec{s}_b}{R_{ee}^3} \right) \tag{2.50}$$

where α is the fine structure constant. The vector $\vec{r}$ is drawn from dipole a to dipole b and is defined as $R_{ee}\hat{n}$. For our purposes, R_{ee} can be approximated as the internuclear separation R. We do not need to include the s-wave contact term (which is important for the hyperfine interaction) because the two electrons repel each other. Therefore, the electron pair wave function is exponentially small in the limit $R_{ee} \to 0$. $H^{\rm ss}$ is most conveniently evaluated in the molecular frame with $\hat{n}$ defining the spin quantization axis. In the spin representation $|S\Sigma\rangle$, the Hamiltonian is diagonal, with matrix elements given by[53]

$$V_{S\Sigma} = -\frac{\alpha^2}{2R^3} \left(3\Sigma^2 - S(S+1) \right) \ . \tag{2.51}$$

Here, $\Sigma = \Sigma_a + \Sigma_b$ represents the total projection of the electronic spin onto the internuclear axis.

The effect of the magnetic dipole term in the molecular frame is to lift the spin projection degeneracy of the triplet state. This behavior is mimicked by an additional effect known as the second-order spin-orbit interaction[53, 29, 54]. The second-order spin-orbit interaction becomes important when the electronic clouds overlap such that indirect perturbative coupling to excited electronic molecular states can modify the direct spin-spin interaction. For ground state alkali collisions, only the $\sum_i (L_i^+ s_i^- + L_i^- s_i^+)/2$ part of the single electron spin-orbit Hamiltonian[53, 54] contributes to the interaction. Here, $L^+ S^-$ are the standard raising and lowering op-

erators for the ith electrons orbital angular momentum and spin, respectively. Mies, **et al.**[54] have shown that the dominant interactions come from coupling the triplet Born-Oppenheimer $^3\Sigma_u$ state with nearby excited $^{(2S+1)}\Pi_u$ states. The interaction is short-ranged and its strength scales with Z. The inclusion of this term is important only for the heavier atoms such as Rb and Cs. Analytical expressions for Rb and Cs have been derived in Ref[54].

Before moving on, it is instructive to examine the operator structure of $H^{\rm ss}$ in the lab frame. Derivations are given in Refs.[29, 50] and accordingly only the final result is given here

$$H^{\rm ss} = -\frac{\sqrt{6}\alpha^2}{R^3}\left[\sum_q (-1)^q C_q^2 (s_a^1 \otimes s_b^1)^2_{-q}\right] \ . \tag{2.52}$$

$(s_a^1 \otimes s_b^1)^2_{-q}$ represents the contraction of two first-rank spin tensors into a second-rank tensor. The important result for cold collisions is the introduction of an angular dependence through the term $C_q^2 = \sqrt{\frac{4\pi}{5}} Y_{2q}(\theta,\phi)$. The second-rank nature of the spherical harmonic implies that incident s-waves will couple only with d-wave exit channels. However, the $H^{\rm ss}$ operator is an overall scalar and thus is rotationally invariant. Therefore, the squared total angular momentum $\vec{F}^2$ ($\vec{F} = \vec{f} + \vec{l}$) still commutes with the zero-field Hamiltonian.

2.2.4 External magnetic field and Feshbach resonances

The cold collisions community has energetically studied the possibility of influencing cold collisions with external fields. In principle this would allow condensate properties to be tailored. Although several methods have been proposed[55, 56, 14] probably the simplest and most robust approach is to induce a Feshbach resonance in the collision of two atoms by applying a static magnetic field. The scattering length can be varied between $\pm\infty$ as the external magnetic field is swept through the resonance field value, as has been demonstrated experimentally now, in Na condensates[15] and in thermal Rb[16, 17] and Cs[18] clouds.

The physics is rather straightforward. First, the magnetic field Hamiltonian is

$$H^{\rm B} = -B\left[g\mu_{\rm e}(s_z^{\rm a} + s_z^{\rm b}) + \mu_{\rm N}(g_{\rm N}^{\rm a}\, i_z^{\rm a} + g_{\rm N}^{\rm b}\, i_z^{\rm b})\right] \ . \tag{2.53}$$

The magnetic field $\vec{B} = B\hat{z}$ is assumed to be constant and in the direction $\hat{z}$ that defines the spin quantization axis. The constants $g\mu_{\rm e}$ and $g_{\rm N}\mu_{\rm N}$ include the gyromagnetic ratio g and magneton $\mu_e = -e\hbar/2m_e$ for the electron and $\mu_n = e\hbar/2m_P$ for the nucleus. The individual atom spins are again labeled by a and b. The effect of Eq. 2.53 is two-fold: first the spin projection degeneracy is lifted which shifts and splits the final state thresholds; second, the magnetic field couples the

entrance channel to additional spin configurations. H^{B} conserves the total angular momentum projection m_F but not its squared magnitude $\vec{F}^2$. ^{85}Rb atomic hyperfine thresholds and the thresholds for a $|2,-2\rangle_{85}+|2,-2\rangle_{85}$ collision complex are shown as a function of magnetic field in Fig. 2.2. (The notation $|f,m_f\rangle_A$ will be used throughout to define the isotope (A) and hyperfine spin state of each colliding atom.) A Feshbach resonance occurs when the collision energy becomes sufficiently close to the energy of a quasi-bound state associated with a closed channel that is coupled to the entrance channel. As a first approximation, one can consider these quasi-bound states as being "attached" to a particular threshold which are then shifted by the magnetic field. A schematic of a magnetic field induced Feshbach resonance is shown in Fig. 2.3. Two situations can occur. A bound state can either be added or removed from the potentials; either case results in a change of the phase shift by π radians as a function of B. A scattering length that approaches $-\infty$ as B increases toward the resonance value B_R (from low-field) indicates that the resonance came "down" out of the continuum (i.e., an additional bound state is added for $B > B_R$). This is the general scenario for magnetically trapped atoms as observed in Ref.[16, 17, 15]. The entrance channel threshold rises with increasing field, which is why they are called "weak-field-seeking" (see Fig. 2.3). Strong-field-seeking states can be trapped with optical methods; their threshold energies decrease with increasing field strength, and the most likely scenario is therefore a bound state that pops above the entrance threshold at $B > B_R$. In this instance, the scattering length $a \to +\infty$ as B approaches B_R from below. This was observed for Na[15] and Cs[18] collisions. The scattering length behavior near the resonance for both situations is shown in Fig. 2.4. The scattering length near a Feshbach resonance is often parameterized with the following expression[15]

$$a = a_0\left(1-\frac{\Delta}{B-B_R}\right) \tag{2.54}$$

where Δ is the width of the resonance and a_0 is the zero-field value of the scattering length.

2.3 Angular momentum representations

Different angular momentum coupling schemes play a key role in different aspects of the collision physics. In this section, I will define the different coupling schemes and outline the advantages of each. Subsection 2.3.1 discusses the symmetrization of each representation and presents the corresponding identical particle selection rules. Subsection 2.3.2 presents the unitary transformation matrix elements to transform back and forth from the short range representation to the various asymptotic representations.

Any collision event begins with atoms trapped in their individual atomic

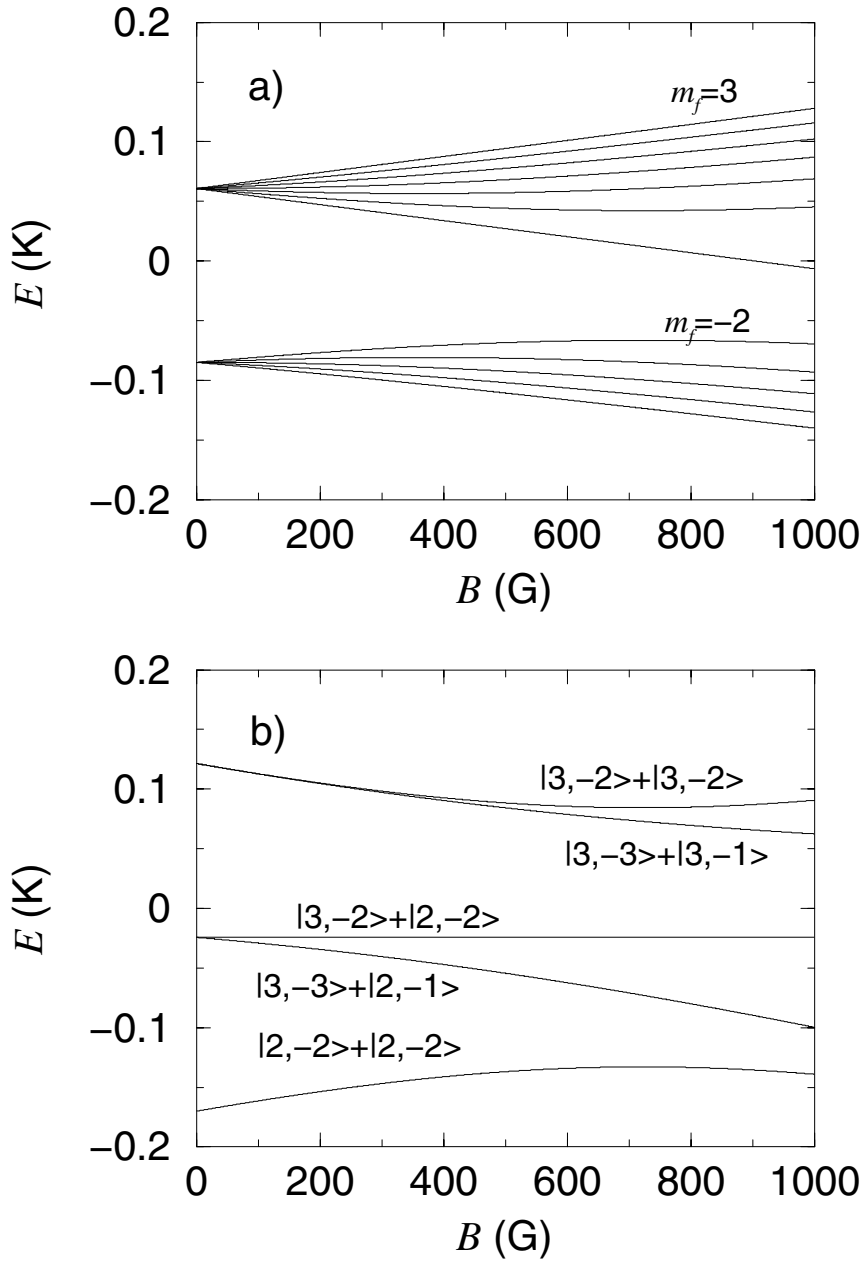

Figure 2.2: a) ^{85}Rb atomic thresholds versus magnetic field. The projection of f_a is labeled for the highest energy state in each hyperfine manifold.
b) Thresholds versus magnetic field for a collision of two $|2,-2\rangle_{85}$ atoms. The channel labels are given in terms of the atomic hyperfine quantum numbers $|f_a m_{f_a}\rangle + |f_b m_{f_b}\rangle$.

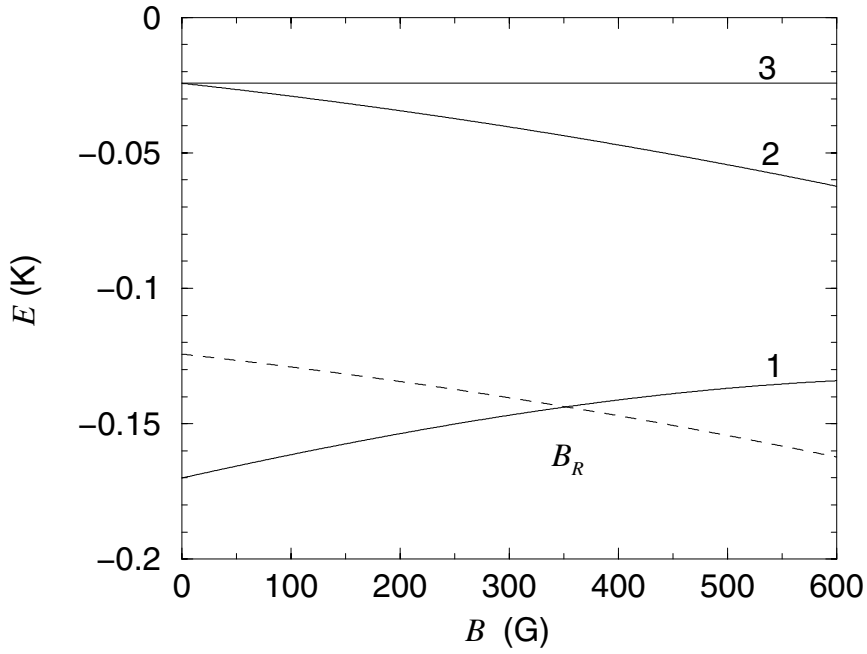

Figure 2.3: Schematic of a Feshbach resonance. The resonance state (dashed lines) is attached to threshold 2. The collision energy is relative to threshold 1 and becomes degenerate with the resonance state energy at the field value labeled B_R. In this example, the scattering length would approach $-\infty$ as B is increased to B_R.

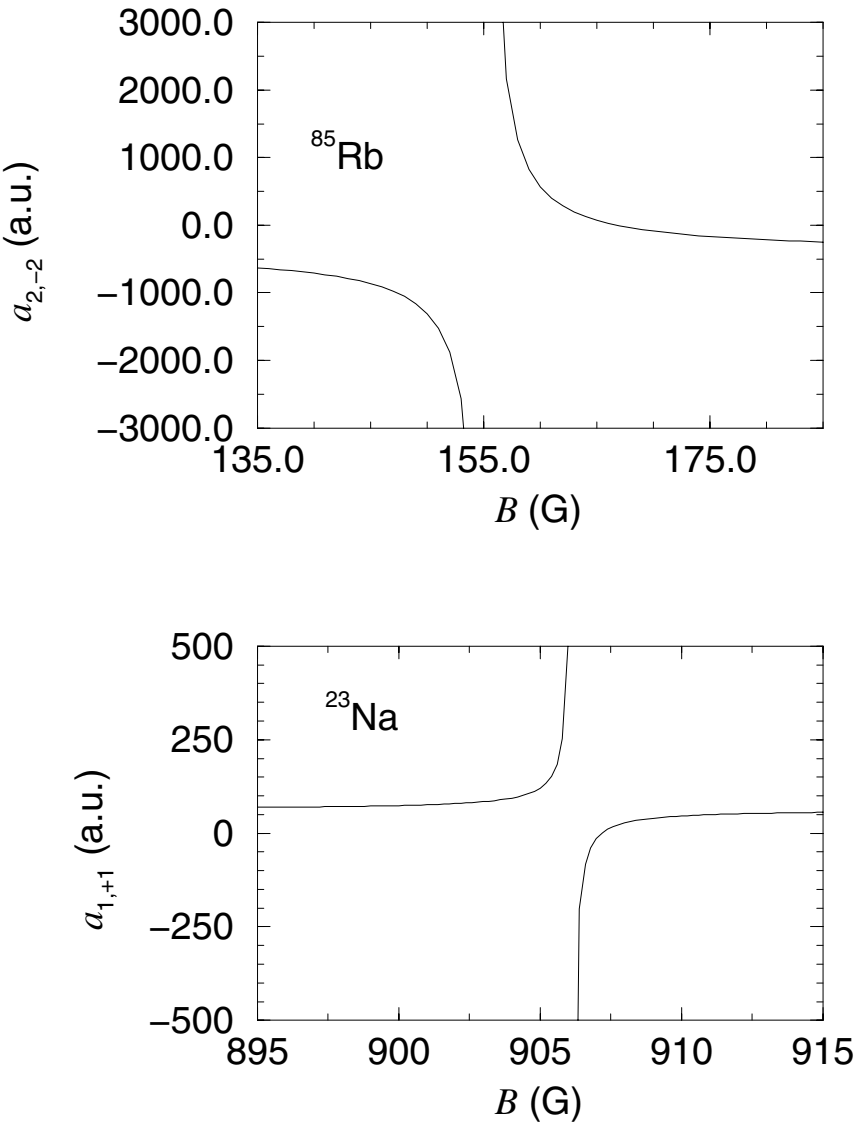

Figure 2.4: Scattering length versus magnetic field in the presence of a Feshbach resonance.
a) Feshbach resonance observed[17] in the collision of two ^{85}Rb $|2,-2\rangle$ atoms. The scattering length behavior on resonance indicates a bound state is added to the potentials.
b) Feshbach resonance observed[15] in the collision of two ^{23}Na $|1,+1\rangle$ atoms. The scattering length behavior on resonance indicates a bound state is removed from the potentials.

hyperfine state $\vec{f}_i = \vec{s}_i + \vec{i}_i$ ($i \equiv \{a, b\}$). This provides the first natural choice for an angular momentum representation and I will refer to it as the

$$\text{uncoupled hyperfine representation} \equiv |f_a m_{f_a},\, f_b m_{f_b},\, l m_l\rangle \ .$$

Here, l represents the nuclear rotation (or partial wave) and m_α the projection of the α angular momentum vector on a space-fixed quantization axis. The collision dynamics are simpler in a coupled representation. In the absence of a magnetic field (and when dipolar relaxation can be neglected), both l^2 and f^2 (where $\vec{f} = \vec{f}_a + \vec{f}_b$) are conserved quantities. The coupled Schrödinger equations therefore have a block diagonal structure in the

$$\text{coupled hyperfine representation} \equiv |(f_a f_b) f m_f,\, l m_l\rangle \ .$$

This representation is still useful in the presence of a magnetic field that is a sufficiently small perturbation. If the dipole interaction is included in the Hamiltonian, the

$$\text{total angular momentum representation} \equiv |(fl) F m_F\rangle$$

is a better basis, because in the absence of a magnetic field the Hamiltonian is again block diagonal.

The Hamiltonian expressed in any of the three representations discussed so far becomes diagonal as $R \to \infty$ (again neglecting magnetic field). In the presence of a magnetic field, the asymptotic Hamiltonian $H(R \to \infty) = H^{\rm hf} + H^B$ is diagonalized. The resulting eigenvectors $\underline{U}$ are used to transform the complete potential matrix $\underline{U}^T \underline{V}(R) \underline{U}$ into this eigenchannel representation. The eigenvalues provide the channel thresholds. For the field strengths I will consider, the eigenchannel representation is very nearly the uncoupled hyperfine representation and will be referred to as such. These representations are the most suitable for solving the coupled Schrödinger scattering equations since the asymptotic boundary conditions can be easily applied. However, at small R the dominant interaction is provided by the Born-Oppenheimer molecular potentials. These are diagonal in a total electronic spin basis ($\vec{S} = \vec{s}_a + \vec{s}_b$) which I will refer to as the

$$\text{short range representation} \equiv |S m_S,\, I m_I,\, l m_l\rangle \ .$$

To help identify nuclear permutation symmetry, the nuclear spins are also coupled to form a resultant $\vec{I} = \vec{i}_a + \vec{i}_b$. The short range representation can also be written in terms of total spin $\vec{f} = \vec{S} + \vec{I}$, but generally what controls most of the coupled-channel dynamics is the projection of the hyperfine states onto the singlet and triplet Born-Oppenheimer states.

2.3.1 Symmetries

Collisions of identical particles are of paramount interest and as such we must consider the symmetrization of the total wave function in accord with the Pauli principle. The radial piece of the total wave function (Eq. 2.2) is automatically symmetric since it depends only on the magnitude of R. We therefore need only to consider the effect of the symmetrization operator $(1 + (-1)^p P_{12})$ on the angular momentum representations presented in the previous section. The $(-1)^p$ phase is included to handle both bosonic ($p = 0$) and fermionic ($p = 1$) symmetries. In the center-of-mass representation, the spatial part of P_{12} is equivalent to the parity operator, which applied to the nuclear rotation part of the wave function ($|lm_l\rangle = Y_{lm}(\theta, \phi)$) yields

$$P_{12}|lm_l\rangle = (-1)^l |lm_l\rangle \ . \tag{2.55}$$

The symmetrization of the uncoupled hyperfine representation is therefore straightforward

$$\begin{aligned}(1 + (-1)^p P_{12})|f_a m_{f_a}, f_b m_{f_b}, lm_l\rangle &= |f_a m_{f_a}, f_b m_{f_b}, lm_l\rangle + \\ &\quad (-1)^{p+l}|f_b m_{f_b}, f_a m_{f_a}, lm_l\rangle \ .\end{aligned} \tag{2.56}$$

Note that this relationship immediately implies that collisions of identical atoms in the same hyperfine state (i.e., indistinguishable spin states) are allowed only for even partial waves for bosons and odd partial waves for fermions. The symmetry of the coupled hyperfine representation can be obtained by first decomposing it into the uncoupled representation and applying P_{12}

$$\begin{aligned}(1 + (-1)^p P_{12})|(f_a f_b) f m_f, lm_l\rangle &= (1 + (-1)^p P_{12}) \sum_{m_{f_a}, m_{f_b}} \\ &\quad \langle f_a m_{f_a}, f_b m_{f_b}|f m_f\rangle |f_a m_{f_a}, f_b m_{f_b}, lm_l\rangle\end{aligned} \tag{2.57}$$

Using the Clebsch-Gordan identity[57]

$$\langle f_a m_{f_a}, f_b m_{f_b}|f m_f\rangle = (-1)^{f_a + f_b - f} \langle f_b m_{f_b}, f_a m_{f_a}|f m_f\rangle \tag{2.58}$$

and recoupling the hyperfine momenta gives our final expression

$$\begin{aligned}(1 + (-1)^p P_{12})|(f_a f_b) f m_f, lm_l\rangle &= |(f_a f_b) f m_f, lm_l\rangle + \\ &\quad (-1)^{f_a + f_b - f + l + p}|(f_b f_a) f m_f, lm_l\rangle \ .\end{aligned} \tag{2.59}$$

In the case $f_a = f_b$ definite selection rules are obtained in terms of f and l. A similiar procedure can be used for the short range representation and one finds

$$\begin{aligned}(1+(-1)^p P_{12})|(s_a s_b)Sm_s,(i_a i_b)Im_I,lm_l\rangle &= \\ |(s_a s_b)Sm_s,(i_a i_b)Im_I,lm_l\rangle & \\ +(-1)^{s_a+s_b-S+i_a+i_b-I+l+p}|(s_b s_a)Sm_s,(i_b i_a)Im_I,lm_l\rangle\ .&\end{aligned} \tag{2.60}$$

The phase factor can be simplified by considering the case of identical alkali atoms ($s_i = 1/2, i_a = i_b$) and noting that $\sum_i (s_i + i_i + p)$ will always be even. In this case, the short range representation is manifestly symmetric with states allowed only when the phase factor $(-1)^{S+I+l}$ is equal to +1. Finally, the symmetry of the total angular momentum representation is given by the symmetry of its components

$$\begin{aligned}(1+(-1)^p P_{12})\,|((f_a f_b)fl)Fm_F\rangle &= |((f_a f_b)fl)Fm_F\rangle + \\ & (-1)^{f_a+f_b-f+l+p}|((f_b f_a)fl)Fm_F\rangle\ .\end{aligned} \tag{2.61}$$

2.3.2 Transformations

The four representations presented in the last section are connected by unitary transformations. Transformations between the different asymptotic hyperfine basis require one or at most two recoupling steps. However, connecting the short range representation with the various asymptotic representations requires a little more effort. The derivations are not tricky, as they require only standard angular momentum algebra techniques and consequently, only the results will be quoted here.

i) uncoupled hyperfine representation $\leftrightarrow$ short range representation

$$\begin{aligned}\{\langle Sm_s Im_I l'm_{l'}|f_a m_{f_a} f_b m_{f_b} lm_l\rangle\} &= \\ \delta_{l,l'}\delta_{m_l,m_{l'}}\sum_{f,m_f}\langle Sm_s,Im_I|fm_f\rangle\langle f_a m_{f_a} f_b m_{f_b}|fm_f\rangle & \\ \sqrt{(2f_a+1)(2f_b+1)(2S+1)(2I+1)} & \\ \begin{pmatrix} s_a & i_a & f_a \\ s_b & i_b & f_b \\ S & I & f \end{pmatrix}\left(\frac{1+(1-\delta_{f_a,f_b})(-1)^{S+I+l}}{\sqrt{2-\delta_{f_a,f_b}}}\right)\ .&\end{aligned} \tag{2.62}$$

The $\{\}$ brackets again indicate that this is a symmetrized matrix element and $\begin{pmatrix}\vdots\vdots\vdots\end{pmatrix}$ represents a 9-J symbol.

ii) coupled hyperfine representation $\leftrightarrow$ short range representation

$$\{\langle Sm_s Im_I l' m_{l'} | (f_a f_b) f m_f l m_l \rangle\} = \delta_{l,l'} \delta_{m_l, m_{l'}} \langle Sm_s, Im_I | f m_f \rangle$$

$$\sqrt{(2f_a+1)(2f_b+1)(2S+1)(2I+1)}$$

$$\begin{pmatrix} s_a & i_a & f_a \\ s_b & i_b & f_b \\ S & I & f \end{pmatrix} \left(\frac{1 + (1 - \delta_{f_a,f_b})(-1)^{S+I+l}}{\sqrt{2 - \delta_{f_a,f_b}}} \right) . \tag{2.63}$$

iii) total angular momentum representation $\leftrightarrow$ short range representation

$$\begin{aligned} \{\langle Sm_s Im_I l' m_{l'} | (fl) F m_F \rangle\} &= \delta_{l,l'} \delta_{m_l, m_{l'}} \sum_{m_f, m_l} \\ &\langle Sm_s, Im_I | f m_f \rangle \langle f m_f l m_l | F m_F \rangle \\ &\sqrt{(2f_a+1)(2f_b+1)(2S+1)(2I+1)} \\ &\begin{pmatrix} s_a & i_a & f_a \\ s_b & i_b & f_b \\ S & I & f \end{pmatrix} \left(\frac{1 + (1 - \delta_{f_a,f_b})(-1)^{S+I+l}}{\sqrt{2 - \delta_{f_a,f_b}}} \right) . \end{aligned} \tag{2.64}$$

The unsymmetrized versions of these transformations are obtained by simply neglecting the $(1 + (1 - \delta_{f_a,f_b})(-1)^{S+I+l})/\sqrt{2 - \delta_{f_a,f_b}}$ term in each equation.

Chapter 3

Numerical techniques for solving the coupled Schrödinger equations

Solving coupled linear differential equations like Eq. 2.3 is a problem found in all branches of physics and as such, extensive literature exists on the subject. In most cases one must resort to numerical techniques to solve these equations. Many different numerical methods have been developed over the years and can be broadly divided into two categories, explicit (sometimes called "propagators") and implicit approaches. Both approaches divide the domain of the independent variable into grids or sectors. Explicit methods require the solution of the dependent variable at the preceding grid point to determine its value at the next adjacent point. Implicit methods typically require the solution of a large set of linear equations (or an eigensystem) and thereby determine the value at all grid points simultaneously. Explicit approaches generally are easy to code, fast, and not memory limited since the solutions are calculated "on the fly". The Numerov[58], Gordon[59], and log derivative propagator[60] methods are examples commonly used in atomic collision physics; a performance review of these algorithms is given in Ref.[61]. However, implicit methods are inherently more stable[62] and often give better accuracy. Extremely good linear algebra packages (e.g., LAPACK[63]) are now commonly available (and free!). These packages are cpu-efficient and vastly reduce the programming complexity associated with the linear algebra steps. In addition, with recent advances in computer technology, memory is not the prohibitive factor it once was.

In this chapter, I present an implicit method to solve the coupled-channel Schrödinger equations. Section 3.1 develops the basic method which is based on a finite-element (FEM) $\underline{\mathrm{R}}$-matrix approach. Section 3.2 connects the $\underline{\mathrm{R}}$-matrix to the physical observables given in terms of a scattering $\underline{S}$-matrix. Section 3.3 develops an alternative adiabatic representation to describe the coupled equations. This is presented mainly as a qualitative tool for understanding two-body collisions. However, the power of the adiabatic FEM $\underline{\mathrm{R}}$-matrix approach is brought to bear to solve the three-body collision equations presented in Chapter 8.

3.1 Finite element R-matrix approach

The $\underline{\mathrm{R}}$-matrix method first introduced by Wigner and Eisenbud[64, 65, 66] (1947) has been extended considerably over the years. The variant presented in Section 3.1.1 is the noniterative eigenchannel $\underline{\mathrm{R}}$-matrix[67, 68, 23] which is based on the familiar Rayleigh-Ritz variational expression for energy eigenvalues. This is a technique which provides a variational solution for the log derivative of a wave function on a given boundary. The $\underline{\mathrm{R}}$-matrix method has been used extensively in photoionization studies which are sometimes dubbed "half-collision" processes. Section 3.1.2 describes the finite element basis (FEM) used to solve the $\underline{\mathrm{R}}$-matrix equations. The use of finite elements to solve differential equations in atomic physics is relatively new[69, 70]. This is one of the first implementations of a FEM $\underline{\mathrm{R}}$-matrix approach (see also Ref.[71]), although a similiar approach using basis splines (B-splines) has been presented elsewhere[72]. The last section 3.1.3 describes a technique to match $\underline{\mathrm{R}}$-matrix box solutions to the expected long-range form of the coupled channel solutions. This is useful if a prohibitively large number of channels or sectors are needed to describe the collision complex, such that computer memory becomes short. In this event, the problem can be side-stepped by dividing the radial domain into several boxes and solving the equations in each box separately. An appropriate transformation equates the asymptotic $\underline{\mathrm{R}}$-matrix with the individual box solutions.

3.1.1 R-matrix equations

The eigenchannel $\underline{\mathrm{R}}$-matrix method solves the coupled Schrödinger equations (i.e., Eq. 2.3) within a finite reaction volume Ω of configuration space, subject to **constant** normal logarithmic derivative boundary conditions on the surface Σ of Ω. The collisional properties of the system, typically represented in terms of an $\underline{S}$-matrix, are easily obtained by a straightforward matching procedure once the normal logarithmic derivative $b = -(\partial\Psi/dn)\Psi^{-1}$ is calculated. The present implementation restricts the discussion to a single coordinate R which represents the internuclear separation. However, the techniques presented here are readily generalized to 2- or 3- dimensions[71].

Rearranging the Rayleigh-Ritz expression, one can obtain the following variational expression for the normal logarithmic derivative b of the solutions Ψ of Eq. 2.3 on the surface Σ[67]:

$$b = \frac{\int_\Omega 2\mu\Psi^*(E-H)\Psi dw - \int_\Sigma \Psi^* \frac{\partial\Psi}{\partial n} dS}{\int_\Sigma \Psi^*\Psi dS} \ . \tag{3.1}$$

Here E represents the relative collision energy, μ the reduced mass, and H the Hamiltonian of the colliding pair. A typical approach for solving the above equation is to approximate Ψ using a basis set expansion. A multi-component wave function

can be represented by $\Psi = \sum_m F_m(R) Y_m(\Omega) \chi_m$, which upon introducing a basis set expansion for the radial wave function becomes

$$\Psi = \sum_{i'} c_{i'} \phi_{i'}(R) Y_{i'}(\Omega) \chi_{i'} \ . \tag{3.2}$$

Here, $Y(\Omega)$ represents a spherical harmonic, χ the spin degrees of freedom, m is an index containing all quantum numbers needed to uniquely define a channel, and i' incorporates the basis function index with m. Arbitrary basis functions are designated by $\phi_{i'}$, and the coefficients $c_{i'}$ are to be determined numerically. Insertion of this expansion (Eq. 3.2) into Eq. 3.1, leads to the following generalized eigenvalue equation

$$\underline{\Gamma}\vec{c} = b\underline{\Lambda}\vec{c} \, . \tag{3.3}$$

The matrix elements of Γ and Λ will be described in the following subsection. In general, Eq. 3.3 can be solved directly obtaining the log derivatives and eigenvectors needed to describe the solution on the boundary Σ. However in practice, the matrices in Eq. 3.3 are quite large and direct diagonalization is inefficient. It has been shown[67] that partitioning the matrices according to whether the basis functions are non-zero (open $\equiv o$) or zero (closed $\equiv c$) on Σ

$$\begin{pmatrix} \underline{\Gamma}^{cc} & \underline{\Gamma}^{co} \\ \underline{\Gamma}^{oc} & \underline{\Gamma}^{oo} \end{pmatrix} \begin{pmatrix} c^c \\ c^o \end{pmatrix} = b \begin{pmatrix} 0 & 0 \\ 0 & \underline{\Lambda}^{oo} \end{pmatrix} \begin{pmatrix} c^c \\ c^o \end{pmatrix} \tag{3.4}$$

Eq. 3.3 can be reduced to a small ($m_P \times m_P$) eigensytem

$$\underline{\Omega}^{oo} \, \vec{c^o} = b \, \underline{\Lambda}^{oo} \, \vec{c^o} \tag{3.5}$$

where $\underline{\Omega}^{oo} = \underline{\Gamma}^{oo} - \underline{\Gamma}^{oc}(\underline{\Gamma}^{cc})^{-1}\underline{\Gamma}^{co}$. The main computational burden is thus shifted to solving a set of linear equations

$$\underline{\Gamma}^{cc}\underline{X}^{co} = \underline{\Gamma}^{co} \tag{3.6}$$

whose solution $\underline{X}^{co} = (\underline{\Gamma}^{cc})^{-1}\underline{\Gamma}^{co}$ provides the needed matrix inverse, after which Eq. 3.5 can be solved efficiently.

3.1.2 Finite element basis

The $\underline{\mathrm{R}}$-matrix equations 3.5 and 3.6 were derived using an arbitrary radial basis expansion. A particularly flexible choice is the FEM basis[73, 74, 69]. The FEM method divides the radial domain into $n_{\max}$ sectors (or elements) and within each sector defines a **local** basis. The six local basis functions $u_k(x_n)$ are fifth order Hermite interpolating polynomials which are non-zero only in sector n. Here, x_n

is a rescaled variable defined on the interval [-1,1] which is related to the physical internuclear separation R through the transformation $R = a_n x_n + d_n$ with sector coefficients $a_n = (R_{n+1} - R_n)/2$ and $d_n = (R_{n+1} + R_n)/2$. The FEM expansion for the radial wave function becomes

$$F(R) = \sum_{i \equiv \{k,m,n\}} c_i u_i(x_n) \ , \tag{3.7}$$

where the set i contains the basis function index k, the channel index m, and the sector index n. The six basis functions are defined through the following boundary conditions (exact expressions are given in Appendix A):

$$\begin{array}{lll} u_k(-1) = \delta_{1k} & u_k(0) = \delta_{3k} & u_k(1) = \delta_{5k} \\ \dfrac{du_k(-1)}{dx} = \delta_{2k} & \frac{du_k(0)}{dx} = \delta_{4k} & \dfrac{du_k(1)}{dx} = \delta_{6k} \ . \end{array} \tag{3.8}$$

The requirement that each channel component and its first derivative must be continuous across sector boundaries imposes the following constraints on the basis function coefficients $c_{k,m,n}$

$$c_{5,m,n} = c_{1,m,n+1} \quad c_{6,m,n} = \tfrac{a_n}{a_{n+1}} c_{2,m,n+1} \ . \tag{3.9}$$

In addition, channel boundary conditions can be imposed quite simply by setting the value of the appropriate coefficient. For example, the large R boundary condition in closed channels can be applied at the outset by simply setting $c_{5,m,n_{max}} = 0$. This eliminates problems with exponential growth in these channels and, if $R_{n_{\max}}$ is chosen well into the classically forbidden region, there is no loss of accuracy.

The matrix elements of Γ and Λ in the finite element representation are given by

$$\Gamma_{ij} = 2\mu \int_{-1}^{1} u_i(x_n)(E - H)u_j(x_n) a_n dx_n - \delta_{m,m'} \delta_{n,n_{\max}} \delta_{k,5} \delta_{k',6} / a_n \tag{3.10}$$

$$\Lambda_{ij} = \delta_{m,m'} \delta_{n,n_{max}} \delta_{k,5} \delta_{k',5} \tag{3.11}$$

where $i \equiv \{k, m, n\}$ and $j \equiv \{k', m', n\}$. H is the Hamiltonian of the system. Because the basis functions are non-zero only within a given sector the corresponding matrices have a block diagonal structure. Each sector has an associated block which is coupled only to its nearest neighbors through the continuity conditions (Eq. 3.9). Note that the overlap matrix $\underline{\Lambda}$, whose elements are given by surface integrals over the basis functions[67], is particularly simple in the FEM representation. It contains only m_P non-zero elements (all equal to one). The integrals representing the matrix elements of $\underline{\Gamma}$ are also particularly simple in the FEM representation. In fact, ex-

cept for the integral over the interaction potential, all can be done once and for all beforehand, significantly decreasing the cpu time necessary to construct the matrix. In addition, the $\underline{\Gamma}$ matrix is symmetric which reduces the effort required to construct the matrix. The closed portion $\underline{\Gamma}^{cc}$, which is by far the largest matrix involved, can be written in banded format with dimensions $(6m_{\max}-1)\times(4m_{\max}n_{\max})$, where the first term is the half-bandwidth. The actual storage required by LAPACK's banded format[63] is 3 times the half-bandwidth. The other large matrix required $\underline{\Gamma}^{co}$ has dimensions $(4m_{\max}n_{\max}) \times m_P$. A general rule of thumb is to use at least four sectors per shortest wavelength in the problem which has achieved roughly 6 digits of accuracy in the phase shift, based on limited tests. The accuracy improves to $\sim$8 digits using 8 sectors/wavelength. Increasing the number of sectors is mainly a concern when memory becomes limited. For example, cpu time tests indicate that a single channel calculation using 1000 sectors requires less than 0.2 seconds on a DEC Alpha 400 MHz workstation. This number of sectors is generally adequate to describe most alkali two-body collisions. The cpu time scales roughly linearly with $n_{\max}$ and quadratically with $m_{\max}$. Performance comparisons of this algorithm with a Numerov, Gordon, and integral equation[75] method are provided in Ref[76]. The FEM $\underline{\mathrm{R}}$-matrix approach was found to be quite comparable to the integral equation method (another implicit approach) in speed, memory requirements, and accuracy. Both of these implicit approaches proved more accurate than the two explicit methods. No time comparisons were conducted with the Numerov and Gordon methods.

I use standard LAPACK[63] routines to solve equations 3.5 and 3.6. The eigenvalues b and eigenvectors $\vec{c^b}$ completely specify the linearly independent solutions of the Schrödinger equation on the surface Σ. This information is generally packaged in terms of a $\underline{\mathrm{R}}$-matrix

$$\mathrm{R}_{mm'} = -\sum_{\beta} Z_{m\beta} b_{\beta}^{-1} (Z^{-1})_{\beta m'} \tag{3.12}$$

where the columns of $\underline{Z}$ are given by the eigenvectors $\vec{c^b}$. Here β is the independent solution index.

3.1.3 Matching $\underline{\mathrm{R}}$-matrix boxes

The method outlined to this point assumes that equations 3.5 and 3.6 need to be solved only once to obtain an $\underline{\mathrm{R}}$-matrix at sufficiently large R to apply the asymptotic boundary conditions. This is not always the case. Situations can arise which require either an unusually large number of sectors or many tens of channels to describe the collision process. This can result in a Γ^{cc} matrix which is too large to reside in memory. However, it is not necessary to abandon the FEM $\underline{\mathrm{R}}$-matrix approach. One need only divide the radial domain into "boxes" and solve the $\underline{\mathrm{R}}$-matrix equations **separately** in each box. The resulting solutions can be combined

in such a way that a final solution is obtained which is equivalent to solving the $\underline{\mathrm{R}}$-matrix equations in a single box encompassing the entire radial domain and this is achieved with no loss of accuracy. This type of approach is sometimes called an "$\underline{\mathrm{R}}$-matrix propagator" method[77].

A description of the matching procedure is simplified by considering the example shown in Fig. 3.1. The radial domain is divided into two boxes, A and B. Boundary conditions are specified on the inner boundary of box A ($R = 0$) and left unspecified (i.e., left open) at $R = R_I$. In box B, the boundary conditions are left open at $R = R_I$ and on the outer boundary $R = R_{II}$, except for channels which are strongly-closed at R_{II}. In these strongly-closed channels, we must impose boundary conditions to eliminate exponential growth. The resulting square solution matrix $\underline{Z}$ has dimensions $m_{\max} \times \beta^{\mathrm{A}}_{\max}$ in A and $(m_{\max} + m_P) \times \beta^{\mathrm{B}}_{\max}$ in B, where $m_{\max}$ is the total number of channels, m_P is the number of channels open or weakly-closed on R_{II}. For our particular example, the number of independent solutions in A is $\beta^{\mathrm{A}}_{\max} = m_{\max}$, and $\beta^{\mathrm{B}}_{\max} = m_{\max} + m_P$ in box B. The first step is to require a linear combination of the independent solutions and their derivatives to be continuous across the boundary (R_I) in each channel. This can be written as:

$$\begin{aligned} \sum_{\beta=1}^{\beta^{\mathrm{A}}_{\max}} Z^{\mathrm{A}}_{m\beta} D^{\mathrm{A}}_{\beta} &= \sum_{\beta'=1}^{\beta^{\mathrm{B}}_{\max}} Z^{\mathrm{B}}_{m\beta'} D^{\mathrm{B}}_{\beta'} \\ \sum_{\beta=1}^{\beta^{\mathrm{A}}_{\max}} Z^{\mathrm{A}}_{m\beta} b^{\mathrm{A}}_{\beta} D^{\mathrm{A}}_{\beta} &= -\sum_{\beta'=1}^{\beta^{\mathrm{B}}_{\max}} Z^{\mathrm{B}}_{m\beta'} b^{\mathrm{B}}_{\beta'} D^{\mathrm{B}}_{\beta'} \end{aligned} \tag{3.13}$$

where D represents the undetermined coefficients, the channel index m runs from 1-$m_{\max}$ and the wave function derivatives have been written as $Z'_{m\beta} = Z_{m\beta} b_{\beta}$. The minus sign in the second condition comes from a reversal of the surface normal direction. As it stands, Eq. 3.13 is not sufficient to fully specify the coefficients D. A final condition is obtained by again requiring **constant** log derivatives on the outer boundary (R_{II}). This requirement selects the $\underline{\mathrm{R}}$-matrix eigenchannel solutions, which will be superimposed later to meet the physical boundary conditions relevant for either a scattering or photoabsorption process. This statement can be written as

$$\sum_{\beta'=1}^{\beta^{\mathrm{B}}_{\max}} Z^{\mathrm{B}}_{m'\beta'} b^{\mathrm{B}}_{\beta'} D^{\mathrm{B}}_{\beta'} = b_{\beta^{\mathrm{f}}} \sum_{\beta'=1}^{\beta^{\mathrm{B}}_{\max}} Z^{\mathrm{B}}_{m'\beta'} D^{\mathrm{B}}_{\beta'} \ . \tag{3.14}$$

where now the channel index m' runs from $m_{\max} + 1$ to $m_{\max} + m_P$. Equations 3.13 and 3.14 can be combined to form a generalized eigenvalue equation whose non-infinite eigenvalues determine the new log derivatives $b_{\beta^{\mathrm{f}}}$ on the boundary R_{II}. The corresponding eigenvectors D give the new solution through expressions such

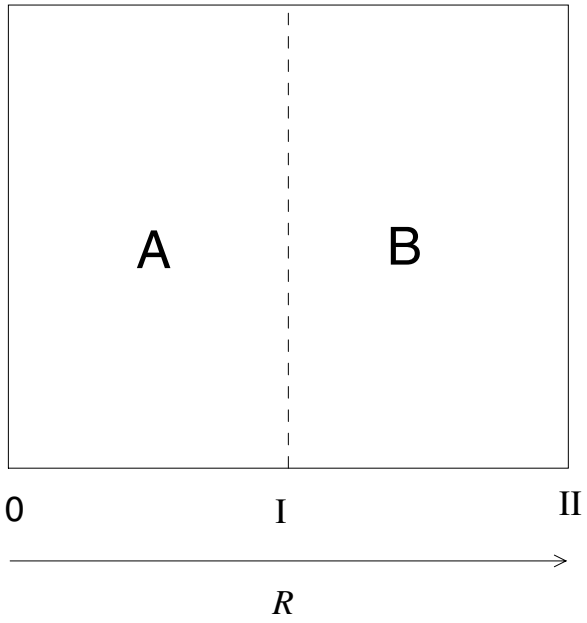

Figure 3.1: Division of the radial domain into two boxes A and B. The $\underline{\mathrm{R}}$-matrix equations are solved separately from $R = 0 \rightarrow R_I$ in A and from $R_I \rightarrow R_{II}$ in B. Appropriate boundary conditions are applied at $R = 0$ and $R = R_{II}$, leaving all channels open across R_I.

as:

$$Z^{\mathrm{f}}_{m'\beta^{\mathrm{f}}} = N_{\beta^{\mathrm{f}}} \sum_{\beta'=1}^{\beta^{\mathrm{B}}_{\max}} Z^{\mathrm{B}}_{m'\beta'} D^{\mathrm{B}}_{\beta'\beta^{\mathrm{f}}} \tag{3.15}$$

where $N_{\beta^{\mathrm{f}}}$ is a normalization constant for each new independent solution. If it becomes necessary to divide the radial domain into many sectors this procedure can be iterated as many times as necessary to obtain the solution matrix and log derivatives on the final boundary.

3.2 Constructing the scattering matrix

At this stage, the $\underline{\mathrm{R}}$-matrix represents mathematically correct solutions of the coupled Schrödinger equations. The physically relevant solutions are obtained by applying asymptotic boundary conditions (Eq. 2.5). At large R, where "large" is typically of the order 10^3 Bohr (occasionally 10^5 Bohr for systems that involve the long-range magnetic dipole interaction), $V(R) \rightarrow$ constant and the two linearly independent solutions are the standard spherical Bessel $j_l(k_m R)$ and Neumann $n_l(k_m R)$ functions in each channel. A set of linearly-independent solutions at energy E can be written in this limit as[23]

$$\underline{M}(R) \overset{R\to\infty}{\longrightarrow} \underline{f} - \underline{g}\,\underline{K} \tag{3.16}$$

where $f_{mm'} = \sqrt{\frac{2\mu}{\pi k_m}} k_m R j_l(k_m R)\delta_{mm'}$ and $g_{mm'} = \sqrt{\frac{2\mu}{\pi k_m}} k_m R n_l(k_m R)\delta_{mm'}$ are diagonal matrices of energy normalized spherical Bessel and Neumann functions. The real-valued constant reaction matrix $\underline{K}$ determines the appropriate linear combination of f and g. It is evaluated by matching the log derivative of the wave function integrated from small R (Eq. 3.12) with the asymptotic form given in Eq. 3.16. The result written in terms of the $\underline{\mathrm{R}}$-matrix is[23]

$$\underline{K} = \left[\underline{f} - \underline{f'}\,\underline{\mathrm{R}}\right]\left[\underline{g} - \underline{g'}\,\underline{\mathrm{R}}\right]^{-1} \quad . \tag{3.17}$$

The $\underline{S}$-matrix, from which all physical observables can be evaluated, is related to the $\underline{K}$-matrix by the following[23]

$$\underline{S} = \left[\underline{1} + i\underline{K}\right]\left[\underline{1} - i\underline{K}\right]^{-1} \tag{3.18}$$

where $i = \sqrt{-1}$. Any scattering observable of interest can then be determined once this $\underline{S}$-matrix is constructed.

3.3 Adiabatic representation

Solving the diabatic two-body cold collision equations is the most straightforward approach for obtaining an $\underline{S}$-matrix. However, it does not always provide the most insight into the collision dynamics. Adiabatizing the equations in R can be a useful step in this regard. A qualitative picture of the collision dynamics is obtained immediately from the adiabatic potentials and couplings. From a numerical standpoint, an $\underline{S}$-matrix obtained by solving the coupled adiabatic equations can be just as accurate as solution determined in a diabatic representation. However, in the two-body case it is actually more work to generate the adiabatic potentials and therefore this approach is presented mainly as a qualitative tool. This is not the case for the 3-body collisions presented in chapter 8, for which potentials and couplings have been calculated using the adiabatic hyperspherical method. An adiabatic variant of the FEM $\underline{\mathrm{R}}$-matrix procedure has been developed to solve these equations and is outlined in Appendix B.

If we choose R as the adiabatic coordinate, the Hamiltonian can be separated into two terms $H = T_R + H^{\mathrm{ad}}$, where the kinetic energy operator T_R contains all the derivative terms with respect to R. The adiabatic Hamiltonian H^{ad} is given by

$$H^{\mathrm{ad}}_{mm'} = \delta_{mm'} \frac{l_m(l_m+1)}{2\mu R^2} + V_{mm'} \tag{3.19}$$

where $V_{mm'}$ includes the interaction potentials discussed in chapter 2.2 evaluated in an appropriate spin basis. Adiabatic eigenfunctions Φ_γ and eigenvalues (adiabatic potentials) $U_\gamma(R)$ of H^{ad} are calculated by parametric diagonalization of Eq. 3.19 as a function of R. The wave function can then be written in terms of the adiabatic eigenfunctions as [78, 79]

$$\Psi = \sum_\gamma \Phi_\gamma(\Omega, \chi; R) M_\gamma(R) \ , \tag{3.20}$$

where Ω represents the angular degrees of freedom and χ the spin degrees of freedom. Substituting this expansion back into the Hamiltonian gives the following representation for the coupled radial equations:

$$\left[-\frac{1}{2\mu} \left(\underline{1} \frac{\partial}{\partial R} + \underline{P} \right)^2 + \underline{U} \right] \ \vec{M} = E \ \vec{M} \ . \tag{3.21}$$

All of the coupling (or nonadiabatic) effects are now contained in the real, antisym-

metric derivative coupling matrix $\underline{P}(R)$ given by

$$P_{\gamma\gamma'} = \left\langle \Phi_\gamma | \frac{\partial}{\partial R} \Phi_{\gamma'} \right\rangle \ . \tag{3.22}$$

The Born-Oppenheimer approximation neglects the $\underline{P}$ matrix. I emphasize that the adiabatic formulation of the coupled Schrödinger equations is exact in principle, if $\underline{P}$ is included and a complete angular momentum basis is used, which in the two-body case will always be possible in the Born-Oppenheimer limit[31], provided external magnetic fields can be neglected. Using a standard identity, Eq. 3.22 can be rewritten as

$$P_{\gamma\gamma'} = \begin{cases} \frac{\langle \Phi_\gamma | \partial H^{\rm ad}/\partial R | \Phi_{\gamma'} \rangle}{U_{\gamma'} - U_\gamma} , & \gamma \neq \gamma' \\ 0, & \gamma = \gamma' \end{cases} \ . \tag{3.23}$$

For two-body collisions, evaluating the $\underline{P}$ matrix is more straightforward with this approach since most of the terms in $\underline{H}^{\rm ad}$ are analytical functions of R. It is only necessary to take numerical derivatives of the small R part of the Born-Oppenheimer potentials.

As an example of the usefulness of this method, adiabatic potentials and derivative couplings are shown in Fig. 3.2 for the case of two ^{87}Rb atoms colliding in an f=2 total spin state. The two-body collision complex consists of three coupled channels (one singlet and two triplet Born-Oppenheimer potentials) with one channel converging to each of the three hyperfine split thresholds (see inset Fig. 2.1). Magnetic dipole couplings have been neglected so this represents a pure spin-exchange collision. The dynamics of spin-exchange collisions are extremely simple. The derivative couplings shown in Fig. 3.2.b indicate that transitions between spin channels occur almost exclusively in the neighborhood of $R \sim 20 - 25$ a.u. This value of R is a fairly generic result for ground-state collisions in all the alkalis. The coupling region indicates the point at which exchange splitting in the Born-Oppenheimer potentials becomes comparable to the hyperfine splittings. Outside this transition region the wave functions in each channel evolve freely in the adiabatic potentials. At small R these potentials are basically the singlet or triplet Born-Oppenheimer potentials. Because the couplings are so localized and all channel crossings occur near the same R, the opportunity arises for the wave functions to interfere in such a way as to shut off spin-exchange losses. This is exactly the fortuitous situation with ^{87}Rb collisions, which will be discussed in more detail in chapter 5.

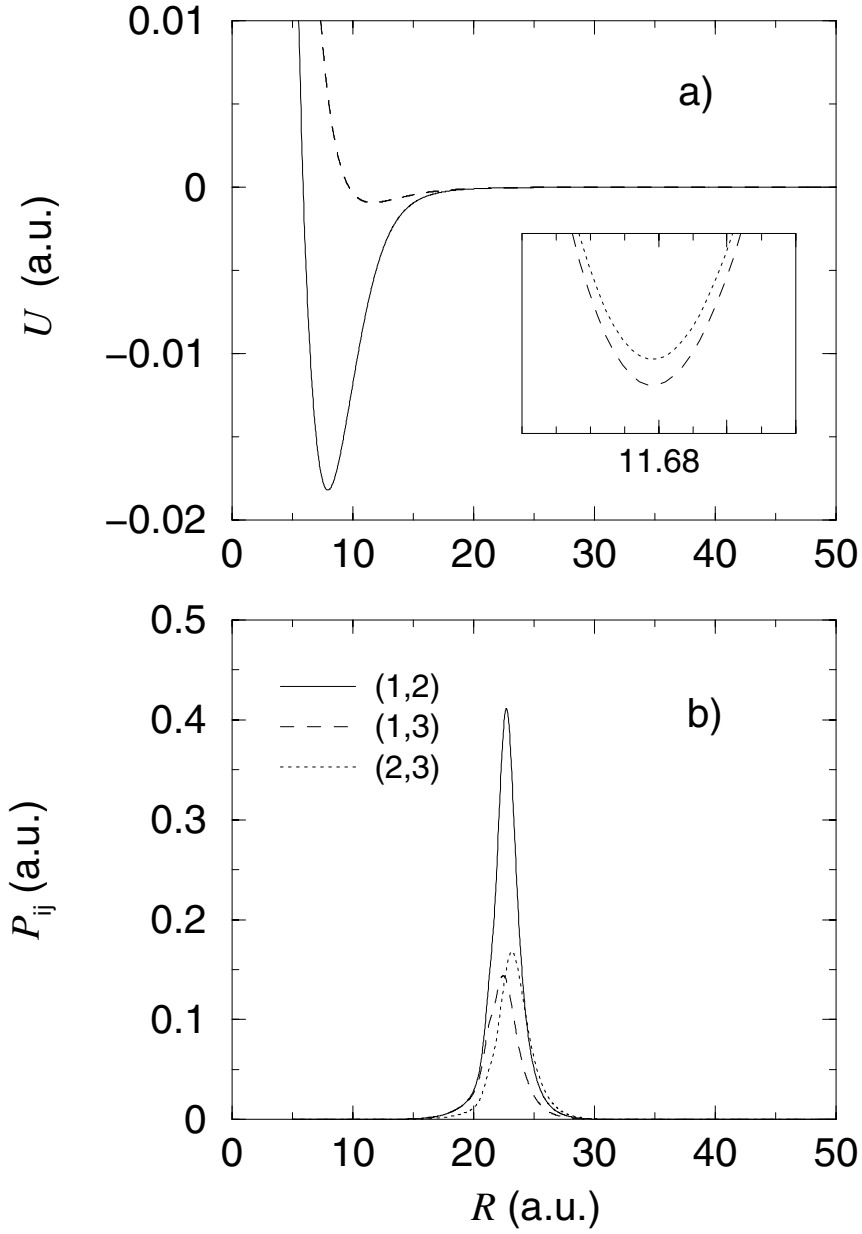

Figure 3.2: Adiabatic potentials a) and $\underline{P}$-matrix couplings b) for the s-wave collision of two ^{87}Rb atoms in a f=2 angular momentum state. The inset of a) shows the splitting of the two triplet-like potentials which is approximately equal to one hyperfine unit of energy ($\Delta_{87} \simeq 10^{-6}$ a.u.). The adiabatic channel indices in b) are defined in order of increasing energy i.e., channel 1 is a singlet-like state converging to the 1+1 threshold. Channels 2 and 3 are predominately triplet states at small R, which correlate adiabatically to the 1+2 and 2+2 thresholds, respectively at $R \to \infty$.

Chapter 4

Multichannel quantum defect treatment of cold collisions

Chapter 2 presented the textbook approach for scattering theory of cold atoms, deriving a set of coupled-channel Schrödinger equations which describe the collision dynamics. Brute-force numerical techniques for solving these equations were developed in Chapter 3. One job that falls to the cold collision practitioner is refining the Born-Oppenheimer potentials such that theoretical calculations agree with experiment. This usually requires the solution of the scattering equations throughout a large parameter space that consists of the Born-Oppenheimer parameters: singlet a_s and triplet a_t scattering lengths, and the C_6 dispersion coefficient. In addition, the calculations often must be performed for a number of magnetic bias fields B and collision energies E. Although the numerical algorithms presented in Chapter 3 are reasonably fast, this still becomes a time consuming project when many thousands of calculations are needed to bound the parameter space, as is frequently the case.

To alleviate this difficulty, our understanding of cold collision physics can be exploited to develop a more compact and efficient framework for solution of the scattering equations. The method outlined here is a fully-developed theory for spin-exchange collisions. The magnetic dipole interaction is neglected throughout this chapter. The techniques developed here should also allow dipolar effects to be calculated conveniently within perturbation theory, though this has not yet been implemented. Referring back to Fig. 2.1, it is obvious that the collision partners experience two very different energy scales in the course of a scattering event. At small R, the Born-Oppenheimer potentials are very deep compared to typical collision energies and the relative kinetic energy of the pair is large. At large R, the hyperfine energy sets the scale. The energy scale of interest for cold ground state collisions ranges up to a few mK. Over this range, the small R wave functions do not change appreciably (see Fig. 4.1) implying that, to a good approximation, this part of the problem is nearly energy-independent. This in itself represents a huge computational savings because the spin-exchange coupling occurs in this small R region (see Fig. 3.2) and only needs to be calculated for a few values (or even just a single value) of E. The energy dependence of the final scattering matrices derives from the large R evolution of the wave function where the channels are uncoupled;

the solutions in this region can therefore be obtained in terms of single-channel solutions to a simple radial Schrödinger equation. In addition, the large R solutions can be parameterized such that the single channel equations need to be solved only once as a function of energy. Moreover, we will see that the parameterization can be made essentially atom-independent. The final scattering solutions can then be obtained through the manipulation of a few small matrices.

This approach has its origins in Seaton's[80] multichannel quantum defect theory (MQDT) and in multichannel effective range theory[81]. I will refer to the method as multichannel spectroscopy or sometimes simply MQDT. It has proven to be a powerful yet simple theoretical tool for describing multichannel collisions and half-collisions, in contexts such as Rydberg electron motion[23] in the field of a structured ionic core. The theory is well known and has been applied to cold alkali collisions by other groups[82, 83, 84, 85, 86, 87, 88]. However, the formulation presented here has two new key developments[89]; i) a new standardization of the long-range field properties which allows a nearly atom-independent parameterization, and ii) a recoupling frame transformation (FT) approximation. The FT approximation combined with the long-range MQDT parameters reproduces the multichannel collision physics, with reasonable accuracy for most systems, completely in terms of single channel parameters. In addition to increased numerical efficiency, MQDT provides a great deal of insight. The techniques developed here are used in later chapters to explain certain aspects of cold collision dynamics.

The structure of this chapter is as follows: In section 4.1, accurate solutions of the Schrödinger equation in the presence of a long-range potential are described. The parameters that connect these solutions with free-particle solutions (j_l, n_l) at $R \to \infty$ are defined and evaluated. In Section 4.2 the matrix equations that allow one to connect the small and large R solutions and ultimately derive an $\underline{S}$-matrix are developed. In addition, it is shown how to construct energy-normalized scattering wave functions from the reference wave functions and long-range parameters. A frame transformation approximation for the short-range reaction matrix is presented in Section 4.3 and finally, example calculations illustrating the MQDT approach are presented in Section 4.4.

4.1 Reference wave functions

In multichannel spectroscopy, the key idea is to express scattering observables in terms of a real, linearly independent base pair (f^0, g^0) of solutions to the radial Schrödinger equation in the appropriate long-range potential. The long-range potential applicable for ground state spin-exchange collisions is

$$V^{lr}(R) = -\frac{\mathrm{C}_6}{R^6} - \frac{\mathrm{C}_8}{R^8} - \frac{\mathrm{C}_{10}}{R^{10}} \ . \tag{4.1}$$

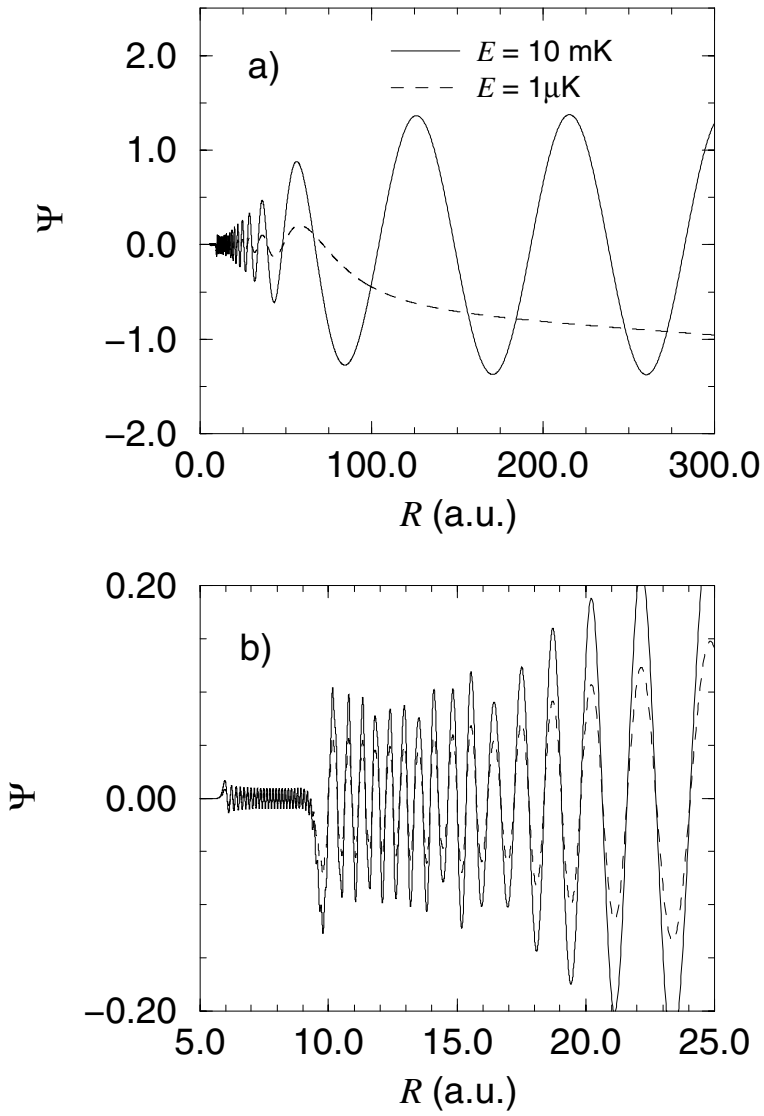

Figure 4.1: Component of a multichannel wave function calculated at two collision energies $E = 1\mu$K and $E = 10$mK. Top figure a) shows the strong energy dependence of the long range part of the wave function. Bottom figure b) is a blowup of the small R part of the wave function. Except for an overall normalization constant the two wave functions are almost identical.

$V^{lr}(R)$ is the exact form of the long range potentials for both singlet and triplet Born-Oppenheimer states once the long-range exchange interaction becomes exponentially small. This occurs at roughly $R \geq 30$ Bohr in all the alkalis (see Fig. 4.2). An advantage to the numerical approach presented here is the fact that this methodology is not restricted to the form 4.1 of $V^{lr}(R)$. The theory can be easily extended to incorporate retardation effects or other forms for the long range potentials.

In Section 4.1.1 the Milne phase amplitude method is used to generate the energy-analytic base pair of radial solutions (f^0, g^0). This pair is then standardized making the MQDT parameters portable from atom to atom. Section 4.1.2 presents transformations that allow the base pair (f^0, g^0) to be written in terms of an asymptotic energy-normalized base pair (f, g) required by scattering theory. The four long-range parameters needed for these transformations are defined and evaluated. Their low-energy properties are then detailed in section 4.1.3.

4.1.1 Milne equation

A convenient, exact representation of (f^0, g^0) can be obtained within the Milne[90] phase-amplitude method, details of which are provided in Ref.[91, 92]:

$$\begin{aligned} f^0(\varepsilon, l, R) &= \sqrt{\tfrac{2\mu}{\pi}}\alpha(R)\sin\left(\int_{R_x}^{R}\tfrac{dR'}{\alpha^2(R')} + b_l\right) \\ g^0(\varepsilon, l, R) &= -\sqrt{\tfrac{2\mu}{\pi}}\alpha(R)\cos\left(\int_{R_x}^{R}\tfrac{dR'}{\alpha^2(R')} + b_l\right) \ . \end{aligned} \tag{4.2}$$

The Milne amplitude $\alpha(R)$ is a particular solution of the Milne nonlinear equation

$$\frac{\partial^2\alpha}{\partial R^2} + k^2(R)\alpha(R) = \alpha^{-3}(R) \ . \tag{4.3}$$

where the R-dependent wave number is defined as

$$k(R) = \sqrt{2\mu(\varepsilon - \frac{l(l+1)}{2\mu R^2} - V^{lr})} \ . \tag{4.4}$$

Eq. 4.3 is solved with a predictor-corrector method[62] subject to WKB-like boundary conditions at some small fixed radius R_x (generally chosen to be R_x = 10 a.u.), namely,

$$\begin{aligned} \alpha(R_x) &= k(R_x)^{-1/2} \\ \alpha'(R_x) &= \frac{\partial}{\partial R}\left[k(R_x)^{-1/2}\right] \ . \end{aligned} \tag{4.5}$$

WKB-type boundary conditions are not strictly necessary, however, Korsch and Laurent have shown[93] that this provides optimal smoothness in the radial and energy variations of α. The choice of R_x= 10 a.u. is somewhat arbitrary, all

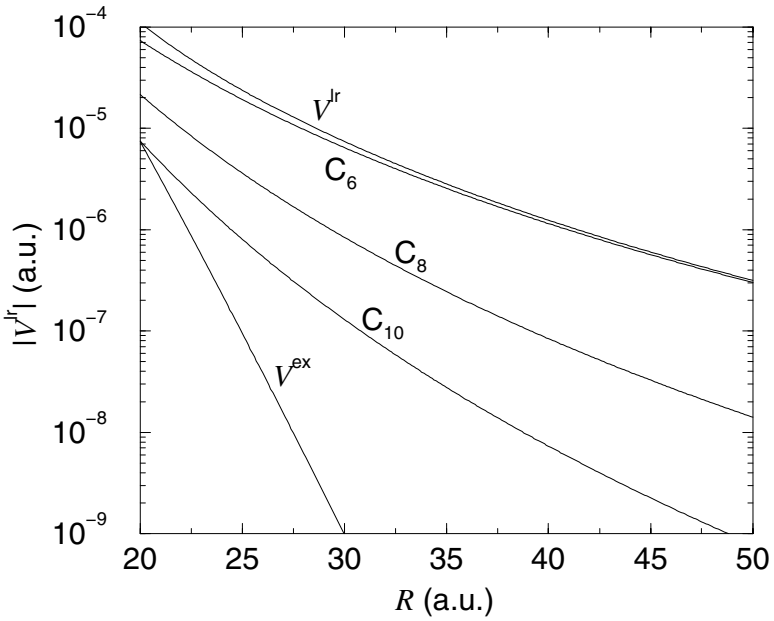

Figure 4.2: Contributions to the the Rb_2 long range potential V^{lr}. These include the three dispersion terms, each of which is labeled by its coefficient C_n. The long-range exchange term V^{ex} which is not included in V^{lr} is also shown.

one requires is that $V^{lr}(R_x)$ is deep enough that the semi-classical approximation is reasonably good where the boundary conditions are applied. An example of the base pair (f^0, g^0) derived from the "smooth" Milne amplitude and phase $\phi(R) = \int \alpha^{-2}(R')dR'$ is shown in Fig. 4.3.

The **energy independent** phase shift b_l in Eq. 4.2 standardizes the low-energy asymptotic structure of (f^0, g^0). Its introduction allows us to develop a nearly atom-independent parameterization of the long-range field properties (subsection 4.1.2). The phase shift b_l is chosen such that

$$f^0(\varepsilon = 0, l, R) \stackrel{R\to\infty}{\longrightarrow} const \times R^{l+1} \ . \tag{4.6}$$

In the s-wave limit this is equivalent to demanding that the scattering length of f^0 must vanish. The standardization phase is determined by integrating the Milne equation from R_x to $R_{max} \sim 200$ Bohr at zero energy and then equating the logarithmic derivative of $f^0(\varepsilon = 0, l, R_{max})$ with the logarithmic derivative of the zero energy solutions of the Schrödinger equation in the presence of a van der Waals potential (i.e., $V^{lr} = -\mathrm{C}_6/R^6$ which is valid beyond $R \sim 200$ Bohr). These solutions[24], $\Psi \sim R^{1/2}J_{\pm\nu}(x)$, are given in terms of Bessel functions of fractional order ν. One independent solution, with $\nu = -(2l+1)/4$, has the proper asymptotic behavior R^{l+1}. Here, x represents a rescaled variable $x = \sqrt{\frac{\mu \mathrm{C}_6}{2}}R^{-2}$. The final expression for the standardization phase is

$$\begin{aligned} b_l \ &= \ -\phi(R_{max}) \ + \\ &\tan^{-1}\left[\frac{2R_{max}J_\nu(x)}{\alpha^2(R_{max})[J_\nu(x) + 2R_{max}J'_\nu(x)] - 2R_{max}J_\nu(x)\alpha(R_{max})\alpha'(R_{max})}\right] \end{aligned} \tag{4.7}$$

The derivative of the Bessel function $J'_\nu(x)$ is taken with respect to R. Setting large R boundary conditions for f^0 is contrary to the "standard" MQDT approach[80, 82, 83, 84, 85, 86, 87, 88] which requires f^0 to vanish as $R \to 0$. However, the reference potential V^{lr} is not physical inside $R \leq 30$ a.u. and the base pair (f^0, g^0) is never used there. This provides a very clean separation of the small and large R physics, as well as a simple standardization of the long range parameters.

4.1.2 Calculating the MQDT parameters

We ultimately want a scattering solution normalized to $\delta(E - E')$. This is obtained by introducing a second energy normalized base pair (f, g), which are non-analytic functions of energy. The energy-normalized base pair is related to (f^0, g^0) through the transformation

$$\begin{pmatrix} f(R) \\ g(R) \end{pmatrix} = \begin{pmatrix} A^{\frac{1}{2}} & 0 \\ A^{-\frac{1}{2}}\mathcal{G} & A^{-\frac{1}{2}} \end{pmatrix} \begin{pmatrix} f^0(R) \\ g^0(R) \end{pmatrix}. \tag{4.8}$$

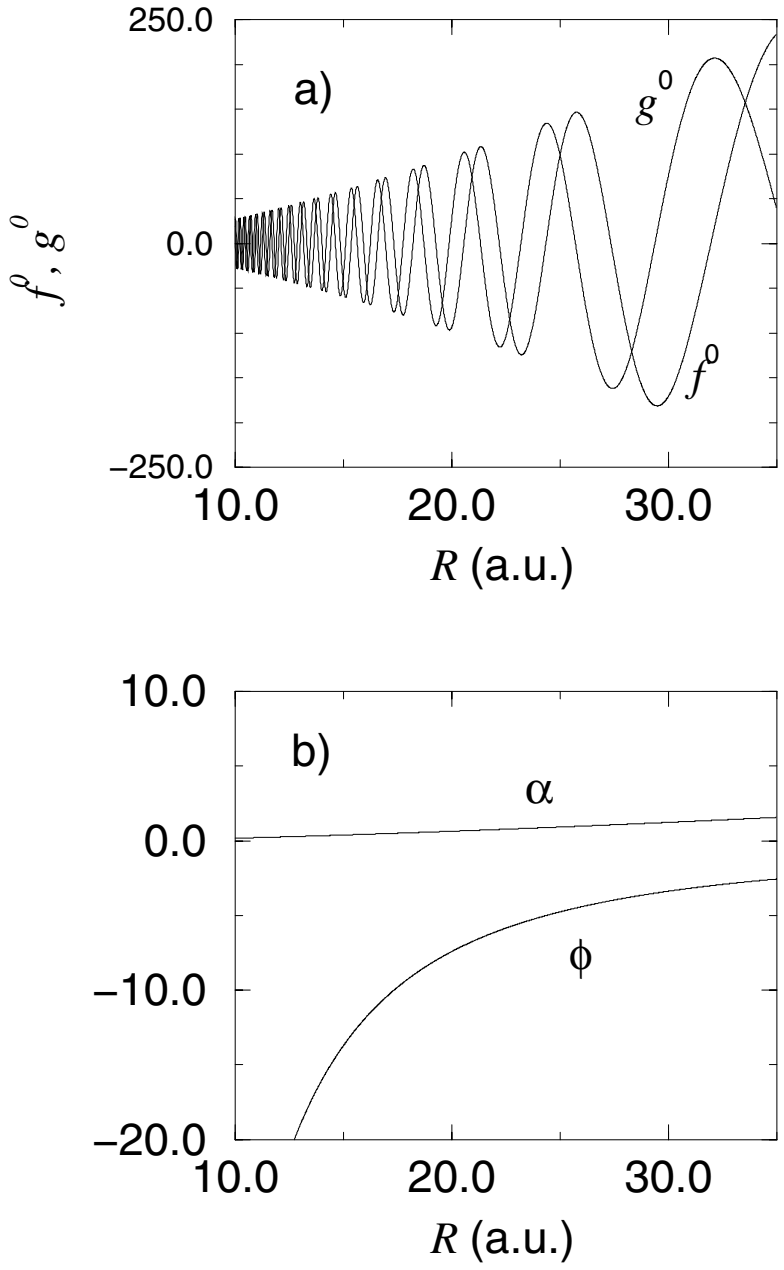

Figure 4.3: a) The base pair (f^0, g^0) are shown as a function of R. These were constructed from the Milne amplitude α and phase ϕ shown in b).

The MQDT parameters $A(\varepsilon, l)$ and $\mathcal{G}(\varepsilon, l)$ are independent of R and are essentially normalization factors. The new base pair are also mathematically correct solutions of the Schrödinger equation in the presence of the long range-field V^{lr}. Moreover, (f, g) can be expressed simply in terms of the energy-normalized spherical Bessel and Neumann functions at large R,

$$\begin{aligned} f(R) &\stackrel{R\to\infty}{\longrightarrow} kR\sqrt{2\mu/\pi k}\,(j_l(kR)\cos\eta - n_l(kR)\sin\eta) \\ g(R) &\stackrel{R\to\infty}{\longrightarrow} kR\sqrt{2\mu/\pi k}\,(j_l(kR)\sin\eta + n_l(kR)\cos\eta)\ . \end{aligned} \tag{4.9}$$

The non-analytic solutions (f, g) incur a phase-shift $\eta(\varepsilon, l)$ (due to the presence of V^{lr}) relative to the free particle solutions. These three parameters $(A, \mathcal{G}, \eta)$ summarize all that is needed to characterize the positive energy solutions. They are obtained by integrating Eq. 4.3 from R_x to $R_\infty \sim 10^4$ Bohr at energy ε. It is only necessary to construct the energy-analytic base pair (Eq. 4.2) and spherical Bessel and Neumann solutions at R_∞. Using Eq. 4.8 and 4.9, the MQDT parameters can be related to the Wronskians $W(\ldots)$ of these two sets of linearly independent solutions through the following relationships:

$$\begin{aligned} \tan\eta &= W(f^0, f^s)/W(f^0, g^s) \\ A &= -\left[\frac{W(g^0, f^s) - \tan\eta\, W(g^0, g^s)}{W(f^0, g^s) + \tan\eta\, W(f^0, f^s)}\right] \\ \mathcal{G} &= -\left[\frac{W(g^0, g^s) + \tan\eta\, W(g^0, f^s)}{W(f^0, g^s) + \tan\eta\, W(f^0, f^s)}\right]\ . \end{aligned} \tag{4.10}$$

Here, f^s, g^s are the energy normalized spherical Bessel and Neumann functions (defined in subsection 3.2). The last long-range parameter that will be needed is a negative energy phase $\beta(\varepsilon, l)$, which represents the phase accumulated in V^{lr},

$$\beta(\varepsilon, l) = \int_{R_x}^{\infty} \alpha(R')^{-2} dR' \quad + b_l\ . \tag{4.11}$$

The standardization of f^0 allows us to tabulate these long-range field parameters once and for all as functions of the single parameter $\gamma = (2\mu)^3 \mathrm{C}_6 \varepsilon^2$, in a.u. This scaling is strictly valid only for a pure van der Waals long-range potential, but in practice holds to a good approximation for the above form of V^{lr}. Examples of the standardized s- through f-wave parameters are shown in Fig. 4.4. The standardization proposed here begins to break down for partial waves greater than $l = 2$ for different atoms (i.e., when you vary the mass and V^{lr} parameters) and beyond $l = 3$ when one simply varies C_6. In addition, the current procedure for determining the nonzero l parameters at very low positive energies is numerically unstable. Both of these problems are likely linked to the large exponential growth

of the Milne amplitude in the classically forbidden region, which eventually leads to a linearly **dependent** base pair. A possible remedy would be to incorporate the analytical van der Waals solutions at finite energy derived in Ref.[88]. This would circumvent most of the exponential growth because it would not be necessary to integrate as far into the classically forbidden region. These issues will be the subject of a future study.

4.1.3 Low energy behavior of the long-range parameters

In the limit of zero energy, the asymptotic solutions for both positive and negative energy versions of the reference wave functions (f^0, g^0) should be equivalent. However, the long-range nature of the potential makes this difficult to achieve numerically. Therefore, it is preferable to develop an analytical connection formula to bridge this gap. The asymptotic form of the positive energy base pair (f^0, g^0) can be written (using equations 4.8 and 4.9) as the following,

$$\begin{aligned} f^0 &\overset{R\to\infty}{\longrightarrow} \sqrt{\frac{2\mu}{\pi k}}\, A^{-1/2} \sin(kR - l\pi/2 + \eta) \\ g^0 &\overset{R\to\infty}{\longrightarrow} -\sqrt{\frac{2\mu}{\pi k}} \left[A^{1/2} \cos(kR - l\pi/2 + \eta) + A^{-1/2}\mathcal{G} \sin(kR - l\pi/2 + \eta)\right] \ . \end{aligned} \tag{4.12}$$

In the zero energy limit, f^0 becomes simply

$$f^0 \overset{R\to\infty}{\longrightarrow} \sqrt{\frac{2\mu}{\pi}}\, A^{-1/2}[k^{l+1/2} R^{l+1} \cos\eta - k^{-(l+1/2)} R^{-l}\ \sin\eta] = R^{2l+1}/C \ . \tag{4.13}$$

Our standardization of f^0 forces its asymptotic behavior to be $f^0 \to R^{l+1}/C$. Therefore in the low-energy limit, $A \to C^2 k^{2l+1}$ and $\eta \to 0$. In addition, we find empirically that $\mathcal{G}$ goes to a constant value, $\mathcal{G}_l \to \mathcal{G}_l(0)$. The Wigner threshold properties of the $\underline{S}$-matrix are ultimately obtained from this low-energy behavior of A. We can now use these relationships to write down the low-energy limit for g^0, which is

$$g^0 \to \frac{C}{R^l} - \frac{\mathcal{G}(0)}{C} R^{l+1} \ . \tag{4.14}$$

The negative energy solutions are written in terms of the Milne phase ($\beta = \phi + b_l$) and amplitude α as originally given in Eq. 4.2. Using $\frac{2\mu}{\pi}\alpha^2 = (f^0)^2 + (g^0)^2$ and equations 4.13 and 4.14, we find

$$\alpha^2 \overset{R\to\infty}{\longrightarrow} \frac{R^{2l+2}}{C^2}[1 + \mathcal{G}^2(0)] \tag{4.15}$$

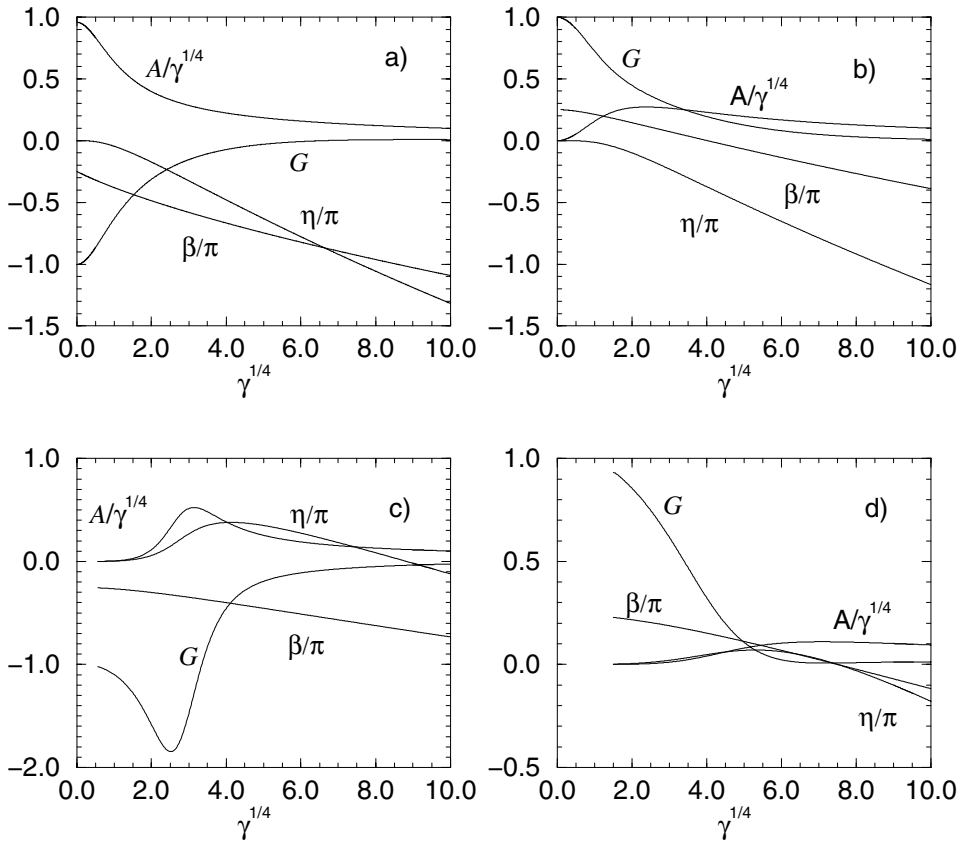

Figure 4.4: The four long-range standardized MQDT parameters are shown for a) $l = 0$, b) $l = 1$, c) $l = 2$, and d) $l = 3$ partial waves as a function of the parameter $\gamma^{1/4} = (2\mu \mathrm{C}_6)^{1/4}|k|$. On this scale, the parameters for $l = 0 - 2$ are nearly indistinguishable for all the alkalis. As a point of reference, the energy range E = 1 μK - 1 mK for a ^{87}Rb atom corresponds with the range $\gamma^{1/4}$ = 0.1-3.7.

and the negative energy reference function becomes

$$f^0 \rightarrow \sqrt{\frac{2\mu}{\pi}}\frac{R^{l+1}}{C}\left[1+\mathcal{G}^2(0)\right]^{1/2}\sin\beta(0)\ . \tag{4.16}$$

Comparing f^0 in equations 4.13 and 4.16 provides the connection between the positive and negative energy parameters,

$$|\sin\beta(0,l)| = \left[1+\mathcal{G}^2(0,l)\right]^{-1/2}\ . \tag{4.17}$$

The correct threshold energy behavior of the elastic scattering cross section is obtained if β satisfies this condition. This is illustrated in Fig. 4.5.

It is useful to have s-wave values for both A and $\mathcal{G}$ in the zero energy limit, as these will be related to the scattering length in the next section. The constants $C^2 = c(2\mu \mathrm{C}_6)^{1/4}$, $\mathcal{G}(0)$ and $\beta(0)$ are tabulated for the nominal set of dispersion parameters for each alkali atom (except Fr) in Table 4.1.

Table 4.1: Zero energy values of the s-wave long-range parameters. A is related to the constant c through the expression $A/k = c(2\mu \mathrm{C}_6)^{1/4}$. Equation 4.17 is used to determine $\beta(0)$.

Atom	c	$\mathcal{G}(0)$	$\beta(0)$
Li	0.96023	-1.0091	-0.78087
Na	0.95857	-1.0055	-0.78266
K	0.95775	-1.0037	-0.78355
Rb	0.95722	-1.0026	-0.78410
Cs	0.95701	-1.0022	-0.78430

Analytical expressions for these constants can be obtained in a pure van der Waals potential, (i.e., $V^{lr} = -\mathrm{C}_6/R^6$). Two linearly independent solutions of the single channel Schrödinger equation, $H = \partial^2/\partial R^2 + 2\mu \mathrm{C}_6/R^6$, are given by

$$\begin{aligned} Y_1 &= R^{1/2}J_{-1/4}(x) \\ Y_2 &= R^{1/2}N_{-1/4}(x) \end{aligned} \tag{4.18}$$

where, again $x = \sqrt{\frac{\mu \mathrm{C}_6}{2}}R^{-2}$ is a rescaled variable. Asymptotically expanding the Bessel J and Neumann N functions and requiring $W(f^0, g^0) = W(Y_1, Y_2)$ leads to

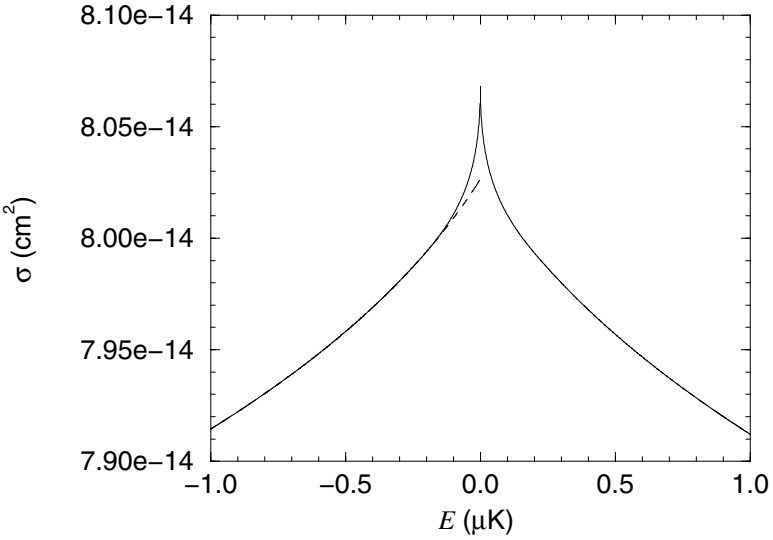

Figure 4.5: Energy dependence of the ^{6}Li $f = 0(1/2, 1/2)$ elastic cross section. The collision complex is described by two channels which consist of both atoms being in either their $f_a = f_b$ = 1/2 or 3/2 hyperfine states. Zero energy indicates the position of the 3/2 + 3/2 threshold. The ($E < 0$) solid line is a calculation using $\beta(0)$ from Eq. 4.17. The ($E < 0$) dashed line uses the numerical $\beta(0)$ which results in a slight artificial discontinuity in the energy dependence of the cross section.

the following expressions:

$$\begin{aligned} Y_1(R) &\rightarrow \frac{2\mu}{\pi k}\frac{2^{1/4}}{(2\mu \mathrm{C}_6)^{1/8}}\sqrt{\frac{\Gamma(5/4)}{\Gamma(3/4)}}\,R \\ Y_2(R) &\rightarrow -\frac{2\mu}{\pi k}\left(\frac{(2\mu \mathrm{C}_6)^{1/8}}{2^{1/4}}\sqrt{\frac{\Gamma(3/4)}{\Gamma(5/4)}} + \frac{2^{1/4}}{(2\mu \mathrm{C}_6)^{1/8}}\sqrt{\frac{\Gamma(5/4)}{\Gamma(3/4)}}\,R\right) . \end{aligned} \tag{4.19}$$

Comparing equation 4.13 with 4.19 yields the following values for C^2 and $\mathcal{G}(0)$:

$$\begin{aligned} C^2 &= \frac{(2\mu \mathrm{C}_6)^{1/4}\Gamma(3/4)}{\sqrt{2}\Gamma(5/4)} = 0.95598(2\mu \mathrm{C}_6)^{1/4} = \bar{a} \\ \mathcal{G}(0) &= -1.0 \ . \end{aligned} \tag{4.20}$$

This expression for C^2 is fairly well known, because it was derived previously in Ref[94]. Gribakin and Flambaum call this parameter the characteristic scattering length $\bar{a}$ that appears in their semi-classical expression for the physical scattering length a. Also, the analytic constants derived from a pure van der Waals potential are very nearly equivalent to the numerical values that include the effects of higher order dispersion terms in V^{lr} (see Table 4.1). This gives us some indication as to why the standardization works as well as it does. Referring back to Fig. 4.2, the C_8 and C_{10} terms contribute little to the potential beyond $R \sim 35$ Bohr. Neglecting the higher order dispersion terms, the Schrödinger equation can be rescaled in terms of the dimensionless parameter γ, which in the process removes all atom specific information from the equation and therefore from the long-range parameters.

4.2 Constructing scattering matrices and wave functions

The procedure outlined in chapter 3 requires the integration of a set of $N = N_o + N_c$ coupled Schrödinger equations outward from the origin to some large internuclear distance of order $R \sim 10^3$ Bohr. However, we have now defined reference wave functions (f^0, g^0) that are mathematically correct solutions beyond $R_0 \geq 35$ Bohr. It is therefore only necessary to integrate the coupled Schrödinger equations to R_0. The $N \times N$ solution matrix $\underline{M}(R)$ at a total energy E can be written as a linear combination of (f_i^0, g_i^0) at all radii $R \geq R_0$. These N independent solutions are standardized to have the following form:

$$\underline{M}(R) = \underline{f}^0(R) - \underline{g}^0(R)\underline{K}^{\mathrm{sr}} \ , \quad R \geq R_0 \ , \tag{4.21}$$

where $M_{ij}(R)$ is the i-th channel component of the j-th independent solution. Here f_i^0 and g_i^0 are diagonal matrices in the channel space, evaluated at the appropriate channel energy $\varepsilon_i = E - E_i$, with E_i the dissociation threshold energy, and l_i

the relevant orbital momentum in the i-th channel. The solution matrix still has components in energetically closed channels, but this method usually works best if all channels included at $R \geq R_0$ are still "locally open", i.e. with $k^2(R_0) > 0$. The short range (atom-dependent) physics is completely encapsulated in the short range reaction matrix $\underline{K}^{\rm sr}$, which varies slowly with E or B, except near isolated poles. The weak energy- and field-dependence of $\underline{K}^{\rm sr}$ is illustrated in Fig. 4.6.

The solution matrix (Eq. 4.21) does not yet satisfy the proper asymptotic scattering boundary conditions. In particular, $\underline{M}$ still contains closed channels. The asymptotic boundary conditions for these channels must be imposed in a simple matrix manipulation at each desired final state energy, through the following procedure[23]. First partition the $\underline{K}^{\rm sr}$ matrix into N_o open channels (those channels $i \in P$, for which $\varepsilon_i = E - E_i \geq 0$) and N_c closed channels ($i \in Q$, for which $\varepsilon_i = E - E_i < 0$). In this notation, $\underline{K}^{\rm sr}$ becomes:

$$\underline{K}^{\rm sr} = \begin{pmatrix} \underline{K}^{\rm sr}_{PP} & \underline{K}^{\rm sr}_{PQ} \\ \underline{K}^{\rm sr}_{QP} & \underline{K}^{\rm sr}_{QQ} \end{pmatrix} . \tag{4.22}$$

The exponentially-growing parts of the wave functions at $R \to \infty$ are next "eliminated" by applying a $N \times N_o$ transformation matrix $\underline{B}(E)$,

$$\underline{B} = \begin{pmatrix} \underline{1} \\ -(\tan \underline{\beta} + \underline{K}^{\rm sr}_{QQ})^{-1} \underline{K}^{\rm sr}_{QP} \end{pmatrix} \tag{4.23}$$

where $\underline{1}$ represents an $N_0 \times N_0$ identity matrix and $\tan \underline{\beta}$ is a diagonal matrix of the negative energy phases defined in the preceding section (4.1.2), evaluated at the appropriate channel energy $\varepsilon_i = E - E_i$. This transformation correctly assembles the linear combination of independent solutions which forces the closed channel components of the wave function to zero as $R \to \infty$. The open channel subspace of the new "physical" solution matrix $\underline{F}^0 = \underline{M}\,\underline{B}$ is given by:

$$\underline{F}^0(E, R) = \underline{f^0} - \underline{g^0}\,\underline{\tilde{K}} . \tag{4.24}$$

The modified reaction matrix $\underline{\tilde{K}}$ has dimensions $N_o \times N_o$ and contains the potentially resonant influence of closed-channel pathways:

$$\underline{\tilde{K}} = \underline{K}^{\rm sr}_{PP} - \underline{K}^{\rm sr}_{PQ} \left(\underline{K}^{\rm sr}_{QQ} + \tan \underline{\beta} \right)^{-1} \underline{K}^{\rm sr}_{QP} . \tag{4.25}$$

Moreover, should all channels be closed, discrete bound states occur at roots of the following determinantal equation:

$$\det \left(\underline{K}^{\rm sr}_{QQ} + \tan \underline{\beta} \right) = 0 . \tag{4.26}$$

Since $\underline{K}^{\rm sr}$ is only weakly-energy dependent and $\beta(\varepsilon)$ has been tabulated for the long-range potential of interest, the search for bound states and resonances is easy.

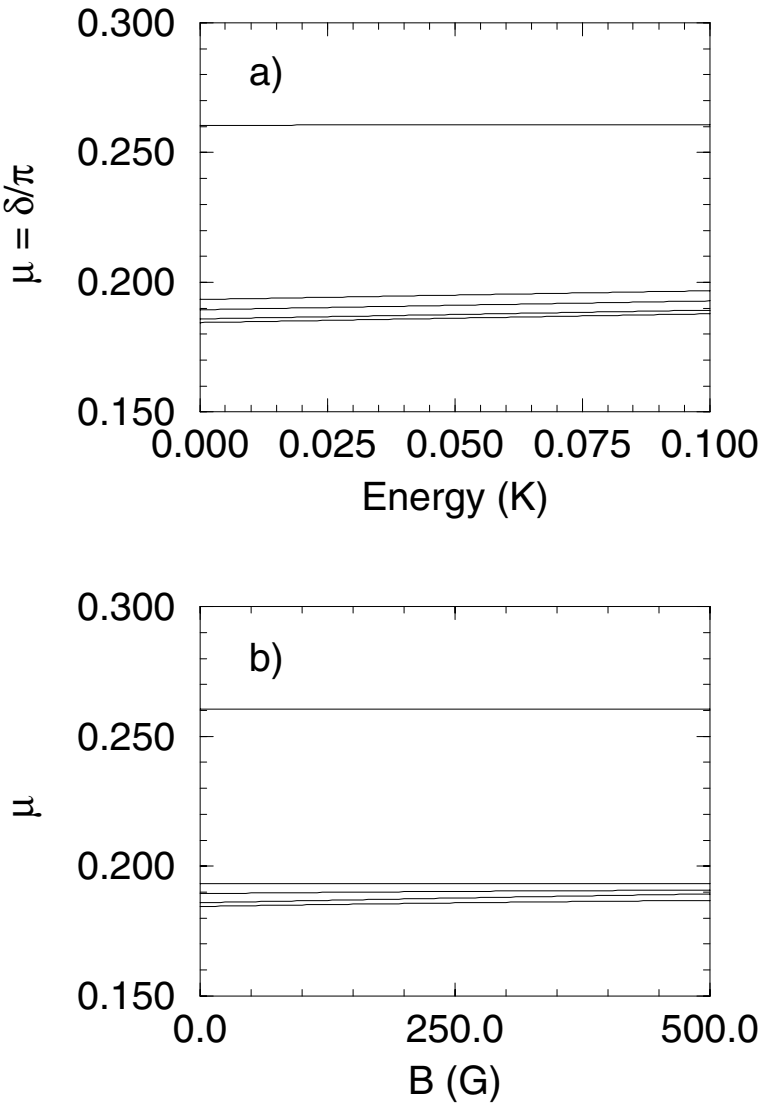

Figure 4.6: The eigenvalues of the short-range matrix $\underline{K}^{\rm sr}$ are plotted as functions of a) energy and b) magnetic field. The eigenvalues of the reaction matrix, $\tan\delta_\lambda$, are known as eigenphase shifts and these have been converted into quantum defects through the relation $\mu_\lambda = \delta_\lambda/\pi$. In both cases, the quantum defects are nearly constant implying that $\underline{K}^{\rm sr}$ can be treated, to a very good approximation, as constant over this range of energy and magnetic field. This particular example is for the collision of two $|2,-2\rangle$ ^{85}Rb atoms.

We want the final scattering solutions to be energy-normalized. This is accomplished by first relating the energy-analytic base pair (f^0, g^0) to the energy-normalized pair (f, g) (using Eq. 4.8):

$$\underline{F}(E,R) = \left[\underline{f} - \underline{g}\,\underline{K}\right] \ . \tag{4.27}$$

(The solution matrices $\underline{F}^0(E,R)$ and $\underline{F}(E,R)$ are related by an R-independent matrix $\underline{C}(E) = \underline{A}^{1/2}(\underline{1} + \underline{\mathcal{G}}\,\underline{\tilde{K}})$, i.e. $\underline{F}^0(E,R) = \underline{F}(E,R)\underline{C}(E)$, which can be ignored since it has no bearing on the final determination of the scattering matrix.) The new $N_o \times N_o$ real, symmetric, "energy-normalized" reaction matrix in the (f, g) representation is obtained using[82]

$$\underline{K} = \underline{A}^{1/2}\left(\underline{\tilde{K}}^{-1} + \underline{\mathcal{G}}\right)^{-1}\underline{A}^{1/2} \ . \tag{4.28}$$

This is still not quite the "physical" reaction matrix $\underline{K}^{\rm phys}$ of conventional scattering theory, owing to the phase shift $\eta(\varepsilon, l)$ of (f, g) relative to (j_l, n_l) at $R \to \infty$. Nevertheless, $\underline{K}$ possesses other properties expected in $\underline{K}^{\rm phys}$, such as the Wigner threshold behavior which is reflected in the dependence $A(\varepsilon, l) \sim \varepsilon^{l+1/2}$ as $\varepsilon \to 0$. $\underline{A}^{1/2}$ and $\underline{\mathcal{G}}$ are diagonal matrices in channel space, again evaluated at the appropriate channel energy $\varepsilon_i = E - E_i$. At this stage, it is a simple matter to construct the "physical" scattering matrix $\underline{S}$. A scattering matrix in the (f, g) representation can be obtained by the relationship given in Eq. 3.18. The additional phase shift of (f, g) relative to (j_l, n_l) is then accounted for when the physical scattering matrix is determined in the following manner,

$$\underline{S} = e^{i\underline{\eta}}\frac{1 + i\underline{K}}{1 - i\underline{K}}\,e^{i\underline{\eta}}. \tag{4.29}$$

Here, $\underline{\eta}$ is a diagonal matrix. The final $\underline{S}$-matrix is given completely in terms of the short-range reaction matrix $\underline{K}^{\rm sr}$ and the four long range parameters $A(\varepsilon, l), \mathcal{G}(\varepsilon, l), \eta(\varepsilon, l)$, and $\beta(\varepsilon, l)$.

Fig. 4.7 compares the elastic s-wave partial cross section calculated with the "essentially exact" FEM $\underline{\rm R}$-matrix approach and a quantum defect calculation performed with an energy-independent $\underline{K}^{\rm sr}$ via equations 4.25, 4.28, and 4.29. The MQDT results quantitatively reproduce all features of the spectrum over tens of mK with a single $\underline{K}^{\rm sr}$ calculated at E=0, relative to the 2+2 threshold. This calculation also predicts the energy of the zero-field Feshbach resonance[17, 16] (near 29 mK) to an accuracy of $\approx$ 0.1 mK. The small shift in the resonance position indicates that $\underline{K}^{\rm sr}$ is not strictly constant over this energy range. Effects associated with this slight energy dependence can be incorporated by interpolation of $\underline{K}^{\rm sr}$ after it is tabulated on a coarse energy grid.

Energy normalized scattering wave functions will be needed for the pho-

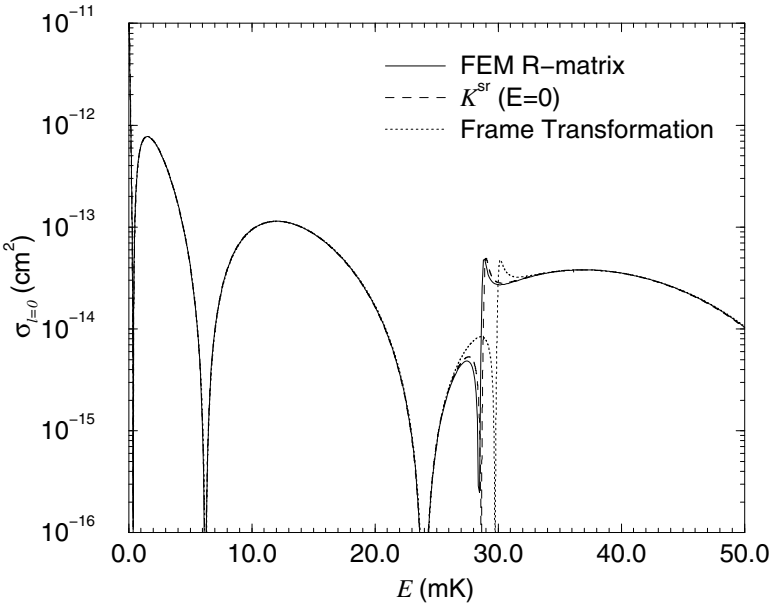

Figure 4.7: Elastic s-wave partial cross section for the collision of two ^{85}Rb atoms in their $|2,-2\rangle$ atomic hyperfine states. The feature near 29 mK is the zero-field position of the Feshbach resonance observed in Refs.[17] and [16]. The solid curve is a FEM $\underline{\mathrm{R}}$-matrix calculation. The dashed curve is an MQDT calculation using a constant $\underline{K}^{\mathrm{sr}}$ calculated at E=0. The short dashed line is a calculation using the energy-dependent frame transformation approximation for $\underline{K}^{\mathrm{sr}}$.

toassociation study in Chapter 7, in the range beyond $R \geq 30$ Bohr. This is achieved by right-multiplication of Eq. 4.27 using a normalization matrix $\underline{N}$ that tranforms the wave function into scattering matrix states (i.e., incoming and outgoing waves) that satisfy the asymptotic boundary condition given in Eq. 2.4. The energy-normalized standing-wave base pair (f, g) are defined in terms of the energy-normalized traveling-wave base pair (f^+, f^-) through the following relationships[23]:

$$f_i = \frac{f_i^+ - f_i^-}{\sqrt{2}\, i} \tag{4.30}$$

$$g_i = \frac{-f_i^+ - f_i^-}{\sqrt{2}} \,, \tag{4.31}$$

and the base pair (f^+, f^-) are defined as:

$$f_i^+ = \sqrt{\frac{2\mu}{\pi\hbar^2 k_i}} \frac{e^{i(k_i R - l_i \pi/2)}}{\sqrt{2}} \tag{4.32}$$

$$f_i^- = \sqrt{\frac{2\mu}{\pi\hbar^2 k_i}} \frac{e^{-i(k_i R - l_i \pi/2)}}{\sqrt{2}} \,. \tag{4.33}$$

Substituting (f_i^+, f_i^-) for (f_i, g_i) into Eq. 4.27 and requiring $(\underline{F}\,\underline{N})_{ii'}$ to equal the asymptotic boundary condition in Eq. 2.4, we find the following expression for the normalization matrix:

$$\underline{N} = (\underline{1} - i\underline{K})^{-1} \,. \tag{4.34}$$

An energy-normalized radial solution valid beyond $R \geq 35$ Bohr is then represented by

$$\underline{\Psi}(E, R) = \underline{F}(E, R)\underline{N}(E) \,. \tag{4.35}$$

Generation of these wave functions requires only $\underline{K}^{\rm sr}$, the four long-range MQDT parameters, and the single channel reference wave functions (f^0, g^0). In the case of a single open channel there is an alternative real representation for $\underline{\Psi}$ that is useful and is given by:

$$\underline{\Psi}(E, R) = \underline{F}^0(E, R) N^0(E) \,. \tag{4.36}$$

Here, $\underline{F}^0(E, R)$ is given by Eq. 4.24 and the normalization constant is equal to the following expression:

$$N^0(E) = \frac{\sin \delta^r}{A^{1/2}\tilde{K}} \tag{4.37}$$

where $\delta^r = \tan^{-1}(K)$.

Finally, we can derive a formula that connects the single channel scattering length a with the MQDT parameters. The physical phase shift is given in terms of the MQDT parameters by $\delta = \delta^r + \eta_i$. In this context δ^rrepresents the phase shift relative to (f, g) which in the zero energy limit is equivalent to the physical phase shift, $\delta^r = \delta$. The scattering length $a = -\tan\delta/k$ can therefore be written in terms of the long-range parameters as follows

$$a = \frac{-C^2\tilde{K}}{1 + \mathcal{G}(0)\tilde{K}} \tag{4.38}$$

where the low energy behavior of the parameter $A \to C^2 k$ has been incorporated.

4.3 Frame transformation approximation

At this stage, the theory presented still requires a full solution of the coupled radial Schrödinger equations to obtain $\underline{K}^{\rm sr}$. However, as discussed in section 3.3 the dominant spin exchange coupling is localized in the range $R \sim 25$ Bohr (see Fig. 3.2). To a good approximation the atoms move at $R \lesssim 20$ a.u. in a set of uncoupled channels, labeled by their total electronic spin quantum number S. We can therefore integrate the single channel Schrödinger equations with all hyperfine interactions omitted, after which each solution can be matched to the energy-analytic base pair (f^o, g^o) to obtain singlet (S=0) and triplet (S=1) quantum defects $\mu_S(\varepsilon)$. (The quantum defects μ_S are related to the singlet or triplet phase shift by $\mu_S = \delta_S/\pi$. The phase shift is given in terms of the single channel short-range reaction matrix by $\delta = \tan^{-1}\underline{K}^{\rm sr}$.) The short range reaction matrix is then approximated by the frame transformation (FT) formula

$$K^{\rm sr}_{i,i'} = \sum_\lambda \langle i|\lambda\rangle \tan\pi\mu_\lambda(\bar{\varepsilon}_\lambda)\,\langle\lambda|i'\rangle. \tag{4.39}$$

Here $X_{i\lambda} = \langle i|\lambda\rangle$ represents the unitary transformation matrix that connects the short range singlet-triplet basis $|\lambda\rangle \equiv |(s_a, s_b)S(i_a, i_b)I\ FM\rangle$ with the asymptotic hyperfine basis $|i\rangle \equiv |(s_a, i_a)f_a(s_b, i_b)f_b\ FM\rangle$. $X_{i\lambda}$ is understood to be the transformation matrix between **symmetrized** kets if the particles are identical. These transformations are discussed in section 2.3.2. One important point to note is that the FT approximation for $\underline{K}^{\rm sr}$ includes energetically closed channels as in previous MQDT studies[23]. Therefore, our FT approximation includes the Feshbach resonance physics which distinguishes it from a related class of approximations (notably the degenerate internal states method of cold collisions[95, 96], or equivalently the adiabatic nuclei method[97, 98, 99] of electron-molecule scattering theory). We have tried two different implementations of the frame transformation approximation. The first and simplest is an **energy-independent** approximation which uses

only the zero energy values of the quantum defects (i.e., $\bar{\varepsilon}_\lambda = 0$ in Eq. 4.39). In a different implementation of the **energy-dependent** FT than used previously, the energy $\bar{\varepsilon}_\lambda$ at which μ_λ is calculated in Eq. 4.39 is chosen to be a weighted average of the channel energies ε_i appropriate for eigenchannel $|\lambda\rangle$,i.e. $\bar{\varepsilon}_\lambda \equiv \sum_i \varepsilon_i |\langle i|\lambda\rangle|^2$. In tests conducted to this point, the energy-independent FT approximation has proven to be more accurate for the diagonal (elastic) $\underline{S}$-matrix elements, while the energy-dependent FT approximation has been more accurate for the off-diagonal (inelastic) $\underline{S}$-matrix elements. However, the quantum defects have only a weak energy-dependence (see Fig. 4.8) so neither approach has been remarkably better than the other. Given the greater simplicity of the energy-independent FT approximation, I would recommend it above the other approach. In particular, only two parameters are needed to determine $\underline{K}^{\rm sr}$. The physical scattering matrix can then be obtained via equations 4.25, 4.28, and 4.29 as before, but now solely in terms of single channel quantities. Examples of the FT approximation are provided in the next section.

As a last item, the quantum defect can be related to the scattering length. In general, it is more useful to parameterize the singlet and triplet Born-Oppenheimer potentials in terms of their quantum defect rather than their scattering length as is commonly done. For one thing, the complete range is covered over $\pm 1/2$ and accordingly they never experience a pole as scattering lengths can. But more importantly, given the quantum defects one can calculate an $\underline{S}$-matrix that is reasonably accurate for the entire entire range of energy and field relevant for cold collisions. This is in contrast to the scattering length, which only allows one to predict an s-wave elastic cross section over a very limited energy range ($E \sim$ 0-few tens of μK in Rb). Returning to the scattering length equation (Eq. 4.38) and substituting in the quantum defect for $\tilde{K}$ gives the relationship between a and μ:

$$a = \frac{-C^2 \tan \pi\mu}{1 + \mathcal{G}(0) \tan \pi\mu} \ . \tag{4.40}$$

This equation is readily inverted to express μ as a function of a:

$$\mu = \frac{1}{\pi} \tan^{-1} \left[\frac{-a}{C^2 + a\,\mathcal{G}(0)} \right] \ . \tag{4.41}$$

From this equation we find the following correspondence between the ranges of a and μ:

$$\begin{aligned} a = 0 \quad &, \quad \mu = 0 \\ a < 0 \quad &, \quad 0 < \mu < \frac{1}{\pi} \tan^{-1} \left[\frac{-1}{\mathcal{G}(0)} \right] \\ a = +\infty \quad &, \quad \mu = \frac{1}{\pi} \tan^{-1} \left[\frac{-1}{\mathcal{G}(0)} \right] \ . \end{aligned} \tag{4.42}$$

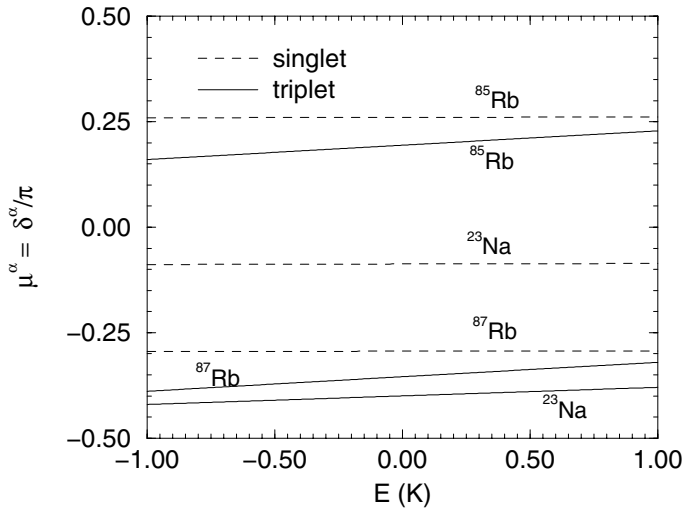

Figure 4.8: The weak energy-dependence of the Rb and Na singlet and triplet quantum defects are shown. The minimum of the triplet potential is not as deep as the singlet (see Fig. 2.1) and therefore the triplet quantum defects are a little more energy-dependent.

Values for $\mathcal{G}(0)$ are given in Table 4.1, from which we can see that a negative scattering length corresponds to $0 < \mu \lesssim 0.25$. All other values of μ (within its defined range) correspond to a positive scattering length. Given no information about the ground state Born-Oppenheimer potential, Gribakin and Flambaum's semi-classical theory[94] predicts that there is a 75% chance that a van der Waals potential will have a positive scattering length. We can find the deviation from this number caused by the inclusion of higher order dispersion terms in the potential by comparing the range of μ for which a is positive with the total allowed range of μ, which is $\sim$ 0.751/1.0. Therefore a potential which includes the higher order dispersion terms has approximately a 75.1% chance of having a positive scattering length.

4.4 Examples

We have verified that no accuracy is lost in our $\underline{S}$-matrix calculated when the multichannel solutions are represented beyond $R = 35$ Bohr by the semianalytic long-range reference functions (f_i^0, g_i^0), rather than the FEM $\underline{\mathrm{R}}$-matrix solution. However, if it required calculating $\underline{K}^{\mathrm{sr}}$ at each energy and field, the method would not be that much of an improvement over the brute force numerical approach. The real utility of the MQDT method comes from the fact that $\underline{K}^{\mathrm{sr}}$ can be treated, to a good approximation, as constant in energy and field and therefore only needs to be calculated once. Moreover, the frame transformation approximation allows $\underline{K}^{\mathrm{sr}}$ to be calculated solely in terms of two single channel quantum defects and a standard recoupling matrix. The accuracy of this approach has already been illustrated in Fig. 4.7. Both approximations produce elastic s-wave partial cross sections that agree within 2% of the FEM $\underline{\mathrm{R}}$-matrix calculations over a 50 mK energy range except near the zero-field Feshbach resonance. The discrepancy in the energy position of the resonance is $\approx$ 0.1 mK with a constant $\underline{K}^{\mathrm{sr}}$ and by $\approx$ 1.4 mK in the energy-dependent FT approximation. This will generally be the case. Both approximations for $\underline{K}^{\mathrm{sr}}$ produce accurate $\underline{S}$-matrices provided no resonances or quantum interferences are present. Using an approximate $\underline{K}^{\mathrm{sr}}$ will still predict these quantum effects but at an energy or field value slightly shifted from its true location. This is examined in more detail in the examples below. (The possibility exists that our method could predict shape resonances that are either spurious or at the wrong energy but we have seen no evidence for this in the partial waves (l=1-4) examined to date. This could occur if the reference potential $V^{lr} + l(l+1)/(2\mu R^2)$ supported a shape resonance.)

Fig. 4.9 shows the magnetic field-induced Feshbach resonance measured in Ref.[17]. Four methods have been used to calculate the scattering length a. The FEM $\underline{\mathrm{R}}$-matrix is considered to be the "exact" solution with a resonance position (defined here to be simply where $a \to \infty$) of B_r = 155.4 G. The second method uses a $\underline{K}^{\mathrm{sr}}$ calculated at $E = 0, B = 0$. The reaction matrix $\underline{K}^{\mathrm{sr}}$ is rotated into the representation in which the asymptotic Hamiltonian is diagonal at each B (see

section 2.3) and then equations 4.25, 4.28, and 4.29 are used to produce the final $\underline{S}$-matrix from which the scattering length is extracted (Eq. 2.34). Treating $\underline{K}^{\rm sr}$ as independent of E and B predicts a resonance field value of B_r = 156.4 G, which is shifted 1 Gauss higher than its true location. The other two methods are the energy-dependent and energy-independent FT approximations. These predict resonance field values B_r equal to 161.8 G and 156.1 G, respectively. The predicted resonance field value from the energy-independent FT is actually more accurate than the one using a multichannel calculation for the constant $\underline{K}^{\rm sr}$, although this is probably just an accident. The coupled-channel version of $\underline{K}^{\rm sr}$ produces more accurate off-resonance values for a. Finally the resonance is shown again in Fig. 4.10, which test our standardization of the long-range parameters. Here, both calculations use the same $\underline{K}^{\rm sr}(E = 0, B = 0)$ as in the previous graph. Two sets of standardized long-range parameters are used, one calculated with ^{39}K atomic properties (i.e., mass and dispersion coefficients) and the other with ^{85}Rb properties (these were used in the previous figure). The off-resonance values of a agree to within $\sim 1\%$. However, the calculation with the ^{39}K standardized parameters predicts a resonance field position of B_r = 136.2 G.

^{87}Rb inelastic loss rates are examined in Fig. 4.11. Again, four different methods have been used, and we regard the FEM $\underline{\rm R}$-matrix calculation as providing the "exact" benchmark rates. Here, we see that treating $\underline{K}^{\rm sr}$ as constant in energy reproduces the inelastic rates to within 7% over a 10 mK energy range. However, in this example the FT approximations are disastrous. This is because the ^{87}Rb singlet a_s and triplet a_t scattering lengths are nearly equivalent producing a suppressed inelastic rate. This suppressed spin-exchange rate was observed in Ref.[100]. The FT approximation will predict suppressed inelastic rates but only when $a_s \simeq a_t$ (the equality holds exactly for the energy-independent FT). The ^{87}Rb inelastic scattering rates are discussed in more detail in Section 5.1. The range over which the FT will provide realistic inelastic rates is examined in Fig. 4.12. Here, the percentage difference of an off-diagonal mod-squared S-matrix element calculated with the energy-independent FT approximation and with the FEM $\underline{\rm R}$-matrix method are compared over the entire ^{23}Na $\mu_s - \mu_t$ plane. There are no closed channels in this particular case of scattering from an $f = 2(2, 2)$ total spin state into an $f = 2(1, 1)$ state. The FT approximation agrees to within 10% of the exact value over most of the parameter space. The exception is along the line of suppressed rates $\mu_s \simeq \mu_t$, just as with ^{87}Rb collisions. The presence of resonances associated with closed channels will modify these results just as it did with elastic scattering. The accuracy of the FT diminishes somewhat with increased hyperfine splitting and with increased mass. At present, it has not been used for Cs calculations but the FT does in general, produce excellent results for Li through Rb with the few exceptions noted in this section.

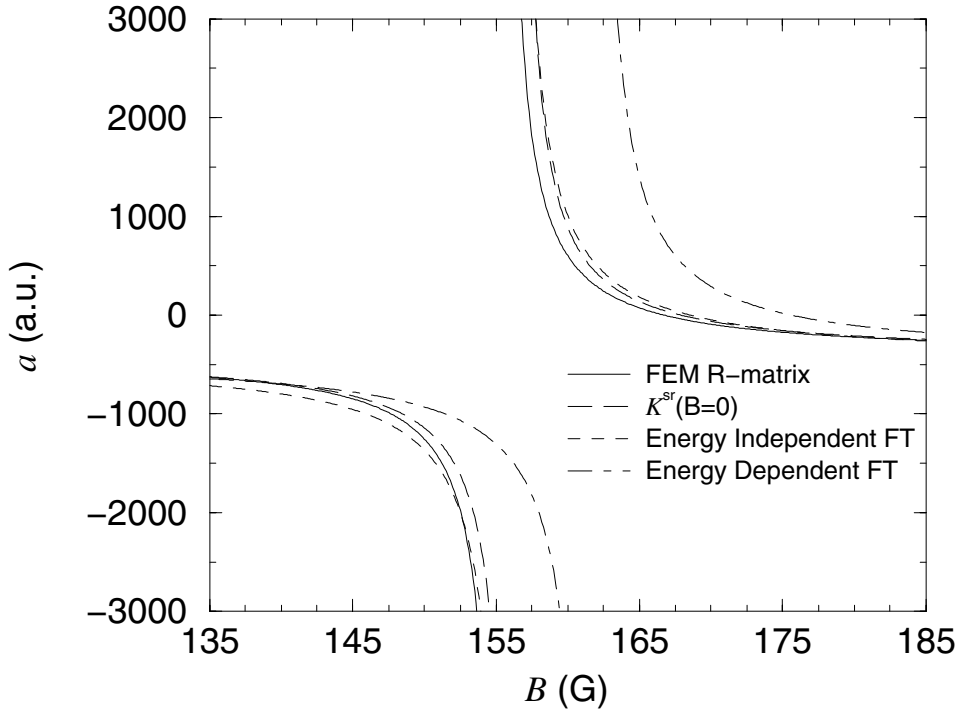

Figure 4.9: Scattering length a versus magnetic field B for the collision of two ^{85}Rb atoms both of which are in their $|2,-2\rangle$ hyperfine state. Three methods using an approximate $\underline{K}^{\rm sr}$ are compared with an "exact" FEM $\underline{\rm R}$-matrix calculation. The FEM $\underline{\rm R}$-matrix approach predicts the Feshbach resonance field position in accordance with Ref.[17]'s measurement. The collision energy was taken to be E = 1 μK.

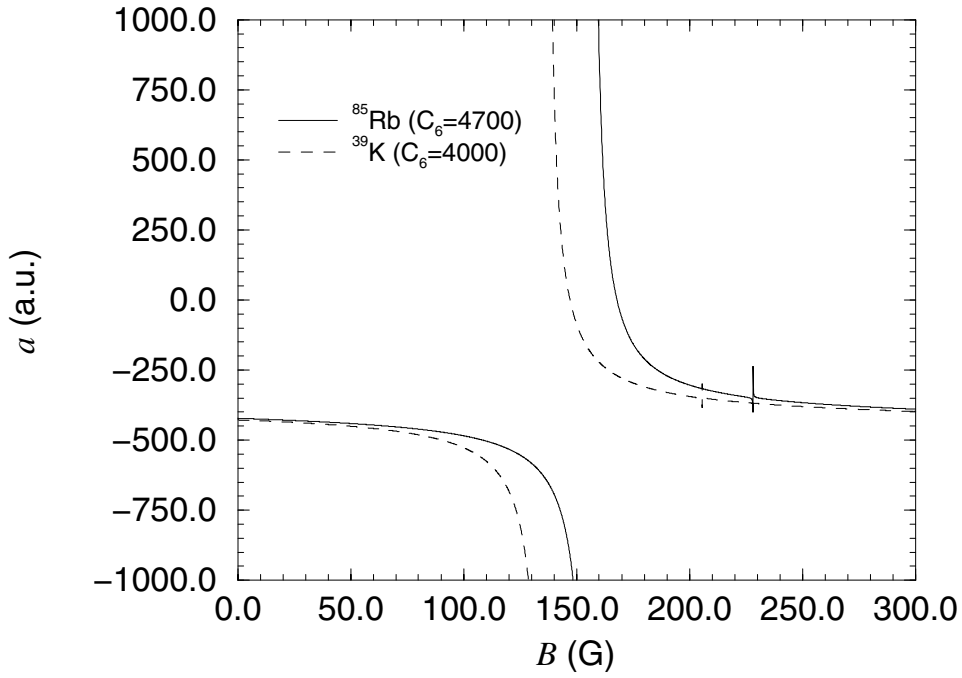

Figure 4.10: Scattering length a versus magnetic field B for the collision of two ^{85}Rb atoms both of which are in their $|2,-2\rangle$ hyperfine state. A constant $\underline{K}^{\rm sr}$ calculated at $E = 0$, $B = 0$ is used for both calculations. One (solid line) uses long-range standardized parameters calculated with ^{85}Rb atomic properties. The other (dashed line) uses long-range standardized parameters calculated with ^{39}K atomic properties. The collision energy was taken to be E = 1 μK.

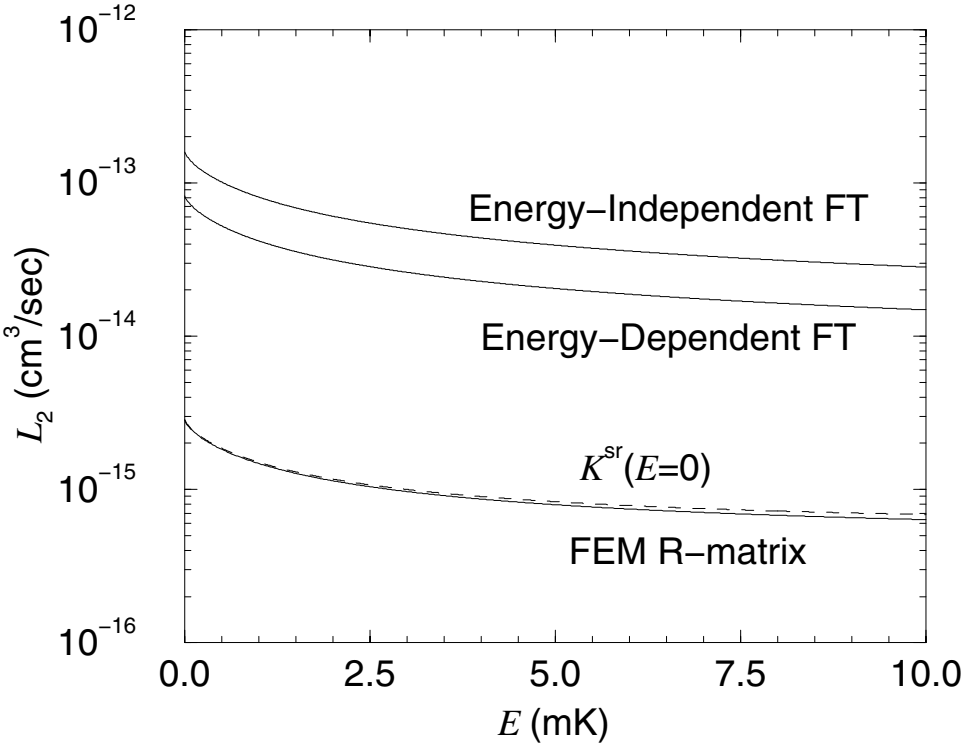

Figure 4.11: The total inelastic loss rate L_2 for a $|2,2\rangle_{87} + |1,-1\rangle_{87}$ collision. Calculations using an approximate $\underline{K}^{\rm sr}$ are compared with the exact rates determined from a FEM $\underline{\rm R}$-matrix solution.

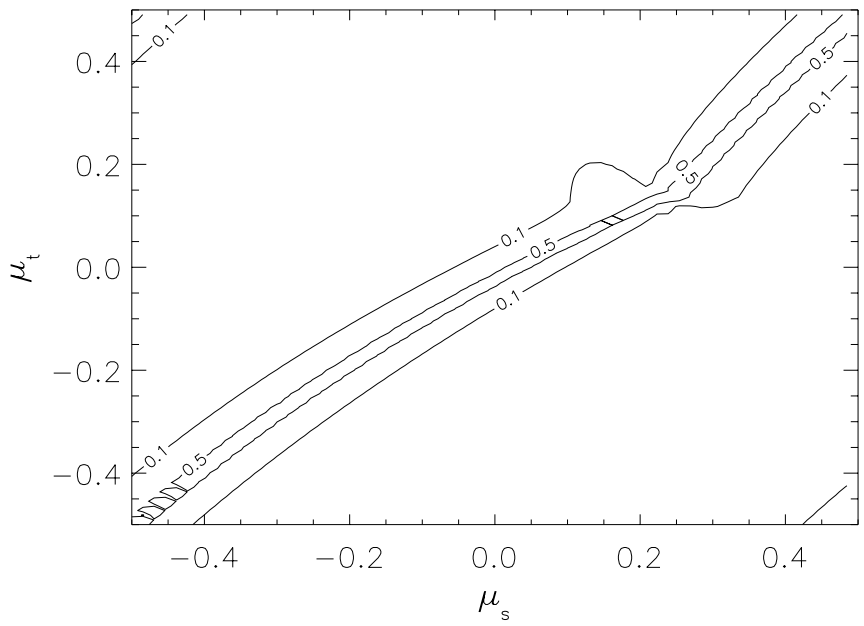

Figure 4.12: Mod-squared off-diagonal S-matrix elements calculated with an energy-independent FT approximation and with the FEM R-matrix approach are compared in this contour plot. These matrix elements are plotted as the absolute value of the percentage difference. The $0.1 = 10\%$ and $0.5 = 50\%$ contour lines are shown. The mod-squared $\underline{S}$-matrix element for this particular case represents the transition probability $f = 2(f_a = 2, f_b = 2) \rightarrow 2(1, 1)$ in the collision of two Na atoms. The physical values of the Na quantum defects are μ_s = -0.087 and μ_t = -0.400.

Chapter 5

A compendium of rubidium scattering properties

The low-energy scattering properties of Rb in a magnetic trap are now well understood. This is a dramatic departure from the situation of just a few years ago. It has taken a number of experiments and corresponding theoretical analyses to provide a clear and consistent picture. Most notable among the early experiments were the observations of d-wave[101] and g-wave[102] shape resonances in scattering of doubly-polarized ^{87}Rb atoms and ^{85}Rb atoms, respectively. In both experiments, the observation of additional rotational lines in the photoassociation spectra signaled the presence of enhanced $l = 2$ or 4 ground state collisions. Cloud temperatures were in range of hundreds of μK range, well below the centrifugal barrier whereby collisions in these higher partial waves should have been suppressed. An analysis of the photoassociation lineshapes provided limits on both the triplet scattering length a_t and the leading order dispersion coefficient C_6.

The singlet scattering length a_s was unknown until the experiment of Myatt, **et al.**[100], that obtained, surprisingly, a pair of Bose condensates coexisting in the same magnetic trap. Prior to this experiment it was generally expected that the two trapped spin-states ($|f_a, m_{f_a}\rangle \equiv |2,2\rangle$ and $|1,-1\rangle$) would suffer huge spin-exchange losses, leading to the destruction of the mixed cloud before it could condense. The anomalous suppression of the spin-exchange loss rate signaled the near equivalence of the singlet and triplet scattering lengths, as was pointed out almost simultaneously by three groups[103, 104, 105]. The other novel aspect of this experiment was that only atoms in one spin-state ($|1,-1\rangle$) was evaporatively cooled. Atoms in the $|2,2\rangle$ spin-state cooled sympathetically (i.e., through elastic collisions with the $|1,-1\rangle$ atoms). This provided a "proof-of-principle" for a new route to condensation that might be applied to other hard to cool species. For example, this might be useful for fermionic isotopes for which s-waves collisions between two atoms in the same spin-polarized state is forbidden. An analysis of the Myatt, **et al.** experiment will be the subject of Section 5.1.

The observation of a magnetically-induced Feshbach resonance by Roberts, **et al.**[17] has provided the most definitive bounds on the Rb interaction parameters (a_s, a_t, and C_6), to date. The same resonance had also been observed using photoassociation spectroscopy techniques[16] but uncertainties in the magnetic field

calibration and the difficulty of the corresponding theoretical analysis led to much larger uncertainties in the potential parameters extracted in Ref.[16]. An analysis of the Roberts, **et al.** experiment will be detailed in Section 5.2.

These experiments, coupled with our theoretical analysis, have provided a set of "state-of-the-art" potentials, from which reliable predictions can be made for other Rb isotopes. In particular, we have identified selected hyperfine states that provide large elastic cross sections, small inelastic cross sections, and novel quantum effects (i.e., interferences and resonances). These states offer prospects not only for interesting collision studies but also for unique degenerate gas experiments, involving both bosons and fermions. This is the subject of Sections 5.3 and 5.4.

5.1 Suppressed ^{87}Rb inelastic cross sections

Myatt, **et al.** measured[100] an inelastic spin exchange rate L_2 of $2.2(9)\times10^{-14}$ cm^3/sec in collisions between the $|2,2\rangle$ and $|1,-1\rangle$ hyperfine states of ^{87}Rb. At the time of the experiment, the triplet scattering length was estimated[102] to be $110\pm$ 10 a.u., whereas the singlet scattering length was completely unknown. Figure 5.1 shows the rate constant (using a_t = 110 a.u.) versus an assumed singlet scattering length a_s. It is immediately apparent that the measured value of L_2 places strict limits on a_s. After the published uncertainties in a_t were incorporated into our analysis, we reported[103] bounds on the singlet scattering length of $72 \leq a_s \leq 102$ (in a.u.).

We can interpret the strong suppression of spin-exchange collisions very simply within the energy-independent frame transformation approximation. First, the structure of the s-wave Hamiltonian in the coupled hyperfine representation (neglecting magnetic dipole and external magnetic field interactions) is as follows (see Fig. 5.2): the collision complex consists of six channels, three of which ($f(f_a,f_b) = 1(1,2)$, $f = 3(1,2)$, and $f = 4(2,2)$), have purely triplet character at small R. The remaining three channels constitute an $f = 2$ spin-exchange coupled block. The zero-field inelastic processes are controlled to a large extent by this $f = 2$ Hamiltonian, which consists of one singlet and two triplet channels with one channel converging asymptotically to each of the hyperfine split thresholds (see Fig. 2.1). (Most inelastic spin-exchange processes for the bosonic isotopes are controlled by a similar three channel Hamiltonian, see Table 5.1). The symmetrized short-range reaction matrix for this f=2 Hamiltonian can be written in the FT limit (Eq. 4.39) as:

$$K^{\rm sr} = \begin{pmatrix} 0.1875\bar{\tau}_s + 0.8125\bar{\tau}_t & 0.2652(\bar{\tau}_s - \bar{\tau}_t) & 0.2864(\bar{\tau}_s - \bar{\tau}_t) \\ 0.2652(\bar{\tau}_s - \bar{\tau}_t) & 0.3750\bar{\tau}_s + 0.6250\bar{\tau}_t & 0.4050(\bar{\tau}_s - \bar{\tau}_t) \\ 0.2864(\bar{\tau}_s - \bar{\tau}_t) & 0.4050(\bar{\tau}_s - \bar{\tau}_t) & 0.4375\bar{\tau}_s + 0.5625\bar{\tau}_t \end{pmatrix} \quad (5.1)$$

and $\bar{\tau}_\lambda = \tan\pi\mu_\lambda$. (The channel labels for $K^{\rm sr}$ are $1 \equiv (f_a,f_bf) = (11)2$, $2 \equiv (12)2$, and $3 \equiv (22)2$). The coefficients of the recoupling matrix (see Eq. 2.63)

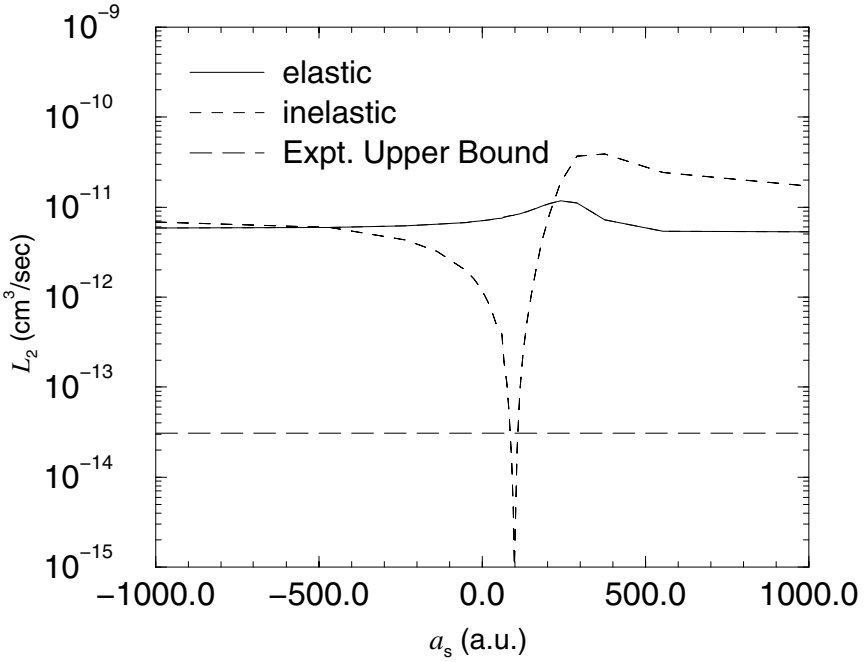

Figure 5.1: Elastic and inelastic event rates L_2 for the collision of $|2,2\rangle_{87} + |1,-1\rangle_{87}$ atoms versus an assumed singlet scattering length a_s. The calculation is for an incident energy of 1μK above threshold with a fixed triplet scattering length of 110 a.u. The upper bound of the measured value L_2 = 2.2(9) $\times 10^{-14}$ cm^3/sec is also displayed.

have been evaluated explicitly to show its structure. However, the transformation between spin representations is unitary and therefore the off-diagonal structure (i.e., proportional to $(\bar{\tau}_s - \bar{\tau}_t)$) is perfectly general for any coupled channel Hamiltonian in the FT limit. Evidently if the singlet (μ_s) and triplet quantum defects (μ_t) (or equivalently the two scattering lengths) are equal, then $\underline{K}^{\rm sr}$ and also the $\underline{S}$ matrix will be diagonal. In such a case the inelastic rates vanish.

Table 5.1: The zero-field Hamiltonian describing an unpolarized gas of identical bosons has a block diagonal structure in the coupled hyperfine representation (neglecting magnetic dipole effects). The total spin f labels and associated number of spin-exchange coupled channels are identified for the naturally abundant alkali isotopes. The single channel blocks are pure triplet channels. The two coupled channel block consists of a singlet and triplet channel converging to each of the two $f_a = f_b$ hyperfine thresholds. The three coupled channel block consists of one singlet and two triplet channels with one channel converging to each of the three hyperfine split thresholds (see Fig. 2.1).

Atom	Nuclear Spin	Single Channel	Two Channels	Three Channels
^{7}Li	3/2	f = 1,3,4	f = 0	f = 2
^{23}Na	3/2	f = 1,3,4	f = 0	f = 2
^{39}K	3/2	f = 1,3,4	f = 0	f = 2
^{41}K	3/2	f = 1,3,4	f = 0	f = 2
^{85}Rb	5/2	f = 1,3,5,6	f = 0	f = 2,4
^{87}Rb	3/2	f = 1,3,4	f = 0	f = 2
^{133}Cs	7/2	f = 1,3,5,7,8	f = 0	f = 2,4,6

The physical picture is only slightly different from the FT approximation. Recall the discussion of spin-exchange in Section 3.3. There it was noted that the localization of the spin-exchange coupling at an internuclear separation of $R_I \sim 20-25$ a.u. presented an opportunity for interference. Physically, the incident wave splits when it propagates inward through the interaction region (R_I), sending amplitude into both singlet and triplet channels at short range. These wave components evolve nearly independently, reflect from their inner turning points, then recombine in the interaction region to produce the final mixture of exit channels. If the components meet with their original relative phase, the outgoing waves recombine constructively reproducing the original channel, in that case the scattering is primarily elastic. Otherwise, the amplitudes recombine destructively requiring scattering flux to exit in other channels. The suppression occurs when $a_s \sim a_t$ since singlet and triplet potentials quickly become degenerate for $R > R_I$, meaning that little additional phase difference accumulates. A similiar interpretation emerges from the analysis of Dalgarno and Rudge[106]. This circumstance also explains the poor quantitative performance of the FT approximation in Fig. 4.11. The FT pre-

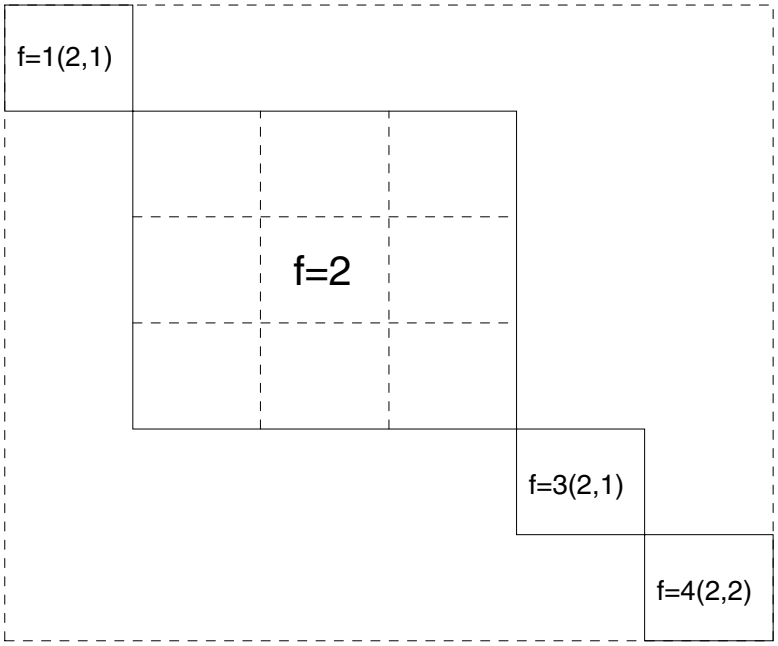

Figure 5.2: Block diagonal structure of the Hamiltonian describing the collision of $|2,2\rangle_{87}$ + $|1,-1\rangle_{87}$ atoms. The 6×6 Hamiltonian is presented in a coupled hyperfine representation with the nonzero matrix elements indicated by the corresponding $(f_a, f_b)f$ hyperfine labels. The f=2 block consists of three coupled channels.

dicts the suppression of the spin-exchange rates, but the suppression is erroneously predicted to be greatest when $a_s = a_t$ (see Fig. 5.3).

This interference picture can be further solidified by examining the singlet and triplet wave functions near R_I. Figure 5.4 shows zero-energy singlet and triplet wave functions. We see that the singlet wave function with a_s = 99 a.u. is very nearly in phase with the triplet, while that with a_s = 553 a.u. is out of phase. Changing the singlet scattering length from $-\infty$ to $+\infty$ introduces one additional node into the singlet wave function, pushing it through a π phase change in the interaction region. The result is one region of inelastic suppression per a_s cycle, as shown in Fig. 5.1.

However, if the collision complex contains asymptotically closed channels as is the case here, there is another interference mechanism that in principle can shut-off spin-exchange losses. As an example, consider the collision entrance channel to be the middle threshold (see Fig. 2.1) with one atom in its $f_a = 1$ hyperfine state and the other in its f_b=2 state (this is channel 2 in the above $\underline{K}^{\rm sr}$, Eq. 5.1). In this case we must follow the procedure outlined in Section 4.2 to eliminate the asymptotically closed channel (channel 3). The new reaction matrix $\underline{\tilde{K}}$ is a 2×2 symmetric matrix with off-diagonal elements given by

$$\tilde{K}_{12} = K^{\rm sr}_{12} - K^{\rm sr}_{13}(\tan\beta(\varepsilon_3) + K^{\rm sr}_{33})^{-1}K^{\rm sr}_{32} \ . \tag{5.2}$$

If $\tilde{K}_{12} \rightarrow 0$ the resulting $\underline{S}$ matrix is diagonal, again eliminating inelastic spin-exchange processes. Feynman path language can be used to interpret the above equation, where $K^{\rm sr}_{ij}$ is a measure of the flux transferred from channel j into channel i. The inelastic loss of atoms in our example can occur along one of two pathways; either flux is lost from channel 2 directly into channel 1, described by $K^{\rm sr}_{12}$, or it is first transferred into the closed channel 3, evolves for awhile, and then hops from channel 3 into channel 1 and is lost, (described by the second term in Eq. 5.2). The two pathways can interfere, shutting off the inelastic processes. Inserting the FT matrix elements from Eq. 5.1, we find that $\tilde{K}_{12} \rightarrow 0$ when

$$\tan\beta(\varepsilon_3) = -\tan\pi\mu_t \ . \tag{5.3}$$

This relationship is general (within the FT approximation) for all three-channel Hamiltonians listed in Table 5.1. This example of spin-exchange suppression depends primarily on the triplet quantum defect (i.e., scattering length) and the threshold splitting (through the relationship $\varepsilon_3 = E - E_3$). It is therefore conceivable that a magnetic field could be employed to induce the interference, although a field necessarily complicates this simple analysis. Evidence for this type of magnetic-field induced interference will be provided in Section 5.3. Figure 5.5 shows the ^{87}Rb $f = (12)2$ inelastic rate over the entire $\mu_s - \mu_t$ plane. Here, we see the line of suppression along $\mu_s \sim \mu_t$ and also a horizontal line of suppression along $\mu_t = -\beta/\pi \sim 0.4$. The topology shown in Fig. 5.5 also was discussed within an

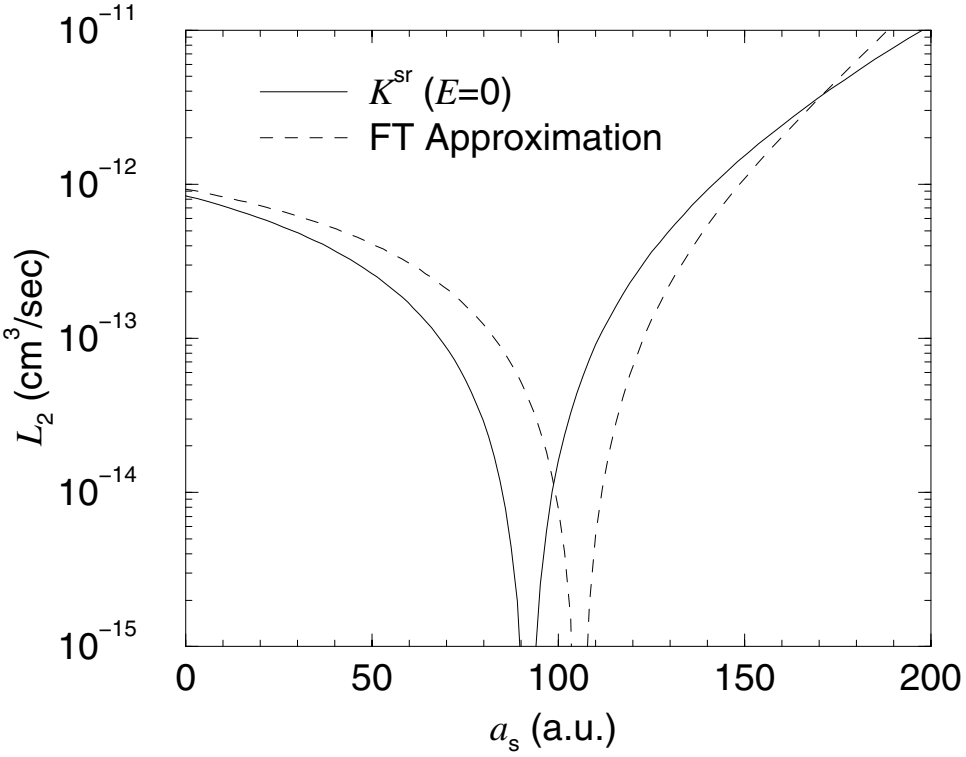

Figure 5.3: The inelastic rate constant L_2 is plotted versus an assumed singlet scattering length a_s. The FT approximation predicts $L_2 \to 0$ when $a_s = a_t$, here a_t is fixed at 106 a.u. However, the exact calculation predicts the minimum will occur at $a_s \simeq 92$ a.u. Our current best estimate of the ^{87}Rb singlet scattering length is 90 ± 1 a.u. The FT provides a poor approximation for ^{87}Rb inelastic rates, misrepresenting the rate by orders of magnitude, because of this small shift in the minimum rate position.

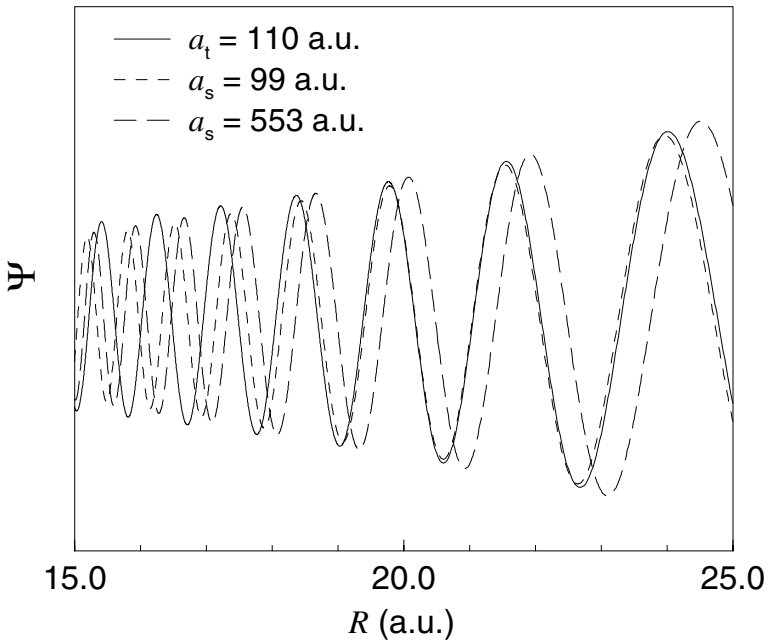

Figure 5.4: Zero-energy single channel wave functions for the singlet and triplet (solid line) Rb Born-Oppenheimer potentials as functions of the internuclear distance R. The singlet wave function is calculated assuming two different scattering lengths a_s = 99 and 553 a.u., while the triplet wave function corresponds to a scattering length of a_t = 110 a.u. The singlet (a_s = 99) and triplet wave functions are almost locked in phase through the region of large spin-exchange coupling (R_I =20-25 a.u.) that accounts for the suppressed inelastic collisions.

adiabatic framework in Ref.[104].

5.2 Observation of a Feshbach resonance in ^{85}Rb collisions

A Feshbach resonance in the collision of two $|2,-2\rangle$ ^{85}Rb atoms, first predicted by Vogels, **et al.**[107], has now been observed independently by two groups[16, 17]. Using spectroscopic techniques, Ref.[16] detected the resonance through the magnetic field dependence of the photoassociation spectrum. Based on a theoretical analysis of the spectra, these authors reported the zero energy position of the resonance to be $B_{\rm max}$ = 164 $\pm$ 7 G with a width of 8.2 $\pm$ 3.8 G. A more precise measurement was reported in Ref.[17]. Here, the technique of "cross-dimensional mixing"[108] was employed. That is, the rf fields used for evaporative cooling quickly "chop-off" part of the atom cloud in a single dimension. The cloud equilibration time is directly related to the elastic collision rate. From these measurements, Roberts, **et al.** found the maximum and minimum collision rates occurred at field values of $B_{\rm max}$ = 155.2 $\pm$ 0.4 G and $B_{\rm min}$ = 166.8 $\pm$ 0.3 G.

The position of the resonance depends on both the singlet a_s and triplet a_t scattering lengths (or corresponding quantum defects) as well as the leading order dispersion coefficient C_6. In addition, the width of the resonance reflects the coupling of bound and continuum channels and therefore provides an accurate measure of the scattering length difference $a_s - a_t$. We performed a parameter search over the singlet-triplet scattering length space for a number of dispersion coefficients. The phaseshifts generated by the Born-Oppenheimer potentials were adjusted by adding small corrections to their inner wall (Eq. 2.45) until the field values associated with the theoretical maximum and minimum of the thermally averaged elastic cross sections agreed with the measured $B_{\rm max}$ and $B_{\rm min}$ within experimental uncertainties. (The procedure for thermal averaging the rates and cross sections is presented in Appendix C.) An example of the allowed $\mu_s - \mu_t$ parameter space for a given C_6 = 4700 a.u. is provided in Fig. 5.6. As can be seen from this figure, the small measured uncertainties of $B_{\rm max}$ and $B_{\rm min}$ tightly constrain the allowed quantum defect ranges. In addition, we found that the area of this allowed parameter region was independent of the dispersion coefficients. Varying these coefficients simply shifted the region in $\mu_s - \mu_t$ space. To bound the parameter space completely, we required that our parameters also reproduced the measured g-wave shape resonance[102] within experimental uncertainties, which limits the van der Waals coefficient to C_6 = 4700 $\pm$ 50. This value for C_6 is slightly larger but with smaller uncertainty than the most recently published value[109] of 4550$\pm$ 100 a.u. We were unable to obtain useful limits on C_8 and C_{10} due to their small influence on the positions of both the shape resonance and the Feshbach resonance. Our final scattering length bounds were first reported[17] in terms of a fractional bound state phase ν to facilitate comparisons with Ref.[16]'s analysis. Here, the results are presented in terms of scattering lengths and corresponding quantum defects (see table 5.2). The final bounds on the

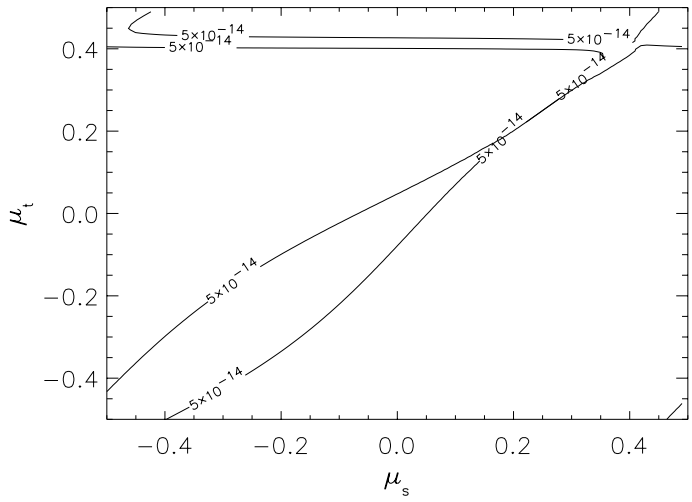

Figure 5.5: Inelastic collision rate L_2 for the process $f = 2(12) \rightarrow f = 2(11)$ in ^{87}Rb. The rates are plotted versus singlet μ_s and triplet μ_t quantum defects. The region of suppressed inelastic collisions are contained within the marked contour lines. These regions are discussed in the text. The physical values of the ^{87}Rb quantum defects are μ_s = -0.294 and μ_t = -0.354.

triplet quantities also include a ± 1 uncertainty[107] in the number of bound states supported by the Born-Oppenheimer potential.

As a further check of the resulting potentials, we confirmed that they predict scattering quantities that are consistent with previous measurements. In particular, our triplet potential supports a ^{87}Rb d-wave shape resonance[101]. The predicted ^{87}Rb $a_{2,1}/a_{1,-1}$ scattering length ratio[110] and thermally averaged $|2,2\rangle$ + $|1,-1\rangle$ inelastic rate constant[100] also agree with their measured values. In addition, we find 10 of the 12 measured ^{85}Rb d-wave bound states[109] within the 2σ experimental uncertainties. The new potentials also permit us to predict additional ^{85}Rb Feshbach resonances: one at $B_{\rm max}$ = 226.0 $\pm$ 4.0 G with a width of ~ 0.01 G, and another at $B_{\rm max}$ = 535.5 $\pm$ 4.0 G with a width of 2.2 $\pm$ 0.2 G.

The Feshbach resonance suggests a way to evaporatively cool ^{85}Rb, which has proven difficult at zero-field. Initially, the poor $B = 0$ evaporative cooling observed experimentally was surprising since it was known that the scattering length was large ($a \sim -400$), implying a large elastic cross section ($\sigma = 8\pi a^2$) at threshold. However, the ^{85}Rb s-wave partial cross section suffers Ramsauer-Townsend[24] type minimum at low energies ($E \approx 375$ μK) (see Fig. 5.7). We can understand the presence of this zero by studying the energy dependence of the elastic phase shift δ_l. Levinson's theorem[24] states that the zero-energy phase shift $\delta_l(0) = N\pi$ where N is the number of l-wave bound states supported by the potential. In the limit of infinite collision energy the phase shift $\delta_l \stackrel{E\to\infty}{\longrightarrow} 0$. Each partial cross section ($\sigma_l \propto \sin^2\delta_l$) will therefore suffer at least N-1 zeros as a function of energy. However, at low energies the s-wave phase shift is related to the scattering length $\delta_{l=0} = -ka$. For negative scattering lengths, the phase shift rises initially and therefore incurs at least N zeros as a function of energy. Levinson's theorem holds strictly only for a single channel interaction. However, we find that the low-energy behavior of the phase shift for multichannel collisions obeys this trend as well. Exceptions to this rule could occur if resonances are present in the relevant energy range.

The energy position of the first s-wave zero in a single channel interaction can be estimated using quantum defect theory. The physical phase shift is given in terms of our standardized quantum defect parameters by

$$\delta(E) = \tan^{-1}\left[\frac{A(E)\tan\pi\mu}{1+\mathcal{G}(E)\tan\pi\mu}\right] + \eta(E)\ . \tag{5.4}$$

For a given value of μ (which can be approximated as energy-independent in Rb up to about E = 0.1 K), this equation can be inverted to find the energy at which the physical phase shift obtains a specified value. In Fig. 5.8, the lines of constant $\delta = \pi/2$ (i.e., unitarity limit) and $\delta = 0$ are shown as a function of the quantum defect μ and the standardization parameter $\gamma^{1/4} = (2\mu C_6)^{1/4}k$, where $k = (2\mu E)^{1/2}$. This figure shows that the first zero in the s-wave partial cross-section will occur at lower energies for a negative scattering length than for a positive one. This does not turn

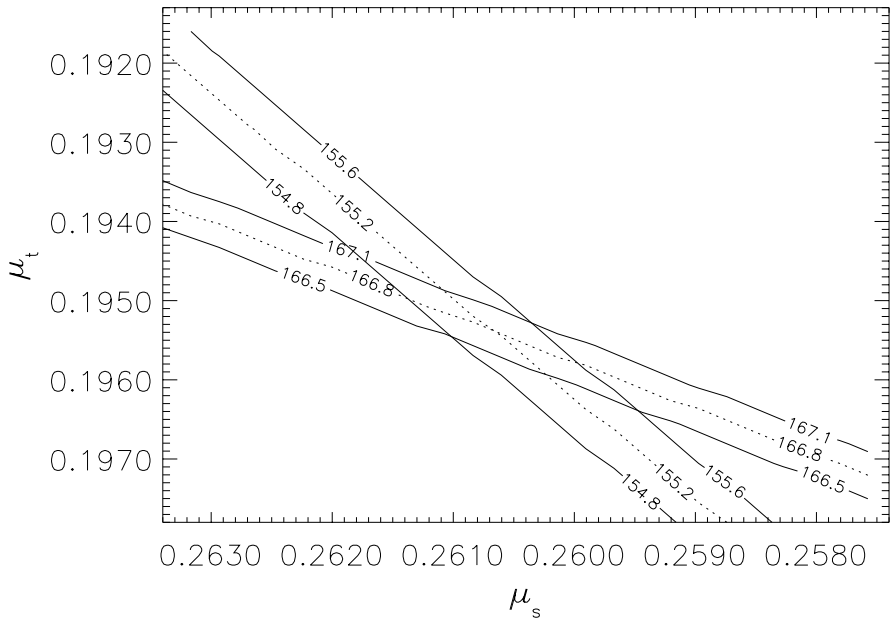

Figure 5.6: Lines of constant maximum $\sigma(B_{\max})$ and minimum $\sigma(B_{\min})$ cross section versus magnetic field are shown in singlet-triplet quantum defect space. The magnetic field values are labeled on each line, (dashed=nominal, solid=bounds). Dispersion coefficient values of C_6=4700, C_8=523070, and C_{10} = 7665(10^4), in a.u., were used for this particular calculation.

Table 5.2: Singlet and triplet scattering lengths a (in a.u.) and quantum defects $\bar{\mu}$ (dimensionless) for the different Rb isotopic pairs given a constant $C_6 = 4700$ a.u. and $C_8 = 550600$ a.u. The uncertainty in the singlet quantum defect $\bar{\mu}_S$ is 0.0014 in all cases. Variations of the scattering lengths with C_6 and C_8 can be determined by the following formulas: $\mu = \bar{\mu} + b_6(C_6 - 4700) - b_8(C_8 - 550600)$ and $a = -C^2 \tan(\pi\mu)/(1 + \mathcal{G}(0)\tan(\pi\mu))$. Here, C^2 = 0.957217$(2mC_6)^{1/4}$, m is the reduced mass of the atom-pair (in a.u.), and $\mathcal{G}(0)$ = -1.0026. The constant b_6 equals 7.5×10^{-5} for the singlet and 1.4×10^{-4} for the triplet. The constant b_8 is the same for both potentials and is given by 2.0×10^{-8}.

Pair	a_s	$\bar{\mu}_s$	a_t	$\bar{\mu}_t$
82-82	-38±1	0.0612	+151±10	-0.491±0.019
83-83	+66±1	-0.2021	+81±3	-0.262±0.013
84-84	+142±1	-0.4678	+15±3	-0.033±0.007
85-85	$+2400^{+600}_{-350}$	0.2603	-369±16	0.194±0.001
86-86	+7±1	-0.0144	+211±7	0.421±0.007
87-87	+90±1	-0.2939	+106±4	-0.354±0.003
82-87	+55±1	-0.1568	-40±4	0.064±0.004
83-87	-990^{+60}_{-70}	0.2263	-295±7	0.184±0.001
84-87	+117±1	-0.3952	$+550^{+45}_{-35}$	0.302±0.004
85-87	+11±1	-0.0233	+213±7	0.418±0.007
86-87	+336±4	0.3443	+143±4	-0.467±0.010

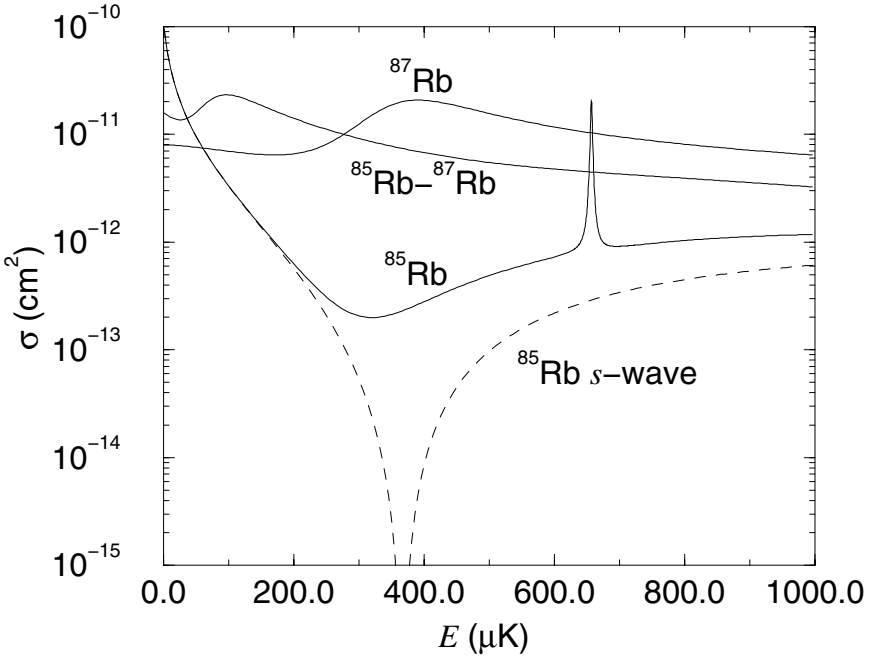

Figure 5.7: Total elastic cross sections for doubly polarized Rb collisions are plotted versus collision energy. The ^{85}Rb s-wave partial cross section suffers a minimum at E = 375 μK. In addition, a g-wave shape resonance (E = 650 μK) is evident in the ^{85}Rb total cross section. The ^{87}Rb cross section exhibits a broad d-wave shape resonance near E = 400 μK and a p-wave shape resonance ($E \approx 100$ μK) enhances the mixed-isotope cross section.

out to be a problem for ^{7}Li (a_t = -27.6) simply because of its small mass. There, the first s-wave zero does not occur until $E > 1$ mK, well beyond the temperature range where evaporative cooling techniques are employed.

Evaporative cooling near a Feshbach resonance must tread a fine line, balancing increased inelastic as well as elastic collision rates. Although zero-field magnetic dipole loss rates for collisions occurring at the lowest hyperfine threshold are exceedingly small ($\sim 10^{-18}$ cm^3/sec in Rb), near a resonance these rates can increase dramatically. The field-dependence of the ^{85}Rb $|2,-2\rangle$ dipole loss rate L_2 is shown in Fig. 5.9. At the measured resonance field value ($B_{\max}$ = 155 G) L_2 peaks at a loss rate of 10^{-13} cm^3/sec. However, the peak loss rate is extremely energy-dependent, growing prohibitively large at energies below 1μK. The good news is that the lineshape is asymmetric, with the minimum loss occurring on the positive scattering length side of the resonance. (Negative scattering length ramifications for a ^{85}Rb condensate are discussed at the end of Section 5.3.) It therefore looks promising for evaporative cooling to work if the bias field is set in the range $B \sim$ 160-165 G. The dipole loss rates also show much more structure than the elastic rates. The broad resonances at $B >$300 G are associated with d-wave spin-exchange coupled channels. A measurement of this structure could provide even tighter constraints on the Rb potentials than we have to date.

5.3 Predictions for ^{85}Rb-^{87}Rb collisions

A second possible way to Bose-condense ^{85}Rb is to cool it sympathetically in a gas of ^{87}Rb atoms. The ^{85}Rb-^{87}Rb triplet scattering length is large and positive ($\sim$ 200 a.u., see table 5.2) implying a large elastic collision rate between the atoms (see Fig.5.7). Generally, collisions between upper and lower manifold hyperfine states suffer large spin-exchange losses. (Note, however, the exception presented in Section 5.1.) Therefore, the two best choices for mixed-isotope condensation require trapping $|3,3\rangle_{85}$ atoms with $|2,2\rangle_{87}$ or trapping $|2,-2\rangle_{85}$ with $|1,-1\rangle_{87}$ atoms, as neither combination suffers spin-exchange losses. Of these two candidates, the second is the more interesting because the scattering length between isotopes can be "tuned" via Feshbach resonances. In principle, this should allow control of the overlap between the two condensates and produce **interpenetrating** quantum fluids. In this section, I provide updated values for the mixed-isotope scattering observables that were first reported in Ref.[111], reflecting our improved knowledge of the Born-Oppenheimer potentials.

The scattering length a for $|2,-2\rangle_{85}$ + $|1,-1\rangle_{87}$ collisions in a magnetic field is shown in Fig. 5.10. Two pronounced resonances are apparent at field values of $B_{\max}$ = 288.5 $\pm$ 15 and 420 $\pm$ 35 G with widths of 4 $\pm$ 1 and 47 $\pm$ 10 G, respectively. The energy-field evolution of these resonances is shown in Fig. 5.11. Here, the time delay operator[27] $Q = 2d\delta/dE$ is introduced. The signature of a resonance is a rapid increase by π radians in the physical phase shift δ. Therefore,

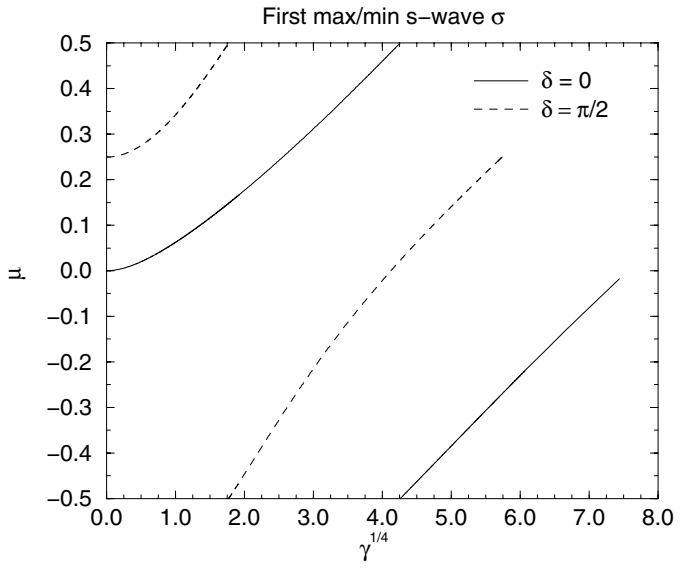

Figure 5.8: Constant lines of the physical s-wave phase shift δ are plotted versus quantum defect μ and the standardization parameter $\gamma^{1/4} = (2\mu \mathrm{C}_6)^{1/4}k$, in a.u.. Negative scattering lengths correlate with $0 < \mu \lesssim 0.25$ (see Eq. 4.42). This figure shows that atom-pairs with negative scattering lengths suffer a zero in the s-wave cross-section at lower energies than positive scattering length pairs. Also, the unitarity limit ($\delta = \pi/2$) is obtained at lower energies for positive scattering lengths. The physical ^{85}Rb triplet quantum defect is 0.194. From this graph one finds the first zero occurs at roughly $\gamma^{1/4}$ = 2.2 that is an energy of 366 μK, in good agreement with the full calculation shown in Fig. 5.7.

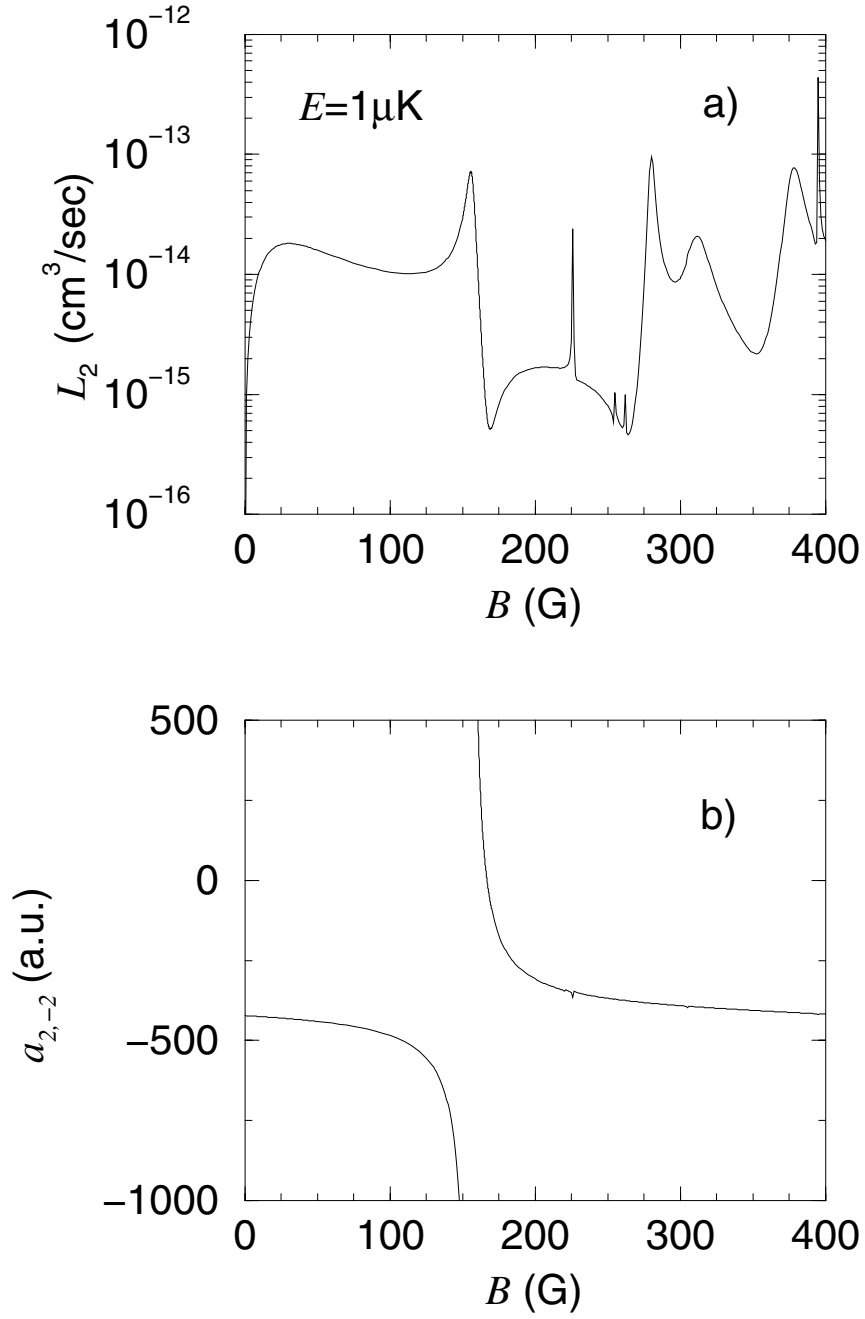

Figure 5.9: a) Magnetic field dependence of the inelastic dipole loss rate L_2 for collisions of two ^{85}Rb atoms in their $|2,-2\rangle$ hyperfine state and b) the corresponding scattering length dependence $a_{2,-2}$. The dipole loss rates exhibit a large increase at the measured Feshbach resonance (B = 155 G) field. The sharp feature in a) at $B \sim 225$ G is the narrow Feshbach resonance predicted previously. The broad features in a) $B > 300$ G are resonances in d-wave spin-exchanged coupled channels.

near a resonance, Q can be fit to a Lorentzian profile

$$Q = \frac{\Delta/2}{(E - E_r)^2 + (\Delta/2)^2} \ , \tag{5.5}$$

from which the maximum value $Q_{\max}$ immediately identifies the width $\Delta = 2/Q_{\max}$ and resonance position E_r. It is sometimes useful to define a similiar operator with respect to the change in field strength $Q_B = 2d\delta/dB$. (This analogous "time-delay" like definition of resonance position and width is not generally used for magnetic field resonances in the cold collision community. Instead, the resonance position is defined as the field $B_{\max}$ at which $a(B_{\max}) \rightarrow \infty$ and the width is given by $\Delta = |B_{\max} - B_{\min}|$ where $a(B_{\min})$=0 (see Eq. 2.2.4). Positions and widths quoted in this work (including the ones given in this section) will adhere to these commonly accepted definitions unless otherwise stated.) The Feshbach resonances originate from f=3 and f=4 quasi-bound states that are nearly degenerate at zero field. The block diagonal structure of the 8×8 Hamiltonian that describes the s-wave collision complex is provided in Fig. 5.12. In zero-field, the f = 3 entrance channel is uncoupled from the f=4 spin-exchange coupled channels and therefore only one resonance appears in Fig. 5.11. As the bias field is turned on, the f=4 resonance immediately appears with an extremely narrow width "on top" of the f=3 resonance. As the coupling (H_B) is increased, the two states repel one another, eventually becoming completely separated in energy before crossing the entrance channel threshold. In addition the f=4 resonance broadens considerably as the coupling strength is increased.

Another interesting magnetic-field dependence is exhibited in the spin-exchange loss rates of $|3,3\rangle_{85} + |1,-1\rangle_{87}$ collisions. Ordinarily, these two hyperfine-states would quickly expel one another from the trap due to their large spin-exchange rate, $L_2 = 3.4(10^{-12})$ cm^3/sec. However, this rate turns out to be nonresonantly suppressed in the presence of a magnetic field. The field dependence of L_2 is shown in Fig. 5.13. The minimum rate of $\sim 10^{-15}$ occurs at B = 297.5 G. A 12×12 Hamiltonian, with five channels open at $R \rightarrow \infty$, describes these s-wave collisions. It is therefore surprising (and nontrivial to explain) how an interference effect can shut down all four inelastic channels at the same value of the magnetic field. MQDT can be used to gain some insight into the dynamics. Figure 5.14 shows the short-range reaction matrix elements between the inelastic channels (labeled j) and the entrance channel (labeled 5), both before ($K^{\rm sr}_{j5}$) and after ($\tilde{K}_{j5}$) eliminating closed channels. The elements of $K^{\rm sr}_{j5}$ are nonzero and almost constant in field. However, when the closed channels are eliminated from the reaction matrix all off-diagonal elements of $\tilde{K}_{j5}$ go to zero over the same small range of magnetic field. Therefore, the closed-pathways are interfering with the direct paths in much the same fashion as discussed at the end of Section 5.1. The loss rate L_2 does not exactly vanish since the off-diagonal elements vanish at slightly different field strengths. This destruc-

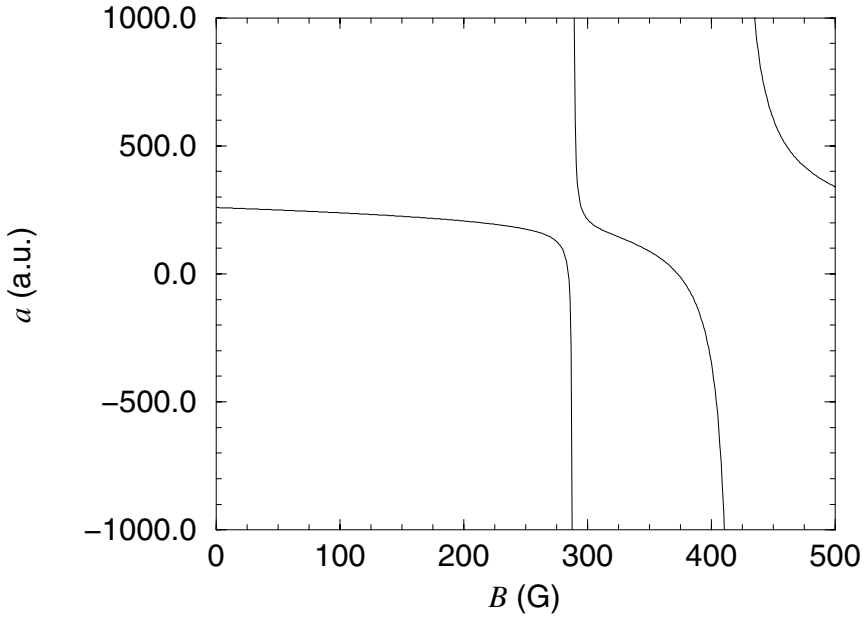

Figure 5.10: The magnetic-field dependence of the $|2,-2\rangle_{85}$ + $|1,-1\rangle_{87}$ scattering length. The zero-energy position of the Feshbach resonances are 287.5 $\pm$ 15 and 420 $\pm$ 35 G with widths of 4 $\pm$ 1 and 47 $\pm$ 10 G, respectively.

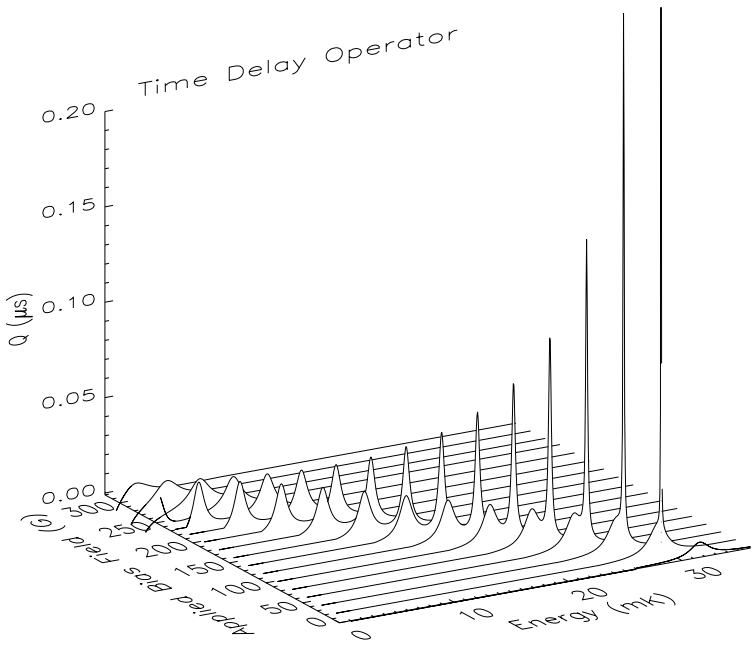

Figure 5.11: The evolution of two Feshbach resonances in energy and field are shown for collisions of $|2,-2\rangle_{85}$ and $|1,-1\rangle_{87}$ atoms. The time delay operator is defined as $Q = 2d\delta/dE$. Its peak value identifies the position and width $\Delta = 2/Q_{\max}$ of each resonance.

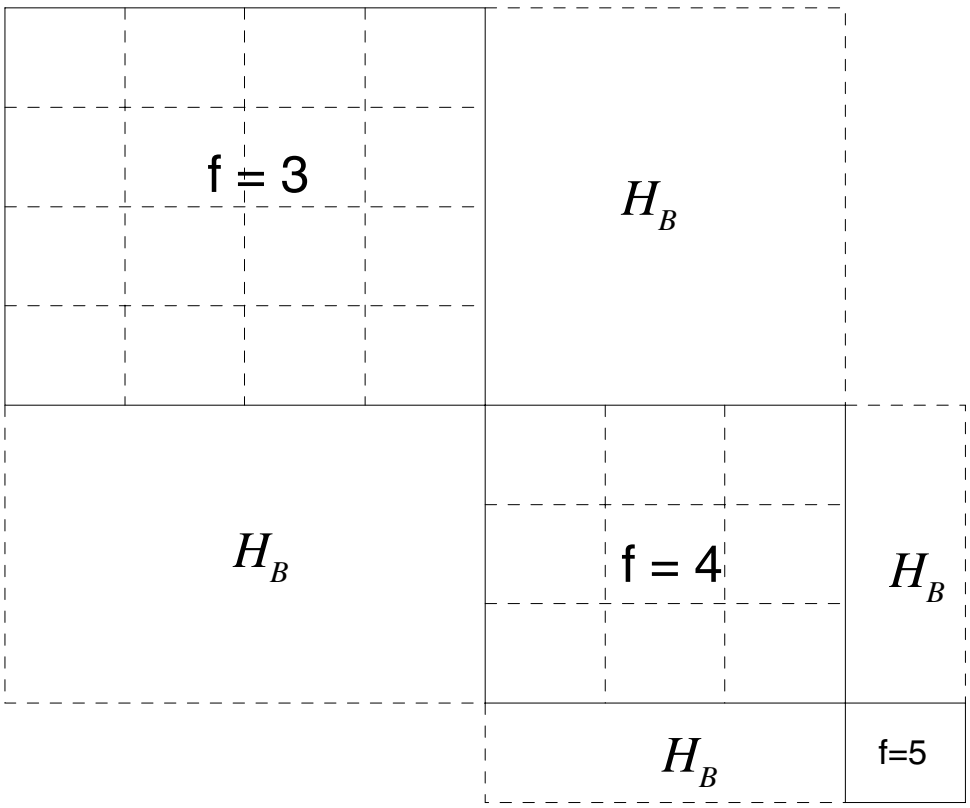

Figure 5.12: Block diagonal structure of the $|2,-2\rangle_{85}$ + $|1,-1\rangle_{87}$ s-wave Hamiltonian. The f=3 spin-exchange coupled channels consist of 1 singlet and 3 triplet channels with one channel converging to each of the four hyperfine-split thresholds (see Fig. 2.1). The f=4 block consists of three channels, 1 singlet and 2 triplets, with one channel converging to each of the three highest energy hyperfine thresholds. The last f=5 block is a single triplet channel converging to the 3+2 hyperfine threshold. A magnetic field H_B introduces additional coupling within each spin-exchange block and couples the $\Delta f = \pm 1$ channels.

tive interference raises the possibility that a triple condensate could be formed in a magnetic trap with the species $|1,-1\rangle_{87}$, $|2,2\rangle_{87}$, and $|3,3\rangle_{85}$. Triple condensates of ^{23}Na atoms in each Zeeman sublevel of the f_a=1 hyperfine state have been observed in an all optical dipole trap[112].

A mixture of ^{85}Rb atoms and ^{87}Rb atoms exhibits interesting cold collision properties. However, this system suffers a drawback from the point of view of condensate mixtures. Namely, the large negative scattering length of ^{85}Rb implies that its condensate is unstable at B = 0 beyond $\sim$ 100 atoms. The ^{85}Rb Feshbach resonance can in principle alter this situation by applying a bias field to tune its scattering length to a positive value, which should then allow large number condensates to be formed. Unfortunately, the ^{85}Rb scattering length is negative at the fields required to tune the 85-87 interaction. Therefore, experiments designed to exploit the 85-87 interaction must account for the small ^{85}Rb condensates. Detecting and studying such small condensates will be no small feat but may be possible[113].

5.4 Scattering properties of the short-lived Rb isotopes

Experimentalists have recently developed the ability to cool and trap short-lived radioisotopes. Experiments with francium[114, 115], sodium[116], as well as ^{82}Rb[117] have been reported. These experiments open up new territory, offering the possibility that these short-lived species can be used in studies of degenerate Fermi and Bose gases. In this section, I highlight some of the interesting scattering properties of the Rb radioisotopes. In particular, mixed isotope collisions of ^{83}Rb-^{87}Rb and mixed spin state collisions of the individual fermionic isotopes ^{84}Rb and ^{86}Rb will be investigated. We first reported these results in Ref.[118]. That work showed that the ^{82}Rb scattering properties are only marginally suitable, at best, for degenerate gas studies and will not be discussed here.

First, consider the scattering properties of the fermionic isotopes. One of the most important considerations for degenerate gas studies is the magnitude of the elastic scattering cross section that enables evaporative cooling. The Pauli exclusion principle prohibits s-wave collisions between identical spin-polarized fermions. Therefore, formation of a degenerate Fermi gas will require sympathetic cooling of the atoms, by using either a different spin state or else a completely different atom. Both ^{84}Rb and ^{86}Rb are ideal candidates for sympathetic cooling with ^{87}Rb, since they have large positive triplet scattering lengths (see Table 5.2). In addition, they both have an "inverted" hyperfine structure, making $f = 5/2$ the lower energy state. (The atomic properties of the Rb isotopes considered here are provided in table 5.3.) This means that spin exchange losses are forbidden in collisions between $|5/2,5/2\rangle_A$ and $|5/2,3/2\rangle_A$ atoms, where $A = 84$ or 86. Evaporative cooling of like-fermions in different spin states has been demonstrated[119] in ^{40}K, which has a similarly inverted hyperfine structure. However, the scattering length is negative for both 84-84 and 86-86 collisions, despite the positive sign of the singlet and triplet

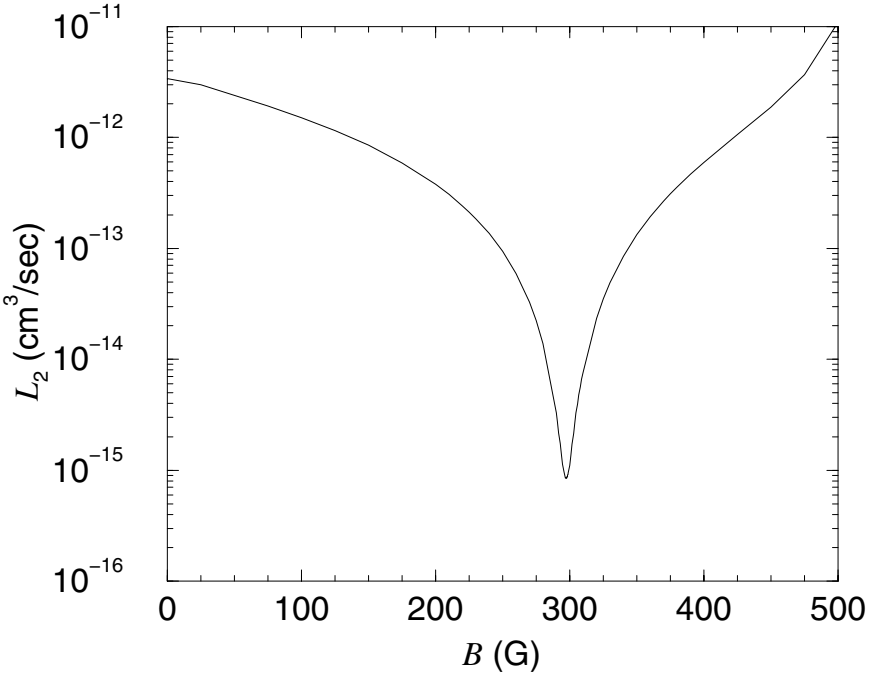

Figure 5.13: Field-dependence of the $|3,3\rangle_{85}$ + $|1,-1\rangle_{87}$ spin-exchange loss rate L_2 is plotted. A nonresonant suppression of the loss rate is observed at 297.5 $\pm$ 40 G.

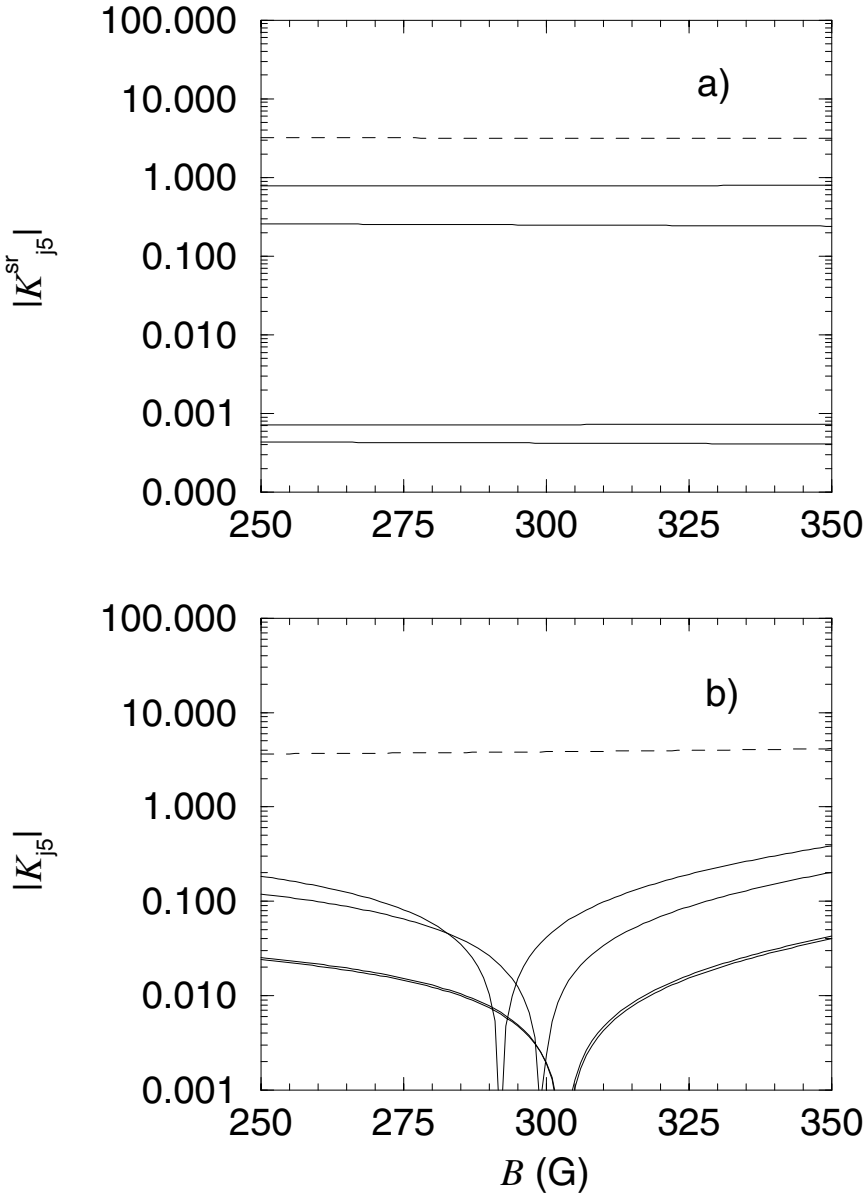

Figure 5.14: Field-dependence of the reaction matrix elements are plotted for collisions of $|3,3\rangle_{85}$ + $|1,-1\rangle_{87}$ atoms. In a) the elements of $\underline{K}^{\rm sr}$ that connect the entrance channel (labeled 5) to the inelastic channels are shown as solid lines and the diagonal element $K^{\rm sr}_{55}$ is represented by a dashed line. In b) the closed channels have been eliminated from $\underline{K}^{\rm sr}$ (Eq. 4.25). The elements of the new reaction matrix $\tilde{K_{j5}}$ are plotted here. (solid = off-diagonal elements, dashed = diagonal element). The destructive interference between the direct and closed inelastic pathways is evident in Fig. b)

scattering lengths (see Table 5.2). Such a result, contrary to the "Degenerate Internal States" (DIS) model of hyperfine state scattering [106], bears exploring here.

Table 5.3: Nuclear spin I, ground-state atomic hyperfine splittings Δ, and half-life τ of the Rb isotopes. A negative value of Δ indicates an "inverted" hyperfine structure. The half-life units are m=minutes, d=days, y=years.

Isotope	I	Δ (GHz)	τ
82	1	1.5474	1.273 m
83	5/2	6.3702	86.2 d
84	2	-3.08316	32.9 d
85	5/2	3.03573	stable
86	2	-3.94688	18.63 d
87	3/2	6.83468	4.88(10^{10}) y

If the magnetic dipole coupled channels are neglected, this is a coupled two channel problem with the $|5/2, 5/2\rangle_A$ + $|3/2, 3/2\rangle_A$ channel energetically closed at $R \to \infty$. The unitary frame transformation connecting the short range basis with the uncoupled hyperfine basis implies that the entrance channel has 80 per cent triplet character. The DIS model, which neglects hyperfine energies, would then predict ($a = 0.8a_t + 0.2a_s$), i.e., that the 84-84 and 86-86 scattering lengths are both reasonably large and positive.

In fact, the positions of bound states relative to the appropriate hyperfine thresholds are crucial for determining the actual scattering length. We can explore the present situation by introducing a mixing angle θ to represent the coupling in this system[24]. The model for our potential is then

$$\underline{V} = \underline{U}(\theta)\underline{V}^S\underline{U}^{\mathrm{T}}(\theta) + \underline{E} \tag{5.6}$$

where $\underline{U}(\theta)$ is a standard 2×2 real orthogonal rotation matrix, $\underline{V}^S$ is a diagonal matrix of singlet and triplet Born-Oppenheimer potentials, and $\underline{E}$ is a diagonal matrix of hyperfine energies. The model in the uncoupled limit (θ=0) gives simply a triplet potential connected to the lowest hyperfine threshold (i.e., the entrance channel) and a singlet channel with one additional unit of hyperfine energy.

The θ-dependences of the ^{84}Rb-^{84}Rb and ^{86}Rb-^{86}Rb bound states are shown in Fig. 5.15. In ^{86}Rb (Fig. 5.15a), we find an extremely high-lying bound state in the uncoupled limit (θ=0) that accounts for the large triplet scattering length. As the coupling is turned on, a nearly degenerate pair of bound states, one singlet and one triplet, begin to repel each other. Eventually the singlet state "pushes" the high-lying triplet state above threshold, resulting in a negative scattering length. In ^{84}Rb (Fig. 5.15b) the highest-lying bound state is rather deep $\sim$ 100 MHz for $\theta = 0$, in accord with this isotope's small positive triplet scattering length. As the coupling is turned

on, this bound state interacts with a "singlet" state lying above threshold pushing it still deeper into the potential, ultimately producing a negative scattering length. In both cases, the position of the singlet states relative to the **upper** hyperfine threshold are the determining factors in the physical scattering length.

Finally, we can compare the DIS scattering length result with that predicted by the frame transformation approximation. The short-range reaction matrix in the frame transformation approximation is given by

$$K^{\rm sr} = \begin{pmatrix} 0.2\bar{\tau}_s + 0.8\bar{\tau}_t & 0.4(\bar{\tau}_s - \bar{\tau}_t) \\ 0.4(\bar{\tau}_s - \bar{\tau}_t) & 0.8\bar{\tau}_s + 0.2\bar{\tau}_t \end{pmatrix} . \tag{5.7}$$

Again, the notation $\bar{\tau}_\lambda = \tan \pi\mu_\lambda$ is used. Channel 2 is then eliminated (see Eq. 4.25) leaving a single elastic matrix element

$$\tilde{K}_{11} = K^{\rm sr}_{11} + \frac{K^{\rm sr}_{12} K^{\rm sr}_{21}}{K^{\rm sr}_{11} + \tan\beta(-\Delta)} . \tag{5.8}$$

The scattering length (Eq. 4.38) is given in terms of this matrix element by

$$a = \frac{-C^2 \tilde{K}_{11}}{1 + \mathcal{G}(0)\tilde{K}_{11}} . \tag{5.9}$$

Inserting values for the quantum defects (Table 5.2), the zero energy constants C^2, $\mathcal{G}(0)$ (Table 4.1), and the phase parameter $\beta(\varepsilon = -\Delta)$ (a table of values for the long-range MQDT parameters is provided in Ref.[120]), the FT approximation predicts scattering lengths (in a.u.) of a = -103 and -286 for ^{84}Rb-^{84}Rb and ^{86}Rb-^{86}Rb, respectively. The frame transformation approximation reproduces the scattering lengths to within 20% of their physical values of a = -115 (^{84}Rb) and a = -237 (^{86}Rb), including the correct sign. The difference in the two models can be seen immediately from Eq. 5.8. In MQDT language, the DIS model is equivalent to setting $\tilde{K}_{11} = K^{\rm sr}_{11}$, which completely neglects the influence of the closed channel. The closed-channel physics is crucial in this particular case and it is the inclusion of this physics that distinguishes the frame transformation approximation from the DIS model.

The (surprisingly) negative scattering length implies a net attraction between the two spin states $|5/2, 5/2\rangle_A$ + $|5/2, 3/2\rangle_A$, which could have important consequences for forming Cooper pairs in these fermionic systems [121, 122]. On the other hand, the negative scattering lengths in these species again produce zeros in their s-wave cross sections, as shown in Fig. 5.16. The good news is that ^{84}Rb exhibits a Feshbach resonance in the presence of modest-sized magnetic fields (Fig. 5.17a). This resonance could then be used to move the position of the s-wave partial cross section zero to higher collision energies (Fig. 5.17b), allowing the atoms to be evaporatively cooled into the degenerate regime. The extremely large width of this

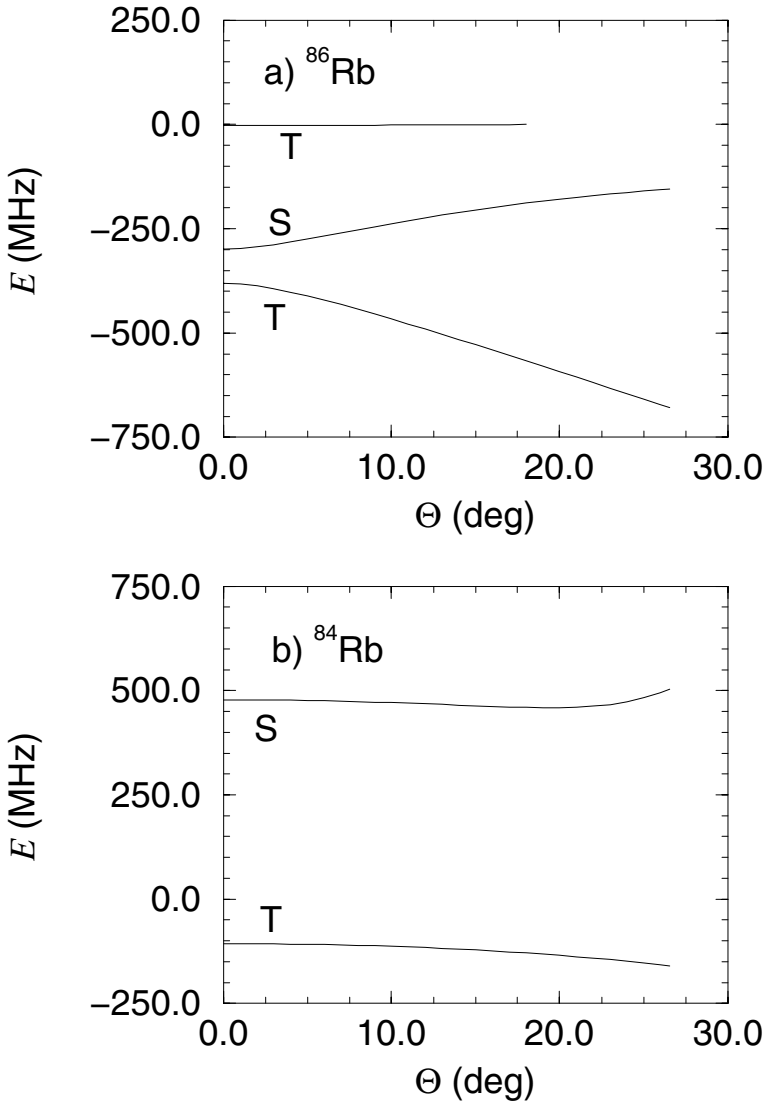

Figure 5.15: Bound and quasi-bound state positions versus the coupling parameter θ. The physical coupling strength is given by θ=26.57°. The labels S, T refer to singlet or triplet states in the θ = 0 limit. Zero energy defines the entrance channel threshold.
a) $|5/2, 5/2\rangle_{86}$ + $|5/2, 3/2\rangle_{86}$.
b) $|5/2, 5/2\rangle_{84}$ + $|5/2, 3/2\rangle_{84}$.

resonance eliminates the need for accurate control of magnetic field strengths. The resonance would also allow the experimentalist a means to study both repulsive and attractive effective interactions between atoms in a single system.

In the ^{86}Rb case, a magnetic field will also influence the scattering length, but will change its sign only at very large fields $\approx$ 2800 gauss (Fig. 5.17a). The position of the cross section zero can be moved to a higher collision energy (Fig. 5.17b), but to a lesser extent than in ^{84}Rb. However, in this case the s-wave zero is not a major problem, since the enhanced p-wave scattering should enable the experimentalist to evaporatively cool the ^{86}Rb mixed spin states without a magnetic field bias. However, introducing a bias field of a few hundred gauss would increase the low energy total cross section by roughly a factor of 3.

Finally, consider the bosonic isotope ^{83}Rb. The singlet and triplet ^{83}Rb scattering lengths are relatively large, positive and very nearly the same (see table 5.2). These are remarkably similiar to ^{87}Rb implying that ^{83}Rb by itself adds little to the field of BEC. However, mixtures of ^{83}Rb and ^{87}Rb atoms do offer some exciting possibilities. First, the ^{83}Rb-^{87}Rb triplet scattering length is large and negative (see Table 5.2), which is not surprising since the ^{83}Rb-^{87}Rb reduced mass is very nearly the same as two ^{85}Rb atoms. Therefore, a double condensate with large numbers of atoms could in principle be formed from the hyperfine states $|3,3\rangle_{83}$ + $|2,2\rangle_{87}$. Within the Thomas-Fermi approximation, a double condensate composed of equal mass atoms with scattering lengths a_1 and a_2 is unstable whenever the mutual scattering length a_{12} satisfies $|a_{12}| > \sqrt{a_1 a_2}$ [123, 124]. This relationship is strictly true only for isotropic like-species condensates. However, a more general derivation[125] for anisotropic mixed-isotope double condensates shows that the instability remains. The nature of this instability has yet to be fully interpreted, particularly in the case of a_{12} negative. The 83-87 mixture would provide a good system to explore this phenomenon. In addition, Feshbach resonances arise in collisions between atoms in the lower hyperfine manifold (see Fig. 5.18) , i.e. $|2,-2\rangle_{83}$ + $|1,-1\rangle_{87}$. Thus, in contrast to the ^{85}Rb-^{87}Rb system, it is possible to envision two large condensates with a tunable interspecies interaction. This capability could enable detailed studies of double condensates, all the way from completely overlapping to utterly immiscible[126, 127], in particular near the stability limits where $|a_{12}| \approx \sqrt{a_1 a_2}$.

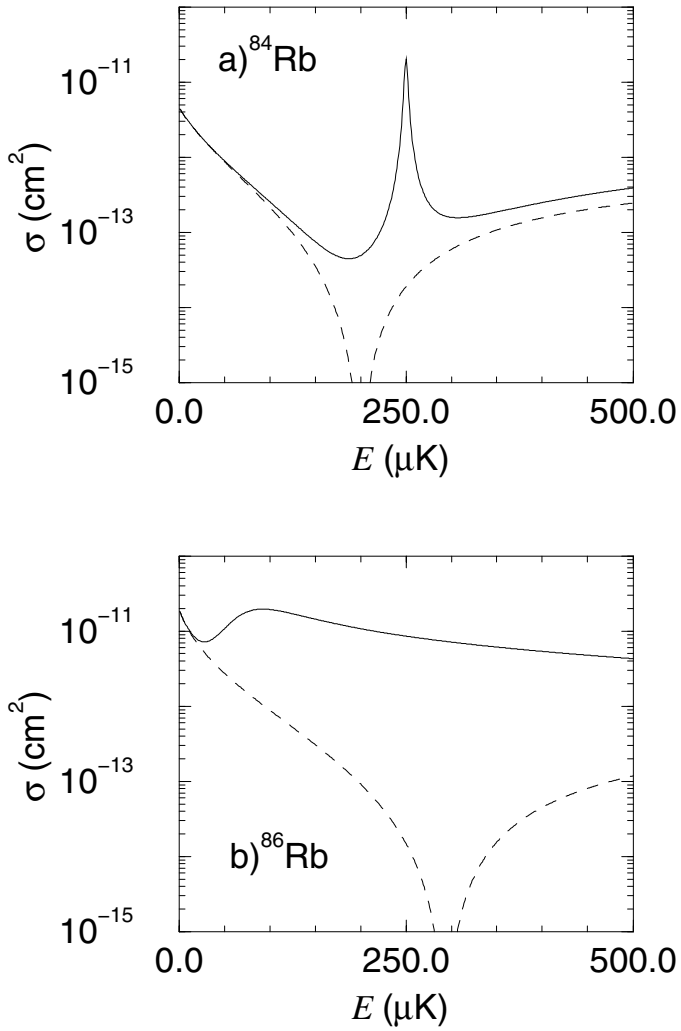

Figure 5.16: Elastic cross sections versus collision energy using our nominal potentials. Solid lines represent the total cross section, dashed lines indicate the s-wave contribution. The energy position of the first zero in the s-wave partial cross section is 200$\pm$30 μK for a) and 295$\pm$25 μK for case b).
a) $|5/2, 5/2\rangle_{84}$ + $|5/2, 3/2\rangle_{84}$.
The feature near 250 μK in the total cross section is a f-wave shape resonance. Although we find the position of this resonance is uncertain to $\pm$ 150 μK, it does not contribute over a broad enough energy range to compensate for the zero in the s-wave cross section.
b) $|5/2, 5/2\rangle_{86}$ + $|5/2, 3/2\rangle_{86}$.
We find a broad p-wave shape resonance near 60μK. The height of the p-wave centrifugal barrier is roughly 80μK. In this case, the strong p-wave scattering is probably enough to compensate for the zero in the s-wave cross section.

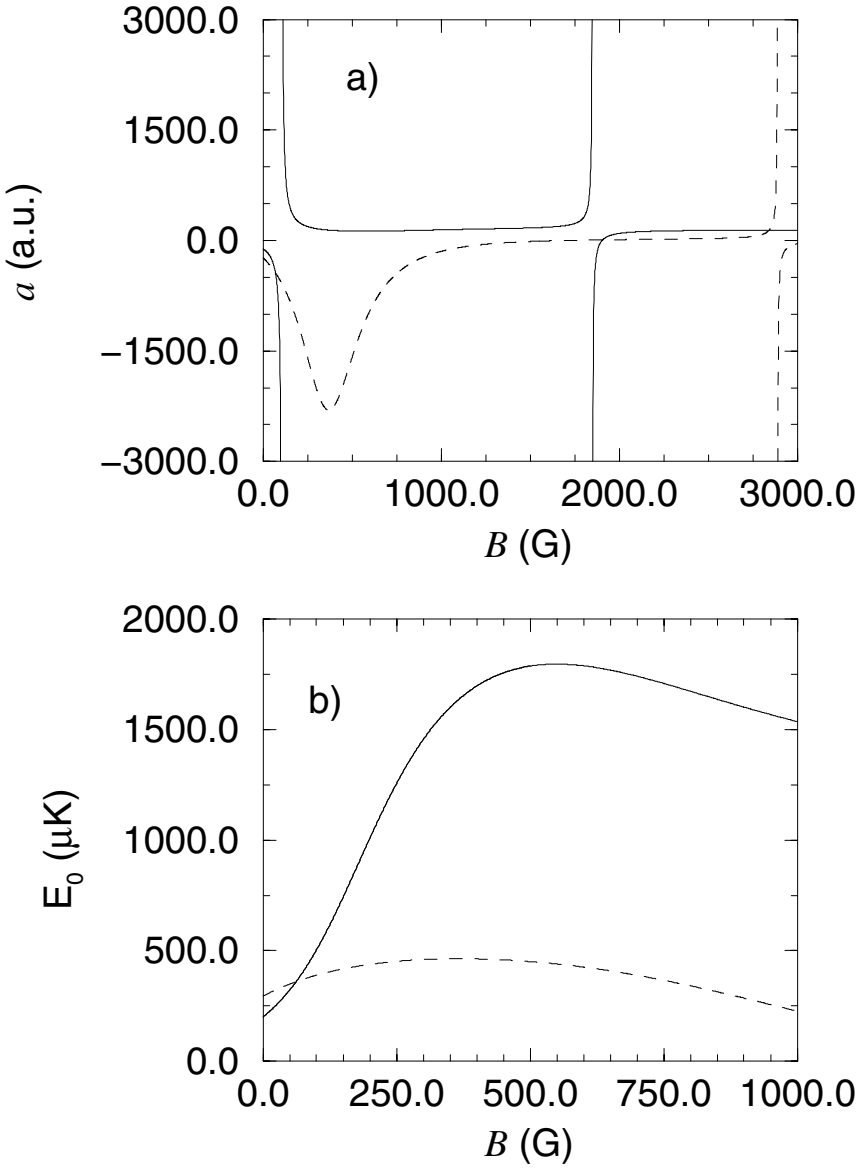

Figure 5.17: Solid lines represent $|5/2, 5/2\rangle_{84}$+$|5/2, 3/2\rangle_{84}$ collision, dashed lines represent the same spin state collision for ^{86}Rb.
a) Scattering lengths versus applied magnetic field. The zero energy positions of the low-field ^{84}Rb resonance is 106$\pm$9 G.
b) Energy position E_0 of the first s-wave partial cross section zero versus applied magnetic field.

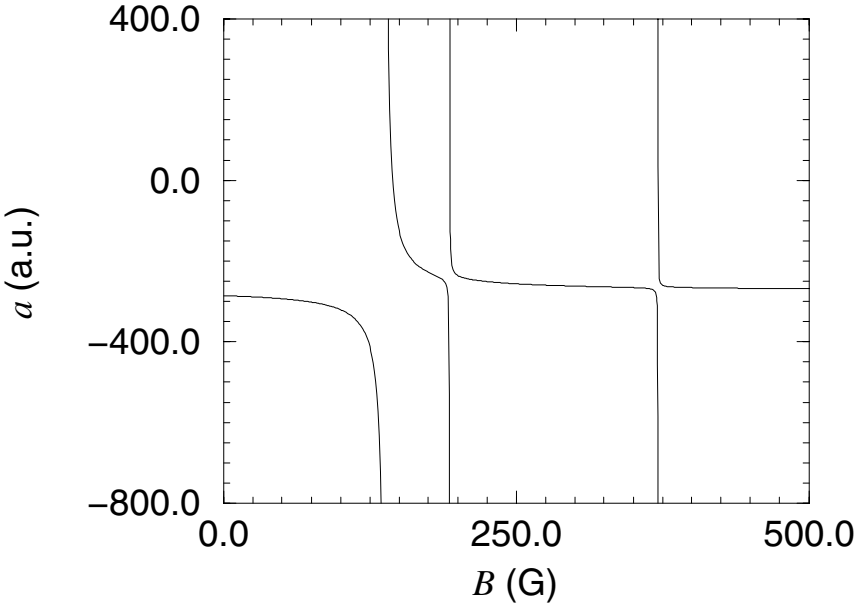

Figure 5.18: Scattering length versus applied magnetic field for a collision of $|2,-2\rangle_{83}$ + $|1,-1\rangle_{87}$ atoms. The zero energy positions of the resonance peaks are 138±10 G, 193±8 G, and 371±3 G. The low-field resonance has a width of Δ = 6.5±2.5 G. The two higher field resonances are extremely narrow ($\Delta \ll 1$ G).

Chapter 6

Theory of photoassociation lineshapes

Photoassociation (PA) spectroscopy has played a significant role in understanding cold collisions. In Chapter 1, photoassociation was described as the process by which an excited molecular bound state is resonantly formed through photoexcitation during the collision of two atoms. Generally, experiments are conducted with the atoms initially in their atomic ground state so that an analysis of the photoassociation lineshapes provides information, via the Franck-Condon overlap, on the colliding ground state wave function. In addition, transitions to the so called "long-range" molecular states[128, 129] that typically have **inner** turning points in the range $\sim 30 - 70$ Bohr, provide information on the ground state wave function at large R. In this way, the s-wave scattering lengths can be determined accurately. In fact, most of the alkali scattering lengths have been determined (at least initially) from an analysis of PA spectroscopy.

Photoassociation spectroscopy was first proposed by Thorsheim, Weiner and Julienne[19]. In that work, the authors developed the theoretical framework needed to analyze a PA spectrum. However, they were mostly concerned with experiments at the comparatively "warm" cloud temperatures of tens of mK. Photoassociation theory has since been extended[130] to include threshold effects of atoms colliding at magneto-optical trap (MOT) temperatures of hundreds of μK (see also Refs.[131, 132, 133] for a discussion of photoabsorption line shapes). In addition, a further development[134, 135] of the theory now includes the effect of a second laser. An extension of the one-color formulation of Ref.[130] to include multichannel scattering along the lines of Ref.[136] is presented in this chapter. This theoretical framework is then applied in Chapter 7 to analyze the measured rovibrational spectrum of the ^{39}K 0_g^- state, and to extract the s-wave scattering lengths.

This chapter is organized as follows: in Section 6.1, the basic lineshape formula is derived. The main component of this formula is a dipole matrix element that provides the radiative coupling between the ground state and the excited state. It is important to construct molecular wave functions that have the proper symmetries in order to evaluate the radiative coupling matrix element. Symmetry rules for diatomic wave functions in a Hund's case (a) representation[137] are presented in Section 6.2. The excited state Hamiltonian and ground state Hamiltonian

are constructed in Section 6.3. Here, the "ground state Hamiltonian" describes the interaction of two ground state atoms (S), while the "excited state Hamiltonian" describes the interaction of one ground state atom (S) and one excited state atom (P). Finally, the dipole matrix element that connects these states is evaluated in Section 6.4.

6.1 One color lineshape formula

The centerpiece of photoassociation theory is an expression for the thermal averaged rate constant K_p that describes the rate at which molecular bound states are resonantly formed during the collision of two atoms. The general approach for evaluating K_p is to treat the photoassociation problem as an inelastic scattering process. The inelastic rate constant K_p for the formation of molecules (i.e., coefficient of squared density in the rate equation) is then proportional to

$$K_p = \left\langle \sum_l (2l+1) \frac{\sigma_l v}{1+\delta} \right\rangle \tag{6.1}$$

where the brackets denote a thermal average over a distribution of incident velocities v, σ_l is the total inelastic cross section for scattering from an incident continuum channel of partial wave l into a molecular bound state channel, and $\delta = 1$ if the initial pair of atoms are identical and in indistinguishable spin states, or $\delta = 0$ otherwise (see Section 2.1.2). Photoassociation experiments are usually conducted with dilute atom clouds at temperatures of a few hundred μK. Therefore, the thermal averaging procedure can be treated by the classical method presented in Appendix C. This expression for the rate constant assumes that the atom density n can be factored out of the thermal average as will be the case for most atom traps. The result of thermal averaging, after writing the cross section in terms of a scattering matrix element $\sigma/(1+\delta) = \frac{\pi v}{k^2}|S_p|^2$, is [130]

$$K_p = \frac{1}{hQ_T} \sum_l (2l+1) \int_0^\infty |S_p|^2 e^{-E/k_B T} dE \ , \tag{6.2}$$

where k_B is the Boltzmann constant, T represents the cloud temperature, and $Q_T = (2\pi\mu k_B T/h^2)^{3/2}$ is the translational partition function. Perturbative expressions for the scattering matrix element $|S_p|^2$, valid for the low laser intensities generally used in these experiments, have been derived in Refs. [130, 135]. The general result can be written as

$$|S_p(E,l,\omega)|^2 = \frac{\gamma_0 \gamma_s(E,l)}{(E + h\nu_1 - E_b)^2 + (\gamma/2)^2} \tag{6.3}$$

where ν_1 is the laser frequency, E_b is the bound state energy, γ is the total width (in energy units) of the bound state, and $\gamma_0/\hbar$ represents the rate at which observable products are produced (i.e., atoms lost from the trap by spontaneous emission or atoms (molecules) ionized by a second laser). The main component of equation 6.3 is the radiative width, which can be expressed in terms of a coupling matrix element as

$$\gamma_s(E,l) = 2\pi|\langle\Psi_b(R)|V_{\rm rad}(R)|\Psi_l^E(R)\rangle|^2 \ . \tag{6.4}$$

Here, $\Psi_b(R)$ represents a unit normalized bound state wave function, $\Psi_l^E(R)$ is the energy-normalized continuum wave function in the incident channel, and $V_{\rm rad}(R) = (2\pi I/c)^{1/2} d(\vec{R})$ represents the radiative coupling that is proportional to the square root of the laser intensity I and the molecular dipole operator $d(\vec{R})$. (The molecular dipole operator is described in Section 6.4.)

The last step is to substitute expressions 6.3 and 6.4 into the rate constant equation (6.2) and generalize the result for multichannel scattering. The final result for K_p is given by[136]

$$\begin{aligned} K_p(v',J',\omega,T) &= \frac{4\pi^2 I}{hcQ_T} \sum_{\beta' p' f l p \alpha} n_f(2l+1) \\ &\int_0^\infty dE \frac{e^{-E/k_B T}\gamma_0 |\langle\Psi_{p'\beta'}^{v'J'}(R)|d_{flp\alpha}^{J'p'\beta'}(R)|\Psi_{flp\alpha}^E(R)\rangle|^2}{(E+h\nu_1 - E_{v'J'})^2 + (\gamma/2)^2} \ . \end{aligned} \tag{6.5}$$

This expression (6.5) is used for the analysis presented in Chapter 7. It includes a sum over all unresolved final states, an average over all initial states and a thermal average over incident energy. In this multichannel context, the bound molecular wave function Ψ_b is labeled by its vibrational quantum number v', rotational quantum number J', parity p', and a set of additional quantum numbers β' required to define the wave function uniquely. For example β' includes the nuclear spin degrees of freedom. The continuum wave function Ψ^E is energy-normalized and satisfies outgoing-wave boundary conditions. It is labeled by the total spin f of the colliding atoms, the partial wave l, parity p, and α includes all other quantum numbers required to define the initial quantum state uniquely. Also present is a constant n_f representing a weighting factor for the population of atoms in the f entrance channel. For a randomly polarized gas of identical particles, this weight is given by $n_f = \frac{(2f+1)}{N_{\{f_a,f_b\}}}$ where $N_{\{f_a,f_b\}} = (2f_a+1)(2f_b+1+\delta_{f_a,f_b})/(1+\delta_{f_a,f_b})$ is the total number of distinct symmetrized spin channels. It should be noted that averaging the dipole matrix elements over initial states cancels both the $(2f+1)$ factor above and the $(2l+1)$ term in Eq. 6.5.

6.2 Symmetry rules for diatomic Hund's case (a) wave functions

The field-free diatomic Hamiltonian possesses a number of discrete symmetries beyond the translational and rotational dynamical symmetries. The Hamiltonian commutes with the electron permutation operator $\hat{P}_e$, the parity operator $\hat{\pi}$, and for homonuclear molecules, the nuclear permutation operator $\hat{P}_n$. In the Born-Oppenheimer limit[31], the electronic part of the factored wave function possesses additional symmetries. These include reflection of the electronic wave function through a plane containing the internuclear axis, whose operator is denoted $\hat{\sigma}_v$; and for nuclei of equal charge, inversion of the electronic wave function through the center of mass in the molecular frame, whose operator is denoted $\hat{i}$.

We can construct an eigenfunction of the molecular Hamiltonian in the Born-Oppenheimer limit from a set of Hund's case (a) basis functions. These basis functions have the following form:

$$\begin{aligned}\Phi(J, M_J, \Omega, \Lambda, S, \Sigma, I, M_I, R, w) &= \sqrt{\frac{2J+1}{4\pi}}\, D^{J*}_{M_J,\Omega}(\alpha, \beta, \gamma)\phi(\Lambda, w) \\ &\quad |(s_a s_b)S\Sigma\rangle |(i_a i_b) I\, M_I\rangle\, F_{J,\Lambda}(R)\ . \quad (6.6)\end{aligned}$$

Here, $D^J_{M_J,\Omega}$ is a matrix element of the $(2J+1) \times (2J+1)$ unitary rotation matrix[57]. It is a function of the Euler angles (α, β, γ) which define the relationship of the space-fixed lab frame with that of the body-fixed molecule frame. Zare's[57] definition for the Euler angles, which agrees with that of other standard angular momentum texts (for example, Brink and Satchler[138]; see also Larsson[139] for a discussion of the different conventions) is adopted here. The normalization factor implies that γ = 0, which is a standard convention for linear molecules[57]. The quantum numbers of the D-function consist of $\vec{J} = \vec{L} + \vec{S} + \vec{l}$, the total angular momentum (neglecting nuclear spin), M_J is the projection of $\vec{J}$ on the space-fixed z axis; and $\Omega = \Lambda + \Sigma$, the projection of J on the body-frame z' axis (taken to be the internuclear axis). The electronic spatial wave function is represented by ϕ, which depends on the projection of the total electronic angular momentum $\vec{L}$ onto the internuclear axis Λ and on the the body-fixed inversion quantum number w that distinguishes gerade (g) and ungerade (u) states. The complete expression for ϕ is worked out later. The total electronic spin and its projection onto the internuclear axis is represented by $|S\Sigma\rangle$. Since, the 0^-_g experiment did not resolve hyperfine structure our analysis is simplified by quantizing the nuclear spin $|IM_i\rangle$ in the lab frame. Finally, $F_{J,\Lambda}(R)$ represents the radial wave function.

First, the electronic orbitals that comprise ϕ must be constructed such that ϕ is an eigenfunction of both $\hat{P}_e$ and $\hat{i}$. We are primarily interested in the molecular wave function at large R, where there is negligible overlap of the electronic charge distributions. There, ϕ can be expressed in terms of properly symmetrized linear

combinations of atomic orbitals U_{L_c} [140]:

$$\begin{aligned}\phi(\Lambda, w) &= N\left\{[U^a_{L_c}(\vec{r_1})U^b_{L_d}(\vec{r_2})]_\Lambda + (-1)^n[U^a_{L_c}(\vec{r_2})U^b_{L_d}(\vec{r_1})]_\Lambda + \right. \\ &\left. (-1)^{n'}[U^a_{L_d}(\vec{r_1})U^b_{L_c}(\vec{r_2})]_\Lambda + (-1)^{n''}[U^a_{L_d}(\vec{r_2})U^b_{L_c}(\vec{r_1})]_\Lambda\right\} .\end{aligned} \tag{6.7}$$

Here, N is a normalization constant and the phase factors n, n', n'' are to be determined. The notation $[U^a_{L_c}(\vec{r_1})U^b_{L_d}(\vec{r_2})]_\Lambda$ indicates an atomic orbital with quantum numbers $L_c(L_d)$ centered on atom $a(b)$ that is a function of electron 1(2)'s coordinates and Λ denotes the total projection of $\vec{L} = \vec{L}_c + \vec{L}_d$ onto the internuclear axis. Each atomic orbital has an associated spherical harmonic to represent its angular degrees of freedom, $Y_{L_i\lambda}(\theta_e, \chi_e)$, where the angles θ_e, χ_e are defined relative to the body-fixed coordinate system defined by the Euler angles α, β, γ, with the origin translated to coincide with the atomic center. The inversion of the electronic wave function through the center-of-mass of the body-fixed frame does two things: first it switches the orbitals, then it inverts each orbital about the new atomic center. This is equivalent to letting $\theta_e \to \pi - \theta_e$ and $\chi_e \to \pi + \chi_e$, which amounts to adding an additional phase factor to the spherical harmonic, $\hat{i}Y_{L_i\lambda}(\theta_e, \chi_e) = (-1)^{L_i}Y_{L_i\lambda}(\theta_e, \chi_e)$. Therefore, the effect of $\hat{i}$ on each component of ϕ (Eq. 6.7) can be determined from the following:

$$\hat{i}[U^a_{L_c}(\vec{r_1})U^b_{L_d}(\vec{r_2})]_\Lambda = (-1)^{L_c+L_d}[U^a_{L_d}(\vec{r_1})U^b_{L_c}(\vec{r_2})]_\Lambda . \tag{6.8}$$

We can make ϕ in Eq. 6.7 an eigenfunction of $\hat{i}$ by simply attaching $(-1)^{L_c+L_d+w}$ phase factors to the third and fourth components. The eigenvalue of $\hat{i}$ is $(-1)^w$, where $w = 0$ defines a gerade (g) symmetry and $w = 1$ defines an ungerade (u) symmetry.

The electronic spin degrees of freedom must be included to antisymmetrize the electronic wave function with respect to electron exchange $\hat{P}_e$. The result when applied to a single component of ϕ (Eq. 6.7) is

$$\begin{aligned}\hat{P}_e\,[U^a_{L_c}(\vec{r_1})U^b L_d(\vec{r_2})]_\Lambda\,|(s_a s_b)S\Sigma\rangle &= (-1)^{s_a+s_b-S}[U^a_{L_c}(\vec{r_2})U^b_{L_d}(\vec{r_1})]_\Lambda \\ &\quad |(s_a s_b)S\Sigma\rangle ,\end{aligned} \tag{6.9}$$

where the phase factor arises from the properties of Clebsch-Gordan coefficients. The electronic wave function must be odd under the permutation of two electrons, i.e.

$$\hat{P}_e\,\phi(\Lambda, w)\,|(s_a s_b)S\Sigma\rangle = -\phi(\Lambda, w)\,|(s_a s_b)S\Sigma\rangle . \tag{6.10}$$

In the case of two alkali atoms $s_a = s_b = 1/2$, this equality requires an additional $(-1)^S$ phase factor to be included in the second and fourth components of Eq. 6.7. The final result for the electronic orbital angular momentum wave function, which

is now an eigenfunction of both $\hat{i}$ and $\hat{P}_e$, is

$$\begin{aligned}\phi(\Lambda,w) &= N\left\{[U^a_{L_c}(\vec{r_1})U^b_{L_d}(\vec{r_2})]_\Lambda + (-1)^S[U^a_{L_c}(\vec{r_2})U^b_{L_d}(\vec{r_1})]_\Lambda + \right.\\ &\quad (-1)^{L_c+L_d+w}[U^a_{L_d}(\vec{r_1})U^b_{L_c}(\vec{r_2})]_\Lambda + \\ &\quad \left.(-1)^{L_c+L_d+w+S}[U^a_{L_d}(\vec{r_2})U^b_{L_c}(\vec{r_1})]_\Lambda\right\}\ . \qquad (6.11)\end{aligned}$$

With the complete basis function defined, we now turn to the effect of the parity operator. Hougen[141] has shown that the parity operator acting on the total wave function is equivalent to $\hat{\pi}\Phi = \hat{\sigma}_v\Phi$, provided that $\hat{\sigma}_v$ acts on **all** degrees of freedom of the wave function. There is more than one plane that can be chosen to define the reflection operator $\hat{\sigma}_v$. We adopt Hougen's convention of reflecting through the $x'z'$ plane (see Ref.[139] for a discussion of the different approaches for this symmetry operation). First, the symmetry rules for the action of $\hat{\sigma}_{x'z'}$ on each component of Φ are provided and then a brief outline of their derivations is given. (The separation of the electronic orbital and spin degrees of freedom, as done here, is strictly valid only in one- and two-electron molecules[142]). The symmetry rules for the reflection operator are as follows:

$$\begin{aligned}\hat{\sigma}_{x',z'}D^{J*}_{M\Omega}(\alpha,\beta,\gamma) &= (-1)^{J-\Omega}D^{J*}_{M-\Omega}(\alpha,\beta,\gamma)\\ \hat{\sigma}_{x',z'}\phi(\Lambda,w) &= (-1)^{\Lambda}\phi(-\Lambda,w)\\ \hat{\sigma}_{x',z'}|S\Sigma\rangle &= (-1)^{S-\Sigma}|S-\Sigma\rangle\\ \hat{\sigma}_{x',z'}|IM_I\rangle &= |IM_I\rangle\ . \qquad (6.12)\end{aligned}$$

There is an additional (-1) phase factor in the relationship for ϕ, if ϕ is a Σ^- electronic state. However, these states are ignored here because they do not factor into our analysis of the 0^-_g spectrum. The parity of a single basis function (Eq. 6.6) is found from these rules (Eq. 6.12) to be $(-1)^{J+S}$ for alkali atoms. A wave function with definite parity $(-1)^p$, which is also an eigenfunction of the symmetry operators $\hat{i}$ and $\hat{P}_e$, is constructed with the following linear combination of basis functions:

$$\begin{aligned}\Psi_{\rm mol} &= \sqrt{\frac{2J+1}{4\pi(2-\delta_{\Sigma,0}\delta_{\Lambda,0})}}\ \left[D^{J*}_{M\Omega}(\alpha,\beta,\gamma)\,\phi(\Lambda,w)\,|S\Sigma\rangle + \right.\\ &\quad \left.(1-\delta_{\Sigma,0}\delta_{\Lambda,0})(-1)^{J+S+p}D^{J*}_{M-\Omega}(\alpha,\beta,\gamma)\,\phi(-\Lambda,w)|S-\Sigma\rangle\right]\\ &\quad |IM_I\rangle\,F_{J,\Lambda}(R)\ , \qquad (6.13)\end{aligned}$$

provided ϕ is constructed according to Eq. 6.11.

The effect of the reflection operator $\sigma_{x',z'}$, which is a sense-reversing symmetry operation, on the rotational degrees of freedom is nontrivial. Hougen discusses the problem at length and eventually adopts the following scheme: $\sigma_{x',z'}D^{J*}_{M\Omega} = C_2(y')D^J_{M\Omega}$. Here, $C_2(y')$ defines a π radians rotation about the y' axis. The outcome of this convention is that $\hat{\sigma}_{x',z'}\Phi$ is equivalent to a π rotation of the molecule-

fixed coordinate system about an axis perpendicular to the internuclear axis (y'), followed by the reflection of all other wave function coordinates through the plane defined by (x', z'). The π rotation about y' amounts to changing the Euler angles by $\alpha \rightarrow \pi + \alpha$, $\beta \rightarrow \pi - \beta$, and $\gamma \rightarrow \pi - \gamma$. Standard identities[57] for the D-functions can be used to determine the symmetry rule for the rotational piece of the factored wave function,

$$D^{J*}_{M\Omega}(\pi + \alpha, \pi - \beta, \pi - \gamma) = (-1)^{(J-\Omega)} D^{J*}_{M-\Omega}(\alpha, \beta, \gamma) \; . \tag{6.14}$$

To assess the effects of $\hat{\sigma}_{x',z'}$ on $\phi(\Lambda, w)$, note that reflection of electronic orbital angular momentum through the x', z' is equivalent to changing the angle $\chi_e \rightarrow -\chi_e$. Each spherical harmonic then transforms as $Y_{L\lambda}(\theta_e, -\chi_e) = Y^*_{L\lambda}(\theta_e, \chi_e) = (-1)^{\lambda} Y_{L\,-\lambda}(\theta_e, \chi_e)$. The total wave function acquires the phase factor $(-1)^{(\lambda+\lambda')} = (-1)^{\Lambda}$. Finally, the action of $\hat{\sigma}_{x',z'}$ on the electronic spin would have no effect if it was quantized in the lab frame (as is the case with $|I, M_I\rangle$). Rotating the electronic spin wave function into the space-fixed frame,

$$|SM_S\rangle = \sum_{\Sigma} D^{S*}_{M_S,\Sigma}(\alpha, \beta, \gamma) |S\Sigma\rangle \; , \tag{6.15}$$

the reflection $\hat{\sigma}_{x',z'}$ of the spin wave function becomes

$$\begin{aligned} \hat{\sigma}_{x',z'}|S, M_S\rangle &= \sum_{\Sigma} [\hat{\sigma}_{x',z'} D^{S*}_{M_S\Sigma}(\alpha, \beta, \gamma)][\hat{\sigma}_{x',z'}|S\Sigma\rangle] \\ &= \sum_{\Sigma} (-1)^{S-\Sigma} D^{S*}_{M_S-\Sigma}(\alpha, \beta, \gamma)[\hat{\sigma}_{x',z'}|S\Sigma\rangle] \; . \end{aligned} \tag{6.16}$$

Thus the lab frame spin wave function will remain invariant only if $\hat{\sigma}_{x',z'}|S\Sigma\rangle = (-1)^{S-\Sigma}|S - \Sigma\rangle$.

The nuclear permutation operator acting on the total wave function provides nuclear selection rules. Hougen has shown[141] that this operation is equivalent to $\hat{P}_n \Psi = \hat{i}\hat{\pi}\hat{P}_I \Psi$, where $\hat{P}_I$ only permutes the nuclear spins. We have already evaluated $\hat{\pi}\Phi$, as well as $\hat{i}\Phi$, which acts only on the electronic orbital. Therefore, applying $\hat{P}_n$ to the wave function in Eq. 6.13, gives:

$$\hat{P}_n \Psi_{\rm mol} = (-1)^{p+w+I-i_a-i_b} \Psi_{\rm mol} \, . \tag{6.17}$$

For the bosonic alkali atoms, which have half-integer nuclear spins, the wave function must be odd under permutation of the nuclei and therefore the equality $(-1)^{p+w+I} = 1$ must be satisfied. It is necessary to include an additional $[1 + (-1)^{p+w+I}]/2$ term in the wave function (Eq. 6.13) to ensure that it is also an eigenfunction of $\hat{P}_n$. The final expression for the wave function, which has definite parity, and is an eigen-

function of $\hat{i}$, $\hat{P}_e$, and $\hat{P}_n$ is then

$$\begin{aligned}\Psi_{\rm mol} &= \sqrt{\frac{2J+1}{4\pi(2-\delta_{\Sigma,0}\delta_{\Lambda,0})}}\left(\frac{1+(-1)^{p+w+I}}{2}\right)|IM_I\rangle\, F_{J,\Lambda}(R) \\ &\quad \left[D^{J*}_{M\Omega}(\alpha,\beta,\gamma)\,\phi(\Lambda,w)\,|S\Sigma\rangle + \right. \\ &\quad \left.(1-\delta_{\Sigma,0}\delta_{\Lambda,0})(-1)^{J+S+p}D^{J*}_{M-\Omega}(\alpha,\beta,\gamma)\,\phi(-\Lambda,w)|S-\Sigma\rangle\right].\end{aligned} \tag{6.18}$$

We are primarily interested in the consequences of these symmetry relationships for the ^{39}K 0^-_g electronic state, i.e. $\Omega = 0$. The rotational levels of an $\Omega = 0$ state have a definite parity and therefore have definite nuclear spin selection rules. This is simply because one way to construct an $\Omega = 0$ wave function is with a single basis function (note the $\delta_{\Sigma,0}\delta_{\Lambda,0}$ function in Eq. 6.18). These individual basis functions (Eq. 6.6) have parity $(-1)^{J+S}$ and the bosonic nuclear permutation symmetry requires $(-1)^{J+S+w+I} = 1$. In the next section, it will be shown that the 0^-_g electronic state is a triplet ($S = 1$) spin state. Therefore, the odd J rotational energy levels have positive parity and the even J rotational energy levels have negative parity. In addition, the nuclear permutation symmetry requires $(-1)^{J+I} = -1$, which limits the nuclear spin states that can contribute to each rotational level. These selection rules play a large role in the analysis of the measured 0^-_g spectra.

6.3 Excited and ground state Hamiltonians

This section is divided into two parts, the bulk of which is presented in 6.3.1. Here, the interactions and general matrix structure for the excited state Hamiltonian are presented. First, the general excited state molecular Hamiltonian is developed and the approximations employed in the analysis of the 0^-_g state are detailed. Next for completeness, the ground state Hamiltonian needed for the analysis presented in Chapter 7 is provided in Section 6.3.2.

6.3.1 S + P Hamiltonian

The interactions that comprise the S + P Hamiltonian include those listed in Section 2.2 and the atomic spin-orbit interaction $H^{\rm so}$. The zero-field total Hamiltonian is thus composed of the following components:

$$H = H^{\rm BO} + H^{\rm so} + H^{l} + H^{\rm ss} + H^{\rm hf} \tag{6.19}$$

where $H^{\rm BO}$ includes the Born-Oppenheimer potentials, H^l is the rotational Hamiltonian, $H^{\rm ss}$ represents the magnetic dipole-dipole interaction, and $H^{\rm hf}$ is the hyperfine interaction. The Hamiltonian is constructed in a Hund's case (a) molecular representation, which will be a convenient representation for evaluating the dipole matrix element. The Born-Oppenheimer potentials that correlate asymptotically with the S

+ P threshold depend on the total spin $\vec{S}$, the projection of the electronic angular momentum on the internuclear axis Λ, and also the inversion symmetry of the electronic wave function in the molecular frame, labeled g (even) or u (odd). There are thus eight unique Born-Oppenheimer potentials for the alkali atoms, labeled $^{2S+1}\Lambda_{\rm g/u}$, and $H^{\rm BO}$ is an 8×8 diagonal matrix in the Hund's case (a) representation.

The good quantum numbers in the Hund's case (c)[137] angular momentum coupling scheme (neglecting nuclear spin) are the total angular momentum $\vec{J} = \vec{L} + \vec{S} + \vec{l}$ and its projection onto the internuclear axis $\Omega = \Lambda + \Sigma$. The nuclear rotation (or partial wave) $\vec{l}$ is oriented at right angles to the internuclear axis. The Hund's case (c) labels become appropriate when the strength of the spin-orbit interaction $H^{\rm so}$ becomes at least comparable to the energy splittings between the Born-Oppenheimer potentials $H^{\rm BO}$. Spin-orbit matrix elements in a Hund's case (a) representation have been evaluated in Ref.[143] and are reproduced here (Δ is the atomic spin-orbit splitting):

$$\begin{aligned}
\langle {}^3\Lambda_w, \Sigma | H^{\rm so} | {}^3\Lambda'_{w'}, \Sigma' \rangle &= \frac{\Delta}{3}\delta_{w,w'}[\Lambda\Sigma\delta_{\Lambda,\Lambda'}\delta_{\Sigma,\Sigma'} + \delta_{\Lambda,\Lambda'-1}\delta_{\Sigma,\Sigma'+1} \\
&\quad + \delta_{\Lambda,\Lambda'+1}\delta_{\Sigma,\Sigma'-1}] \\
\langle {}^1\Lambda_w, \Sigma | H^{\rm so} | {}^3\Lambda'_{w'}, \Sigma' \rangle &= -\frac{\Delta}{3}\delta_{w,w'}[\Lambda\delta_{\Lambda,\Lambda'}\delta_{\Sigma,0} - \delta_{\Lambda,\Lambda'-1}\delta_{\Sigma,-1} \\
&\quad + \delta_{\Lambda,\Lambda'+1}\delta_{\Sigma,+1}] \\
\langle {}^1\Lambda_w, \Sigma | H^{\rm so} | {}^1\Lambda'_{w'}, \Sigma' \rangle &= 0 \ . \qquad (6.20)
\end{aligned}$$

The atomic spin-orbit interaction $H^{\rm so}$ breaks the electronic spin projection degeneracy, resulting in 24 Hund's case (c) electronic states. These 24 states can be broken down into four different six-channel blocks which correspond to a definite parity and definite g/u symmetry. In addition, the Hamiltonian $H = H^{\rm BO} + H^{\rm so}$ is block diagonal with respect to the value of Ω. Nonvanishing contributions of $H^{\rm BO} + H^{\rm so}$ are illustrated in figures 6.1 and 6.2 for opposite parity states.

Evaluation of the rotational Hamiltonian $H^l = \frac{1}{2\mu R^2}\vec{l}^2$ in a Hund's case (a) representation is simplified by first decomposing the nuclear rotation angular momentum vector $\vec{l} = \vec{J} - \vec{L} - \vec{S}$, and then using the commutation properties of each Cartesian component of these operators, i.e. $[J_i, S_i] = 0$. The final expression for H^l, written in terms of the angular momentum operators J, L, S, is[53]

$$\begin{aligned}
H^l &= \frac{1}{2\mu R^2}\left[(J^2 - J_{z'}^2) + (L^2 - L_{z'}^2) + (S^2 - S_{z'}^2)\right. \\
&\quad \left. + (L_+S_- + L_-S_+) - (J_+L_- + J_-L_+) - (J_+S_- + J_-S_+)\right] \qquad (6.21)
\end{aligned}$$

where $J_\pm = J_{x'} \pm iJ_{y'}$ represents standard raising and lowering operators defined in the body-fixed coordinate system, ($L_\pm$ and $S_\pm$ are defined similarly). There are two difficulties with this expression. First, Hund's case (a) wave functions are not

$0^-_{g/u}$ parity

	$^3\Pi_{g/u}(\Omega=0)$	$^3\Sigma^+_{g/u}(\Omega=0)$	$^3\Pi_{g/u}(\Omega=1)$	$^3\Sigma^+_{g/u}(\Omega=1)$	$^1\Pi_{g/u}(\Omega=1)$	$^3\Pi_{g/u}(\Omega=2)$
$^3\Pi_{g/u}(\Omega=0)$	$H^{BO}+H^{so}+H^l$	$H^{so}+H^l$	H^l	H^l	0	0
$^3\Sigma^+_{g/u}(\Omega=0)$	$H^{so}+H^l$	$H^{BO}+H^l$	H^l	H^l	0	0
$^3\Pi_{g/u}(\Omega=1)$	H^l	H^l	$H^{BO}+H^l$	$H^{so}+H^l$	H^{so}	H^l
$^3\Sigma^+_{g/u}(\Omega=1)$	H^l	H^l	$H^{so}+H^l$	$H^{BO}+H^l$	H^{so}	H^l
$^1\Pi_{g/u}(\Omega=1)$	0	0	H^{so}	H^{so}	$H^{BO}+H^l$	0
$^3\Pi_{g/u}(\Omega=2)$	0	0	H^l	H^l	0	$H^{BO}+H^{so}+H^l$

Figure 6.1: Block Structure of the 6×6 S + P Hamiltonian. The parity $(-1)^p = (-1)^{J+1}$ of the eigenfunctions composing the matrix elements is determined by the symmetry rules for the $0^-_{g/u}$ electronic state. The structure of this matrix is the same for both g and u symmetries. The origin of the nonzero matrix elements are indicated by $H^{\rm BO} \equiv$ Born-Oppenheimer potentials, $H^{\rm so} \equiv$ spin-orbit interaction, and $H^l \equiv$ the rotational Hamiltonian.

$0^+_{g/u}$ parity

	$^3\Pi_{g/u}(\Omega=0)$	$^1\Sigma^+_{g/u}(\Omega=0)$	$^3\Pi_{g/u}(\Omega=1)$	$^3\Sigma^+_{g/u}(\Omega=1)$	$^1\Pi_{g/u}(\Omega=1)$	$^3\Pi_{g/u}(\Omega=2)$
$^3\Pi_{g/u}(\Omega=0)$	$H^{BO}+H^{so}+H^{I}$	H^{I}	H^{I}	H^{I}	0	0
$^1\Sigma^+_{g/u}(\Omega=0)$	H^{I}	$H^{BO}+H^{I}$	H^{I}	H^{I}	0	0
$^3\Pi_{g/u}(\Omega=1)$	H^{I}	H^{I}	$H^{BO}+H^{I}$	$H^{so}+H^{I}$	H^{so}	H^{I}
$^3\Sigma^+_{g/u}(\Omega=1)$	H^{I}	H^{I}	$H^{so}+H^{I}$	$H^{BO}+H^{I}$	H^{so}	H^{I}
$^1\Pi_{g/u}(\Omega=1)$	0	0	H^{so}	H^{so}	$H^{BO}+H^{I}$	0
$^3\Pi_{g/u}(\Omega=2)$	0	0	H^{I}	H^{I}	0	$H^{BO}+H^{so}+H^{I}$

Figure 6.2: Opposite parity block as that shown in Fig. 6.1(with same notation for nonzero matrix elements). The eigenfunctions composing these matrix elements have a $(-1)^p = (-1)^J$ parity which can be derived from the symmetry rules for a $0^+_{g/u}$ electronic state. In the absence of rotation, the $\pm$ parity eigenstates are degenerate for Ω = 1 and 2

eigenfunctions of $\vec{L}^2$. However, electronic orbitals constructed in the separated atom limit, as in Section 6.2, can be treated as approximate eigenfunctions of $\vec{L}^2$. The second difficulty is that the total angular momentum J in the body-fixed frame obeys anomalous commutation rules[57], i.e. $[J_{x'}, J_{y'}] = -iJ_{z'}$. A standard approach[57] for resolving the anomalous commutation problem is to redefine the raising and lowering operators such that $J_\pm \rightarrow J_\mp$. Matrix elements for H^l in a Hund's case (a) representation have been evaluated in Ref.[141].

The matrix structure of H^l in the Hund's case (a) representation can be determined from the operators comprising the Hamiltonian (Eq. 6.21). The first three terms in Eq. 6.21 are diagonal in the Hund's case (a) representation. The fourth term ($\propto L_+ S_-$) gives rise to rotational coupling within a constant Ω block of the Hamiltonian. The last two terms are responsible for electronic-rotational couplings and are often denoted as Coriolis couplings. The rotational Hamiltonian preserves the g/u symmetry of the electronic wave function and therefore preserves the block diagonal matrix structure of H. This is illustrated in figures 6.1 and 6.2. Finally the matrix values of $H^{\rm ss}$, which are diagonal in a Hund's case (a) representation, were given in Section 2.2.3. These matrix elements are relatively small in the excited state (roughly 10^{-5} the value of the Born-Oppenheimer potentials at large R) and are neglected. In addition, $H^{\rm hf}$ is neglected in the analysis presented in Chapter 7. In Ref.[21], it was shown that the bound state energies of the lowest few vibrational levels of the $0_{\rm g}^-$ state were essentially independent of the hyperfine interaction.

In practice, $0_{\rm g}^-$ potentials that accurately describe the lowest few vibrational levels are obtained by considering only $H^{\rm BO}$ + $H^{\rm so}$, along with the diagonal elements of the rotational Hamiltonian H^l (the Ω=0 off-diagonal rotational coupling elements for ^{39}K are of the order $\sim 1/\mu$ times smaller than the spin-orbit coupling). This results in the following 2×2 matrix in the representation ($^3\Pi_g$,$^3\,\Sigma_g^+$):

$$\underline{H} = \begin{pmatrix} V_\Pi + V_\Pi^l - \frac{\Delta}{3} & \frac{\sqrt{2}}{3}\Delta \\ \frac{\sqrt{2}}{3}\Delta & V_\Sigma + V_\Sigma^l \end{pmatrix} \tag{6.22}$$

where Δ = 57.706 cm^{-1} represents the atomic spin-orbit splitting. The Born-Oppenheimer potentials at large R are well-approximated by a multipole expansion,

$$V_{\Lambda'} = -f^{\Pi/\Sigma}\frac{\mathrm{C}_3^{\Pi/\Sigma}}{R^3} - \frac{\mathrm{C}_6^{\Pi/\Sigma}}{R^6} - \frac{\mathrm{C}_8^{\Pi/\Sigma}}{R^8}\ , \tag{6.23}$$

and the ^{39}K dispersion coefficients were taken from Ref.[144]. Retardation effects are also incorporated in $f^{\Pi/\Sigma}$. These have the form[145]

$$\begin{aligned} f^\Pi &= \cos(R/\lambda) + (R/\lambda)\sin(R/\lambda) - (R/\lambda)^2\cos(R/\lambda) \\ f^\Sigma &= \cos(R/\lambda) + (R/\lambda)\sin(R/\lambda)\,. \end{aligned} \tag{6.24}$$

Here, $\lambda = \lambda_{4S\rightarrow 4P}/2\pi$ is the transition wavelength. The rotational matrix elements $V^l_{\Lambda'}$ incorporate only the first three terms from Eq. 6.21 and are given explicitly by

$$\begin{aligned} V^l_{\Pi} &= \frac{\hbar^2}{2\mu R^2}\left[J'(J'+1)+2\right] \\ V^l_{\Sigma} &= \frac{\hbar^2}{2\mu R^2}\left[J'(J'+1)+4\right] \ . \end{aligned} \tag{6.25}$$

The J'-dependent 0^-_g potentials, $V^{J'}$, are determined by first diagonalizing Eq. 6.22 and then incorporating non-adiabatic diagonal corrections[78]. Bound state energies $E_{v'J'}$ and single channel wave functions $\chi_{v'J'}(R)$ are now easily obtained for the potentials $V^{J'}$. The radial part of the excited state wave function Ψ_b is then conveniently written as an R-dependent linear combination of the two Hund's case (a) basis functions

$$F_b(R) = \sum_{\Lambda'} b_{J'\Lambda'}(R)\chi_{v'J'}(R) \tag{6.26}$$

where $b_{J'}(R)$ is the eigenvector obtained from the diagonalization of Eq. 6.22 that correlates with the potential whose asymptote is $S_{1/2} + P_{3/2}$. This form (6.26) facilitates the evaluation of the dipole matrix element.

6.3.2 S + S Hamiltonian

The ground state Hamiltonian has already been described in detail in Section 2.2. Here, I briefly outline the pertinent details needed for the analysis presented in Chapter 7. The ^{39}K photoassociation experiment[146] was conducted with unpolarized $f_a = f_b$=1 ground state atoms trapped in a dark-spot MOT with cloud temperatures of $\sim$ 400 μK. The experiment resolved J'=0-4 rotational peaks for a number of vibrational levels. Since no rotational lines were observed with $J' > 4$, it was only necessary to include partial waves up to l=2 in the analysis ($\vec{J} = \vec{l} + \vec{L} + \vec{S}$, L=1, S=1). Neglecting the magnetic dipole interaction, the Hamiltonian for collisions among f_a=1 atoms can be separated into five pieces (see Table 5.1). These include f=0,2 s-wave and d-wave components, and an $f = 1$ p-wave component. The analysis required thermal averaged radial wave functions for each Hamiltonian. However, the nonzero radial overlap of the ground state wave function and the 0^-_g excited state wave function occurs at $R > 40$ a.u.. Therefore, the MQDT method outlined in Chapter 4 provides an extremely efficient method for generating these wave functions. A single $\underline{K}^{\rm sr}$ matrix calculated at $E = 0$ for each Hamiltonian (which are functions of the singlet and triplet scattering length and the C_6 coefficient) proved sufficient to obtain accurate radial overlaps over the entire energy range E = 0-3 mK required for the thermal average. A comparison of the integrated radial overlaps using MQDT-generated ground state wave functions and FEM R-

matrix generated wave functions is shown in Fig. 6.3.

6.4 Dipole matrix element

The molecular dipole matrix element needed to evaluate the rate constant K_p (Eq. 6.5) is constructed in this section. This derivation provides "nuts and bolts" intermediate steps. The reader more interested in the photoassociation analysis can skip ahead to the next chapter without loss of continuity. The approach detailed here is to first evaluate the molecular dipole matrix in a Hund's case (a) molecular representation and then to project the ground state molecular wave function onto coupled hyperfine states.

The excited $\Psi'_{\rm mol}$ and ground state $\Psi_{\rm mol}$ molecular wave functions are assumed to have the form given in Eq. 6.18. The radial piece of the wave function will be neglected in the intermediate steps since it has no bearing on the angular momentum algebra. The electronic orbital angular momentum ϕ piece of the factored wave function can be constructed from Eq. 6.11. The excited state orbital is given by:

$$\begin{aligned}\phi(\Lambda', w') &= \frac{1}{2}\Big\{[S^a(\vec{r_1})P^b(\vec{r_2})]_{\Lambda'} + (-1)^{S'}[S^a(\vec{r_2})P^b(\vec{r_1})]_{\Lambda'} + \\ &\quad (-1)^{w'+1}[S^b(\vec{r_1})P^a(\vec{r_2})]_{\Lambda'} + (-1)^{S'+w'+1}[S^b(\vec{r_2})P^a(\vec{r_1})]_{\Lambda'}\Big\}\ ,\end{aligned} \tag{6.27}$$

and the ground state orbital is given by the expression:

$$\phi(0, w = S) = \frac{1}{\sqrt{2}}\left\{[S^a(\vec{r_1})S^b(\vec{r_2})] + (-1)^S[S^a(\vec{r_2})S^b(\vec{r_1})]\right\}\ . \tag{6.28}$$

Here, the orbitals are designated by the L_i quantum numbers, i.e. S^a represents an atomic S-orbital on atom a. Primed and unprimed quantities are used to denote excited state and ground state quantum numbers, respectively. The molecular dipole operator $d(\vec{R})$ is approximated as the sum of two atomic dipole operators, which can be rotated into the body-fixed frame as follows:

$$d(\vec{R}) = \sum_q D^{1*}_{mq}\left[d_q(\vec{r_1}) + d_q(\vec{r_2})\right]\ . \tag{6.29}$$

Here, $d_q(\vec{r_i})$ is an atomic dipole operator that acts only on electron i. This ensures that only one electron absorbs a photon at a time. The quantum numbers q and m refer to the projection of the dipole operator onto the body-fixed and space-fixed frames, respectively. The dipole matrix element for an $S \rightarrow P$ transition in the

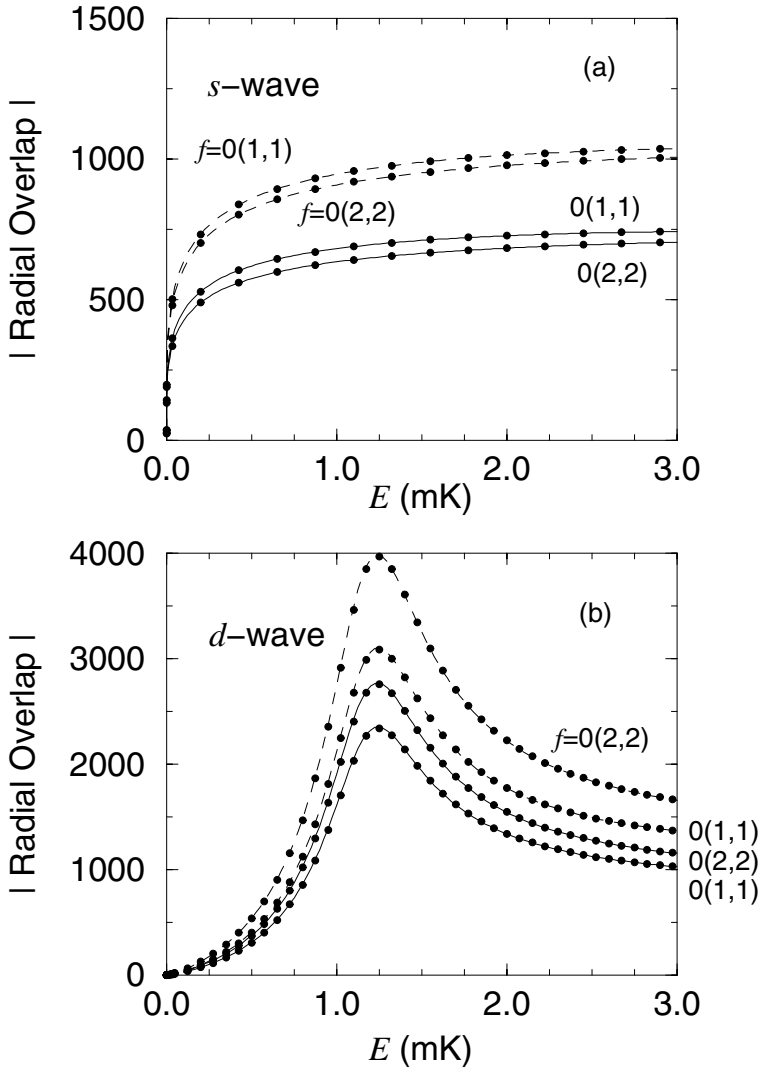

Figure 6.3: ^{39}K Franck-Condon overlaps of the v'=0, J'=2, 0_g^- rovibrational level with a f = 0 s-wave state (a) and a f = 0 d-wave state (b) are compared using two different methods to calculate the ground state wave functions. These were: 1) MQDT approach (Eq. 4.35) using a constant $\underline{K}^{\rm sr}$ calculated at E=0, denoted by the solid and dashed lines and a 2) FEM $\underline{\rm R}$-matrix approach. The FEM $\underline{\rm R}$-matrix calculations are denoted by the closed circles. Each graph shows the absolute value of the four components that comprise the total overlap. Each component depends on the f_a, f_b ground state quantum numbers and the excited state Λ' quantum number. The $f(f_a, f_b)$ quantum numbers are labeled on the graph. A solid line represents the $\Lambda' = 0$ state, and a dashed line is used for the $\Lambda' = 1$ state. The presence of a f = 0 d-wave shape resonance near 1.2 mK is evident from the radial overlaps in (b).

Hund's case (a) representation is given by the following expression:

$$\begin{aligned}
\langle \Psi'_{\rm mol}|d(\vec{R})|\Psi_{\rm mol}\rangle &= \delta_{I',I}\delta_{M'_I,M_I}\delta_{S',S}\delta_{\Sigma',\Sigma}\sqrt{\frac{1}{(2-\delta_{\Lambda',0}\delta_{\Sigma',0})(2-\delta_{\Sigma,0})}}\times \\
&\left(\frac{1+(-1)^{p'+I'+w'}}{2}\right)\left(\frac{1+(-1)^{p+I+w}}{2}\right)\times \\
&\sqrt{\frac{(2J'+1)(2J+1)}{16\pi^2}}\times \\
&\sum_q\left[\langle\phi(\Lambda',w')|d(\vec{R})|\phi(0,w)\rangle\int d\Omega D^{J'}_{M'_J\Omega'}D^{1\,*}_{mq}D^{J}_{M_J\Omega}\right. \\
&+(-1)^{p'+p+J'+J}(1-\delta_{\Lambda',0}\delta_{\Sigma',0})(1-\delta_{\Sigma,0})\times \\
&\left.\langle\phi(-\Lambda',w')|d(\vec{R})|\phi(0,w)\rangle\int d\Omega D^{J'}_{M'_J-\Omega'}D^{1\,*}_{mq}D^{J}_{M_J-\Omega}\right]
\end{aligned} \tag{6.30}$$

First, the electronic dipole piece of this expression is evaluated:

$$\langle\phi(\Lambda',w')|d(\vec{R})|\phi(0,w)\rangle = \frac{d\,\delta_{\Lambda',q}}{\sqrt{2}}\left[1+(-1)^{S+1+w'}\right]. \tag{6.31}$$

Evaluating the second dipole term in Eq. 6.30 leads to the same result after replacing $\delta_{\Lambda',q}\rightarrow\delta_{-\Lambda',q}$. The constant d represents the atomic dipole matrix element. Next, the integrals over the rotational functions are evaluated:

$$\begin{aligned}
&\sqrt{\frac{(2J'+1)(2J+1)}{16\pi^2}}\int d\Omega D^{J'}_{M'_J\Omega'}D^{1\,*}_{mq}D^{J}_{M_J\Omega} = \\
&\sqrt{\frac{(2J+1)}{(2J'+1)}}\langle JM_J,1m|J'M'_J\rangle\langle J\Omega,1q|J'\Omega'\rangle
\end{aligned} \tag{6.32}$$

The same result is obtained for the second integral in Eq. 6.30 except $\Omega\rightarrow-\Omega$ and $\Omega'\rightarrow-\Omega'$. The final expression for the Hund's case (a) dipole matrix element is

given by:

$$\begin{aligned}\langle \Psi'_{\rm mol}|d(\vec{R})|\Psi_{\rm mol}\rangle &= \frac{d}{\sqrt{2}}\,\delta_{I',I}\delta_{M'_I,M_I}\delta_{S',S}\delta_{\Sigma',\Sigma}\left(\frac{1+(-1)^{p'+I'+w'}}{2}\right)\times \\ &\left(\frac{1+(-1)^{p+I+w}}{2}\right)\left(1+(-1)^{S+1+w'}\right)\times \\ &\left[1+(-1)^{p'+p+1}(1-\delta_{\Lambda',0}\delta_{\Sigma',0})(1-\delta_{\Sigma,0})\right]\times \\ &\sqrt{\frac{1}{(2-\delta_{\Lambda',0}\delta_{\Sigma',0})(2-\delta_{\Sigma,0})}}\sqrt{\frac{(2J+1)}{(2J'+1)}}\times \\ &\langle JM_J,1m|J'M'_J\rangle\langle J\Omega,1\Lambda'|J'\Omega'\rangle\,. \end{aligned} \tag{6.33}$$

The first two factors in parentheses enforce the nuclear permutation symmetry rules for the excited state and ground state, respectively. The third factor in parentheses guarantees the g↔u dipole selection rule is obeyed. This can be seen from the $(-1)^{S+1+w'}$ phase factor and recalling that $(-1)^S$ determines the ground state g/u symmetry. The fourth factor in parentheses ensures that only terms of opposite parity are coupled. The first Clebsch-Gordan coefficient guarantees that the dipole selection rules $m + M_J = M'_J$ and $J' = J, J \pm 1$ (excluding $J' = J = 0$ transitions) are satisfied.

Next, the transformation from the Hund's case (a) basis into the coupled hyperfine representation is needed for the ground state wave function. Each component (f_a, f_b) of the multichannel wave function in the coupled hyperfine representation has the form

$$\begin{aligned}\Psi_{\rm hf} &= \left(\frac{1+(-1)^{f+l}}{2}\right)\frac{1}{\sqrt{2-\delta_{f_a,f_b}}}\,F^E_{(f_bf_a)fl}(R)\times \\ &\left[|(f_af_b)fm_f,lm_l\rangle+(-1)^{f+l-f_a-f_b}(1-\delta_{f_a,f_b})|(f_bf_a)fm_f,lm_l\rangle\right]\,,\end{aligned} \tag{6.34}$$

where $F^E_{(f_bf_a)fl}(R)$ represents a component of the energy-normalized radial wave function. The transformation matrix element that connects the ground state molecular wave function $\Psi_{\rm mol}(J, M_J, \Omega, S, \Sigma, I, M_I, p, w)$ with the ground state coupled

hyperfine wave function $\Psi_{\rm hf}((f_a f_b) f m_f, l m_l)$ is given by:

$$\begin{aligned}\langle \Psi_{\rm mol} | \Psi_{\rm hf} \rangle &= \sqrt{\frac{(2f_a+1)(2f_b+1)(2S+1)(2I+1)(2l+1)}{(2J+1)(2-\delta_{\Sigma,0})(2-\delta_{f_a,f_b})}} \times \\ &\left[1 + (1-\delta_{\Sigma,0}) + (-1)^{l+S+I}(1-\delta_{f_a,f_b}) \right. \\ &\left. + (-1)^{l+S+I}(1-\delta_{\Sigma,0})(1-\delta_{f_a,f_b})\right] \langle S\Sigma, l0 | J\Omega \rangle \times \\ &\begin{pmatrix} s_a & i_a & f_a \\ s_b & i_b & f_b \\ S & I & f \end{pmatrix} \sum_{M_S} \langle S M_S, I M_I | f m_f \rangle \langle S M_S, l m_l | J M_J \rangle \ .\end{aligned} \tag{6.35}$$

The final result for the dipole matrix element that couples the excited state wave function $\Psi'_{\rm mol}(J', M'_J, \Omega', \Lambda', S'\Sigma', p', w')$ with the ground state hyper-

fine wave function $\Psi_{\rm hf}$ is obtained from equations 6.33 and 6.35:

$$\begin{aligned}
\langle \Psi'_{\rm mol}|d(\vec{R})|\Psi_{\rm hf}\rangle &= \sum_{J,M_J,\Omega,S,\Sigma} \langle \Psi'_{\rm mol}|d(\vec{R})|\Psi_{\rm mol}\rangle\langle\Psi_{\rm mol}|\Psi_{\rm hf}\rangle \qquad (6.36)\\
&= \frac{d}{\sqrt{2}}\sum_J \left(\frac{1+(-1)^{p'+I'+w'}}{2}\right)\left(\frac{1+(-1)^{l+I'+S'}}{2}\right)\\
&\quad \left(\frac{1+(-1)^{f+l}}{2}\right)\left(1+(-1)^{S'+w'+1}\right)\times\\
&\quad \Big[1+(-1)^{J'+p'+J+l}(1-\delta_{\Lambda',0}\delta_{\Sigma',0})(1-\delta_{\Sigma',0})\Big]\times\\
&\quad \Big[1+(1-\delta_{\Sigma',0})+(-1)^{l+S'+I'}(1-\delta_{f_a,f_b})\\
&\quad +(-1)^{l+S'+I'}(1-\delta_{\Sigma',0})(1-\delta_{f_a,f_b})\Big]\times\\
&\quad \langle J\, M'_J-m,1m|J'M'_J\rangle\langle J\,\Omega'-\Lambda',1\Lambda'|J'\Omega'\rangle\times\\
&\quad \langle S'\,M_f-M'_I,I'M'_I|fm_f\rangle\langle S'\,M_f-M'_I,l M_l|J\,M'_J-m\rangle\times\\
&\quad \begin{pmatrix} s_a & i_a & f_a\\ s_b & i_b & f_b\\ S & I & f\end{pmatrix}\langle S'\Sigma',l0|J\,\Omega'-\Lambda'\rangle\times\\
&\quad \int dR\, b_{J'\Lambda'}(R)\chi_{J'}(R)F^E_{(f_af_b)fl}(R)\,.
\end{aligned}$$

Here, the excited state radial wave function has been written in terms of an adiabatic eigenvector, $F'_{J',\Lambda'}(R) = b_{J',\Lambda'}(R)\chi_{J'}(R)$ (see Eq. 6.26). The complete mod-squared dipole matrix element that is needed for the rate constant equation (Eq. 6.5) is given by a coherent sum of the dipole matrix elements in Eq. 6.36 over the internal quantum numbers of the excited and ground state wave functions, an incoherent average over all initial states, and an incoherent sum over all unresolved final states. For the particular experiment presented in Chapter 7, this expression is:

$$\begin{aligned}
\sum_{\beta'p'flp\alpha} n_f(2l+1)|\langle\Psi^{v'J'}_{p'\beta'}(R)|d^{J'p'\beta'}_{flp\alpha}(R)|\Psi^E_{flp\alpha}(R)\rangle|^2 &= \qquad (6.37)\\
\frac{1}{N_{\{f_a,f_b\}}}\sum_{M'_J,I',M'_I}\sum_{f,M_f,l,M_l}\left|\sum_{\Lambda',f_a,f_b}\langle\Psi'_{\rm mol}|d(\vec{R})|\Psi_{\rm hf}\rangle\right|^2 &\quad .
\end{aligned}$$

As a final test of this formulation, we have checked that all dipole selection rules are obeyed and that the lifetime of each rotational level (J', M'_J) of the 0^-_g state is equal to one half the atomic lifetime[128]. In addition, to ensure that all pieces of the theory were integrated properly, we have reproduced the Na 0^-_g spectra illustrated in Ref.[136].

Chapter 7

Determination of potassium scattering lengths

The theory of photoassociation (PA) lineshapes developed in Chapter 6 is herein applied to analyze measured ^{39}K 0_g^- rovibrational spectra. In particular, synthetic spectra are generated that reproduce most features of the experimental spectra. Requiring that the theoretical relative intensities and rotational linewidths agree with the experimentally measured counterparts, within experimental uncertainties, allowed us to place limits on the singlet and triplet s-wave scattering lengths. These results were first reported in Ref.[147]. Previous estimates of the K scattering lengths had in fact already appeared in the literature[148, 149]. However, the older works were based on conventional molecular spectroscopy. These data alone proved insufficient to reliably extrapolate the potentials to the dissociation threshold. The analysis presented here, which makes use of both the conventional spectroscopic data as well as the new photoassociation data, should therefore provide a more reliable prediction for the scattering lengths. In addition, an independent analysis[150] of the ^{39}K 1_u spectra confirms many of the results presented here. This chapter is broken into two sections. First, an overview of the experiment is provided in Section 7.1. The analysis of the spectra and the resulting bounds on scattering lengths are presented in Section 7.2.

7.1 Photoassociation experiment

The experiment discussed here was conducted by H. Wang, P. L. Gould, and W. C. Stwalley at the University of Connecticut. They have published complete details of the experimental setup in Ref.[144, 146]. This section provides a brief description of those experimental details that are necessary to understand the analysis presented in Section 7.2. In particular, the experimental checks taken to ensure the quality of the data are emphasized.

A sample of 10^7 ^{39}K atoms, at a density greater than 10^{11} cm^{-3} and a temperature of $\sim 400\mu$K, are prepared in a "dark spot" vapor cell magneto-optical trap (MOT). The atoms are trapped predominately in their f_a = 1 hyperfine state (for ^{39}K, $i_a = 3/2$). Separate single-mode tunable ring Ti:sapphire lasers provide the trapping beams and induce the PA transitions. The total output power of the

trapping laser is $\sim$ 300 mW at 766.5 nm while the PA laser intensity is typically 50 mW/cm^2. The analysis presented in Section 7.2 concentrates on the v' =0-6 vibrational levels of the 0_g^- state. For these low lying states, trap loss spectra are not easily observed because the local kinetic energy is not large enough to allow atoms to escape from the trap when the excited vibrational state decays through bound-free spontaneous emission of a photon. The PA resonances can then be detected by recording ion production following a double-resonance transition from the 0_g^- rovibrational state to an autoionizing 1_u state at an energy below the highly excited $4S+nD$ (n = 5 or 6) asymptote[151]. In particular, a tunable ring dye laser provides the second photon, at frequency ν_2 and typical intensity 12 W/cm^2, for the double-resonance process and a channeltron multiplier records the subsequent production of ions. A schematic of the transition steps is provided in Fig. 7.1.

Unfortunately, there is essentially no information on the excited state potentials $4S + nD$, which prevents us from applying the two-color theory presented in Ref.[134, 135]. It was therefore necessary to ascertain the influence of the second laser on the PA spectrum of the 0_g^- state experimentally. These tests included recording spectra using final autoionizing states below both the $4S+5D$ and $4S+6D$ asymptotes. Representative examples of these spectra are shown in Fig. 7.2. The autoionizing final states are structureless and broad[151] with widths ranging from $\sim$ 1 GHz for levels near the 4S+5D threshold to $\sim$ 2 GHz for levels near the 4S+6D asymptote. General trends in the PA spectra of the 0_g^- state, such as weak or missing odd J' rotational levels, anomalous $J' = 2$ linewidths, and large $J' = 4$ relative intensities were consistent in both cases. The only noticeable differences occur in the $J' = 4$ relative intensity which was typically a factor of 1.5-2 bigger in the spectra observed using final states below the 4S + 6D threshold. This difference can apparently be attributed to slightly hotter atoms in the MOT for the $4S + 6D$ experiment (based on linewidths), and to the broader final state that experiment.

PA spectra of the 0_g^- state were measured by fixing the second laser frequency ν_2 to a $0_g^-(v'J' = 2) \rightarrow 1_u(v)$ transition near the 4S+nD asymptote, then scanning the PA laser frequency (ν_1). Altering this setup so that ν_2 was tuned from J' = 0 or J' = 4 to the final autoionizing state again produced no qualitative changes in the measured 0_g^- spectra. The only quantitative difference again appeared in the $J' = 4$ relative intensities. These were roughly a factor of 1.5 larger when the second laser was tuned from $J' = 4$ instead of $J' = 0$ or 2 (see Fig. 7.3). Changing the power of laser ν_2 only affected the total ion production rate. In addition, the experimentalists varied the PA laser intensity by a factor of two and observed no noticeable power broadening. Based on this near independence of the spectra on the second laser, we attribute the bulk of the relative peak intensities to the first transition. The single color theory presented in Chapter 6 should therefore provide a good approximation to the measured lineshapes.

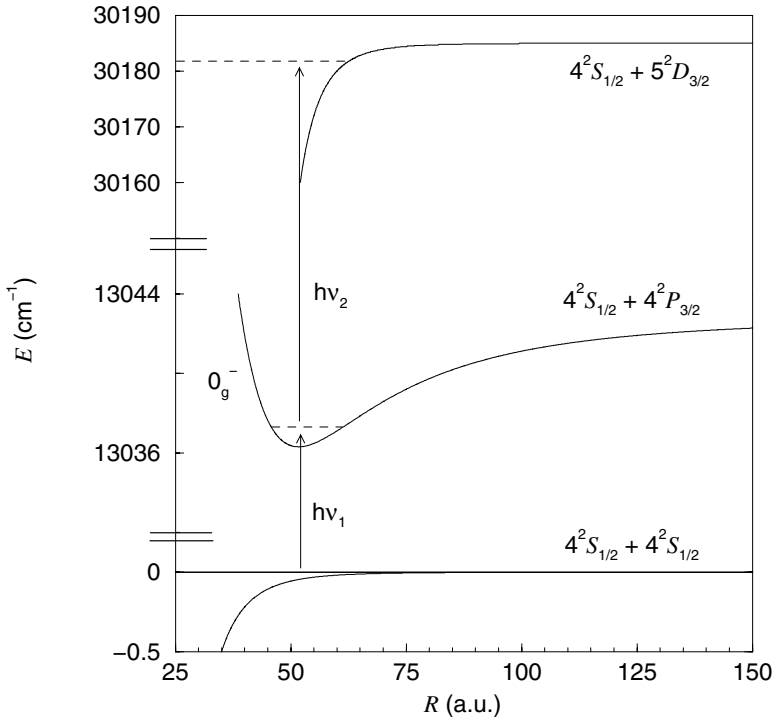

Figure 7.1: Schematic of the ^{39}K photoassociation transition sequence. Ground state atoms are first excited (hν_1) to a rovibrational level of the 0_g^- electronic state. The free-bound transition is detected by exciting the molecule at frequency ν_2 to an autoionizing state below either the $4S + 5D$ or $4S + 6D$ threshold and then measuring the resulting production of ions.

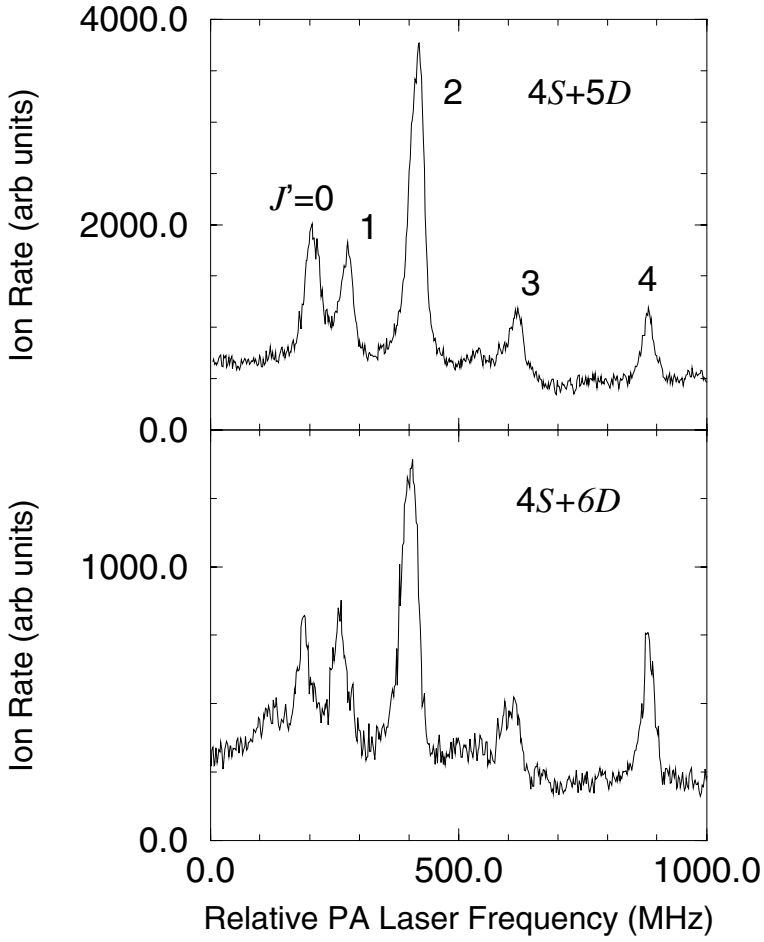

Figure 7.2: Representative examples of the 0_g^- v'=0 spectra obtained using autoionizing final states below the $4S + 5D$ and the $4S + 6D$ thresholds. The rotational assignment J' for each peak is indicated in the top graph.

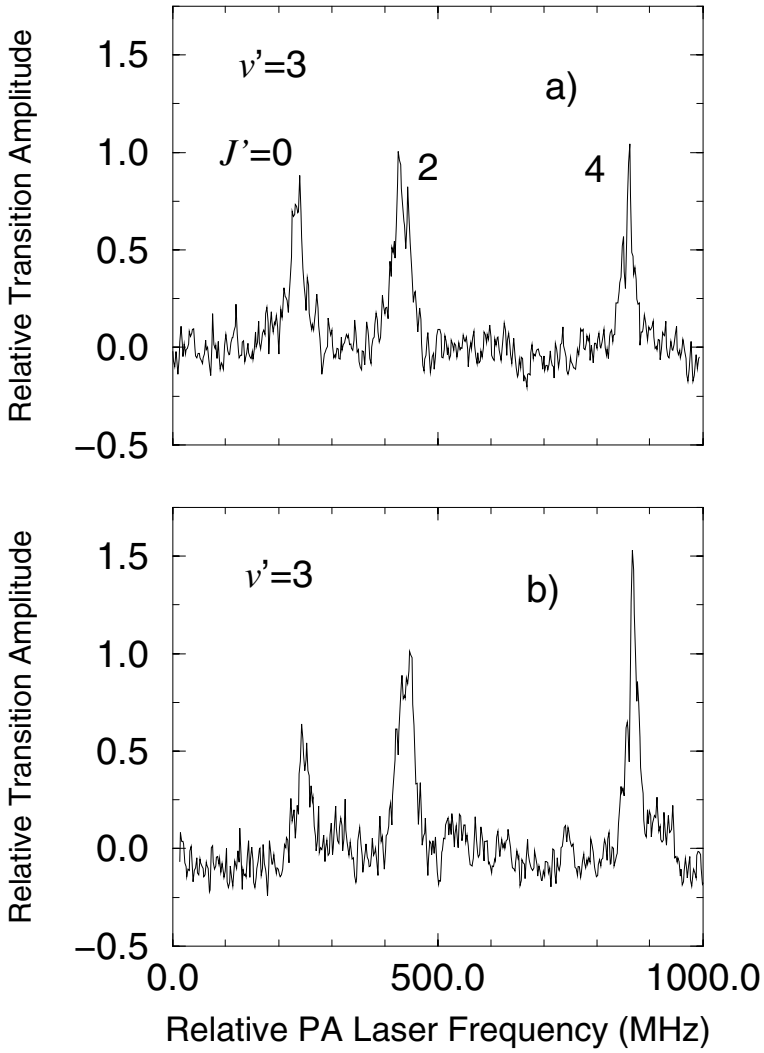

Figure 7.3: Representative examples of the 0_g^- v'=3 spectra obtained for different values of ν_2. The peaks correspond to the J' = 0, 2, 4 rotational levels, respectively.
a) ν_2 fixed to a $0_g^-(J'=2) \rightarrow 1u(v)$ transition near the $4S + 6D$ asymptote.
b) ν_2 fixed to a $0_g^-(J'=4) \rightarrow 1u(v)$ transition near the $4S + 6D$ asymptote.

7.2 Analysis

The analysis of the 0_g^- spectra is simplified somewhat by its symmetry rules. These were discussed briefly in Section 6.2 and are elaborated on here. The parity of a 0_g^- rotational wave function is $(-1)^{J'+1}$, while the ground state wave function parity is simply $(-1)^l$. Therefore, dipole selection rules restrict transitions from ground state collisions in even partial waves l to even rotational levels J' and likewise odd partial waves to odd J''s. More specifically, s-wave collisions contribute to J' = 0,2; d-wave collisions contribute to J' = 0,2,4; and p-wave collisions contribute only to J' = 1,3. In addition the 0_g^- electronic state for like atoms has a nuclear permutation symmetry which requires $(-1)^{J'+I'}$ to be odd.

The measured spectra show several distinct trends. First, the p-wave features are extremely weak or missing from all vibrational scans except v' = 0 and 2. Second, the relative intensity of the J' = 4 (pure d-wave) peak is found to be quite large in all the scans. This is surprising since the height of the ^{39}K d-wave centrifugal barrier is roughly 1.5 mK and at cloud temperatures around 400 μK one would expect, in the absence of resonances, the d-wave features to be suppressed by the Wigner threshold law. Finally, the J' = 2 linewidths are quite large $\sim$ 35 MHz compared to the other rotational lines $\sim$ 25 MHz. The analysis of the measured data will focus on these particular features.

Suppressed p-wave features were also observed[136] in the Na 0_g^- spectra. However, in sodium the Franck-Condon overlap was controlled essentially by a node in the open channel wave function. In potassium, the closed channel wave functions can contribute substantially to the transition, as can be seen from Fig. 7.4. The Franck-Condon contribution from each channel must be added coherently (Eq. 6.37), which can contribute to the suppressed p-wave features. The outer turning points of the closed channel potentials occur at roughly the same internuclear separation as the inner turning point of the excited state potential. This means that the closed channels, which are on their last half cycle at the Condon point, can have a large effect on the radial overlap integral. Moreover, the shapes of the closed channel wave functions near the Condon point are essentially "fixed" in R, as they must begin their exponential decay. Varying the singlet and triplet scattering lengths thus only affects the relative amplitudes in the channels. For example, the amplitudes will be quite small when $a_s \sim a_t$ just as ^{87}Rb spin exchange inelastic rates[100] are suppressed by this criterion. It is therefore not obvious (or unique) where the open channel node needs to be placed in order to reproduce the observed suppression of the p-wave features.

This complication prompted us to perform a complete search of singlet-triplet scattering length space to ensure that our final fits to the spectra provided a unique set of parameters. The ground state potentials were systematically varied (Eq. 2.45) such that the singlet a_s and triplet a_t scattering lengths ranged between $\pm\infty$. This search was also conducted for a number of different C_6 coefficients rang-

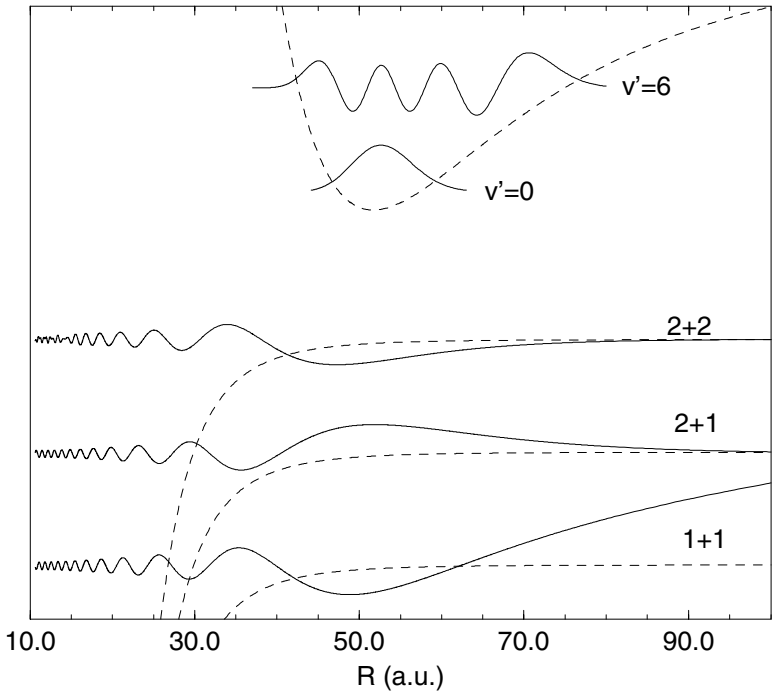

Figure 7.4: Schematic of the ground and excited state potentials (dashed lines) and wave functions (solid lines). The ground state thresholds are labeled by their $f_a + f_b$ quantum numbers. The ground state wave functions are computed at zero energy. The excited state wave functions correspond to the lowest and highest vibrational levels ($v' = 0$ and 6, respectively) used in the analysis. Notice that the closed channel components of the ground state wave function can contribute significantly to the Franck-Condon overlap with the excited state wave function. The potentials are not shown to scale.

ing from 3600-4000 a.u., to allow for the stated $\pm 5\%$ uncertainty given in Ref.[38]. Ground state wave functions for each set (a_s, a_t,C_6) of potentials were generated using the MQDT method outlined in Section 4.2 (see also Section 6.3.2 for a discussion of the ground state wave functions needed for this analysis). For each set of potentials, a thermally averaged synthetic rotational J'=0-4 series was generated for vibrational levels v'=0-6 (equations 6.5 and 6.37). A "match" to the measured data required that the theoretical relative intensities and linewidths of a rotational progression within a given v' agree within experimental bounds simultaneously for each vibrational level v'=0-6. A constant cloud temperature, estimated to be 400 $\pm$ 100 μK from fits to the measured spectra, was assumed for each vibrational level. Absolute intensities are quite uncertain, therefore each vibrational spectrum was normalized to $K_p^{\max}(J'=2) = 1$. In addition, the absolute PA laser frequency ν_1 was adjusted such that the blue edge of the synthetic and measured J'=2 lines are aligned for each vibrational spectrum. The absolute intensity and absolute frequency are the only two adjustable fit parameters incorporated into the theory.

The data obtained from the $4S + 6D$ autoionizing final state was used exclusively in this analysis. The uncertainties associated with the second laser were better characterized for this data and therefore more precise bounds could be placed on the scattering lengths. A comparison of spectra calculated with our "nominal" set of potentials is shown in Fig. 7.5. The J'=4 relative intensity is the main discrepancy between experiment and theory. This can be attributed to optimizing the double resonance experiment using the J'=2 intermediate level which then under represents the J'=4 intensities (see Fig. 7.3). The final values for the singlet and triplet scattering lengths, as well as quantum defects, are given in Table 7.1. The table also translates these results into scattering lengths for other K isotopes. In addition, a table of K atomic parameters is provided (Table 7.2).

In the following discussion, the contribution of each spectral feature to the final limits placed on either the singlet or triplet scattering length is slightly artificial. Bear in mind that it is only through the combination of these features that unique limits on a_s and a_t are obtained. The large $J' = 2$ linewidths are a particularly interesting feature. We find that these linewidths are a result of a broad f=0 d-wave shape resonance, at an energy $E_R = 1.15 \pm 0.35$ mK with a width Δ = 0.5 $\pm$ 0.2 mK (the time-delay definition of position and width has been used here, see Eq. 5.5). The $J' = 2$ spectral width provides a fairly sensitive probe of the position of the shape resonance. Figure 7.6 shows the effect on the $J' = 2$ linewidth as the position of the shape resonance is varied. Recall that atoms scattering in both s and d partial waves contribute to the intensity of the $J' = 2$ rotational level. Moving E_R to larger energies shifts the d-wave contribution to the red of the s-wave contribution, thereby increasing the overall width. However, if E_R becomes too large relative to the cloud temperature, the thermal averaging suppresses the d-wave intensity contribution effectively reducing the linewidth. Similarly, if E_R is moved to smaller energies not only is the red shift reduced but the d-wave contribution

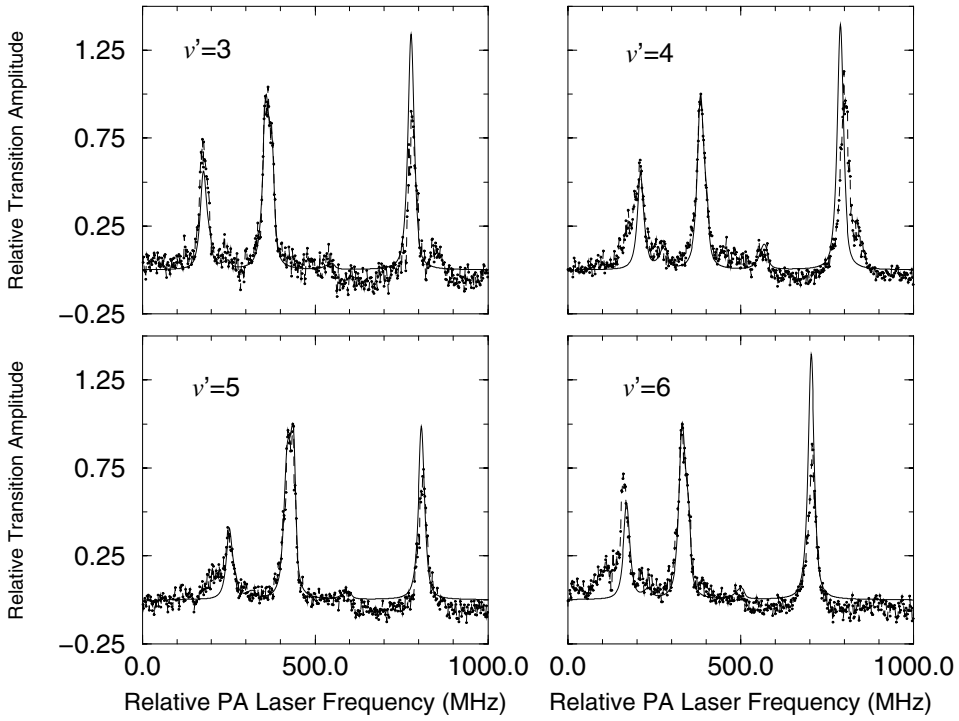

Figure 7.5: Comparison of experimental (dashed line) and theoretical (solid line) spectra. The synthetic spectra were calculated using our nominal set of potentials, a_s = 140 a.u., a_t = -17 a.u. and C_6=3800 a.u., assuming a cloud temperature of 400 μK. The prominent peaks in each vibrational spectra are the rotational levels J' = 0, 2, 4, reading from left to right. It is believed that the red wing of the J' = 0 experimental peaks correspond to additional flux obtained from f_a=1 + f_b=2 collisions. These collisions were not theoretically modeled since they contribute little to the spectrum.

Table 7.1: Singlet and triplet scattering lengths a (in a.u.) and quantum defects μ (dimensionless) for collisions among different pairs of potassium isotopes assuming a constant $\bar{\mathrm{C}}_6$=3800 a.u. The scattering length is related to the quantum defect by: $a = -C^2 \tan(\pi\mu)/(1 + \mathcal{G}(0)\tan(\pi\mu))$ where $C^2 = 0.95775(2m\mathrm{C}_6)^{1/4}$, m is the reduced mass of the atom-pair and $\mathcal{G}(0)$ = -1.0037. The singlet quantum defect uncertainties are $^{+0.019}_{-0.011}$ for each collision pair, independent of the C_6 value. Finally, the uncertainties associated with each triplet quantum defect and its variation with C_6 is given by: $\mu_t = \bar{\mu}_t + 8.0(10^{-5})(\mathrm{C}_6 - \bar{\mathrm{C}}_6)\ ^{+0.04}_{-0.06}$.

Isotopes	a_s	$\bar{\mu}_s$	a_t	$\bar{\mu}_t$
$39+39$	140^{+6}_{-9}	0.460	-17 ± 25	0.039
$40+40$	105^{+3}_{-5}	-0.445	194^{+114}_{-35}	0.388
$41+41$	85 ± 3	-0.366	65^{+13}_{-8}	-0.268
$39+40$	-1^{+4}_{-8}	0.002	$-460^{+330}_{-\infty}$	0.212
$39+41$	113 ± 5	-0.474	205^{+140}_{-40}	0.379
$40+41$	-50^{+9}_{-18}	0.089	104^{+20}_{-11}	-0.441

Table 7.2: Mass in ^{12}C amu, nuclear spin i, nuclear g-factor g_n, and ground-state atomic hyperfine splittings of the K isotopes. A negative value of Δ indicates an "inverted" hyperfine structure.

Isotope	Mass	i	g_n	Δ (MHz)
39	38.963707	3/2	0.39146	461.72
40	39.963999	4	-1.298	-1285.79
41	40.961825	3/2	0.21487	254.01

with its extra (2l+1) phase space factor overwhelms the s-wave contribution, again resulting in a smaller linewidth. The large J' = 4 peaks are also a by-product of this shape resonance and their relative intensities are quite sensitive to the position of the resonance.

These constraints force E_R to lie in the range 1.15$\pm$ 0.35 mK, which creates an "allowed" strip in Fig. 7.7. In particular, the position of the resonance depends sensitively on the singlet scattering length and thus imposes tight bounds on this quantity. However, because the resonance is near the top of the centrifugal barrier and therefore quite broad, the spectral linewidths are relatively insensitive to the C_6 value. In fact, we find the bounds on the singlet scattering length are unchanged when C_6 is allowed to vary between 3600-4000 a.u. Allowing a quarter linewidth uncertainty on each J' = 2 peak, places the following bounds on a_s = 140^{+6}_{-9} a.u., which is in good agreement with Ref.[149]. Comparison of the J' = 2 measured linewidths with our "best" fit potentials are shown in Fig. 7.8. Finally, it should be noted that this $f = 0$ d-wave shape resonance manifests itself in other features seen in the 1_u spectra[150]. However, we do not agree on the exact position of the resonance and therefore have different constraints on the singlet scattering length. We believe this discrepancy indicates a limitation of the "naive" PA theory (which was also applied to the 1_u spectra) that disregards the effect of the ionizing laser. This point is discussed in more detail in Ref.[150].

There is, in fact, another bound on E_R. Raising E_R above $\sim$ 1.3 mK introduces an additional $f = 2$ g-wave shape resonance[150]. The existence of a g-wave resonance should manifest itself in the 0^-_g spectrum as an additional J' = 6 peak (as well as contributing to J' = 2 and 4). However, there is no experimental evidence for an additional rotational peak. Also, the presence of a g-wave resonance would be inconsistent with the 1_u spectra[150]. The exclusion of the g-wave resonance thus reduces slightly our allowed parameter space (see Fig. 7.7).

Placing bounds on a_t is more complex. The suppression of the p-wave features ultimately controls the allowed a_t range, but it is only after limiting the available parameter space by considering the d-wave shape resonance that we find an unambiguous result. However, these combination of features require that the wave function nodes are bounded as follows: f=1, p-wave node 68^{+9}_{-6} a.u. and the f=2, s-wave node is 62^{+4}_{-3} a.u. The positions of these nodes in our allowed a_s-a_t parameter space are controlled almost exclusively by the triplet scattering length. Unfortunately the suppression of the p-wave features is fairly robust in this region which is largely responsible for the bigger uncertainty in the triplet scattering length. Variations in C_6 require a corresponding change in the triplet scattering length to preserve the nodal positions. We found changing the value of the C_6 coefficient simply shifted our allowed parameter region along the triplet axis of the a_s-a_t plane while preserving the area. The triplet scattering length is therefore parameterized in the following manner a_t = -17 - 0.045(C_6 - $\bar{C}_6$) $\pm$ 25 a.u., $\bar{C}_6$ = 3800. The two most important scattering lengths for BEC are the triplet scattering length a_t and the

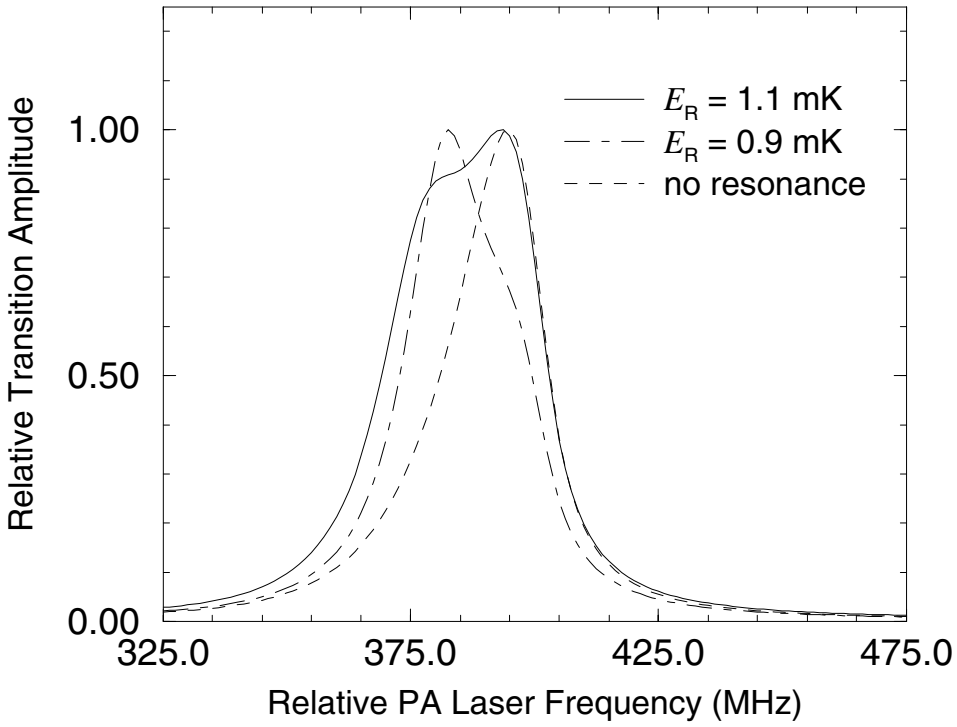

Figure 7.6: Comparison of the J' = 2 linewidths versus the position E_R of the f=0 d-wave shape resonance. The no resonance case indicates the s-wave contribution to the linewidth. The position of the resonance controls the relative d-wave contribution to the peak and the amount it is red-shifted relative to the s-wave contribution.

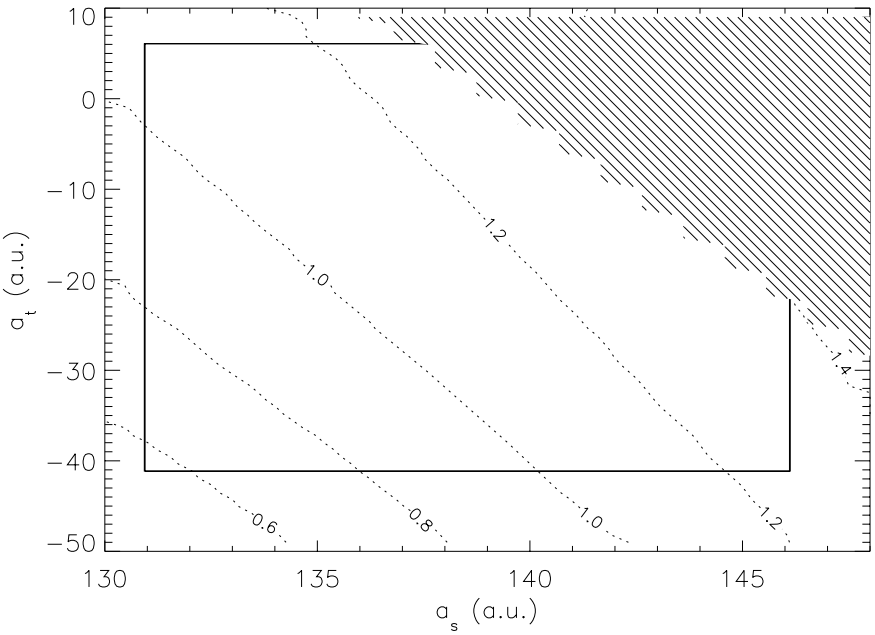

Figure 7.7: The dashed lines indicate the energy position E_R (in mK) of the d-wave shape resonance in the a_s-a_t plane. The solid rectangle represents our allowed individual singlet and triplet parameter ranges (C_6 = 3800 a.u.) including the $\pm$ 100 μK uncertainty in cloud temperature. The hatched region indicates the parameter space excluded by the absence of the f = 2 g-wave shape resonance.

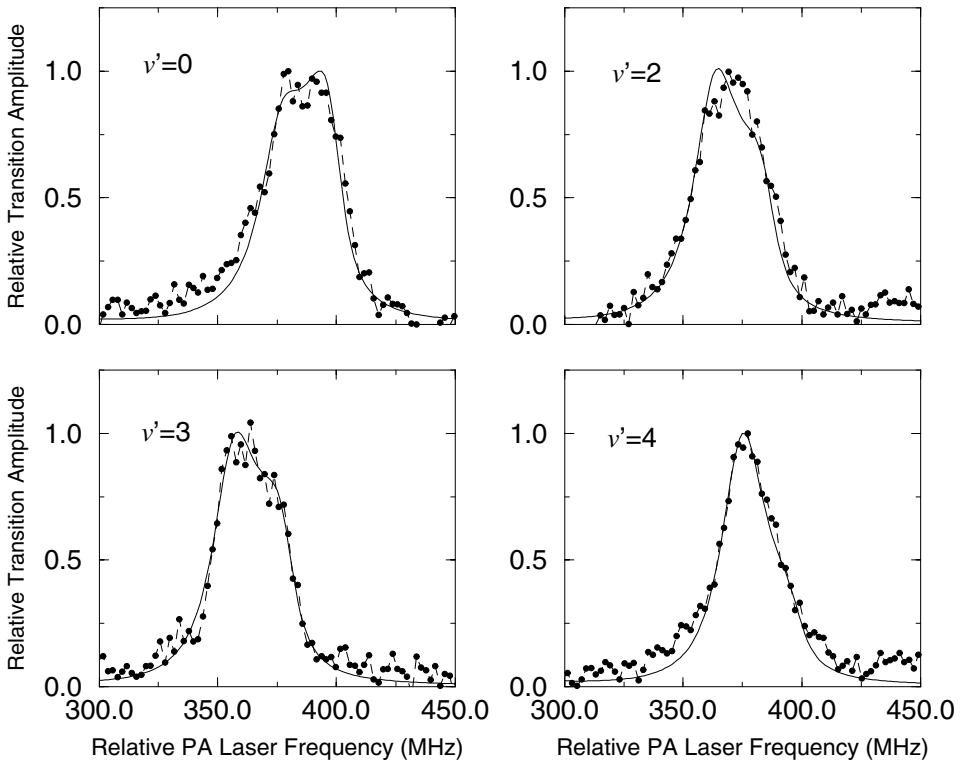

Figure 7.8: Comparison of experimental (closed circles) and theoretical (solid line) $J' = 2$ linewidths. The synthetic spectra was calculated using our nominal set of potentials, a_s = 140 a.u., a_t = -17 a.u. and C_6=3800 a.u., assuming a cloud temperature of 400 μK.

$f = 2$ s-wave scattering length a_{2s}. From our final potentials, we find a_{2s} = -20 - 0.055(C_6 - $\bar{C}_6$) $^{+35}_{-45}$ a.u. Both a_t and a_{2s} are in agreement with the results from the 1_u analysis[150]. In addition, our ^{40}K triplet scattering length is consistent with the value extracted from a recent elastic scattering measurement[119]. Finally, we have used these refined Born-Oppenheimer potentials to survey the threshold scattering properties of a number of K hyperfine-selected states. These considerations were reported in Ref.[152].

Chapter 8

Three-body recombination

As greater densities are attained in ultracold atom experiments, their description in terms of two-body interactions is no longer sufficient. In fact, condensate densities limited by three-body inelastic collisions[153] have been achieved. It is conceivable that, in some regimes, an accurate theoretical treatment of mean-field energetics in a dense condensate will need to account for both two- and three-body elastic collisions. Probably the most dramatic three-body effect measured to date in a cold atom trap is the catastrophic loss of atoms from a Na condensate that was magnetically tuned to a Feshbach resonance[15]. It is believed that this loss was driven by three-body recombination, in which three free atoms coalesce allowing two to form a molecule while the third atom carries away most of the excess binding energy. Qualitatively, one might reason that the probability of three atoms colliding increases near a two-body resonance simply because the effective range of interaction between the atoms, characterized by the two-body scattering length a, becomes quite large. However, the Na experiment measured dramatic recombination rates even near $a \sim 0$, causing losses that severely limited the ability of that experiment to study the condensate near the resonance field value. It is not known whether this effect is unique to the Na atom or if it is instead an inevitable consequence of the three-body recombination physics.

Three-body recombination has been a largely neglected area of theoretical ultracold collision physics. A recent theoretical effort[154] predicted an a^4 scaling for the field-free recombination rate. However, the approximations used in that treatment are valid only in the limit of large positive a. Recombination of spin-polarized hydrogen[155, 156] was studied in the '80's and more recently in other alkali atoms[157], mostly within the confines of the Jastrow approximation. Those treatments based the recombination rates on a perturbative formulation that approximates the initial three-body wave function as a product of two-body wave functions. Using the Jastrow approximation, Moerdijk, **et al.**[157] obtained an a^2 scaling for the recombination rate which is at odds with the scaling proposed in Ref.[154]. In short, the physical processes that control three-body recombination have been poorly understood even at a qualitative level.

In this chapter, our first steps towards understanding the recombination

process are presented. In particular, we develop a quantitative method that can be used to calculate recombination rates that are stable as a function of both hyperradius and three-body continuum channels. Based on calculations using a wide range of two-body model potentials, we have been able to uncover universal systematics of the recombination physics. This work was first reported in Ref.[158]. The chapter is divided into two sections. In Section 8.1 the numerical method is developed. In Section 8.2 the results of our calculations are given and mechanisms for the recombination process are discussed.

8.1 Adiabatic hyperspherical representation

The formulation presented here has its origins in the work of Delves, who showed[159] that the three-body continuum can be represented by a countable set of channels in a hyperspherical representation. Most importantly the scattering matrix $\underline{S}$ is symmetric and unitary in this representation. The hyperspherical coordinate method has been applied successfully to a number of diverse quantum mechanical three-body problems. (A review of these treatments can be found in Ref.[160]). The basic approach involves a coordinate transformation that first separates out the unimportant center-of-mass motion. The remaining six degrees of freedom are represented by three Euler angles and three internal coordinates, the hyperradius R and two hyperangles, θ and ϕ. It is unlikely that a resonance will occur over the range of collision energies available to cold magnetically trapped atoms. The Wigner threshold law leads to $K_3 \propto E^J$ near threshold therefore, it is sufficient to concentrate on collisions with total angular momentum J = 0. In this case the collisions are isotropic and the three-particle dynamics are described by a three-dimensional Schrödinger equation, which can be written in terms of hyperspherical coordinates.

There are numerous conventions for defining the hyperradial coordinates. In the case of identical particle scattering, the Smith and Whitten "democratic" coordinate system[161, 162] is the most useful. The definitions for the hyperangles (θ, ϕ) and hyperradius (R) are best developed in two stages, as shown in Ref.[163]. After separating out the center-of-mass motion, the remaining internal degrees of freedom are defined in terms of Jacobi coordinates $(\vec{\rho}_1, \vec{\rho}_2)$. The relationship between the Jacobi coordinates and the space-fixed atom coordinates $\vec{r}_i$ is given by[163]

$$\begin{aligned} \vec{\rho}_1 &= (\vec{r}_2 - \vec{r}_1)/d \\ \vec{\rho}_1 &= d\left[\vec{r}_3 - \frac{(m_1\vec{r}_1 + m_2\vec{r}_2)}{(m_1 + m_2)}\right] \end{aligned} \tag{8.1}$$

where m_i represents the atomic mass of atom i and the mass-weighting factor d is

given by

$$\begin{aligned} d^2 &= \frac{(m_3/\mu)(m_1+m_2)}{m_1+m_2+m_3} \\ \mu^2 &= \frac{m_1 m_2 m_3}{m_1+m_2+m_3}\,. \end{aligned} \tag{8.2}$$

The hyperradius and hyperangles are defined in terms of the Jacobi coordinates as follows[161]:

$$R^2 = \rho_1^2 + \rho_2^2 \tag{8.3}$$

and

$$\begin{aligned} (\rho_1)_{x'} &= R\cos\theta\cos\phi \quad , \quad (\rho_1)_{y'} = -R\sin\theta\sin\phi \\ (\rho_2)_{x'} &= R\cos\theta\sin\phi \quad , \quad (\rho_2)_{y'} = R\sin\theta\cos\phi\,. \end{aligned} \tag{8.4}$$

Here, (x', y') are Cartesian coordinates referred to the principal axes of the body-fixed system. Qualitatively, the hyperradius is a measure of the size of the three-body system. With these definitions, the hyperspherical coordinates have convenient symmetry properties that simplify the application of boundary conditions for identical particle scattering. In fact, for identical particle scattering it is only necessary to define the hyperangles over the range $0 \le \theta \le \pi/4$ and $0 \le \phi \le \pi/6$.

In general, the three-body interaction $V(R,\theta,\phi)$ can be approximated accurately by a sum of two-body interactions $v(r_{12}) + v(r_{23}) + v(r_{31})$. The first correction to this expression, the Axilrod-Teller term[32], has an R^{-9} dependence and should be unimportant for our problem. The three-body potentials used in this work are discussed in more detail in the next section. The two-body internuclear radii r_{ij} are defined in terms of the hyperradial coordinates by[163]

$$\begin{aligned} r_{12} &= 3^{-1/4} R[1+\cos(2\theta)\cos(2\phi)] \\ r_{23} &= 3^{-1/4} R[1+\cos(2\theta)\cos(2\phi+2\pi/3)] \\ r_{31} &= 3^{-1/4} R[1+\cos(2\theta)\cos(2\phi-2\pi/3)]\,. \end{aligned} \tag{8.5}$$

The Schrödinger equation that describes the three particle dynamics is given in the hyperspherical representation by the following expression[163]:

$$\left\{ \frac{-\hbar^2}{2\mu}\left[\frac{1}{R^5}\frac{\partial}{\partial R}R^5\frac{\partial}{\partial R} - \frac{\Lambda^2(\theta,\phi)}{R^2}\right] + V(R,\theta,\phi)\right\}\Psi = E\Psi\,. \tag{8.6}$$

The first derivative operator can be removed from this expression by introducing a

rescaled wave function $\psi = R^{5/2}\Psi$. The Schrödinger equation for ψ is then

$$\left\{ \frac{-\hbar^2}{2\mu} \left[\frac{\partial^2}{\partial R^2} - \frac{\Lambda^2 + 15/4}{R^2} \right] + V(R,\theta,\phi) \right\} \psi \;\; = \;\; E\psi \; . \tag{8.7}$$

Here, the grand angular momentum operator Λ^2 is given by the following expression:

$$\Lambda^2 \;\; = \;\; \frac{-1}{\sin 4\theta} \frac{\partial}{\partial \theta} \sin 4\theta \frac{\partial}{\partial \theta} - \frac{1}{\cos^2 2\theta} \frac{\partial^2}{\partial \phi^2} \; . \tag{8.8}$$

A standard approach to solve this three-dimensional Schrödinger equation begins by writing the three-body wave function as an adiabatic channel decomposition

$$\psi(R,\Omega,\chi) = \sum_{\nu=0}^{\infty} F_\nu(R) \Phi_\nu(R;\Omega,\chi) \; . \tag{8.9}$$

Here Ω represents the two hyperangles and χ represents the spin degrees of freedom, while ν indexes the channel functions. The adiabatic channel functions $\Phi_\nu(R;\Omega,\chi)$, which vary smoothly in R except near avoided crossings, are eigenfunctions of the fixed-R hyperspherical Hamiltonian

$$\left[\frac{\hbar^2(\Lambda^2 + 15/4)}{2\mu} + V(R,\Omega) \right] \Phi_\nu(R;\Omega,\chi) \;\; = \;\; U_\nu(R) \Phi_\nu(R;\Omega,\chi) \; . \tag{8.10}$$

The adiabatic potentials $U_\nu(R)$ form a set of effective potentials that can be used to gain qualitative insight into the particle dynamics. Further, insertion of the channel decomposition of $\psi(R,\Omega,\chi)$ into Eq. 8.7 leads a set of coupled one-dimensional equations

$$\left[\frac{-\hbar^2}{2\mu} \left(\underline{1} \frac{d^2}{dR^2} + 2\underline{P} \frac{d}{dR} + \underline{Q} \right) + \underline{U} - \underline{E} \right] \underline{F} = 0 \; . \tag{8.11}$$

Here, $P_{\mu\nu} = \langle \Phi_\mu | \frac{d}{dR} \Phi_\nu \rangle$ and $Q_{\mu\nu} = \langle \Phi_\mu | \frac{d^2}{dR^2} \Phi_\nu \rangle$ represent coupling matrices. In practice, only the $P^2_{\mu\nu} = -\langle \frac{d}{dR} \Phi_\mu | \frac{d}{dR} \Phi_\nu \rangle$ component of $Q_{\mu\nu}$ (see Eq. B.2) is needed to solve the coupled equations, which can be added to the potential matrix to form $\underline{W} = \underline{U} - \frac{\hbar^2}{2\mu} \underline{P^2}$.

Once the symmetric matrix $\underline{\mathrm{W}}$ and antisymmetric matrix $\underline{\mathrm{P}}$ are determined, the coupled hyperradial equations can be solved using essentially the same approach that was presented in Chapter 3 for two-body scattering. The coupled equations (Eq. 8.11) are solved using the adiabatic FEM $\underline{\mathrm{R}}$-matrix code described in Appendix B subject to $F_\nu(0) = 0$ boundary conditions. The scattering matrix is then derived from the $\underline{\mathrm{R}}$-matrix solutions according to the procedure developed in Section 3.2. However, we do find it necessary to integrate out to surprisingly large $R \sim 10^5$ a.u.

before matching to energy-normalized channel functions. A code that calculates $\underline{W}$ and $\underline{P}$ by first expanding the angular coordinates in a B-splines basis[164] followed by a diagonalization of the Hamiltonian using banded iterative techniques[165] has been developed by Dr. B. Esry. In practice, we use this code to calculate $\underline{W}$ and $\underline{P}$ over the hyperradial range $0 \leq R < 8a$, where a is the two-body scattering length. Beyond, $R \sim 8a$ the matrix elements of $\underline{W}$ and $\underline{P}$ are smooth and can be fitted to an inverse polynomial series. We use the following series expansions to define the asymptotic values of these matrix elements[166]:

$$\begin{aligned} W_{\lambda,\lambda} &= [c_1 + \frac{c_2}{R^2} + \frac{c_3}{R^3}] \\ W_{\lambda,\gamma'} &= [\frac{c_1}{R^2} + \frac{c_2}{R^3} + \frac{c_3}{R^4}] \\ W_{\gamma,\gamma'} &= [\frac{c_1}{R^2} + \frac{c_2}{R^3} + \frac{c_3}{R^4}] \\ P_{\lambda,\lambda'} &= [\frac{c_1}{R^1} + \frac{c_2}{R^2} + \frac{c_3}{R^3}] \\ P_{\lambda,\gamma'} &= [\frac{c_1}{R^{5/2}} + \frac{c_2}{R^{7/2}} + \frac{c_3}{R^{9/2}}] \\ P_{\gamma,\gamma'} &= [\frac{c_1}{R^2} + \frac{c_2}{R^3} + \frac{c_3}{R^4}] \ , \end{aligned} \tag{8.12}$$

where λ, λ' label the recombination channels and γ, γ' index the three-body continuum channels. The coefficients c_i are determined by a least squares fit to matrix elements calculated with the B-splines code at large R. Tests indicate that the coefficients c_i are relatively insensitive to the range of R used in the fit, provided that it corresponds to hyperradii greater than $\sim 6a$.

The last step needed is to relate the scattering matrix to the recombination rate. A generalization of the two-body cross section derivation given in Section 2.1 has been developed[167], which defines the three-body recombination cross section for identical particle scattering in the following manner:

$$\sigma_3 = \frac{1152\pi^2}{k^5} |S_{A_2+A \leftarrow A+A+A}|^2 \ . \tag{8.13}$$

Here, $k = \sqrt{2\mu E/\hbar^2}$ is the hyperradial wavenumber in the incident three-body continuum channel. The large coefficient in Eq. 8.13 is a result of Bose-Einstein statistics and is a $(3!)^2$-fold enhancement of the cross section compared to one that would be obtained for nonidentical particle scattering. The generalized cross section has dimensions $(length)^5$ as is expected for radial flux scattered in six dimensions. The cross section defined here follows the Mott and Massey[24] convention for identical particle scattering. That is, the cross section is defined as the ratio of scattered radial flux to the incident flux in one of the six permutations of the incident plane wave. As with two-body scattering, the event rate constant K_3 per atom triplet

is defined in terms of the cross section as

$$K_3 = \frac{\hbar k}{\mu}\sigma_3 \, . \tag{8.14}$$

Finally, the atom-loss rate is given by

$$L_3 = 3K_3/6 \, . \tag{8.15}$$

Here, the factor of three denotes the loss of both the diatom and the final state atom from the trap. The division by six comes from the fact that there are $N^3/6$ atom triples in a fixed volume. These formulae (equations 8.13, 8.14, and 8.15) were derived for collisions in a thermal gas and need to be divided by a factor of six to describe collisions in a condensate[168].

8.2 Recombination rates and mechanisms

The three-body interaction potential used is a sum of triplet Born-Oppenheimer two-body potentials. This choice is appropriate for collisions of doubly-polarized atoms. The major numerical challenge of a fully quantum mechanical approach to solving the recombination problem is the sheer multiplicity of two-body bound states. This is evident from Fig. 8.1, which shows the adiabatic hyperspherical potential curves for the collision of three doubly-polarized ^{7}Li atoms. Each bound state supported by the two-body interaction is represented by exactly one hyperspherical three-body potential that converges asymptotically to a dimer bound state. For doubly-polarized ^{7}Li, this amounts to 118 recombination channels and the number grows still larger for the heavier alkalis, with 1466 recombination channels available for doubly-polarized ^{87}Rb collisions.

However, it is physically plausible that the dominant pathways for recombination will involve vibrational states closest to threshold, particular those with low angular momentum l. In fact, previous studies[154, 157, 169] suggest that the two-body scattering length a ultimately controls ultracold recombination rates. Based on this assumption, we rescale the two-body triplet potentials by an overall scaling factor γ, where $0 \leq \gamma \leq 1$. This scheme allows us to reduce the total number of recombination channels, which alleviates many of the numerical complexities, while allowing us to control a. This premise is tested by treating two-body potentials that support different numbers of bound states but which generate the same scattering length. In addition, a number of calculations have been performed using a potential of the form $v(r_{12}) = D\,\mathrm{sech}^2(r_{12}/r_0)$, which was utilized in the three-body study of Ref.[169]. If the recombination rate is controlled by a, then the exact form of the short-range potential should not matter.

We have performed calculations with roughly 125 different two-body potentials, including a wide range of scattering lengths and different numbers of two-

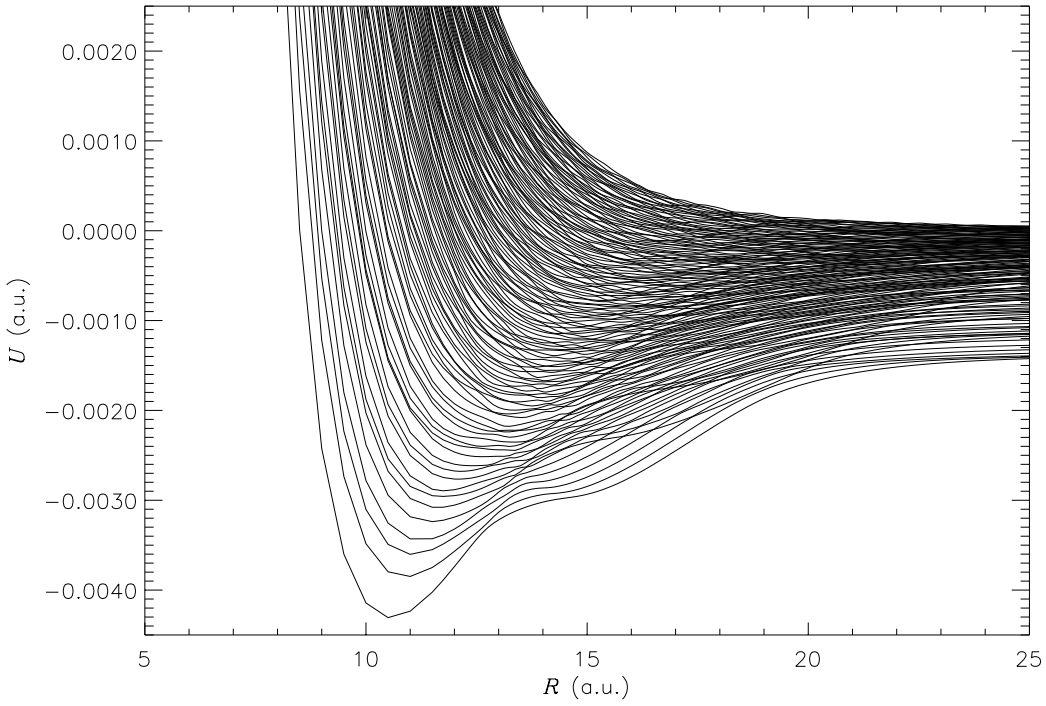

Figure 8.1: The J=0 hyperspherical potential curves for ^{7}Li are shown as a function of hyperradius R. These potential curves describe doubly-polarized collisions of three ^{7}Li atoms, i.e. all in the same $f_a = 2, m_{f_a} = 2$ spin state. All of the roughly 120 bound and continuum channels shown must be included in order to carry out a full calculation of the scattering matrix. Data courtesy of Dr. B. Esry.

body bound states. The potentials used include Na-Na, K-K, and Rb-Rb rescaled Born-Oppenheimer triplet potentials, and sech^2 potentials using r_0=5 and 15 a.u. Fig. 8.2 shows the resulting scattering length dependence of the "recombination length". The recombination length is defined as

$$\rho_3 = \left(\frac{\mu}{\hbar} K_3\right)^{1/4} . \tag{8.16}$$

Here, $\mu = m/\sqrt{3}$ is the three-body reduced mass. This definition is intended to present a quantity largely independent of the atomic properties other than the scattering length, and to reduce to a number roughly comparable to the scattering length in order of magnitude.

The most striking result of Fig. 8.2 is the manner in which the calculated recombination lengths cluster along a single curve. This implies that the recombination rates are in fact predominantly controlled by the two-body scattering length. In addition, Fig. 8.2 shows two additional features of the recombination process that had not appeared before in the literature. Specifically, an interference minimum occurs near $a \approx 290$ a.u. and a shape resonance occurs near $a \approx -175$ a.u. These features can be explained qualitatively by the two following mechanisms.

Recombination for positive scattering lengths is controlled primarily by a distant avoided crossing between the three-body entrance channel and the highest s-wave recombination channel that occurs near $R_{\rm peak} \approx 3a$. Figure 8.3(a) shows the hyperspherical potential curves for the sech^2 two-body potential scaled to give a = 100 a.u. but with only a single s-wave bound state. In this case the hyperspherical potentials are very simple and their main features are consistent with Refs.[169, 170]. Figure 8.3(a) also shows the crossing near $R_{\rm peak} \approx 3a$, as a peak in the dimensionless coupling strength parameter, $P^2/\mu\Delta U$. The approximate hyperradial peak position of $P^2/\mu\Delta U$ is plotted in Fig. 8.4 for a number of rescaled alkali potentials. The position of the crossing is consistent for the Rb-Rb and K-K rescaled potentials but approaches $R_{\rm peak} \approx 4a$ for the large positive Na scattering lengths. It is not yet understood whether this deviation from the "nominal" behavior of the crossing position is an isolated occurrence.

The suppression of the recombination rates near $a \approx 290$ a.u. is analogous to that of the ^{87}Rb spin exchange rates discussed in Section 5.1. Namely, two competing pathways interfere destructively, which effectively "turns off" the flux exiting along the inelastic path. One minor difference between these two cases of so-called "Stückelberg oscillations" is that here the kinetic energy in the entrance channel is negative at the crossing. This case has been treated by Nakamura[171] who calls this process "nonadiabatic tunneling". The scattering probability for recombination

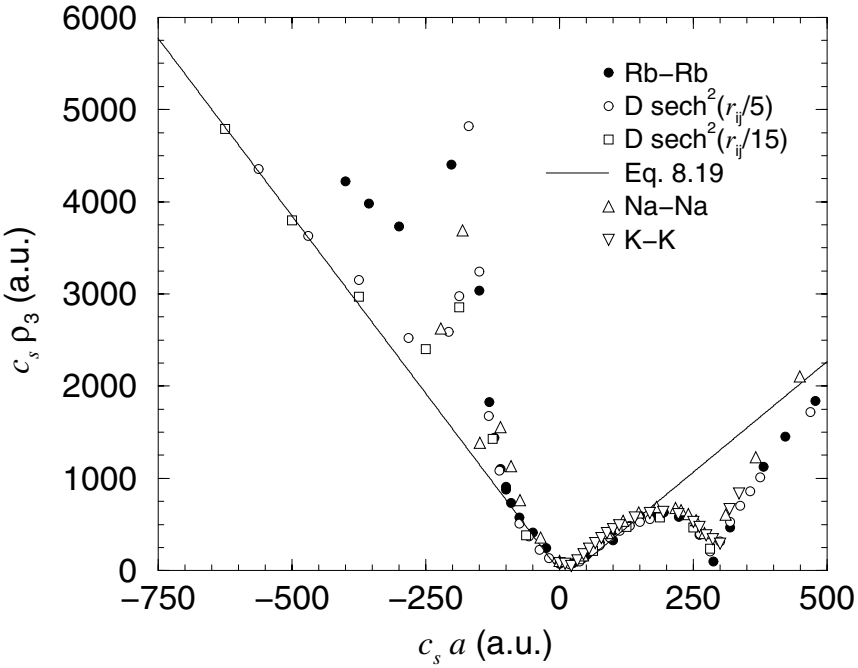

Figure 8.2: Numerically calculated recombination lengths for a wide range of two-body potentials, which are discussed in the text. We find that each set of two-body potentials has a characteristic length scale, labeled r_0. In the case of the sech^2 potentials, r_0 is part of the definition of the potential, i.e. $v(r_{12}) = D\,\mathrm{sech}^2(r_{12}/r_0)$, r_0= 5 and 15 used here . The value of r_0 for the alkali potentials is determined "empirically" from the calculated position of the interference minimum and a zero of the phase factor $\sin^2[\ln(3a/2r_0)]$. (The phase factor is discussed in the text.) We find r_0(Rb) = 18.8, r_0(K) = 16.8, and r_0(Na) = 12.4 (in a.u.). The dimensionless scale factor is set to $c_s = r_0$(Rb)/$r_0(V_i)$, i.e. $c_s = 1$ for the Rb potentials. Using this rescaling, each set of potentials produces an interference minimum near $c_s a \approx 290$ a.u. and a shape resonance near $c_s a \approx 175$ a.u. The solid line is the analytical formula given in Eq. 8.19 with the $\sin^2$ phase factor set equal to $\frac{1}{2}$. These calculations were performed at $E = 1\mu$K, except for the range $a \leq -300$ a.u., where an energy of 0.1μK was used in order to reach the ultracold limit.

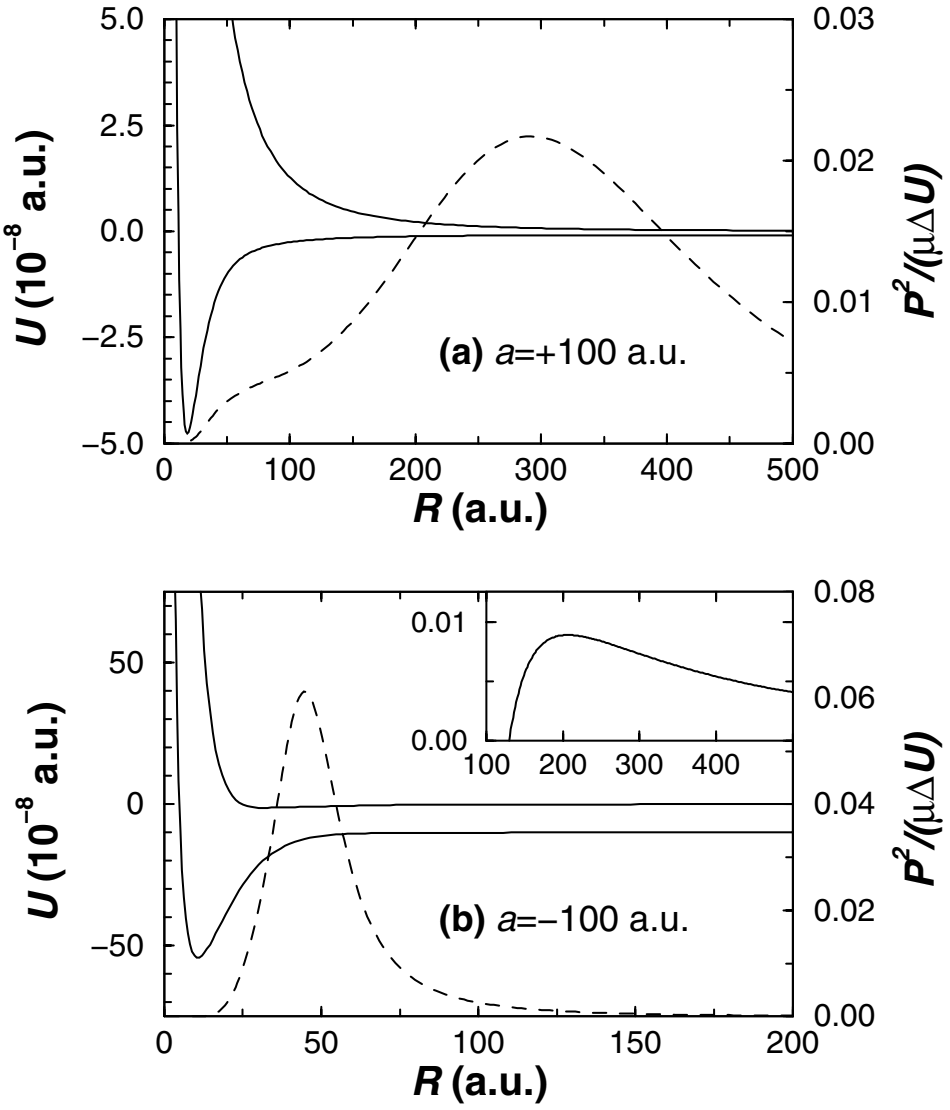

Figure 8.3: Different qualitative mechanisms control ultracold recombination at $a > 0$ (a) and $a < 0$ (b), as is clear from the lowest two adiabatic hyperspherical potential curves (solid line) depicted along with their nonadiabatic coupling strength (dashed line). We define a dimensionless measure of the nonadiabatic coupling strength in terms of the the squared first derivative coupling matrix element $P_{12}^2(R)$, the difference in the adiabatic hyperspherical potential curves $\Delta U(R)$, and the reduced mass μ. These were calculated using the sech^2 two-body potential (r_0 = 15 a.u.) discussed in the text, for the simplest situation of a single two-body s-wave bound state. The basic nature of these potentials remains the same even as the number of two-body bound states is increased. The inset of (b) shows the potential barrier in the three-body entrance channel discussed in the text.

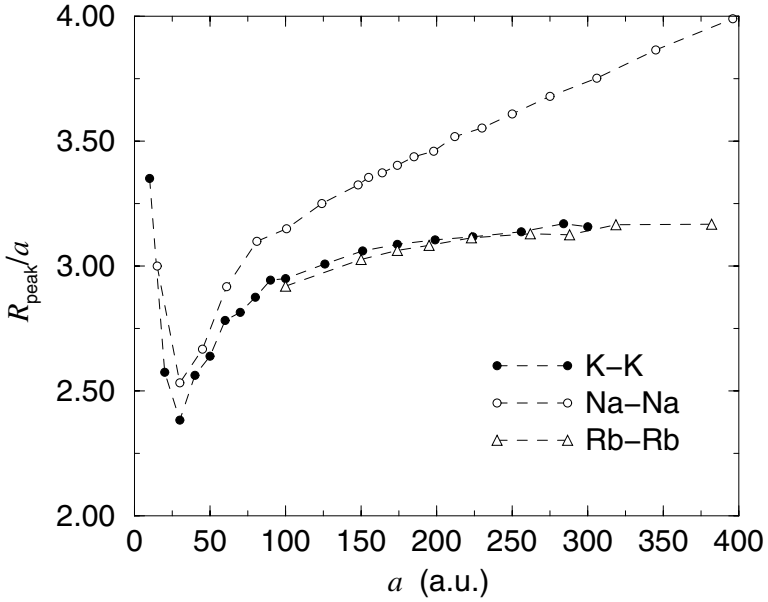

Figure 8.4: Hyperradial position of the long-range avoided crossing $R_{\rm peak}$ as a function of two-body scattering length a for a number of alkali potentials rescaled to support only one s-wave bound state.

into the highest s-wave dimer channel is given approximately by the expression:

$$|\mathbf{S}_{A_2+A\leftarrow A+A+A}|^2 \underset{a\to+\infty}{\longrightarrow} 0.067\,(ka)^4\sin^2\Phi, \tag{8.17}$$

where Φ is the phase difference between the amplitudes associated with the two competing pathways. An estimate of Φ can be made in the limit of large a by approximating the hyperspherical potential curve converging to the highest s-wave dimer potential as an "Efimov potential curve"[169], i.e. $V \to -0.631/\mu R^2$, for hyperradii less than the crossing point. In this limit, the phase factor at zero energy is approximately

$$\sin^2\Phi \underset{a\to+\infty}{\longrightarrow} \sin^2\left[\ln\left(\frac{3a}{2r_0}\right)\right], \tag{8.18}$$

where r_0 defines a characteristic length scale for the two-body potentials. (This is discussed in more detail in the caption of Fig. 8.2.) We expect that $\sin^2\Phi$ can be approximated by $\frac{1}{2}$ in most systems having numerous two-body bound states because the amplitude of the interfering returning wave is likely to be dissipated into other recombination channels at small R. This point will require further study. However there is one atom, ^{4}He, for which the physical two-body potentials do support only one s-wave bound state and in fact, our calculations show that the interference minimum occurs near the physical value of the scattering length. This is shown in Fig. 8.5.

Returning to Fig. 8.3, the (b) panel shows the hyperspherical potential curves, for a sech^2 two-body potential that generates a scattering length of $a = -100$ a.u., which supports a single s-wave bound state. Again, the hyperspherical potential curves are simple, but for the negative a case we find that the rate-limiting crossing occurs at small R. In fact, the hyperradius of the crossing and its coupling strength are largely independent a. The scattering length dependence of the recombination rates in the range $a < 0$ is the result of quantum mechanical tunneling under a barrier (previously identified in Ref.[169]), whose peak occurs at $R_B \approx 2a$ with a maximum height of $W(R_B) \approx \frac{0.079}{\mu a^2}$ in a.u. (see the inset of Fig. 8.3(b)). In order to reach the avoided crossing(s) at small R, the incoming wavefront in the three-body recombination channel must tunnel inside the barrier. If the incident particle does tunnel successfully, then we expect that it has a high probability to undergo a nonadiabatic Landau-Zener transition into one or more recombination channels. On the other hand, the probability per collision to tunnel into the small R region is a strong function of the barrier height and the collision energy. In fact, the probability varies as $(ka)^4$ at energies well below the barrier peak. This leads to an approximate a^4 dependence of the recombination rates for both positive and negative scattering lengths even though the recombination mechanisms are different. The existence of

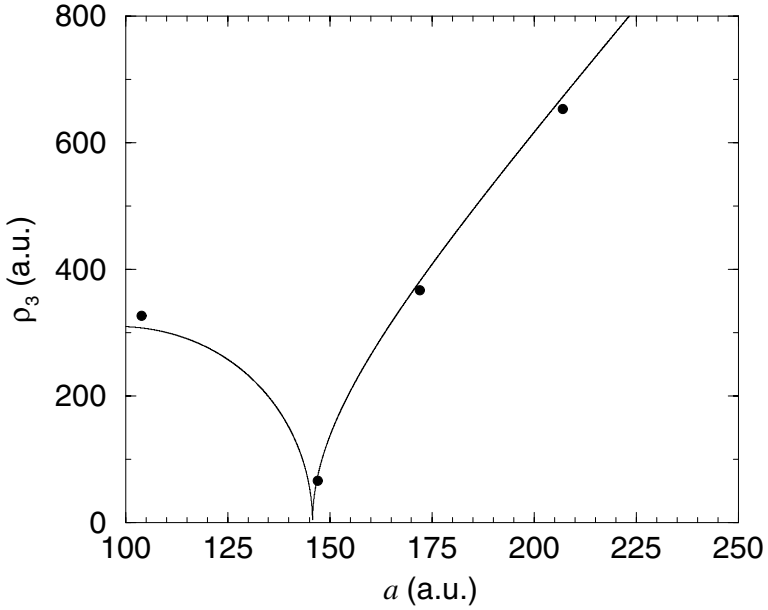

Figure 8.5: The recombination length versus scattering length a for collisions of three ^{4}He atoms (closed circles). The physical scattering length is a=172 a.u. The solid line is the analytical recombination length defined in Eq. 8.19 using r_0=9.4.

a potential barrier also provides the opportunity for a shape resonance in the three-body continuum to dramatically increase the recombination rates. This effect is demonstrated in Fig. 8.2 near $a \approx -175$ a.u. However, in the absence of a full calculation the positions of these resonances will be hard to predict for any real alkali system.

We have developed the following expression for the recombination length based on the roughly 125 calculations using a variety of two-body potentials:

$$\rho_3^{\rm th}(a) \simeq \max \left\{ \begin{array}{l} \left\{ \begin{array}{l} 5.0 \left(a - \frac{3}{2} r_0\right) \left[2 \sin^2 \left(\ln \frac{3a}{2r_0}\right)\right]^{\frac{1}{4}},\ a > 0 \\ -7.7a,\ a < 0 \end{array} \right\}, \\ \\ 4r_0, \end{array} \right. \tag{8.19}$$

where the slopes in this expression are accurate to about $\pm 10\%$. The lower limit is set to $\rho_3 = 4r_0$ because we never see the recombination length decrease below 50-100 a.u. in the alkalis. This effect is presumably due to other recombination channels becoming more important as the dominant s-wave channel weakens sufficiently. A comparison of our analytic expression for ρ_3 with the numerically calculated $+a$ recombination lengths is shown in Fig. 8.6.

Table 8.1 provides our best estimate of the recombination rates and compares these with the available experimental information and other theoretical predictions. For the estimates of alkali rates, we have replaced the $\sin^2 \Phi$ phase factor in Eq. 8.19 with its average value of 1/2. This was not necessary for ^{4}He since the calculation of its recombination rate used a realistic two-body interaction potential. Table 8.1 presents the results in terms of event rates K_3. Where necessary the quoted experimental loss rates L_3 have been converted to event rates using Eq. 8.15. In addition, the experimental results quoted for atoms in a condensate have been multiplied by a factor of 6 to compare with our theoretical results for atoms in a thermal cloud[168]. Our estimates are in reasonable agreement with most of the measured rates. The lone experiment that deviates substantially from our predicted dependence of K_3 on a is the magnetic field Feshbach resonance studied in Na[15, 172]. In particular, that experiment observed an **increase** in the recombination rate as a was **decreased** from its nominal value of $a = 54.6$ a.u. to $a = 0$. We have not observed that type of behavior in our calculations, which might suggest that the mechanism controlling the Na recombination differs from those discussed here.

The majority of the calculations performed to date used two-body potentials scaled to include only a single s-wave bound state. In order to assess the generality of our results, it is important to study the dependence of K_3 on the number of s-wave bound states, n_S, for a given a. Our preliminary results indicate that the dependence is not particularly strong. For example, the recombination event rate

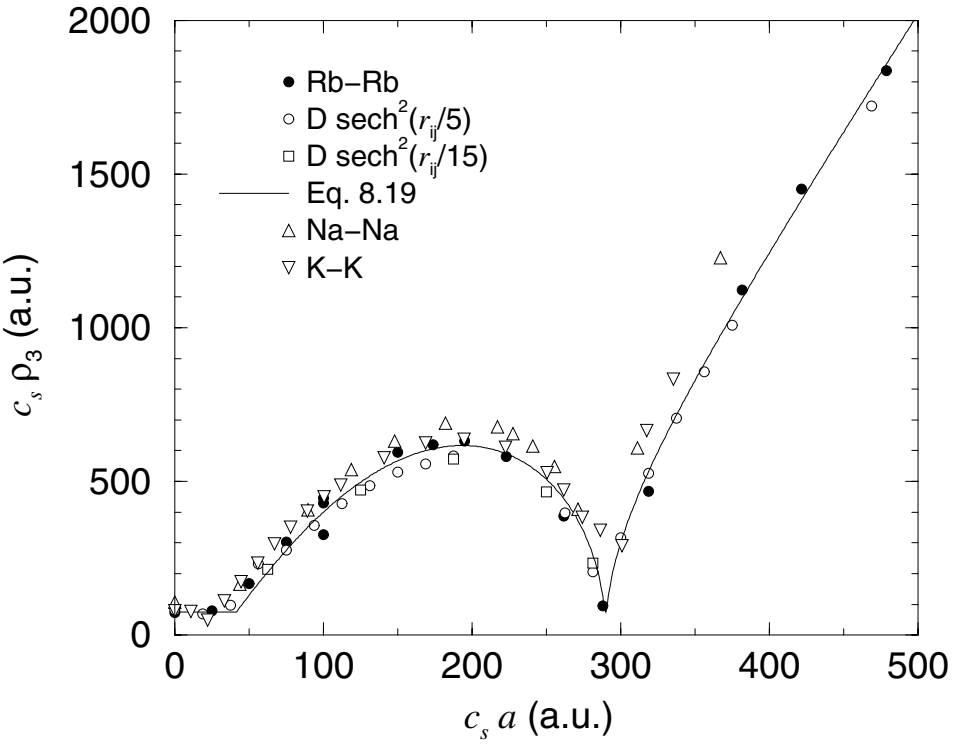

Figure 8.6: Numerical recombination lengths are compared with the $+a$ analytic formula given in Eq. 8.19 ($r_0 = 18.8$). The numerical data are discussed in the caption of Fig. 8.2.

Table 8.1: Recombination event rate constants

		present	experiment	other
Atom	a (a.u.)	$K_3^{\rm th}$ (cm^6/s)	$K_3^{\rm exp}$ (cm^6/s)	$K_3^{\rm th}$ (cm^6/s)
^{4}He	172	4.2×10^{-27}	—	2.5×10^{-27}[154]
^{7}Li	-27.6	2.5×10^{-28}	$< 6\times10^{-27}$[173]	5.2×10^{-28}[157]
^{23}Na(1,1)	54.6	1.1×10^{-28}	1×10^{-27}[172]	4.0×10^{-28}[157]
^{39}K	-33	9.2×10^{-29}	—	—
^{85}Rb	-370	6.6×10^{-25}	—	—
^{87}Rb(1,-1)	106	2.0×10^{-28}	9×10^{-29}[168]	8×10^{-30}[157]
^{87}Rb(2,2)	106	2.0×10^{-28}	2.2×10^{-28}[174]	1.7×10^{-29}[154]
^{133}Cs(3,3)	-1250	5.6×10^{-23}	$< 10^{-23}$[18]	1×10^{-28}[175]

K_3 was found to decrease by a factor of three when the potentials were rescaled from $n_S = 1$ to $n_S = 3$ while maintaining $a = +100$. Examining the bound state dependence of the position and strength of the rate-limiting crossing suggests that this difference will not grow much larger (see Fig. 8.7) as n_S is increased farther. The negative scattering length recombination rates have an even weaker dependence on n_S. In fact, our preliminary tests indicate that, excluding resonances, the recombination rate is essentially converged with $n_S = 1$, (see Fig. 8.8). However, these results are not conclusive and we plan to conduct more tests in the future.

It is also important to understand the energy dependence of K_3 and the energy range over which the threshold values of K_3 are applicable. For positive scattering lengths, we find that K_3 is reasonably constant over collision energies ranging from $E = 0$ to several hundred μK. However, owing to the low energy barrier in the entrance channel, K_3 is far more energy-dependent for the negative scattering lengths. In fact, the threshold limit for K_3 is achieved at $a < 0$ only for collision energies well below the barrier maximum. At higher energies, the scattering probability saturates and K_3 decreases due to the k^{-4} factor (see equations 8.13 and 8.14). The energy dependence of the recombination rates for $\pm a$ are shown in Fig. 8.9. This behavior should have a dramatic effect on the ^{133}Cs recombination rates if $a \approx -1250$ as quoted in Ref.[18]. In this case, the peak of the barrier in the three-body entrance channel is roughly $W(R_B)$ = 0.1μK. Our experience suggests that K_3 will decrease several orders of magnitude as the collision energy rises to 10μK. The resulting rate would then be consistent with the experimental bound set in Ref.[18] even though our threshold value is greater than the bound quoted in Ref.[18](see Table 8.1).

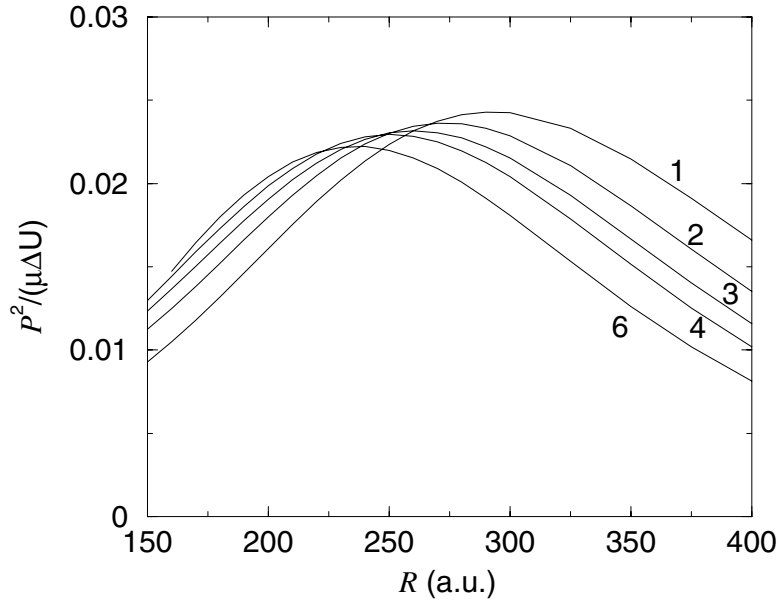

Figure 8.7: Coupling between the three-body entrance channel and the highest s-wave recombination channel is shown as a function of hyperradius. Each curve represents a Rb-Rb potential rescaled to hold n_S s-wave bound states with a=+100. The labels on each curve denote the number n_S.

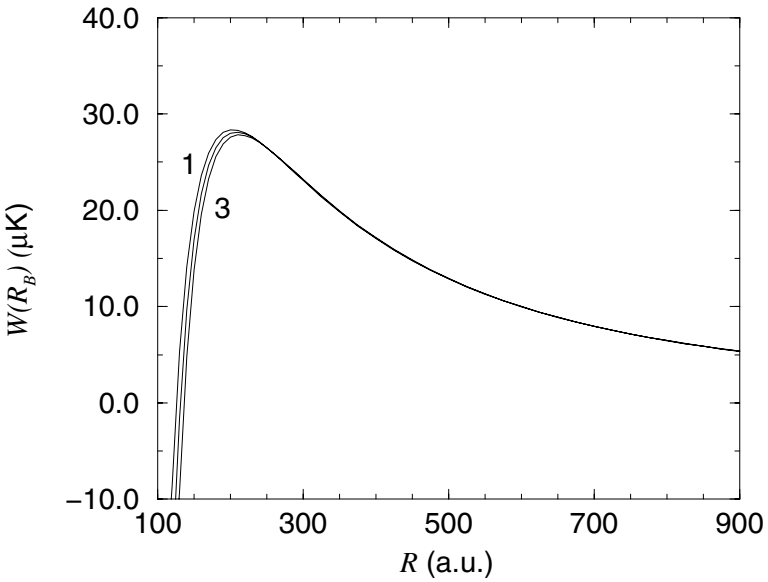

Figure 8.8: The centrifugal barrier in the three-body entrance channel is shown as a function of hyperradius. Each curve represents a Rb-Rb potential rescaled to hold n_S s-wave bound states with a = -100 a.u. Curves with $n_S = 1$ and 3 are labeled, $n_S = 2$ is the unlabeled curve. The height and position of the barrier are essentially independent of n_S. The event rates K_3 calculated for these three potentials varied by roughly 30%.

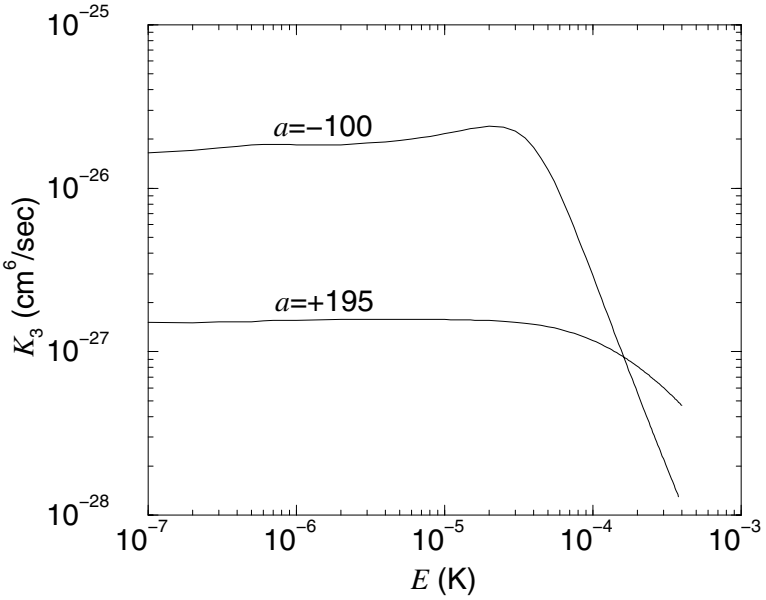

Figure 8.9: The energy dependence of K_3 is shown for $\pm a$. These data used Rb-Rb potentials rescaled to support one s-wave bound state. The negative scattering length recombination rate exhibits an E^{-2} dependence for collision energies above the barrier in the three-body entrance channel ($W(R_B) \approx 30\mu$K for this example).

Chapter 9

Summary

This dissertation has extended the theoretical methods needed to calculate and understand two-body and three-body collisions of trapped alkali atoms. The "conventional" theory of two-body collisions in a magnetic trap was developed in Chapter 2. Numerical techniques for solving the resulting coupled differential equations that describe the collision dynamics were presented in Chapter 3. Chapter 4 developed an alternative formalism to describe the two-body dynamics. Here, multichannel quantum defect methods were applied to the two-body collisions, yielding a more comprehensive understanding of the collision physics as well as substantially improving the efficiency of the calculations. These theoretical techniques were applied in Chapter 5 to a set of Rb collision experiments. From an analysis of these experiments, we were able to derive state-of-the art Rb_2 Born-Oppenheimer potentials. In addition, we used the refined potentials to investigate the scattering properties of several Rb isotopes. From these surveys, we have been able to identify specific hyperfine states whose collisional properties could lead to novel degenerate gas experiments. The theory of two-body collisions in a magnetic trap seems well in hand. However, with the recent demonstration of trapping atoms outside the alkali family[176, 177, 178] there are certainly more surprises to come.

Photoassociation spectroscopy has been an essential tool in cold collision physics. A theory of photoassociation lineshapes was presented in Chapter 6. This theory was applied in Chapter 7 to interpret measured ^{39}K rovibrational spectra, which permitted us to derive improved ground state potentials. The analysis of photoassociation lineshapes provides vital information on the ground state scattering wave functions. However, attempts to better quantify these results have suffered from uncertainties associated with the second, ionizing, laser. Theories to include multiple transitions[134, 135] have been devised but remain untested. These issues will need to be addressed in the future.

A new theoretical description of three-body recombination in collisions of doubly-polarized alkali atoms, was presented in Chapter 8. This theory is a fully quantum mechanical treatment of the recombination process. From our numerical calculations we have been able to identify two separate mechanisms that control the recombination physics depending on the sign of the two-body scattering length a.

Remarkably, we find that the recombination rate scales as a^4 in both cases, although the coefficient is much larger at $a < 0$. The treatment presented here used rescaled two-body potentials to simplify the numerical calculations. In the future, it will be necessary to test our results by using more realistic two-body potentials. In addition, it seems conceivable to introduce both hyperfine and magnetic field interactions into our formalism. This would then allow a more realistic treatment of the Na Feshbach resonance experiment. Three-body recombination physics remains in its infancy, but Chapter 8 develops a framework upon which future studies can build.

Bibliography

[1] M. H. Shamos, Great Experiments in Physics, (Dover, New York, 1987).

[2] D. W. Gough, G. C. Maitland and E. B. Smith, Mol. Phys. 24 (1972) 1551.

[3] R. A. Dawe and E. B. Smith, J. Chem. Phys. 52 (1970) 693.

[4] F. A. Guevara, B. B. McInteer and W. E. Wageman, Phys. Fluids 12 (1969) 2493.

[5] J. Kestin, H. E. Khalifa, S. T. Ro and W. A. Wakeham, Physica 88A (1978) 242.

[6] W. D. Phillips, J. V. Prodan and H. J. Metcalf, J. Opt. Soc. Am. B 2 (1985) 1751.

[7] J. Dalibard and C. Cohen-Tannoudji, J. Opt. Soc. Am. B 2 (1985) 1707.

[8] M. H. Anderson, J. R. Ensher, M. R. Matthews, C. E. Wieman and E. A. Cornell, Science 269 (1995) 198.

[9] C. C. Bradley, C. A. Sackett, J. J. Tollet and R. G. Hulet, Phys. Rev. Lett. 75 (1995) 1687.

[10] K. B. Davis, M. O. Mewes, M. R. Andrews, N. J. van Druten, D. D. Durfee, D. M. Kim and W. Ketterle, Phys. Rev. Lett. 75 (1995) 3969.

[11] P. A. Ruprecht, M. J. Holland, K. Burnett and M. Edwards, Phys. Rev. A 51 (1995) 4704.

[12] F. Dalfovo, S. Giorgini, L. P. Pitaevskii and S. Stringari, Rev. Mod. Phys. 71 (1999) 463.

[13] C. W. Gardiner, M. D. Lee, R. J. Ballagh, M. J. Davis and P. Zoller, Phys. Rev. Lett. 81 (1998) 5266.

[14] W. C. Stwalley, Phys. Rev. Lett. 37 (1976) 1628.

[15] S. Inouye, M. R. Andrews, J. Stenger, H. J. Miesner, D. M. Stampur-Kurn and W. Ketterle, Nature (London) 392 (1998) 151.

[16] Ph. Courteille, R. S. Freeland, D. J. Heinzen, F. A. van Abeelen and B. J. Verhaar, Phys. Rev. Lett. 81 (1998) 69.

[17] J. L. Roberts, N. R. Claussen, Jr. J. P. Burke, C. H. Greene, E. A. Cornell and C. E. Wieman, Phys. Rev. Lett. 81 (1998) 5109.

[18] V. Vuletić, A. J. Kerman, C. Chin and S. Chu, Phys. Rev. Lett. 82 (1999) 1406.

[19] H. R. Thorsheim, J. Wiener and P. S. Julienne, Phys. Rev. Lett. 58 (1987) 2420.

[20] H. B. G. Casimir and D. Polder, Phys. Rev. 73 (1948) 360.

[21] K. M. Jones, P. S. Julienne, P. D. Lett, W. D. Phillips, E. Tiesinga and C. J. Williams, Europhys. Lett. 35 (1996) 85.

[22] H. Wang, J. Li, X. T. Wang, C. J. Williams, P. L. Gould and W. C. Stwalley, Phys. Rev. A 55 (1997) R1569.

[23] M. Aymar, C. H. Greene and E. Luc-Koenig, Rev. Mod. Phys. 68 (1996) 1016.

[24] N. F. Mott and H. S. W. Massey, The Theory of Atomic Collisions, (Clarendon Press, Oxford, 1965).

[25] L. S. Rodberg and R. M. Thaler, Introduction to the Quantum Theory of Scattering, (Academic Press, New York, 1967).

[26] S. Gasiorowicz, Quantum Physics, (John Wiley and Sons, New York, 1974).

[27] U. Fano and A. R. P. Rau, Atomic Collisions and Spectra, (Academic Press, New York, 1986).

[28] J. Wiener, V. S. Bagnato, S. Zilio and P. S. Julienne, Rev. Mod. Phys. 71 (1999) 1.

[29] D. H. Levy, Adv. Mag. Res. 6 (1973) 1.

[30] A. Carrington, D. H. Levy and T. A. Miller, Adv. Chem. Phys. 18 (1970) 149.

[31] M. Born and J. R. Oppenheimer, Ann. Phys. (Leipzig) 84 (1927) 457.

[32] G. C. Maitland, M. Rigby, E. B. Smith and W. A. Wakeham, Intermolecular Forces, (Clarendon Press, Oxford, 1981).

[33] M. Krauss and W. J. Stevens, J. Chem. Phys. 93 (1990) 4236.

[34] A. L. G. Rees, Proc. Phys. Soc. Lond. A 59 (1947) 998.

[35] C. R. Vidal, Comments At. Mol. Phys. 17 (1986) 173.

[36] B. M. Smirnov and M. I. Chibisov, JETP 21 (1965) 624.

[37] R. Côté, A. Dalgarno, H. Wang and W. C. Stwalley, Phys. Rev. A 57 (1998) R4118.

[38] M. Marinescu, H. R. Sadeghpour and A. Dalgarno, Phys. Rev. A 49 (1994) 982.

[39] A. Derevianko, W. R. Johnson, M. S. Safronova and J. F. Babb, Phys. Rev. Lett. 82 (1999) 3589.

[40] S. H. Patil and K. T. Tang, J. Chem. Phys. 106 (1997) 2301.

[41] W. T. Zemke and W. C. Stwalley, J. Chem. Phys. 97 (1993) 2053.

[42] Z.-C. Yan, J. F. Babb, A. Dalgarno and G. W. F. Drake, Phys. Rev. A 54 (1996) 2824.

[43] W. T. Zemke and W. C. Stwalley, J. Chem. Phys. 100 (1994) 2661.

[44] M. Marinescu, (private communication).

[45] C. Amiot, J. Verges and C. E. Fellows, J. Chem. Phys. 103 (1995) 3350.

[46] G. Zhao, W. T. Zemke, J. T. Kim, B. Ji, H. Wnag, J. T. Bahns, W. C. Stwalley, L. Li, A. M. Lyyra and C. Amiot, J. Chem. Phys. 105 (1996; and references therein) 7976.

[47] C. Amiot, J. Chem. Phys. 93 (1990) 8591.

[48] W. Weickenmeier, U. Diemer, M. Wahl, M. Raab and W. Demtröder, J. Chem. Phys. 82 (1985) 5354.

[49] E. Tiesinga, C. J. Williams, P. S. Julienne, K. M. Jones, P. D. Lett and W. D. Phillips, J. Res. Natl. Inst. Stand. Technol. 101 (1996) 505.

[50] C. Cohen-Tannoudji, B. Diu and F. Laloe, Quantum Mechanics, (John Wiley and Sons, New York, 1977).

[51] J. D. Jackson, Classical Electrodynamics, (John Wiley and Sons, New York, 1999).

[52] E. Arimondo, M. Inguscio and P. Violino, Rev. Mod. Phys. 49 (1977) 31.

[53] H. Lefebvre-Brion and R. W. Field, Perturbations in the Spectra of Diatomic Molecules, (Academic Press, New York, 1986).

[54] F. H. Mies, C. J. Williams, P.S. Julienne and M. Krauss, J. Res. Natl. Inst. Stand. Technol. 101 (1996) 521.

[55] P. O. Fedichev, Yu. Kagan, G. V. Shlyapnikov and J. T. M. Walraven, Phys. Rev. Lett. 77 (1996) 2913.

[56] J. L. Bohn and P. S. Julienne, Phys. Rev. A 56 (1997) 1486.

[57] R. N. Zare, Angular Momentum, (John Wiley and Sons, New York, 1988).

[58] B. Numerov, Publ. Observatoire Central Astrophys. Russ. 2 (1933) 188.

[59] R. G. Gordon, J. Chem. Phys. 51 (1969) 14.

[60] B. R. Johnson, J. Comp. Phys. 13 (1973) 445.

[61] L. D. Thomas, M. H. Alexander, B. R. Johnson, Jr. W. A. Lester, J. C. Light, K. D. McLenithan, G. A. Parker, M. J. Redmon, T. G. Schmalz, D. Secrest and R. B. Walker, J. Comp. Phys. 41 (1981) 407.

[62] W. H. Press, S. A. Teukolsky, W. T. Vetterling and B. P. Flannery, Numerical Recipes in Fortran: The Art of Scientific Computing, (Cambridge University Press, New York, 1992).

[63] E. Anderson, Z. Bai, C. Bischof, J. Demmel, J. Dongarra, J. Du Cros, A. Greenbaum, S. Hammerling, A. Mckenney, S. Ostouchov and D. Sorensen, LAPACK Users Guide, (SIAM, Philadelphia, 1992).

[64] E. P. Wigner, Phys. Rev. 70 (1946) 15.

[65] E. P. Wigner and L. Eisenbud, Phys. Rev. 72 (1947) 29.

[66] T. Teichman and E. P. Wigner, Phys. Rev. 87 (1952) 123.

[67] C. H. Greene, Phys. Rev. A 28 (1983) 2209.

[68] H. Le Rouzo and G. Raseev, Phys. Rev. A 29 (1984) 1214.

[69] L. R. Ram-Mohan, S. Saigal, D. Dossa and J. Shertzer, Comput. Phys. 4 (1990) 50.

[70] J. Shertzer and J. Botero, Phys. Rev. A 49 (1994) 3673.

[71] K. W. Meyer, C. H. Greene and B. D. Esry, Phys. Rev. Lett. 78 (1997) 4902.

[72] H. W. van der Hart, J. Phys. B 30 (1997) 453.

[73] K. J. Bathe, Finite Element Procedures in Engineering Analysis, (Prentice Hall, Englewood Cliffs, NJ, 1976).

[74] K. J. Bathe and E. Wilson, Numerical Methods in Finite Element Analysis, (Prentice Hall, Englewood Cliffs, NJ, 1976).

[75] R. A. Gonzales, S. Y. Kang, I. Koltracht and G. Rawitscher, (submitted to J. Comput. Phys.).

[76] G. H. Rawitscher, B. D. Esry, E. Tiesinga, Jr J. P. Burke and I. Koltracht, (submitted to J. Chem. Phys.).

[77] T. G. Schmalz, E. B. Stechel and J. C. Light, J. Chem. Phys. 70 (1979) 5660.

[78] H. Klar, Phys. Rev. A 15 (1976) 1452.

[79] H. Klar and U. Fano, Phys. Rev. Lett. 37 (1976) 1132.

[80] M. J. Seaton, Rep. Prog. Phys. 46 (1983) 167.

[81] C. M. Lee, Phys. Rev. A 11 (1975) 1692.

[82] F. H. Mies, J. Chem. Phys. 80 (1984) 2514.

[83] F. H. Mies and P. S. Julienne, J. Chem. Phys. 80 (1984) 2526.

[84] F. H. Mies and M. Raoult, (unpublished).

[85] M. J. Cavagnero, Phys. Rev. A 50 (1994) 2841.

[86] M. J. Cavagnero, (unpublished).

[87] B. Gao, Phys. Rev. A 54 (1996) 2022.

[88] B. Gao, Phys. Rev. A 58 (1998) 4222.

[89] J. P. Burke, C. H. Greene and J. L. Bohn, Phys. Rev. Lett. 81 (1998) 3355.

[90] W. E. Milne, Phys. Rev. 35 (1930) 863.

[91] B. Yoo and C. H. Greene, Phys. Rev. A 34 (1986) 1635.

[92] C. H. Greene, A. R. P. Rau and U. Fano, Phys. Rev. A 26 (1982) 2441.

[93] H. J. Korsch and H. Laurent, J. Phys. B 14 (1981) 4213.

[94] G. F. Gribakin and V. V. Flambaum, Phys. Rev. A 48 (1993) 546.

[95] A. Dalgarno and M. R. H. Rudge, Proc. R. Soc. London, Ser. A 286 (1965) 519.

[96] H. T. C. Stoof, J. M. V. A. Koelman and B. J. Verhaar, Phys. Rev. B 38 (1988) 4688.

[97] D. M. Chase, Phys. Rev. 104 (1956) 838.

[98] R. K. Nesbet, Comments At. Mol. Phys. 11 (1981) 25.

[99] H. Gao and C. H. Greene, J. Chem. Phys. 91 (1989) 3988.

[100] C. J. Myatt, E. A. Burt, R. W. Ghrist, E. A. Cornell and C. E. Wieman, Phys. Rev. Lett. 78 (1997) 586.

[101] H. M. J. M. Boesten, C. C. Tsai, J. R. Gardner, D. J. Heinzen and B. J. Verhaar, Phys. Rev. A 55 (1997) 636.

[102] H. M. J. M. Boesten, C. C. Tsai, B. J. Verhaar and D. J. Heinzen, Phys. Rev. Lett. 77 (1996) 5194.

[103] J. P. Burke, J. L. Bohn, B. D. Esry and C. H. Greene, Phys. Rev. A 55 (1997) R2511.

[104] P. S. Julienne, F. H. Mies, E. Tsienga and C. J. Williams, Phys. Rev. Lett. 78 (1997) 1880.

[105] S. J. J. M. F. Kokkelmans, H. M. J. M. Boesten and B. J. Verhaar, Phys. Rev. A 55 (1997) R1589.

[106] A. Dalgarno and M. R. H. Rudge, Proc. R. Soc. London, Ser. A 286 (1965) 519.

[107] J. M. Vogels, C. C. Tsai, R. S. Freeland, S. J. J. M. F. Kokkelmans, B. J. Verhaar and D. J. Heinzen, Phys. Rev. A 56 (1997) R1067.

[108] C. R. Monroe, E. A. Cornell, C. A. Sackett, C. J. Myatt and C. E. Wieman, Phys. Rev. Lett. 70 (1993) 414.

[109] C. C. Tsai, R. S. Freeland, J. M. Vogels, H. M. J. M. Boesten, B. J. Verhaar and D. J. Heinzen, Phys. Rev. Lett. 79 (1997) 1245.

[110] M. R. Matthews, D. S. Hall, D. S. Jin, J. R. Ensher, C. E. Wieman and E. A. Cornell, Phys. Rev. Lett. 81 (1998) 243.

[111] J. P. Burke, J. L. Bohn, B. D. Esry and C. H. Greene, Phys. Rev. Lett. 80 (1998) 2097.

[112] H.-J. Miesner, D. M. Stamper-Kurn, J. Stenger, S. Inouye, A. P. Chikkatur and W. Ketterle, Phys. Rev. Lett. 82 (1999) 2228.

[113] E. Cornell, (private communication).

[114] Z.-T. Lu, K. L. Corwin, K. R. Vogel, C. E. Wieman, T. P. Dinneen, J. Maddi and H. Gould, Phys. Rev. Lett. 79 (1997) 994.

[115] J. E. Simsarian, L. A. Orozco, G. D. Sprouse and W. Z. Zhao, Phys. Rev. A 57 (1998) 2448.

[116] Z.-T. Lu, C. J. Bowers, S. J. Freedman, B. K. Fujikawa, J. L. Mortara, S.-Q. Shang, K. P. Coulter and L. Young, Phys. Rev. Lett. 72 (1994) 3791.

[117] R. Guckert, X. Zhao, S. G. Crane, A. Hime, W. A. Taylor, D. Tupa, D. J. Vieira and H. Wollnik, Phys. Rev. A 58 (1998) R1637.

[118] J. P. Burke and J. L. Bohn, Phys. Rev. A 59 (1999) 1303.

[119] B. DeMarco, J. L. Bohn, J. P. Burke, M. Holland and D. S. Jin, Phys. Rev. Lett. 82 (1999) 4208.

[120] http:/condon.colorado.edu/ chg/Collisions.

[121] H. T. C. Stoof, Phys. Rev. Lett. 76 (1996) 10.

[122] A. G. K. Modowi and A. J. Legget, J. Low Temp. Phys. 104 (1997) 625.

[123] T. L. Ho and V. B. Shenoy, Phys. Rev. Lett. 77 (1996) 3276.

[124] B. D. Esry, C. H. Greene, J. P. Burke and J. L. Bohn, Phys. Rev. Lett. 78 (1997) 3594.

[125] B. D. Esry, Many-Body Effects in Bose-Einstein Condensates of Dilute Atomic Gases, PhD thesis University of Colorado, Boulder 1997.

[126] H. Pu and N. Bigelow, Phys. Rev. Lett. 80 (1998) 1130.

[127] B. D. Esry and C. H. Greene, Nature (London) 392 (1998) 434.

[128] M. Movre and G. Pichler, J. Phys. B 10 (1977) 2631.

[129] W. C. Stwalley, Y.-H. Uang and G. Pichler, Phys. Rev. Lett. 41 (1978) 1164.

[130] R. Napolitano, J. Weiner, C. J. Williams and P. S. Julienne, Phys. Rev. Lett. 73 (1994) 1352.

[131] K. Burnett, J. Cooper, R. J. Ballagh and E. W. Smith, Phys. Rev. A 22 (1980) 2005.

[132] K. Burnett and J. Cooper, Phys. Rev. A 22 (1980) 2027.

[133] K. Burnett and J. Cooper, Phys. Rev. A 22 (1980) 2044.

[134] J. L. Bohn and P. S. Julienne, Phys. Rev. A 54 (1996) R4637.

[135] J. L. Bohn and P. S. Julienne, Phys. Rev. A 60 (1999).

[136] E. Tiesinga, C. J. Williams, P. S. Julienne, K. M. Jones, P. D. Lett and W. D. Phillips, J. Res. Natl. Inst. Stand. Technol. 101 (1996) 505.

[137] G. Herzberg, Molecular Spectra and Molecular Structure, Vol. 1, (Krieger, Malabar, Fl., 1989).

[138] D. M. Brink and G. R. Satchler, Angular Momentum, (Clarendon Press, Oxford, 1968).

[139] M. Larsson, Physica Scripta 23 (1981) 835.

[140] R. W. Heather and P. S. Julienne, Phys. Rev. A 47 (1993) 1887.

[141] J. T. Hougen, N. B. S. Monograph 115 (1970) 1.

[142] I. Roeggen, Theor. Chim. Acta. 21 (1971) 398.

[143] M. Ya. Ovchinnikova, Theoret. Exptl. Chem. 1 (1965) 22.

[144] H. Wang, P. L. Gould and W. C. Stwalley, J. Chem. Phys. 106 (1997) 7899.

[145] W. J. Meath, J. Chem. Phys. 48 (1968) 227.

[146] H. Wang, P. L. Gould and W. C. Stwalley, Phys. Rev. A 53 (1996) R1216.

[147] J. P. Burke, C. H. Greene, J. L. Bohn, H. Wang, P. L. Gould and W. C. Stwalley, (submitted to Phys. Rev. A).

[148] R. Côté, A. Dalgarno, H. Wang and W. C. Stwalley, Phys. Rev. A 57 (1998) R4118.

[149] H. M. J. M. Boesten, J. M. Vogels, J. G. C. Tempelaars and B. J. Verhaar, Phys. Rev. A 54 (1996) R3726.

[150] C. J. Williams, E. Tiesinga, P. S. Julienne, H. Wang, W. C. Stwalley and P. L. Gould, (submitted to Phys. Rev. A).

[151] H. Wang, X. T. Wang, P. L. Gould and W. C. Stwalley, Phys. Rev. Lett. 78 (1997) 4173.

[152] J. L. Bohn, J. P. Burke, C. H. Greene, H. Wang, P. L. Gould and W. C. Stwalley, Phys. Rev. A 59 (1999) 3660.

[153] D. M. Stampur-Kurn, M. R. Andrews, A. P. Chikkatur, S. Inouye, H. J. Miesner, J. Stenger and W. Ketterle, Phys. Rev. Lett. 80 (1998) 2027.

[154] P. O. Fedichev, M. W. Reynolds and G. V. Shlyapnikov, Phys. Rev. Lett. 77 (1996) 2921.

[155] Yu. Kagan, I. A. Vartan'yants and G. V. Shlyapnikov, Zh. Eksp. Teor. Fiz. 81 (1981) 1113.

[156] L.P.H. de Goey, H.T.C. Stoof, B. J. Verhaar and W. Glöckle, Phys. Rev. B 38 (1988) 646.

[157] A. J. Moerdijk, H.M.J.M. Boesten and B.J. Verhaar, Phys. Rev. A 53 (1996) 916.

[158] B. D. Esry, C. H. Greene and J. P. Burke, (submitted to Phys. Rev. Lett.).

[159] L. M. Delves, Nuclear Physics 20 (1960) 275.

[160] C. D. Lin, Phys. Rep. 257 (1995) 1.

[161] R. C. Whitten and F. T. Smith, J. Math. Phys. 9 (1968) 1103.

[162] A. Kupperman, J. Phys. Chem. 100 (1996) 2621.

[163] J. G. Frey and B. J. Howard, Chem. Phys. 99 (1985) 415.

[164] C. de Boor, A Practical Guide to Splines, (Springer, New York, 1978).

[165] R. B. Lehoucq, D. C. Sorensen and C. Yang, http://www.caam.rice.edu/software/ARPACK.

[166] J. Macek and E. Nielsen, (private communication).

[167] C. H. Greene, (notes).

[168] E. A. Burt, R. W. Ghrist, C. J. Myatt, M. J. Holland, E. A. Cornell and C. E. Wieman, Phys. Rev. Lett. 79 (1997) 337.

[169] B. D. Esry, C. H. Greene, Y. Zhou and C. D. Lin, J. Phys. B 29 (1996) L51.

[170] B. D. Esry, C. D. Lin and C. H. Greene, Phys. Rev. A 54 (1996) 384.

[171] H. Nakamura, Int. Rev. Phys. Chem. 10 (1991) 123.

[172] J. Stenger, S. Inouye, M. R. Andrews, H. J. Miesner, D. M. Stampur-Kurn and W. Ketterle, Phys. Rev. Lett. 82 (1999) 2422.

[173] J. M. Gerton, C. A. Sackett, B. J. Frew and R. G. Hulet, Phys. Rev. A 59 (1999) 1514.

[174] J. Söding, D. Guéry, P. Debiolles, F. Chevy, H. Inamori and J. Dalibard, (preprint cond-mat/9811339).

[175] E. Tiesinga, A. J. Koerdijk, B. J. Verhaar and H. T. C. Stoof, Phys. Rev. A 46 (1992) R1167.

[176] T. P. Dinneen, K. R. Vogel, E. Arimondo, J. L. Hall and A. Galllagher, Phys. Rev. A 59 (1999) 1216.

[177] J. D. Wienstein, R. deCarvalho, J. Kim, D. Patterson, B. Friedrich and J. M. Doyle, Nature (London) 395 (1998) 148.

[178] M. Walhout, U. Sterr, C. Orzel, M. Hoogerland and S. L. Rolston, Phys. Rev. Lett. 74 (1995) 506.

[179] M. Holland, (private communication).

Appendix A

FEM basis functions

The six Hermite interpolating polynomials used as a local FEM basis are given by

$$\begin{aligned} u_1(x) &= x^2 - 1.25x^3 - 0.5x^4 + 0.75x^5 \\ u_2(x) &= 0.25(x^2 - x^3 - x^4 + x^5) \\ u_3(x) &= 1.0 - 2.0x^2 + x^4 \\ u_4(x) &= x - 2.0x^3 + x^5 \\ u_5(x) &= x^2 + 1.25x^3 - 0.5x^4 - 0.75x^5 \\ u_6(x) &= 0.25(-x^2 - x^3 + x^4 + x^5)\,. \end{aligned} \tag{A.1}$$

Appendix B

Adiabatic FEM R-matrix

The equations for the adiabatic FEM R-matrix method can be derived by inserting the adiabatic channel decomposition (Eq. 3.20) into Eq. 3.1. Using the relationships, $H = T_R + H^{\rm ad}$, $H^{\rm ad}\Phi_\gamma(\Omega,\sigma;R) = U_\gamma\Phi_\gamma(\Omega,\sigma;R)$, Eq. 3.22 for the derivative coupling, and the orthonormality of the $\Phi_\gamma(\Omega,\sigma;R)$'s leads to the following equation for b

$$\begin{aligned} b\sum_\gamma M_\gamma(R_0)M_\gamma(R_0) &= \sum_\gamma \int 2\mu M_\gamma(E-U_\gamma)M_\gamma dR \\ &\quad -\sum_\gamma M_\gamma(R_0)M'_\gamma(R_0) \\ &\quad -\sum_{\gamma,\gamma'} M_\gamma(R_0)P_{\gamma,\gamma'}(R_0)M_{\gamma'}(R_0) \\ &\quad -\int_\Omega 2\mu\Psi^* T_R\Psi dw \end{aligned} \tag{B.1}$$

where R_0 is the internuclear separation on the boundary. In order to evaluate the last integral, I need to introduce the second derivative coupling matrix Q[78]

$$Q_{\gamma\gamma'} = \left\langle \Phi_\gamma | \frac{\partial^2}{\partial R^2}\Phi_{\gamma'} \right\rangle \tag{B.2}$$

which can be related to $\underline{P}$ using[78]

$$Q_{\gamma\gamma'} = (P^2)_{\gamma\gamma'} + \partial P_{\gamma\gamma'}/\partial R\ . \tag{B.3}$$

The last integral in Eq. B.1 becomes

$$-\int_\Omega 2\mu\Psi^* T_R\Psi dw = \sum_{\gamma,\gamma'}\int M_\gamma\left[\frac{\partial}{\partial R} + P_{\gamma\gamma'}\right]^2 M_{\gamma'}dR \tag{B.4}$$

The original diabatic equations are recovered exactly provided $\partial/\partial R$ is replaced

with $\partial/\partial R + \underline{P}$. The matrix elements of Λ remain the same, however the new Γ matrix elements are given in the FEM representation by

$$\begin{aligned}\Gamma_{ij} &= 2\mu \int_{-1}^{1} u_i(x_n)(E-H)u_j(x_n)a_n dx_n \\ &\quad -\delta_{\gamma,\gamma'}\delta_{n,n_{\max}}\delta_{k,5}\delta_{k',6}/a_n \\ &\quad -\delta_{n,n_{\max}}\delta_{k,5}\delta_{k',5}P_{\gamma,\gamma'} \ . \end{aligned} \tag{B.5}$$

Again, the indices i and j include the basis function index k, the channel index γ, and the sector index n, ($i \equiv \{k\gamma n\}$ and $j \equiv \{k'\gamma' n\}$). This equation can be improved upon by first squaring the kinetic energy operator T_R and using Eq. B.3

$$(T_R)_{\gamma,\gamma'} = \delta_{\gamma\gamma'}\frac{\partial^2}{\partial R^2} + 2P_{\gamma,\gamma'}\frac{\partial}{\partial R} + \left(\frac{\partial}{\partial R}P_{\gamma,\gamma'}\right) + (P^2)_{\gamma,\gamma'} \ . \tag{B.6}$$

Plugging in the FEM basis expansion and integrating the $\underline{P}\frac{\partial}{\partial R} + \frac{\partial}{\partial R}\underline{P}$ term by parts results in the following expression for the $\underline{\Gamma}$ matrix elements

$$\begin{aligned}\Gamma_{ij} &= \int_{-1}^{1} u_k(x_n)\left[\frac{\partial^2}{\partial(a_n x_n)^2} + (P^2)_{\gamma\gamma'} + 2\mu(E - U_{\gamma\gamma'})\right] u_{k'}(x_n)a_n dx_n \\ &\quad + \int_{-1}^{1} P_{\gamma\gamma'}\left(u_k\frac{\partial u_{k'}}{\partial x_n} - \frac{\partial u_k}{\partial x_n}u_{k'}\right)dx_n \\ &\quad -\delta_{\gamma,\gamma'}\delta_{n,n_{\max}}\delta_{k,5}\delta_{k',6}/a_n \ . \end{aligned} \tag{B.7}$$

Numerical derivatives of the $\underline{P}$ matrix are no longer required in this formulation which generally improves the accuracy of the calculations. From this point on, the procedure to solve the $\underline{\mathrm{R}}$-matrix equations is exactly as outlined in chapter 3.1.

Appendix C

Thermal averaging

The total number of two-body collisions N between atoms of type a and b per unit trap volume V per unit time t is given by $n_a n_b \sigma(v_{\rm r}) v_{\rm r}$, where n_i is the density of i atoms, $v_{\rm r}$ the relative velocity of atom a with respect to atom b, and σ is the cross section. To get an average expression for the collision rate as a function of the atom cloud temperature T, we must consider the distribution $f(\vec{x}_a, \vec{x}_b, \vec{p}_a, \vec{p}_b)$ of atoms in a trap volume element dV with momenta (measured in the lab frame) $\vec{p}_a$ and $\vec{p}_b$. Further, we require the distribution function f to be unit normalized, i.e.

$$\int f(\vec{x}_a, \vec{x}_b, \vec{p}_a, \vec{p}_b) d^3x_a d^3x_b d^3p_a d^3p_b = 1 \ . \tag{C.1}$$

The thermally averaged value is then simply

$$\langle n_a n_b \sigma(v_{\rm r}) v_{\rm r} \rangle_T = \int n_a(\vec{x}_a) n_b(\vec{x}_b) \sigma(v_{\rm r}) v_{\rm r} f(\vec{x}_a, \vec{x}_b, \vec{p}_a, \vec{p}_b) d^3x_a d^3x_b d^3p_a d^3p_b \tag{C.2}$$

If the thermal de Broglie wavelengths of the atoms are small compared to the average spacing between atoms, then the gas can be treated with classical Maxwell-Boltzmann statistics. This condition can be stated numerically as

$$\left(\frac{1}{n}\right)^{1/3} \gg \frac{h}{\sqrt{3mk_B T}} \tag{C.3}$$

where m is the atomic mass, k_B is the Boltzmann constant, and T the cloud temperature. A 1 μK cloud of Rb atoms with density of the order 10^8 atoms/cm^3 easily falls into the classical regime. Assuming the cloud is in thermal equilibrium (or at least close to it) the canonical distribution function is given by the $f = C \exp(-H/k_B T)$, where H is the Hamiltonian of the system and C is a normalization constant. Moreover, in this classical regime we can neglect particle interactions. Accordingly, the

Hamiltonian for two particles in an isotropic harmonic trap is given by

$$H = \frac{1}{2m_a}\vec{p_a}^{\,2} + \frac{1}{2m_b}\vec{p_b}^{\,2} + \frac{1}{2}m_a\omega^2\vec{x_a}^{\,2} + \frac{1}{2}m_b\omega^2\vec{x_b}^{\,2} \tag{C.4}$$

where ω represents the trap frequency, and all coordinates and momenta are defined in the lab frame. (Trap anisotropies only effect the spatial density distribution of atoms, which is an experimentally measured quantity.) Next, H must be converted into the center-of-mass frame in the usual way by introducing center-of-mass and relative coordinates: where, $\vec{X}_{\rm cm} = m_a\vec{x}_a + m_b\vec{x}_b/(m_a + m_b)$, and $\vec{x}_{\rm r} = \vec{x}_a - \vec{x}_b$, $M = m_a + m_b$, $\mu = m_a m_b/(m_a + m_b)$. The transformed Hamiltonian is given by the expression:

$$H = \frac{1}{2M}\vec{P}^2_{\rm cm} + \frac{1}{2\mu}\vec{p}^{\,2}_{\rm r} + \frac{1}{2}M\omega^2\vec{X}^2_{\rm cm} + \frac{1}{2}\mu\omega^2\vec{x}^2_{\rm r}\ . \tag{C.5}$$

Equation C.2 can now be evaluated by inserting the center-of-mass Hamiltonian (Eq. C.5) into the distribution function, resulting in the following expression

$$\begin{aligned}\langle n_a n_b \sigma(v_{\rm r}) v_{\rm r}\rangle \;\; &= \;\; \frac{\int n_a(\vec{x}_a) n_b(\vec{x}_b)\, e^{-V(X_{\rm cm},x_{\rm r})/k_BT} d^3X_{\rm cm} d^3x_{\rm r}}{\int e^{-V(X_{\rm cm}+x_{\rm r})/k_BT} d^3X_{\rm cm} d^3x_{\rm r}} \times \\ &\qquad \frac{\int \sigma(v_{\rm r})\, v_{\rm r} e^{-T(p_{\rm r})/k_BT} d^3p_{\rm r}}{\int e^{-T(p_{\rm r})/k_BT} d^3p_{\rm r}}\ .\end{aligned} \tag{C.6}$$

Here, the Hamiltonian is written as sum of three terms, $H = T(P_{\rm cm}) + T(p_{\rm r}) + V(X_{\rm cm}, x_{\rm r})$. The center-of-mass momenta drops out of Eq. C.6 since the densities, cross section, and relative velocity have no explicit $\vec{P}_{\rm cm}$ dependence. Eq. C.6 can be separated into a term that depends only on the spatial coordinates and another term that depends only on the relative momenta. The spatially dependent term is effectively the total number of atoms N times the density-weighted-density $\langle DWD\rangle$,

$$N\langle DWD\rangle = \frac{\int n_a(\vec{x}_a) n_b(\vec{x}_b)\, e^{-V(X_{\rm cm},x_{\rm r})/k_BT} d^3X_{\rm cm} d^3x_{\rm r}}{\int e^{-V(X_{\rm cm},x_{\rm r})/k_BT} d^3X_{\rm cm} d^3x_{\rm r}} \tag{C.7}$$

which is an experimentally determined quantity. The remaining term is the thermal averaged rate constant K_2

$$\langle K_2\rangle = \frac{\int \sigma(v_{\rm r})\, v_{\rm r} e^{-T(p_{\rm r})/k_BT} d^3p_{\rm r}}{\int e^{-T(p_{\rm r})/k_BT} d^3p_{\rm r}}\ . \tag{C.8}$$

This expression can be simplified by evaluating the denominator and converting the integral over momenta to an integral over energy, $E = p_{\rm r}^2/2\mu$. The final expression

for the thermal averaged rate constant is given by

$$\langle K_2 \rangle = 2\sqrt{\frac{2}{\mu\pi}}\,(k_B T)^{3/2} \int_0^\infty \sigma(E) E\, e^{-E/k_B T} dE \ . \tag{C.9}$$

Cold collision experimental observables are often the rate for some process to occur. Therefore, the standard definition for the thermal averaged cross section is taken to be

$$\langle \sigma \rangle = \frac{\langle K_2 \rangle}{\langle v_{\rm r} \rangle} = (k_B T)^{-2} \int_0^\infty \sigma(E) E\, e^{-E/k_B T} dE \ . \tag{C.10}$$

Finally, in cross-dimensional mixing experiments[108] such as the one used to observe the Feshbach resonance discussed in Section 5.2, the experimental observable is actually the rate of **energy** transfer[179]. In this case, the relevant thermal average is $\langle E K_2 \rangle$, i.e. the integral in equation C.9 must include an additional factor of E.

Appendix D

Related publications

- "Recombination of three atoms in the ultracold limit", B. D. Esry, C. H. Greene, and J. P. Burke, Jr., (submitted to Phys. Rev. Lett.).
- "Determination of ^{39}K scattering lengths using photoassociation spectroscopy of the 0_g^- state", J. P. Burke, Jr., C. H. Greene, J. L. Bohn, H. Wang, P. L. Gould, and W. C. Stwalley, (submitted to Phys. Rev. A).
- "Comparison of numerical methods for the calculation of cold atom collisions", G. H. Rawitscher, B. D. Esry, E. Tiesinga, J. P. Burke, Jr., and I. Koltracht, (submitted to J. Chem. Phys.).
- "Observation of p-wave threshold law using evaporatively cooled Fermionic atoms", B. DeMarco, J. L. Bohn, J. P. Burke, Jr., M. Holland, and D. S. Jin, Phys. Rev. Lett. **82**, 4208 (1999).
- "Ultracold scattering properties of the short-lived Rb isotopes", J. P. Burke, Jr. and J. L. Bohn, Phys. Rev. A **59**, 1303 (1999).
- "Collisional properties of ultracold potassium: consequences for degenerate Bose and Fermi gases", J. L. Bohn, J. P. Burke, Jr., C. H. Greene, H. Wang, P. L. Gould, and W. C. Stwalley, Phys. Rev. A **59**, 3660 (1999).
- "Resonant magnetic field control of elastic scattering in cold ^{85}Rb", J. L. Roberts, N. R. Claussen, J. P. Burke, Jr., C. H. Greene, E. A. Cornell, and C. E. Wieman, Phys. Rev. Lett. **81**, 5109 (1998).
- "Multichannel cold collisions: simple dependences on energy and magnetic field", J. P. Burke, Jr., C. H. Greene, and J. L. Bohn, Phys. Rev. Lett. **81**, 3355 (1998).
- "Prospects for mixed-isotope Bose-Einstein condensates in rubidium", J. P. Burke, Jr., J. L. Bohn, B. D. Esry, and C. H. Greene, Phys. Rev. Lett. **80** 2097 (1998).
- "Hartree-Fock approximation for double condensates", B.D. Esry, C.H. Greene, J.P. Burke, Jr., and J.L. Bohn, Phys. Rev. Lett. **78**, 3594 (1997).
- "Impact of the ^{87}Rb singlet scattering length on suppressing inelastic collisions", J.P. Burke, Jr., J.L. Bohn, B.D. Esry, and C.H. Greene, Phys. Rev A **55**, R2511 (1997).